CBM

Compressed Baryonic Matter experiment at FAIR

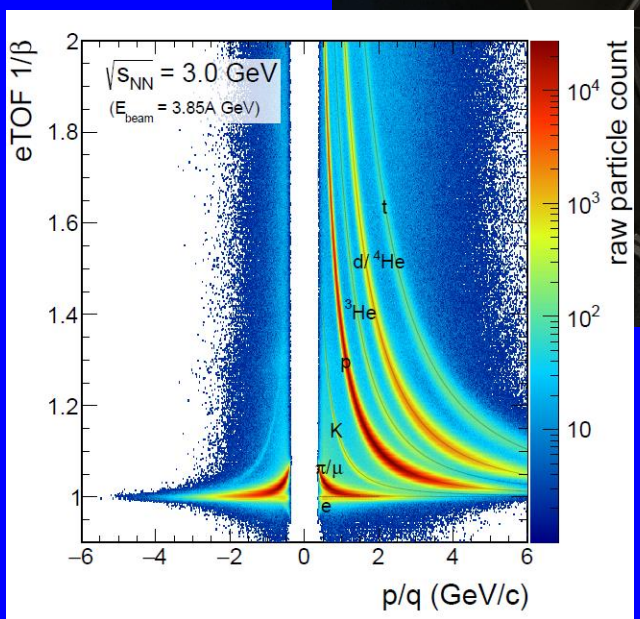

PROGRESS REPORT

2019

CBM Progress Report 2019

Imprint

Editor and responsible:

CBM Collaboration (https://fair-center.eu/for-users/experiments/cbm-and-hades/cbm.html)
Peter Senger (p.senger@gsi.de)

Reviewers:

C. Blume, S. Chattopadhyay, J. de Cuveland, I. Deppner, D. Emschermann, V. Friese, F. Guber, J. Heuser, C. Höhne, M. Kis, C. Müntz, I. Selyuzhenkov, P. Senger, C. Sturm, A. Toia

Cover page: The end-cap TOF detector at STAR, comprising 108 CBM Multi-Gap Resistive Plate Chambers

Published 2020 by GSI Helmholtzzentrum für Schwerionenforschung GmbH, Darmstadt, Germany
(http://www.gsi.de)
GSI is member of the Helmholtz association of national research centers (http://www.helmholtz.de)

ISBN 978-3-9815227-8-5

DOI: 10.15120/GSI-2020-00904 (https://dx.doi.org/10.15120/GSI-2020-00904)

Printed in Darmstadt by GSI, June 2020

The activities within the CBM project are supported by:
Bundesministerium für Bildung und Forschung, Germany, through grants 05P19RGFCA and 05P19PXFCA,
FAIR Facility for Antiproton and Ion Research through cooperation contracts FAIR-INR,
GSI Helmholtzzentrum für Schwerionenforschung GmbH through F&E cooperation contracts with Goethe-Universität Frankfurt, Justus-Liebig-Universität Giessen, and Technical University Darmstadt,
HGS-HIRe for FAIR,
HIC for FAIR Helmholtz International Center,
EU Horizon2020 “STRONG” and “ESCAPE”,
National Program on Key Basic Research Project of China-973 Program under grants 2015CB856902 and 2016YFA0400100,
Ministry of Science and Technology of China under grant 2015CB856905,
National Natural Science Foundation of China for International cooperation and Exchanges under grants 11420101004, 11461141011, and 11275108,
Czech MEYS - LM2015049, OP VVV - CZ.02.1.01/0.0/0.0/16_013/0001677,
Department of Atomic Energy (DAE), Government of India,
Department of Science and Technology, Government of India,
Ministry of Science and Higher Education, Poland,
Romanian Ministry of Research and Innovation RO-FAIR F04/16.09.2016 and NUCLEU Project Contract PN 19060103,
Russian Science Foundation grant 17-72-20234, and
FAIR-Russia Research Center.

Preface

The exploration of the QCD phase diagram at high net-baryon densities is one of the most fascinating aspects of modern nuclear physics, as it links laboratory heavy-ion collisions to cosmic objects and phenomena like neutron stars, supernova explosions, and neutron star mergers. Moreover, accelerator based experiments have the potential to unravel the microscopic degrees-of-freedom of strongly interaction matter at high density, which may undergo phase transitions, featuring phase coexistence and a critical endpoint. The mission of the CBM experiment is to shed light on the nature of high-density QCD matter by investigating diagnostic probes, which never have been measured before in the FAIR energy range, where the highest net-baryon densities will be created.

The experimental task is the high-precision measurement of multi-differential observables like the collective flow of identified particles including multi-strange (anti-) hyperons, fluctuations and correlations of various particles, and pairs of electrons and muons. To meet the various experimental requirements for the successful execution of this challenging physics program, we develop for more than a decade fast and radiation hard detectors, free-streaming read-out electronics, a high-speed data acquisition chain and ultra-fast algorithms for online event reconstruction and data analysis. The recent progress in these developments is documented in this report.

A very relevant component of our preparatory activities is the CBM phase 0 program, which includes the test of CBM prototype detectors and the free-streaming data read out and acquisition chain with beams from SIS18 within the mCBM project, the operation of TOF detector modules under experimental conditions at STAR together with the application of the CBM track and particle reconstruction software, the use of the RICH photodetectors in HADES experiments, and the test of PSD modules in the BM@N setup in Dubna, and in the NA61experiment at the CERN-SPS. It turned out, that these activities are an extremely valuable experience concerning the identification and solution of problems, which appear under realistic experimental conditions with intense heavy-ion beams.

In the recent years, the definition and realization of interfaces and infrastructures became increasingly important. The progress in the construction of the CBM cave enforces timely decisions on support structures, supply units and circuits, floor plans and radiation protection. The photo below depicts the site of the CBM cave in March 2020, the shell construction will be finalized at the end of this year. Our cave will be the first experimental location at FAIR, which is foreseen to receive beams from SIS100. For us, this is an incentive as well as a challenge to be ready in time with a CBM day one setup, and the articles in this report illustrate the various efforts undertaken by the whole collaboration towards this goal.

Many thanks to all of you for your contributions to the realization of CBM.

Darmstadt, May 2020

Peter Senger

Contents

Several of the contributions to this volume also appear in the GSI Scientific Report 2019.

Executive summary: Status of the CBM Experiment

N. Herrmann
Universität Heidelberg, Germany

The exploration of the QCD phase diagram in the region of high baryon densities remains the primary goal of the physics program of the Compressed Baryonic Matter (CBM) experiment at FAIR.

CBM will contribute with high statistics measurements to this world wide effort at the SIS100 synchrotron that despite recent development of costs is still forseen to become operational in 2025 as confirmed by FAIR council decisions in 2019. Although eventually part of the FAIR project might be slightly delayed CBM will be the first user of the heavy ion beams accelerated by the SIS100 machine. Thus all the effort of the collaboration is targeted towards constructing and setting up the so called day-1 version of CBM (see Fig. 1). This initial configuration comprises all subsystems of CBM except for the electromagnetic calorimeter. The front-end electronics will be built with full granularity and connectivity of the final plans. Although the compute system will be initially slightly reduced, measurements will be possible at unprecedented rates from the very beginning.

To achieve the goal of first measurements in 2025 with a short commissioning period the work of the CBM collaboration is shifting from R&D to validating the detector prototypes or pre-series assemblies and the full setup and preparing the production of all the components. The individual steps are shown impressively in this report.

The validation of the experimental methods is distinctly linked to CBM's Phase-0 program, i.e. (i) the operation of mCBM [1], (ii) the participation in HADES with the RICH photo detectors [2] and (iii) the participation in STAR with hardware (eTOF) [3] and software (KFParticle) [4]. Highlights from these activities that address more the system aspect of the involved devices are:
(i) mCBM:
demonstration of synchronous operation of several subsystems (STS, MUCH, TRD, TOF, RICH and PSD), common data transport via FLES to the GreenCube with high bandwidth, and offline correlation of detector hits from particle tracks in space and time.
(ii) HADES:
enhancing the number of photo electrons to above 12 per ring, development and operation of the DiRich FPGA based frontend electronics cards for dual use with TRBnet and CBM free streaming readout,
(iii) STAR:
recognition of a weakness of the CBM-TOF frontend electronics against particle flux overload resulting in the replacement of all eTOF frontend cards in 2019, demonstration of a high quality clock distribution system with a jitter of 35 ps, stable operation of a CBM DAQ/FLES subsystem with 12 data processing boards and parallel processing eventbuilders employing FairMQ over several month, demonstration of the PID capability of the CBM-TOF system, integration of the KFParticle software package into the STAR software framework and extraction of lifetime of light hypernuclei.

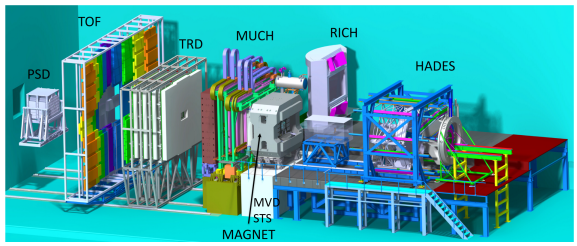

Figure 1: Day-1 setup of CBM shown together with the HADES experiment.

The progress in den subsystems towards production is equally impressive and documented in detail in the body of this report. .

- CBM building (Cave)

  During 2019 the construction of the CBM building was continued, at the present stage the ground plate is done and outer walls are erected. Also effectively the first part of the experimental setup, the beam dump, is almost finished. All this activity was reflected in preparation of the common infrastructure for experimental setup, which in this phase primary refers to the mechanical infrastructure and integration. The installation related to the upstream platform, was conceptually developed to better serve different usage cases, in particular the magnet foundation was optimized, together with HADES platform area. For the placement of downstream detectors the rail system concept is finalized and ready for tendering; the initial preparation of the ground plate for the installation of rail system has taken place. The status of the CAD representation of our experiment is shown in Fig. 1.

  Apart form the mechanical installation, the experimental infrastructure is still under development especially when it comes to installation of supplies (power, bias, gas, etc.) for the various detector subsystems. Here the progress was made in overall installation preparation and devise of plans for subsystem preassembly and installation.

  In November 2019 the Cost Assessment of the Com-

mon Infrastructure document was presented in a joint meeting of the FAIR ECE and ECSG. The document was accepted in April 2020 and served as important input to the Construction MoU, the signing of which will unlock funds for above mentioned common infrastructure activities.

- Magnet

  Having agreed on the cooling concept the magnet is in the prototyping phase of the superconducting coil. The work is proceeding according to the project plan aiming to deliver the magnet in 2023 to FAIR.

- MVD

  For the CBM Micro-Vertex Detector, the year 2019 was shaped by following our road map towards the CBM pixel sensor MIMOSIS. With MIMOSIS-0 the first sensor prototype was available and extensively tested, both in Frankfurt and in Strasbourg (IPHC). In parallel, the submission of the first full-size sensor MIMOSIS-1 was prepared, also considering the positive test results of MIMOSIS-0. The MIMOSIS-1 design was successfully reviewed during a 2-day meeting at IPHC in summer, which finally led to initializing the submission to Tower Jazz in fall. The second line of activity deals with sensor integration and vacuum operation of prototype stations (PRESTO), realized in two dedicated vacuum test stands. The second, new test stand, called UFO, highlights thermal performance studies. With the results gained in 2019, in part documented in CBM Technical Notes, the Technical Design Report was significantly updated and improved.

- STS

  The Silicon Tracking System (STS) project achieved effective start of detector construction: (1) In November 2019, series production of the silicon microstrip sensors began in industry. Scheduled for one year, monthly delivered batches of sensors are quality-inspected using dedicated test stations set up at GSI's detector laboratory. (2) The low-mass mechanical support structures for the detector ladders were manufactured from carbon fiber in industry and surveyed at GSI. (3) The engineering design review for the readout ASIC STS-XYTER was concluded and the chips' pilot production in industry prepared. A fully integrated STS module mounted on a carbon fiber ladder was tested with proton beam extracted from COSY, demonstrating excellent system performance, including the anticipated system noise. Experience gained with emerging detector components led to significant progress with detailing the system design.

- MUCH

  The MUCh system advanced by (1) PNPI and VECC teams working on the design of the mechanical system of MuCh including superstructure, absorbers and detector mounting system along with services, (2) planning of the gas system for GEM and RPC chambers, (3) testing two real-size GEM chambers suitable for the 1st MuCh station in the mCBM setup, (4) RPC R&D being carried out using a 30cm x 30cm low resistivity bakelite RPC employing readout of STS-XTER based electronics, (5) optimisation of materials in the various absorber by detailed MC studies.

- RICH

  The CBM-RICH project profited substantially from the successful participation in the 4 weeks HADES beamtime in spring 2019. 428 MAPMTs, i.e. nearly 28 000 single readout channels were running very stably and at a high performance. A timing precision of better than 220 ps could be achieved which allows efficient suppression of non-event correlated noise. The same front-end electronics' firmware was modified for integration into the mCBM streaming data taking where it performed equally well. Time and position correlations with mTOF tracks were achieved demonstrating the feasibility of adapting to triggered and untriggered data taking concepts.

  In addition the mechanical concept of the mirror wall as well as the conceptual design of a shielding box and the mechanical integration of the RICH camera into the overall detector setup were advanced. A prototype of the mirror wall has been built and 6 mirror prototypes were installed, aligned, and surveyed, with the aim to conclude for the final overall setup by end 2020.

- TRD

  The TRD project progressed significantly: (1) it saw a successful engineering design review for the outer modules of the TRD, (2) the design of the TRD support structure is close to final, (3) the development of the gas system is ongoing, (4) the readout ASIC SPADIC 2.2 has been produced within a CBM-wide engineering run, (5) Front-End-Boards have been designed and are used in mCBM, (6) the FASP-based readout chain for the inner modules is designed and being tested, (7) new time-based simulation software with detailed detector response was implemented, (8) new firmware for DPB-based data readout was prepared for the participation in the mCBM campaign, and (9) a test in summer 2019 at the DESY electron beam was run for readout validation and evaluation of different radiator arrangements.

- TOF

  The main focus in 2019 was the execution of the phase-0 experiments mCBM and eTOF at STAR that delivered valuable information for the final design of

the MRPC detectors and the readout chain. In the first year of running in the BES-II campaign of STAR at RHIC/BNL we destroyed essentially all of the eTOF front-end electronics channels by beam related events at RHIC. This could be cured by the addition of an input protection diode and the replacement of all detector mounted front-end boards. This demonstrates the usefulness of the FAIR phase-0 program for detector optimization since the behaviour has not been observed in any of the test runs before.

Besides the preparation of the Production Readiness Reviews (PRR) by taking relevant data with mCBM and eTOF the project is complemented by the exploration of new electrode materials and prototype BFTC counters at ELBE (Rossendorf) and finalizing the design of the inner wall that is exposed to the highest particle flux.

- PSD

  The PSD project advanced in 2019 by installing 20 modules as FHCal in the BM@N experiment. This installation as well as the deployment of 13 CBM-PSD modules in the NA61/Shine experiment at CERN provides important information about the characteristics of our CBM calorimeter modules as well as on suitable calibration strategies.

  The calibration concept was refined by referring to cosmic ray muons that were demonstrated to provide an excellent reference for a relative calibration of all modules within a given setup.

- DAQ/FLES

  Besides enabling the successful data taking of the mCBM and eTOF phase-0 experiments highlighted above the DAQ and FLES projects focussed on the future developments where a transition from the AFCK/FLIB system to a CRI based readout is necessary. 4 BNL-712/CRI boards were purchased from the BNL/ATLAS group and a strategic cooperation contract with BNL for the common production of BNL-712 / CRI boards was signed. In addition Infiniband HDR hardware was acquired and the procurement of new entry nodes (ASUS ESC 8000 G4) started.

- Software

  In the Computing project substantial progress was made in handling online detector data and combining the various detector subsystems in common runs merging the data to a common data stream. The successful operation of mCBM witnesses the validity of the chosen concepts. First steps were taken to change from the TObject based root classes used in the task oriented ROOT framework to more lean data classes that are suitable for efficient use in the FairMQ framework as well. A first implementation was successfully done in mCBM in terms of monitoring the T0 - counter at full rate. Optimizations are also going on in cleaning up the software structure and the software repository.

- Physics performance simulations

  The CBM Physics Working Groups were focused on establishing a coherent environment for large scale Monte-Carlo simulations required for next round of detailed physics performance studies. In particular a significant effort was made towards i) integrating different heavy-ion collision event generators with realistic particle production as well as fragment formation, which is important for realistic event characterization, ii) development of common data format for physics analysis, which is optimized for data storage usage, iii) development and integration of various physics analysis frameworks into cbmroot (such as centrality, charged hadron identification, collective flow and azimuthal correlations techniques), and iv) validation and switching to GEANT4 engine for physics simulations.

In summary, the CBM collaboration is preparing for a timely start of SIS100 operation and eagerly awaits its first physics run in 2025.

References

[1] Ch. Sturm *et al.*, CBM Progress Report 2019, this report

[2] C. Höhne *et al.*, CBM Progress Report 2019, this report

[3] I. Deppner *et al.*, CBM Progress Report 2019, this report

[4] I. Vassiliev *et al.*, CBM Progress Report 2019, this report

Micro-Vertex Detector

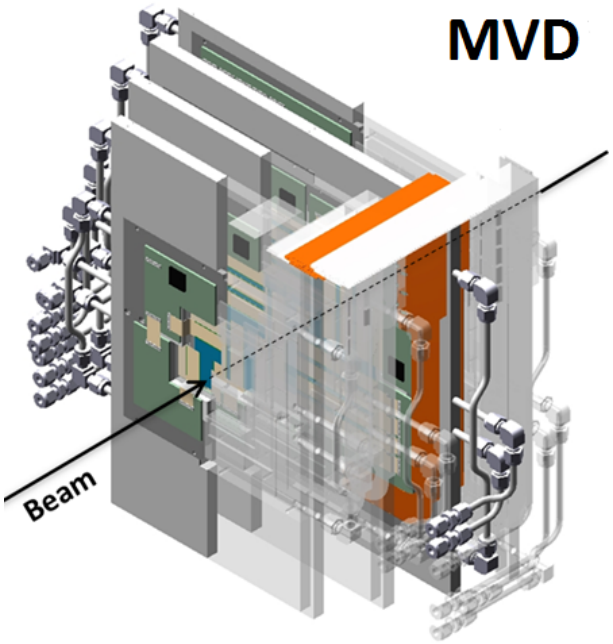

Micro Vertex Detector - Summary

C. Müntz[1], *M. Deveaux*[1], *J. Stroth*[1,2], *and the CBM MVD team*[1,2,3]
[1]Goethe University Frankfurt, Germany; [2]GSI, Darmstadt, Germany; [3]PICSEL group, IPHC Strasbourg, France

For the CBM Micro-Vertex Detector, the year 2019 was shaped by following our road map towards the CBM pixel sensor MIMOSIS. With MIMOSIS-0 the first sensor prototype was available and extensively tested, both in Frankfurt and in Strasbourg (IPHC). In parallel, the submission of the first full-size sensor MIMOSIS-1 was prepared, also considering the positive test results of MIMOSIS-0. The MIMOSIS-1 design was successfully reviewed during a 2-day meeting at IPHC in summer, which finally led to initializing the submission to Tower Jazz in fall. The second line of activity deals with sensor integration and vacuum operation of prototype stations (PRESTO), realized in two dedicated vacuum test stands. The second, new test stand, called UFO, highlights thermal performance studies. With the results gained in 2019, in part documented in CBM Technical Notes, the Technical Design Report was significantly updated and improved.

Sensor:
The MIMOSIS sensor is designed to achieve a spatial precision of better than 5 µm in combination with a time resolution of 5 µs, a thickness of 50 µm and a peak rate capability of 70 MHz/cm^2. The design was started from the successful ALPIDE sensor used in the ALICE ITS upgrade, but complemented with numerous new features aiming, among others, for substantially improved radiation tolerance and rate capability. A dedicated logic to pre-process, flatten and readout the enormous free streaming data flow is being developed, coping with both the expected fluctuations in beam intensity and the in-homogeneous occupancy over the sensor surface due to the fixed target geometry. The MIMOSIS-0 prototype, which is to demonstrate the pixel architecture and the first, priority-encoded data processing stage was tested in 2019. The timing performance was found to remain comfortably below the 5 µs frame readout time, which is by one order of magnitude better than initially considered for CBM. Therefore, in contrast to earlier worries, mostly no event or single channel pile-up is to be expected for operating the MVD at a nominal mean collision rate of 100 kHz Au+Au.

After irradiating the sensor to doses of up to 3 MRad and one year room temperature annealing, we observe the noise of the pixels to increase from 13 e ENC to about 16 e ENC at room temperature. This noise increase, which is complemented by a ~ 25 e threshold shift is not considered to endanger the operation of the sensor. Weak points in the DACs were also observed, understood and presumably eliminated by suited design improvements.

The improved structures will be found in the MIMOSIS-1 prototype, which is expected back from production in Q2/2020. This first full size sensor will host improved pixel structures and most digital processing and data compression circuits. Moreover, the sensor will be protected from single event upsets as caused by direct heavy ion hits by implementing a triple redundant logic in the most crucial circuit elements. Testing MIMOSIS-1 will be a major activity in 2020/21 and guide the optimization of the final sensor design.

Sensor integration: prototype operation and thermal performance:
Operating detector prototype modules continuously under most realistic conditions is a mandatory step for validating their technological concept. In case of the MVD, a dedicated vacuum vessel is available since years and mainly used for long-term operation studies with the full-size MVD prototype module PRESTO. EPICS-based DCS runs PRESTO, equipped with MIMOSA-26 sensors, under defined conditions for many months in a row, yielding insights in long-term effects. Lately, a vacuum-compatible radioactive ^{55}Fe source was placed close to PRESTO to study e.g. effects on S/N and data quality in more detail. At the same time, DAQ and DCS including archiving of environmental data is exercised.

A second vacuum test stand, called "UFO", was set up and put into operation with the focus to further tune the cooling concept of the MVD. It relies on mono-phase cooling of heat converters holding sensor carriers which efficiently conduct the produced heat of the sensors to the converters. While TPG and pCVD diamond were identified quite early in the project as optimum materials for the sensor carrier, the layout of the heat converters as well as the running parameters of the cooling system was to be further detailed. Measurements employing UFO allowed for systematic studies w.r.t. (i) optimizing the heat converter, (ii) selecting the coolant, and (iii) comparing measurements with expectations from simulations. As a result, we found that predictions on parameters characterizing the thermal performance of the cooling concept fit well with the measured ones. With the coolant NOVEC-649 we have identified a medium which will safely allow for the projected $<0^o$ C operation of the MVD[1]

[1]Note, this result relies on the projected low heat dissipation of MIMOSIS.

Toward the MIMOSIS sensor of the CBM-MVD*

F. Morel[1], *M. Deveaux*[†3], *J. Stroth*[2,3], *M. Winter*[‡1], *and the CBM MVD team*[1,2,3]
[1]IPHC, Strasbourg; [2]GSI, Darmstadt; [3]Goethe University Frankfurt am Main

The MIMOSIS CMOS Monolithic Active Pixel Sensor will be used as sensor technology for the CBM Micro Vertex Detector (CBM-MVD). We update the development goals, the status and the plans for the related R&D.

The CBM-MVD aims to measure secondary decay vertices of particles decaying via the weak force with an precision of ~ 50 µm. Moreover, it will assist the tracking of low momentum particles in CBM. Both calls for its sensor technology to feature a spatial precision of $\lesssim 5$ µm and a material budget of about $0.05\ \%\ X_0$ per station. Moreover, to allow for operating at an average collision rate of 100 kHz Au+Au, the sensor has to resist a peak particle rate of up to 70 MHz/cm^2 and to withstand very inhomogeneous radiation doses peaking at 7×10^{13} n_{eq}/cm^2 and 5 MRad per year. We aim for a time resolution better than 5 µs, which is considered sufficient to separate the individual collisions.

To match those ambitious requirements, we are developing a next generation CMOS Monolithic Active Pixel Sensor named MIMOSIS. The ~ 5 cm^2 large and 50 µm thin sensor will feature 504 rows of 1024 pixels with a surface of 26.9×30.2 µm^2. Three buffer stages will flatten out the spatial and temporal occupancy fluctuations expected and reduce the peak data rate to 2.4 Gbps.

MIMOSIS is being developed starting from ALPIDE [1] but hosts a number of novel features. It forms a highly complex and radiation tolerant system-on-chip. The signals of minimum ionizing particles comprised of few $100\,e$ will be amplified and discriminated on the pixel itself. Hereafter, the data is concentrated by a multi-staged priority encoder. Internal digital data processing circuits will perform limited cluster finding, compress the data and translate it to a high level data protocol before sending it out.

MIMOSIS is being designed to tolerate high integrated radiation doses. It is planned to realize the steering logic in triple redundant electronics, which is to compensate for possible bit flips as typically generated by the impact of heavy ions in CMOS electronics. Those functionalities are complemented by numerous test and self-diagnosis circuits.

To develop MIMOSIS, we foresee to submit four prototypes. The first prototype, the small sized MIMOSIS-0 [2, 3], aimed to test the design of the analog readout chain, the internal trim-DACs, and the priority encoder. Moreover, it hosts innovative AC coupled pixels optimized for depleting the active volume. Based on the result of successful test conducted with MIMOSIS-0 in 2019, MIMOSIS-1 was submitted in Q1/2020. This first full-sized sensor hosts the buffers used for flattening the data and innovative sensing elements [4]. The latter will be fully depleted and thus feature outstanding radiation hardness, potentially with mild draw-backs in spatial resolution. The tests will guide our future design choices on the pixel flavor. MIMOSIS-2, which is scheduled for submission in Q2/2021, will host the final pixel design and all features including full triple redundancy and data processing. The final chip, MIMOSIS-3 is scheduled for submission by the end of 2022 and is foreseen to eliminate possible weaknesses spotted during the tests of the previous prototypes. The latter are each submitted together with a number of smaller chips. Those are to address questions on specific building blocks, which are hard to access on the fully integrated MIMOSIS-prototypes.

	MIMOSIS	Status
Pixel	1024×504	OK
Pixel size	26.9×30.2 µm^2	OK
Spatial precision	$\lesssim 5$ µm	Test pending
Thickness	50 µm	OK
Time resolution	~ 5 µs	OK [3]
Readout	Global shutter	OK
Max. data rate	8×320 Mbps	Test pending
Ionizinig rad. tol.	5 MRad	> 3 MRad
Non. Io. rad. tol.	$>$ 5E13 n/cm^2	$\gg$ 1E13 n/cm^2

Table 1: Selected design goals for MIMOSIS and status of the sensor R&D. Ionizing and non-ionizing rad. tolerance as reported for MIMOSIS-0 [3] and for ALPIDE [1], respectively. ($n/cm^2 \equiv n_{eq}/cm^2$)

The development of MIMOSIS is complemented by an intense test program carried out by IPHC, GSI and Goethe University Frankfurt.

References

[1] M. Suljic et al., JINST 11.11 (2016): C11025

[2] M. Deveaux et al., NIM-A Vol. 958 (2020) 162653, https://doi.org/10.1016/j.nima.2019.162653

[3] B. Arnoldi-Meadows et al., this progress report.

[4] M. Munker et al., arXiv:1903.10190v1 [physics.ins-det] 25 Mar 2019

* This work was supported by BMBF (05P15RFFC1), GSI and HIC for FAIR.

† m.deveaux@gsi.de

‡ Now at IJCLab, Orsay

First Observations on the TID Tolerance of MIMOSIS-0*

B. Arnoldi-Meadows[1], *M. Deveaux*[†1], *J. Stroth*[1,2], *and the CBM MVD team*[1,2,3]

[1]Goethe University Frankfurt, Germany; [2]GSI, Darmstadt, Germany; [3]PICSEL group, IPHC Strasbourg, France

MIMOSIS-0 is the first prototype for the future MIMOSIS CMOS monolithic active pixel sensor (CPS) to be used in the micro vertex detector (MVD) of CBM. We show first results on the noise and total ionization dose (TID) tolerance of the device.

Being operated at a collision rate of 100 kHz Au+Au or 10 MHz p+Au, the MVD will be exposed to highly in-homogeneous radiation doses peaking at up to 7×10^{13} n_{eq}/cm^2 and 5 MRad per year. MIMOSIS [1] will have to tolerate those doses before being routinely replaced. Its small (26.88×30.24 μm^2) pixels cannot host trim DACs. All pixel amplifiers and shapers of the 504×1024 pixel matrix share essentially[1] the same reference voltages and have thus to be operated with a common tuning. One expects that radiation damage will modify the properties of the transistors amplifying the few 100 e signal created by minimum ionizing particles (MIP). The expected radiation dose gradients of one order of magnitude over the pixel matrix do not allow to compensate those changes by modifying the reference voltages. The sensor must thus tolerate the doses without such compensation, which forms a particular design challenge.

MIMOSIS-0 was designed by the PICSEL group of IPHC Strasbourg and tested within a common project. We irradiated MIMOSIS-0 prototypes [2] featuring the same pixels as foreseen for the final MIMOSIS with up to 3 MRad with the soft X-ray source at KIT. The on-chip DACs of the chips showed features short after the fast irradiation. The features were understood and an improved DAC was designed. The consecutive MIMOSIS-1 prototype was submitted in March 2020. It should be mentioned that the initial DACs were found operational without significant damage after one year of room temperature annealing.

As the initial test protocol failed, the pixels of the irradiated sensors could only be tested after this annealing time. The tests were performed by setting a given threshold, injecting pulses with increasing amplitude to the charge collection node of the pixels and measuring the probability of the pixel to detect the pulse. This S-curve scan yields the threshold and the noise of the individual pixels. The thresholds of the pixels follow a mostly Gaussian distribution, which reflects the production tolerances of the in-pixel transistors. The width of this distribution is referred to as fixed pattern noise (FPN). It determines the minimum detection threshold and thus ultimately the detection efficiency of the CPS for MIPs.

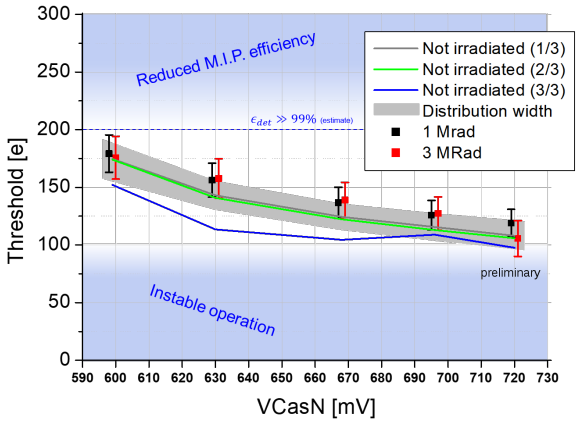

Figure 1: Threshold of irradiated and three non-irradiated sensors as function of the threshold steering voltage VCasN. The error bars represent the Fixed Pattern Noise (see text).

The results of the study are shown in Fig. 1 for DC coupled pixels being operated with a reverse bias of -1 V and fast settings [3]. One observes two out of three non-irradiated sensors and the irradiated sensors to show an almost identical FPN (about 12 e ENC) and no radiation induced threshold shift above 25 e is seen. A third non-irradiated sensor exhibits different results, which remains to be understood. The thermal noise remained below 6 e ENC, which is the sensitivity limit of the noise measurement protocol.

A vulnerability of the sensors to fast, non-annealed total ionization dose (TID) remains to be excluded. However, the results presented support the statement that MIMOSIS will fulfill the challenging requirements of CBM. This holds in particular as radiation tolerance tests on transistors manufactured in the same technology [4] suggest a saturation of the TID effects for doses between 1 and 10 MRad.

References

[1] F. Morel et al., this report.

[2] M. Deveaux et al., NIM-A Vol. 958 (2020) 162653, https://doi.org/10.1016/j.nima.2019.162653

[3] B. Arnoldi-Meadows et al., this report.

[4] H. Hillemanns et al., Proceedings of IEEE NSS/MIC 2013

*This work was carried out in a common R&D program with the PICSEL group of IPHC Strasbourg. It was supported by BMBF (05P15RFFC1), GSI and HIC for FAIR.

† m.deveaux@gsi.de

[1]As exception, the threshold may be tuned differently for four sub-sectors.

The Time Resolution of the MIMOSIS-0 CPS Prototype*

B. Arnoldi-Meadows[1], *M. Deveaux*[†1], *J. Stroth*[1,2], *and the CBM MVD team*[1,2,3]
[1]Goethe University Frankfurt, Germany; [2]GSI, Darmstadt, Germany; [3]PICSEL group, IPHC Strasbourg, France

MIMOSIS-0 is the first prototype for the future MIMOSIS CMOS monolithic active pixel sensor (CPS) to be used in the micro vertex detector (MVD) of CBM. We report about the time resolution of this prototype.

MIMOSIS-0 [1] was developed by the PICSEL group of IPHC Strasbourg. It hosts 8064 AC and as many DC coupled pixels. 24 pixels of each kind feature an analog output of the comparator signal of the on-pixel preamplifier line. The preamplifiers of one randomly chosen sensor were tested by injecting defined pulses with charge Q via a 160 aF capacitor to their input and observing this comparator response with an oscilloscope.The steering voltages of the preamplifiers were optimized to obtain a fast pixel response together with a reasonably low noise (see [2] for noise performance).

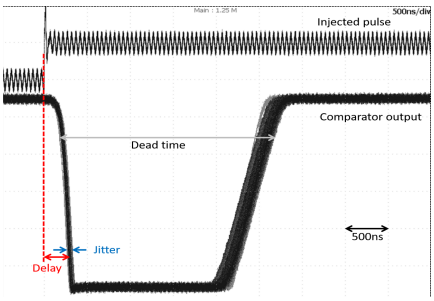

Figure 1: Charge injection and analog test output signal after comparator with response time definitions.

MIMOSIS will feature a frame oriented, 5 µs global shutter readout to separate Au+Au collisions at a collision rate of 100 kHz. The amplifier-shaper-discriminator chain of the individual pixels detects particle impacts and samples and holds it until a "next frame" signal is set. The pixel will become sensitive again if i) the next frame has started and ii) the analog pixel signal has fallen below threshold. A good timing accuracy of the analog signal is needed to assign the hit to the correct frame. A short time-over-threshold minimizes the number of inactive pixels at the time of the next physics event.

The comparator output signal and the charge injection pulse into the pixel are shown in figure 1. We measure the delay ($t_{\mathrm{D}}(Q)$) between the charge injection and the time the comparator output reaches 80 % of its saturation amplitude. The jitter ($t_{\mathrm{J}}(Q)$) is defined as min. to max. of this delay for 10k pulses. The time-over-threshold (corresponds to the dead time) reflects the time the comparator remains above 20 % of the saturation value. The results of the measurements as function of the injected signal are shown in figure 2.

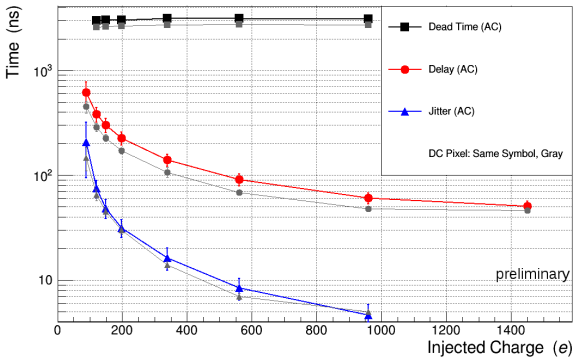

Figure 2: Response times at – 1 V reverse bias. Error bars represent pixel-to-pixel variations in response.

We consider that the analog time resolution amounts to the time walk $t_{\mathrm{TW}} = t_{\mathrm{D}}(1450\ e) - t_{\mathrm{D}}(90\ e)$ plus half the jitter $t_{\mathrm{J}}(90\ e)$. It amounts to $\lesssim$ 700 ns according to the measurements, which matches our requirements. The estimated most probable signal charge amounts to 850 e for a 25 µm thick active medium. Therefore, presumably more than 95 % of all hits will be recorded with a time resolution of $\lesssim$ 300 ns. The time-over-threshold remains slightly above 3µs and thus below the frame time.

We conclude that the pixel design of MIMOSIS-0 is suited to separate collisions at a 100 kHz Au + Au collision rate. Moreover, the channel dead time remains below the average time between the events. Therefore, mostly no event pile-up is to be expected.

References

[1] M. Deveaux et al., NIM-A Vol. 958 (2020) 162653, https://doi.org/10.1016/j.nima.2019.162653

[2] B. Arnoldi-Meadows et al., this progress report.

*This work was carried out in a common R&D program with the PICSEL group of IPHC Strasbourg. It was supported by BMBF (05P15RFFC1), GSI and HIC for FAIR.

† m.deveaux@gsi.de

CBM-MVD: Status of Operating the Prototype PRESTO 24/7 in Vacuum*

P. Klaus† [1], *M. Koziel*[1], *C. Müntz*[1], *J. Stroth*[1,2], *and the CBM MVD team*[1,2,3]

[1]Goethe University Frankfurt, Germany; [2]GSI, Darmstadt, Germany; [3]PICSEL group, IPHC Strasbourg, France

The CBM Micro-Vertex Detector will be operated in vacuum to minimize multiple scattering. Hence, it is mandatory to operate and characterize already prototypes like "PRESTO"[1] 24/7 in a dedicated vacuum test stand, which provides all required services, including cooling, as well as means to run the DAQ and access and archive environmental parameters. Recently, the focus was put to long term operation with a data load provided constant irradiation with X-rays of a ^{55}Fe source. Figure 1 shows the setup mounted inside the vacuum chamber.

Figure 2 (b) exhibits data from one of the PRESTO sensors exposed for seven hours to a ^{55}Fe source through an Al-plate (Fig. 2 a) with machined cut-outs of typically 1 and 2 mm width. These cut-outs are clearly visible in the hit pattern shown. The detailed analysis of these structures, after properly correcting for geometrical effects (aspect ratio, setup and source dimensions) might allow for assessing long-term trends of sensor properties.

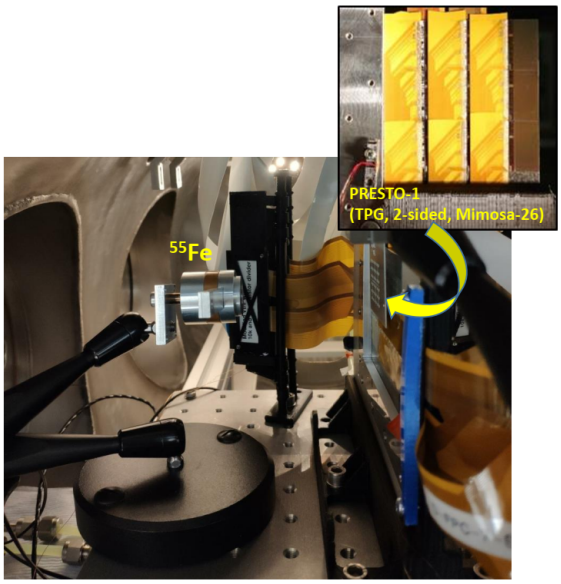

Figure 1: PRESTO 24/7 in vacuum: Setup with an ^{55}Fe radioactive source (left) irradiating the sensors through an Al-plate mask with a precisely CNC-machined pattern.

The presence of hits in regions covered with the Al-plate indicates sources other than photons emitted by the radioactive source. The quantitative analysis has not yet concluded. Possible candidates are fake hits, common-mode noise and cross-talk inside the sensor r/o architecture, e.g. due to the need to use one detection threshold for each of the four banks of the sensor employed, respectively. However, the cluster size analysis of hits might reveal also other sources due to natural radioactivity and cosmic rays.

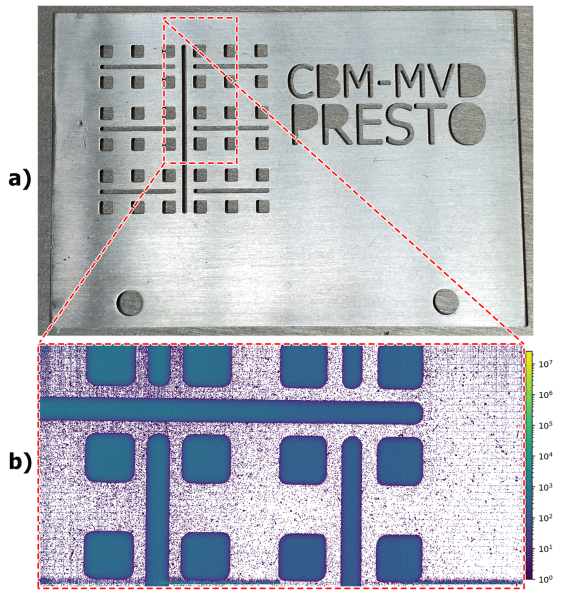

Figure 2: a) Al-plate mask with a precisely CNC-machined pattern. b) Hit pattern of a PRESTO sensor MIMOSA-26 (21.2 $\times$ 10.6 mm^2), irradiated for seven hours with ^{55}Fe photons shielded by the mask. The quadratic structures correspond to 2 $\times$ 2 mm^2 openings in the Al-plate.

24/7 operation of MVD prototypes will continue to systematically investigate long-term operation of sensors (like MIMOSIS-1) mounted on dedicated carriers and read-out with state-of-the-art FEE in a realistic environment. This also enables us to monitor material properties and evaluate integration concepts w.r.t. vacuum operation at below 0^{o}C temperatures, as well as optimizing the grounding strategy of the detector.

References

[1] M. Koziel et al., Nuclear Instruments and Methods in Physics Research A, doi:10.1016/j.nima.2016.05.093

* Work supported by BMBF (05P19RFFC1), GSI and HIC for FAIR.

† P.Klaus@gsi.de

CBM-MVD: A Test Stand for the Thermal Characterization of MVD Stations*

P. Klaus† [1], *M. Koziel*‡ [1], *C. Müntz*[1], *J. Stroth*[1,2], *and the CBM MVD team*[1,2,3]

[1]Goethe University Frankfurt, Germany; [2]GSI, Darmstadt, Germany; [3]PICSEL group, IPHC Strasbourg, France

The MVD will be operated in the target chamber vacuum, to minimize multiple scattering. Hence, an efficient cooling concept is mandatory, which also comprises vacuum compatibility of the components employed. This motivates the construction of a dedicated test chamber, called "UFO", optimized to characterize/evaluate the thermal performance of MVD stations in vacuum. This includes components of the MVD (e.g., heat sink and carriers loaded with Kapton heaters) as well as the cooling system with its coolant. The results will be used to optimize the heat-sinks and tune our simulation models (Spice- and CFD- based). The latter will be used to further optimize the heat-sink performance prior to its production.

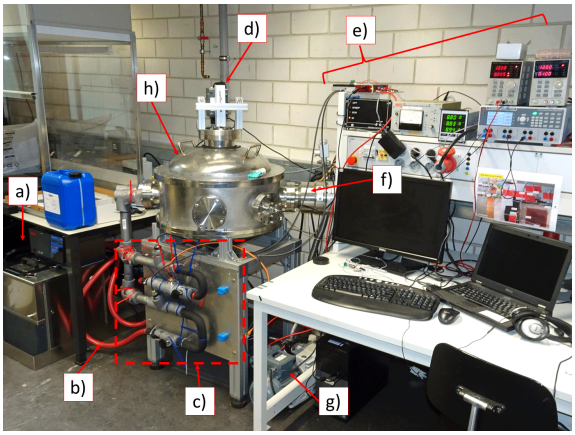

Figure 1: The test setup at IKF (GUF) named "UFO": a) HUBER cooling system, b) cooing pipes, c) distribution and control panel, d) IR camera, e) steering and R/O electronics, f) turbo molecular pump, g) scroll pump, h) vacuum chamber.

The test-stand "UFO" is shown in Fig. 1 and 2, and a device under test in Fig. 3. The setup comprises a cooling system, vacuum chamber ($\varnothing \approx 65$ cm and height ≈ 57 cm), scroll and turbo-molecular vacuum pumps (vacuum of 10^{-8} mbar can be reached.), cooling distribution panel based on Swagelok 12 mm components, infra-red camera with a dedicated view-port, and steering and monitoring electronics that could be connected to the EPICS control and monitoring system. We constantly monitor and archive the cooling liquid flow, its pressure and temperature at the heat-sink inlet and outlet. The device under test (heat-sink and carrier) is populated with multiple PT-100 sensors providing readout with precision better than 0.5 °C. So far, the system was used for thermal characterization of a heat-sink comprising $80\times80\times0.15$ mm^3 pCVD diamond and $80\times80\times0.38$ mm^3 TPG carriers. The outcome is reported in [1].

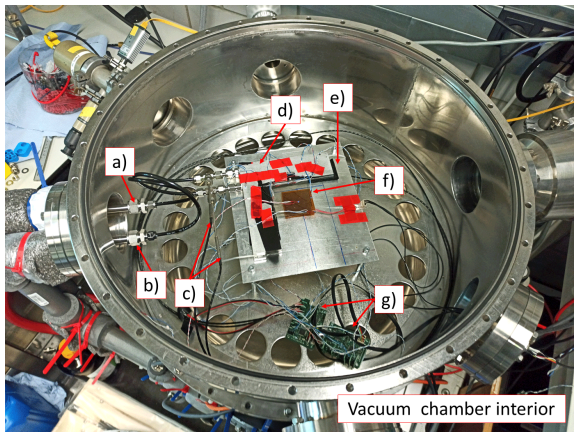

Figure 2: Vacuum chamber interior: a) inlet, b) outlet, c) PT-100 temperature sensors, d) heat-sink, e) support table, f) carrier material under study with heater attached, g) R/O for PT-100 sensors.

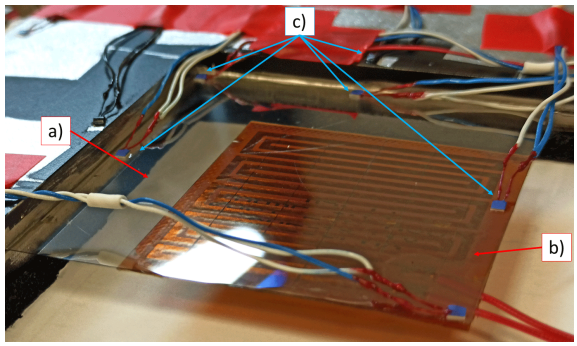

Figure 3: $80\times80\times0.15$ mm^3 pCVD diamond a) equipped with a Kapton heater b) and multiple PT-100 temperature sensors c).

References

[1] P. Klaus et al., "CBM-MVD: Measurements and Simulations on Thermal Performance.", this report.

* Work supported by BMBF (05P19RFFC1), GSI and HIC for FAIR.

† P.Klaus@gsi.de

‡ M.Koziel@gsi.de

CBM-MVD: Measurements and Simulations on Thermal Performance*

P. Klaus[1], *M. Koziel*[1], *C. Müntz*[†1], *J. Stroth*[1,2], *and the CBM MVD team*[1,2,3]

[1]Goethe University Frankfurt, Germany; [2]GSI, Darmstadt, Germany; [3]PICSEL group, IPHC Strasbourg, France

The MVD of CBM offers high-precision particle tracking and vertex reconstruction close to the target. Hence, vacuum operation is mandatory, triggering an additional effort w.r.t. cooling of electronic components inside the vacuum, that is sensors and front-end electronics. The total power dissipation is expected to be lower than 250 W only, thanks to the announced low power dissipation of $<$50 mW/cm^2 of the sensors (MIMOSIS). However, to allow for a baseline sensor operation temperature below 0^o C, efficient cooling is mandatory. The MVD concept relies on mono-phase fluid cooling, employing dedicated heat converters outside the acceptance, and high-performance materials (pCVD diamond and Thermal Pyrolytic Graphite (TPG) sheets as sensor carriers clamped to the heat converters) optimized for heat conduction. This report presents first results on the thermal performance of those sensor carriers and heat converters, in comparison to expectations. The measurements have been conducted in vacuum (UFO setup [1]), employing heat foils to mimic sensor operation.

Sensor carriers: Temperature differences on carriers with a lateral size of 80$\times$80 mm^2 and a thickness of 380 (TPG) and 150 μm (pCVD diamond) have been studied.

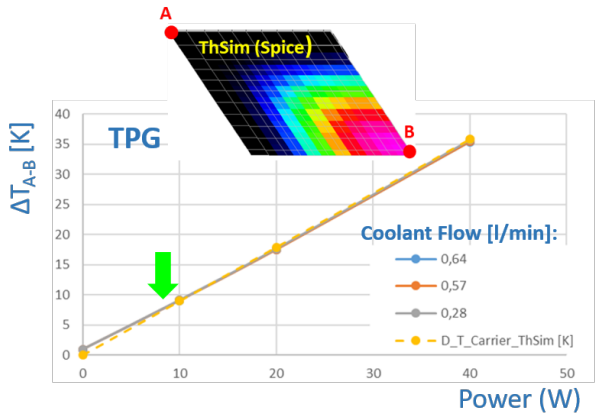

Figure 1: Temperature difference between the hottest and coldest point of a TPG carrier vs. the total power, produced by a dedicated heat sheet covering approximately the same area as occupied by the MVD sensors, aligned to the corner B. The coolant temperature was adjust such that the point A was kept at -10^o C. The inlay sketches the temperature distribution simulated by the ThSim package (based on Spice), the dashed line in the diagram indicates the simulation results, compared to measurement (symbols). Green arrow: MVD operation region.

* Work supported by BMBF (05P19RFFC1), GSI and HIC for FAIR.

† C.Muentz@gsi.de

Fig. 1 compares for TPG measurements to simulations results from ThSim [2], a software which translates thermal to electrical properties to allow for (Lt)Spice evaluation. The match between measurement and simulation for both, pCVD diamond (not shown) and TPG is almost perfect. For TPG, a 2-dimensional material with outstanding heat conduction in lateral dimensions only, the reduced heat conduction into the bulk does obviously not play a sizable role due to the thickness.

Heat converters extract the heat of one station quadrant, respectively, and are made of Aluminum with customizes buried heat channels. Fig. 2 depicts a performance plot based on the temperature difference between Aluminum bulk and the coolant, a measure of how efficient heat is extracted. The measurements are compared to calculations

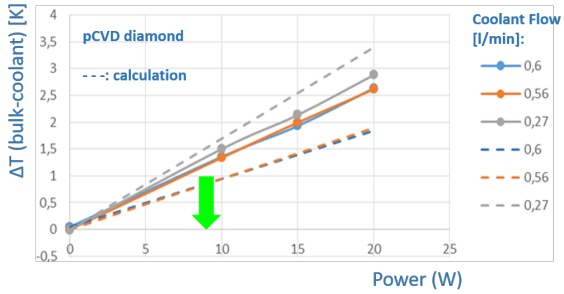

Figure 2: Measured (symbols) and calculated (dashed lines) temperature difference between heat converter bulk and coolant (Glycol:water = 1:1) for different flows. Temperature at point A (Fig.1) = -10^o C. Green arrow: MVD operation region.

(formulas) based on assessing the convective and conductive heat transfer properties of the system (geometry and coolant specifications). Both exhibit a linear dependence on the power. Deviations as a function of coolant flow indicate that the dedicated cooling channel geometry cannot be easily described with linear equations. However, the deviations are below 1 K in the region of interest.

The results gained so far suggest that the projected operation temperature range of the sensors below 0^o C can be guaranteed with the proposed MVD cooling concept.

References

[1] P. Klaus et al., "Test stand for heat-sink thermal characterization", CBM Progress Report 2019

[2] `http://thsim.sourceforge.net/`, `https://www.analog.com(LtSPice)`

Silicon Tracking System

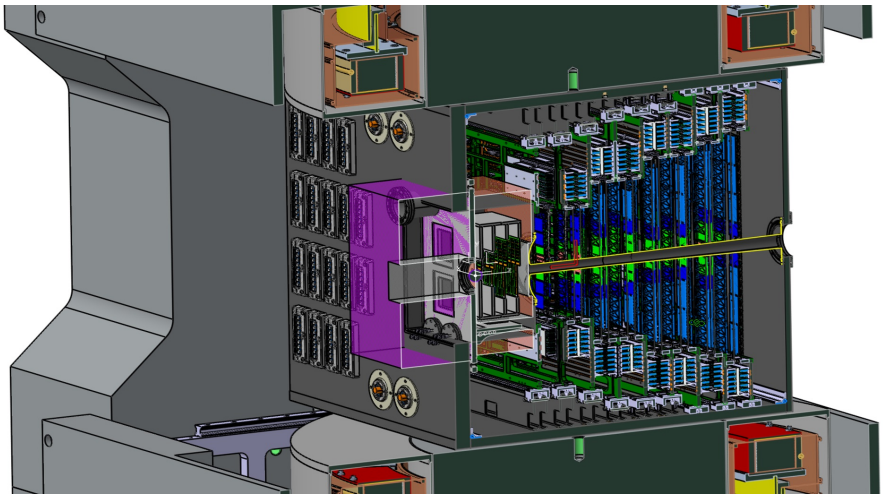

Silicon Tracking System – Summary

J. M. Heuser[1], *H. R. Schmidt*[1,2], *and the CBM STS working group*
[1]GSI, Darmstadt, Germany; [2]Universität Tübingen, Germany

In the reporting year of this Progress Report, effective start of construction has been achieved for CBM's main tracking detector, the Silicon Tracking System (STS). Main achievements are highlighted hereafter and are further detailed in the individual contributions of this chapter.

Series production of silicon sensors started

The STS detector will consist of 8 logical tracking stations, realized with 9 mechanical units that carry 876 detector modules, is to be installed in a 1 Tm dipole magnetic field close to the target. Its most central components, the silicon microstrip sensors, were awarded for production at Hamamatsu Photonics, as a result of a sensor readiness review held in 2018 and a subsequent tendering procedure that concluded in March 2019. Production of the silicon microstrio sensors was launched in Summer 2019, and monthly deliveries of batches up to 100 sensors commenced in November of the same year. The production will comprise about 1100 sensors, doubly-sided segmented and in four dimensional variants, and will be completed after one year. A key criterion for Hamamatsu was the vendor's capability to produce on 6“ wafers, and within the mentioned time slot. The sensor purchase, representing a significant fraction of the STS project costs, has been financed through project funds contributed in particular by the Russian and German partners. Order and delivery is made to FAIR at the site in Darmstadt. Consequently, the STS project allocated the site acceptance testing also there, installing specific quality assurance testing stations developed in the CBM STS project teams at GSI and the University of Tübingen into the Clean Room space of GSI's Detector Laboratory. There, electrical and optical inspection is being carried out and the information is combined with the final inspection at the vendor's to be available for the series STS detector module construction.

Carbon fiber ladders produced

Further components that have been serially produced in 2019 are the carbon-fiber support structures onto which the detector modules, i.e. functional building block with silicon sensors, microcables and front-end electronics, will be mounted to. In total 109 detector ladders will be arranged on the STS mechanical units. After different trials in industry, a small engineering company in Darmstadt was able to produce the structures with the required specifications for the STS detector project. The mechanical and form stability at low mass was confirmed on prototypes using a dedicated optical survey procedure at GSI, before the series production was started.

Fully integrated module tested in beam

A system demonstrator, mSTS, was operated in mCBM in March 2019, having one module mounted on a carbon fiber ladder and installed on a mechanical C-frame equipped with prototype powering and data aggregation electronics. An issue with a protective glue, lifting electrical contacts under thermal stress, made only a fraction of the module's front-end electroncics functional. The module assembly was reworked with a different glue, solving the issue. A fully operational module was tested in the intense proton beam at COSY in November 2019. The targeted system noise was demonstrated, as well as further excellent system performance. This gave important input to concluding the design review of the readout ASIC STS-XYTERv2.2 for its series production [1] in 2020. Returned from the COSY beamtime, the module was operated also in mCBM. A 8 kHz noise source only there, and mSTS sensitivity to it, has been subject to detailed investigation with respect to grounding, power supplies filtering, and signal path. This work is still to be continued.

Progress with system integration

Various aspects of system integration are being worked on. The module assembly procedure has been fully developed. The standard procedure is based on aluminum microcables. A first module with alternative copper microcables has been tested. The ladder assembly demonstrated its precision on mCBM prototypes; first full-scale assembly tools have been designed and produced. A different assembly procedure has been developed at JINR, and tooling deployed. Cooling of the front-end and powering electronics is a central topic of the system design. It was topic of a Conceptual Design Review [2] in December 2019, resulting in a recommendation for a conventional NOVEC based liquid cooling system. A thermal demonstrator has been conceived to verify experimentally the efficiency of liquid electronics cooling and gas cooling of sensors. The system engineering has been further advanced in 3D detailling. The cover picture of this chapter, as well as Fig. 1, shows the current design status of STS, target vacuum, MVD and beampipe together with passive materials of the enclosure in the dipole magnet. Renewed simulation studies have been carried out to assess the detecor's physics performance, as well as geometrical alignment procedures

for its components. The application of STS-like modules and ladders in the silicon tracker of the BMN experiment at Nuclotron, JINR, a related project in terms of detector technology and physics, is being advanced in parallel.

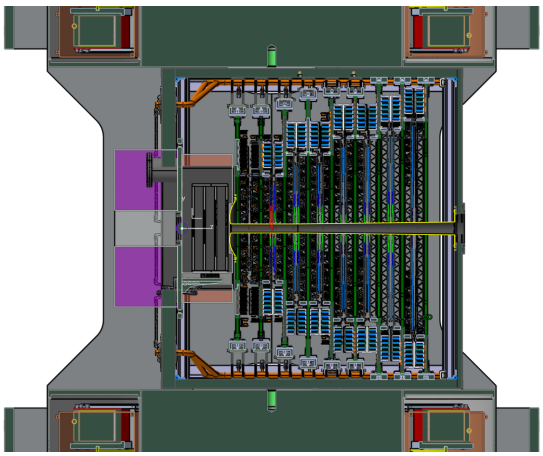

Figure 1: Cut-through view of STS detector system with target vacuum box, Micro Vertex Detector (MVD) and beam pipe in the dipole magnet.

Timeline, project members

The series assembly of the STS modules, ladders, and the system integration are panned from 2021 to 2024. An Engineering Design Review on the modules and ladders will take place in 2020. Coronavirus impact on the timeline has to be considered. The assembly centers are GSI, JINR (modules and ladders), KIT (modules). System assembly and commissioning will take place at GSI.

During the 33^{rd} CBM Collaboration Meeting, held from 1-5 April 2019 at GSI, a group from Japan's High Energy Accelerator Research Organization joined as associate member [3]. It enlarges the STS partners to the following list of teams: GSI (Germany), Universität Tübingen (Germany), Goethe Universität (Germany), KIT (Germany), JINR (Russia), AGH (Poland), JU (Poland), WUT (Poland), KINR (Ukraine), and KEK (Japan).

References

[1] STS-XYTERv2.2 Engineering Design Review, GSI, 18 Sept. and 15 Nov. 2019, https://indico.gsi.de/event/9429/, https://indico.gsi.de/event/9421/

[2] STS Cooling Conceptual Design Review, GSI, 10 Dec. 2019, https://indico.gsi.de/event/9671/

[3] CBM news, https://fair-center.eu/for-users/experiments/cbm/newsview-cbm/article/new-cbm-associate-members.html

Start of STS microstrip sensor series production and testing

J. M. Heuser[1], O. Bertini[1], J. Eschke[1,2], E. Lavrik[2], I. Panasenko[3], C. J. Schmidt[1], H. R. Schmidt[1,3], U. Frankenfeld[1], C. Simons[1], K. Schünemann[1], S. Mehta[3], M. Bajdel[1,4], M. Shiroya[1], A. Wilms[1], H. Al-Turany[1], J. Bailey[1], and J. Neumann[1]

[1]GSI, Darmstadt, Germany; [2]FAIR, Darmstadt, Germany; [3]Universität Tübingen, Germany; [4]Goethe Universität, Frankfurt, Germany

With the start of silicon microstrip sensor series production in Summer 2019, the STS project achieved an important milestone towards the construction of CBM's main tracking detector. The production of all sensors was awarded in March 2019 to the company Hamamatsu Photonics, Japan, through their branch in Germany. The decision was made upon the result of a tendering procedure through the FAIR GmbH, launched in 2018 after a dedicated review in the CBM Collaboration [1]. The Hamamatsu offer met all criteria in terms of the required technical specifications, production time, and budget.

The double-sided silicon microstrip sensors for the CBM Silicon Tracking System have been overviewed in [2]. The final sensor layout now in production has been described in [3]. About 1100 specimen (including 15% extra material to compensate limited integration yield onto detector modules and ladders) are required in four variants: 6.2 cm width; 2.2, 4.2, 6.2 and 12.4 cm height. They feature on a 320 μm thick substrate 1024 strips per side, arranged at 58 μm pitch under 7.5° between front- and back sides. The biasing and read-out contacts are optimized for the attachment via tab-bonding of ultra-thin microcables made from Aluminum[1] leads and polyimide substrate.

After a lead time of about six months, the delivery of sensors takes place in monthly batches of about 100 sensors, featuring all 4 sizes, starting in November 2019, for a duration of about 11 months. The delivery place is FAIR GmbH in Darmstadt. The costs of the sensors represent a significant part of the STS project costs, which are shared by joining contributions from several STS project institutes, in particular from Russia and Germany.

Quality assurance has been aggregated at GSI in the Detector Laboratory's clean room. In addition to the test station for electrical sensor quality inspection, developed over the past years by the STS team there, two further custom-built, optimized benches for electrical [4] and optical [5] sensor inspection were conceived by the STS group at the University of Tübingen, transferred to GSI in Fall 2019.

Key quality parameters have been agreed on with the sensor vendors. They include:

- Full depletion voltage: 40 - 150 V;
- Breakdown voltage: 200 V (max. possible at vendor);
- Leakage current: $<$ 1.5/3/4.5/9 μA at 200 V (for sensors 6.2 by 2.2 / 4.2 / 6.2 / 12.4 cm);
- Bias resistance: 0.5 / 1 / 2 MΩ (min / typical / max);
- Defect strips: max. 15 per side/1024 strips, i.e. max. 30 per sensor. Defects include: Short ("pin hole") in the AC coupling insulation, Aluminum opening, and Aluminum short to neighbour strips.

[1]A Copper alternative with matching interconnects is under study.

Electrical Quality Assurance

As certified in the final inspection data sheets supplied by Hamamatsu, all sensors fulfill the agreed criteria. A summary of the defective strips per sensor variant, extracted from the data sheets, is shown in Fig. 1. The validity of the information has been verified on sensors from a prototype production, and selected samples from the series production.

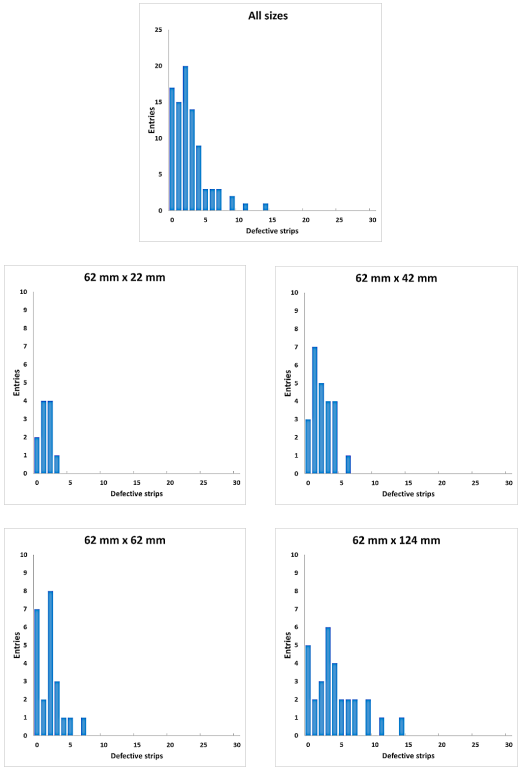

Figure 1: Distribution of defective strips per sensor, on a sample of 88 selected sensors from the first six batches. The data stems from the factory final inspection.

After delivery to the GSI/FAIR campus, for every batch a subset of sensors has been verified electrically (extending the bias voltage scan[2] up to 500 V), and optically, scanning additionally for any mechanical defects. For the electrical tests, additional fixtures based on miniature pogo pins have been developed and produced in industry, allowing two-sided contacting for bias application and subsequent current/capacitance measurements as function of the applied reverse bias voltage. The fixtures also serve as cradles for save allocation of sensors in the probe station. An example of a current/capacitance-voltage scan for a 6.2 by 6.2 cm sensor is shown in Fig. 2.

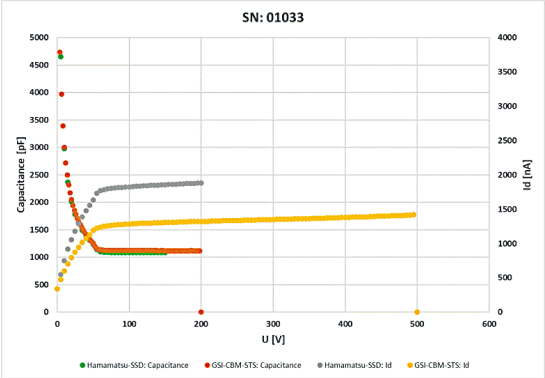

Figure 2: Current-voltage and capacitance-voltage measurements from Hamamatsu and CBM compared. Despite of both data normalized to 20 °C, the GSI measurement current is close to a factor of 2 lower. This is attributed to the direct two-sided pogo-pin contacting as opposed to the through-via contacting done at Hamamatsu.

So far, 83 sensors have been inspected electrically, with random specimen taken from every of the 6 deliveries received by now. They distribute as follows across the variants: 22 mm (14×), 42 mm (24×), 62 mm (21×), and 124 mm (24×).

The sensor currents at defined bias voltages 150, 250, 350 and 500 V have been looked at. Ratios of those currents can be used to define grades with respect to optimal sensor positioning in detector stations where different radiation load occurs. An example for the distribution non-ionizing energy loss is shown in Fig. 3, overlaying the integrated non-ionizing radiation dose[3] with the pattern of sensor arrangment in the most downstream STS tracking station. Sensor current ratios have been established as of Equation (1) and then used for a – pragmatic – sensor radiation tolerance classification applying the cuts listed in Table 1, using the lowest grades determined.

[2]maximum voltage determined to keep up high charge collection efficiency of the later irradiated sensors [6].

[3]"Standard" running scenario: One month 10^9 Au collisions at 25 GeV per nucleon on a 250 μm Au target, yielding $2.6 \cdot 10^{13}$ interactions in its 1% nuclear interaction length [6].

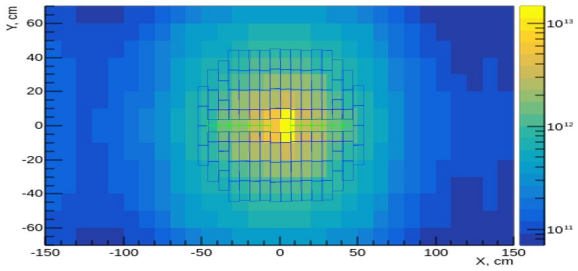

Figure 3: Non-ionizing radiation dose [1 MeV $n_{eq}cm^{-2}$] in a "standard" running scenario [6] at the most downstream STS tracking station.

$$\begin{aligned} \text{IR1} &= I(250\ V)/I(150\ V) \\ \text{IR2} &= I(350\ V)/I(150\ V) \\ \text{IR3} &= I(500\ V)/I(150\ V) \end{aligned} \quad (1)$$

Table 1: Definition of radiation tolerance grades.

current ratio	Grade A	Grade B	Grade C
IR1	[1.015; 1.035]	[1.0; 1.05]	else
IR2	[1.0; 1.1]	[1.0; 1.1]	else
IR3	[1.0; 1.12]	[1.12; 3.5]	else

As seen in Fig. 4, grade A sensors, the ones with highest performance and fit to the highest particle fluences, are the ones where the ratios establish linear correlations. Grade B sensors show linear correlations but less stringent, while grade C sensors having larger current ratio scattering are to be used at the lowest particle fluences. They distribute as seen in Table 2. An extrapolation towards the required sensor variant by radiation tolerance quality grade is forthcoming with higher statistics accumulated.

Table 2: Radiation tolerance grades of 83 sensor specimen. Absolute numbers (top), and relative fractions (bottom).

sensor variant	Grade A	Grade B	Grade C
6.2 × 2.2	11	3	0
6.2 × 4.2	15	6	3
6.2 × 6.2	16	3	2
6.2 × 12.4	1	16	7
all	43	28	12

sensor variant	Grade A	Grade B	Grade C
6.2 × 2.2	79%	21%	0%
6.2 × 4.2	63%	25%	12%
6.2 × 6.2	76%	14%	10%
6.2 × 12.4	4%	67%	29%
all	52%	34%	14%

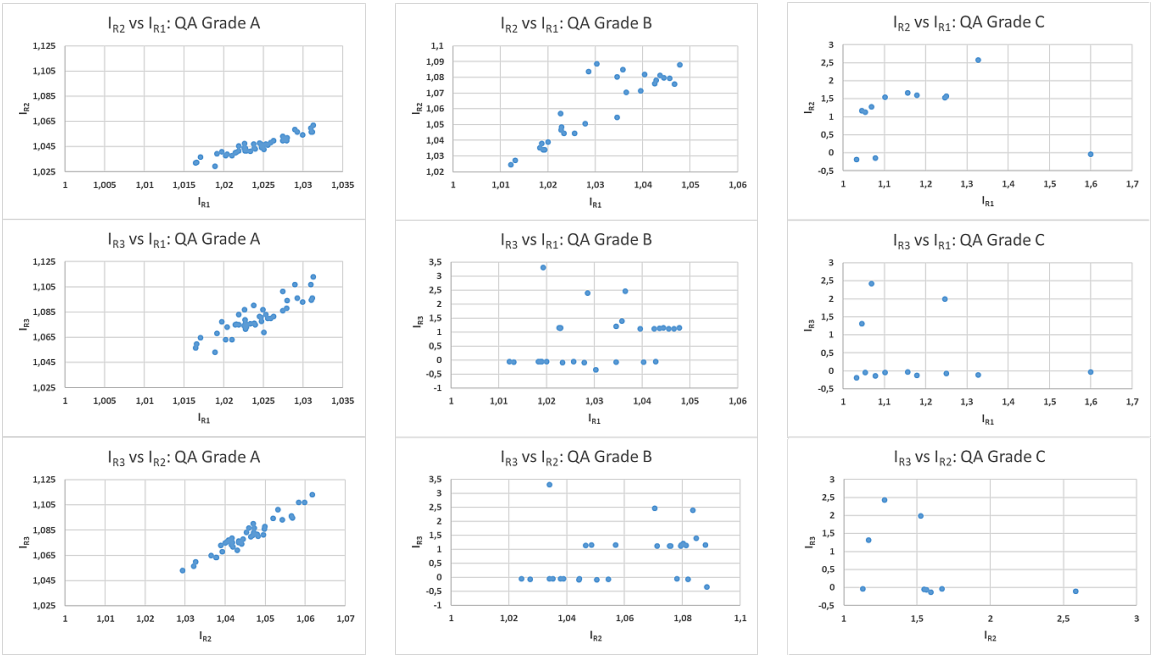

Figure 4: Relation of sensor current ratios, defined in Equation 1, grouped according to the radiation tolerance grades defined in Table 1. The left column of histograms corresponds to Grade A (highest radiation region), the middle to Grade B (moderate radiation region), and the rightmost column to Grade C (lowest radiation region).

Optical Quality Assurance

By the time of the report, 160 sensors have been optically inspected, overlapping with the sample quality assured electrically. The image recognition system identifies as defective strips those with Aluminum open, Aluminum short, but also can see into the silicon and notices (to be verified) implant breaks and p-stop breaks, as well as surface alterations - e.g. scratches, passivation openings or features on the second layer metallization. Not all of those may be actual defects, some features are still to be verified for having an effect on the sensor operation. The defect types differ mostly from the ones found through electrical inspection, overlap only with the Aluminum open and shorts. The structures are listed in Fig. 5. The distributions of those defects across the sensor variants, and in total, are presented in Fig. 6.

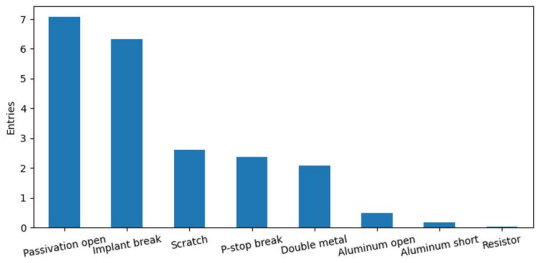

Figure 5: Types of anomalies, identified through optical inspection. The histogram displays the findings, averaged over 160 sensors.

Outlook towards series module and ladder assembly

An overall quality grade will be finally calculated from the information available, combining input from vendor data (in particular on strip tests), extended electrical and optical acceptance measurements done at GSI, and specific measurements if necessary. This is still work in progress. As part of approved inbound logistics, dedicated sensor parameters originating from vendor data, as well as relevant logistic parameters of each sensor, are stored in an electronic logbook hosted at GSI. In addition the evaluated overall quality grade of each sensor will be stored in there. The sensor characteristics and inspection results are also exported for a long-time storage and analysis into a dedicated component database. The information will be of relevance later as input for appropriate sensor selection in the course of STS module and ladder assembly work.

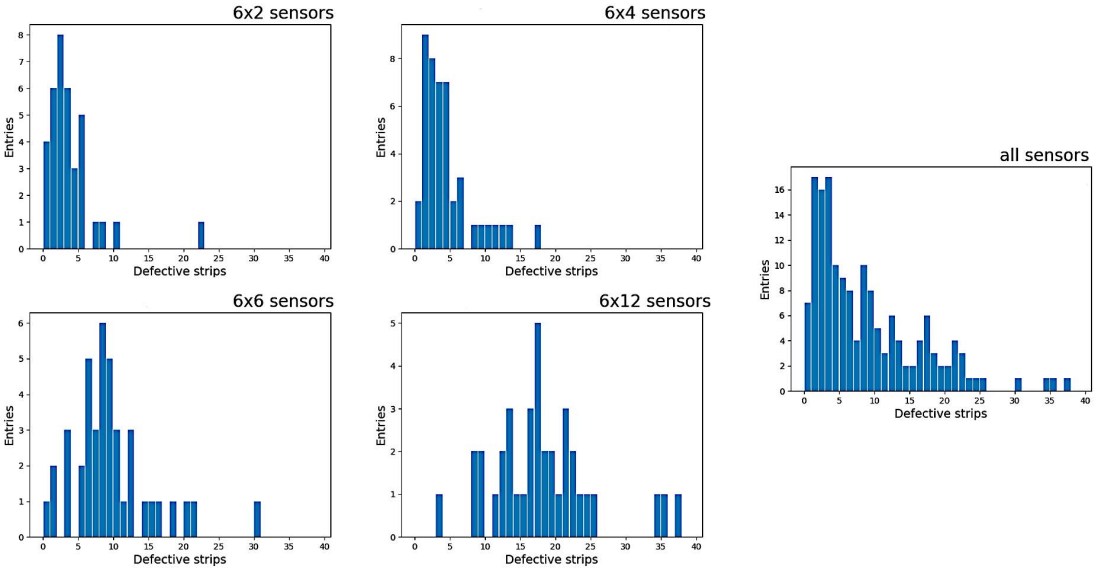

Figure 6: Distribution of anomalies per sensor as identified through optical inspection.

References

[1] J. M. Heuser et al., *Production readiness of STS microstrip sensors*, CBM Progress Report 2018, p. 11

[2] J. M. Heuser et al., *Status of micro-strip sensor development for the CBM Silicon Tracking System*, CBM Progress Report 2016, p. 22

[3] J. M. Heuser, *Description of the STS microstrip sensors for series production*, CBM-TN-19005, 21 May 2019

[4] I. Panasenklo et al., *A Custom Probe Station for Testing of CBM Silicon Strip Detectors*, this progress report

[5] E. Lavrik, I. Panasenko, and H. R. Schmidt, *Optical quality assurance procedures for the STS detector*, CBM Progress Report 2017, p. 20

[6] CBM Collaboration, Technical Design Report for the CBM Silicon Tracking System, GSI-Report 2013-4, 83-88, http://repository.gsi.de/record/54798

A Custom Probe Station for Testing of CBM Silicon Strip Detectors

I. Panasenko[1], *H. R. Schmidt*[1,2], *E. Lavrik*[3], *and O. Bertini*[2]
[1]University of Tübingen, Germany; [2]GSI, Darmstadt, Germany; [3]FAIR, Darmstadt, Germany

The CBM Silicon Tracking System will employ 876 double-sided silicon microstrip sensors. Every sensor has 1024 strips placed with 58 μm pitch on each side [1]. Delivery of newly produced sensors started at the end of 2019. Quality assurance (QA) tests have to be performed prior to assembly of the sensors into detector modules and are currently in progress.

Electrical QA comprises two steps: global (bulk) tests, and strip integrity tests. Global tests are IV-CV measurements and require a relatively simple setup with a properly configured and calibrated pico ampere and LCR meters. In contrary, strip integrity tests require a dedicated probe station and advanced methods for reliable and efficient detection of defective strips in order to confirm that manufactured sensors comply with the CBM specifications.

One of the quality test centers was based in Tübingen. A highly specialized and automated setup for electrical characterization has been built there to cope with the foreseen QA task. To limit, even avoid transportation of the sensors between distributing and testing sites, it was decided in the STS project to transfer all QA infrastructure to the GSI Detector Laboratory, thus minimizing risk of damaging the sensors.

Figure 1 shows the custom-built probe station which is already installed in the clean room of the GSI Detector Laboratory. The mechanical setup consists of a custom-designed vacuum chuck to hold the microstrip sensor, which can be positioned in $XYZ\Theta$ with Aerotech motor stages with accuracy better than 1 μm. It also accommodates a movable microscope Navitar Zoom 12x with 3 MP camera and light source. Four probes with 5 μm tip diameter on a support table are available for contacting individual strips. The setup employs computer controlled switching scheme which allows wide variety of tests without time consuming manual interaction. The electrical circuit is designed for measurement of small currents (pA) and small capacitances (pF) at bias voltages up to 200 V. Figure 2 shows the inside of the probe station. Dedicated custom LabVIEW-based software allows to perform complete electrical characterization of the CBM microstrip sensors. The Tübingen setup is flexible for testing strips and pixels, objects with different layouts without hardware modification. It demonstrated excellent performance during in-depth characterization of the CBM sensor prototypes and was used for qualification of the sensors for mSTS [2].

The QA program will be carried out during a period of about one year, for the entire production phase of the sensors [1]. The sensors are delivered in monthly batches of up to 100 pieces. The throughput of the Tübingen setup is one sensor per 5 hours, including the time-consuming strip integrity tests. This allows to qualify about 10% of the sensors. The Setup will be operated by a technician who was taught and trained accordingly.

Figure 1: View of the Tübingen setup which is installed in the clean room of the GSI detector laboratory.

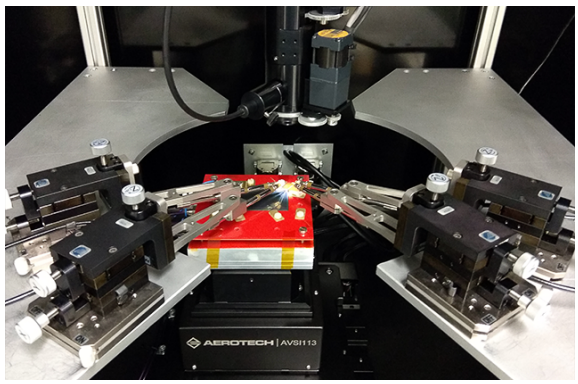

Figure 2: View into the probe station while performing measurement of the inter-strip capacitance of a microstrip sensor.

References

[1] J. M. Heuser, and the STS workgroup, *Description of the STS microstrip sensors for series production*, CBM-TN-19005, 2019

[2] I. Panasenko et al., *Electrical qualification of the microstrip sensors for mSTS*, CBM Progress Report 2018, pp. 12-13, 2019

Test of the STS-XYTERv2.1 ASIC

O. Maragoto Rodriguez[1,2], K. Kasinski[3], J. Lehnert[1], P. Pfistner[4], and A. Rodriguez Rodriguez[1,2]
[1]GSI, Darmstadt, Germany; [2]Goethe Universität, Frankfurt, Germany; [3]AGH, Krakov, Poland;
[4]KIT, Karlsruhe, Germany

Characterization of the analog front-end

The characterization of the STS-XYTERv2.1 ASIC is an important step before using the chip in the readout of the silicon sensors. A test setup was built at the STS laboratory in order to test the analog performance of the ASIC. The prototype readout chain consisted of:

- Prototype FEB type C carrying one STS-XYTERv2.1 ASIC.
- AFCK, FPGA based board implementing the STS-XYTER-DPB Protocol backend.
- Low voltage power supply.

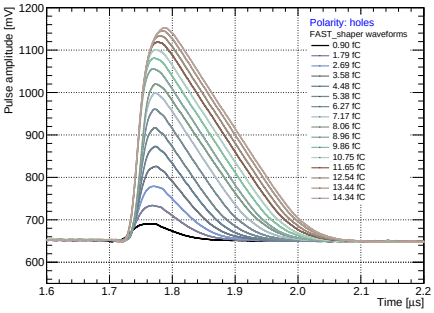

Figure 1: Waveforms for Fast shaper.

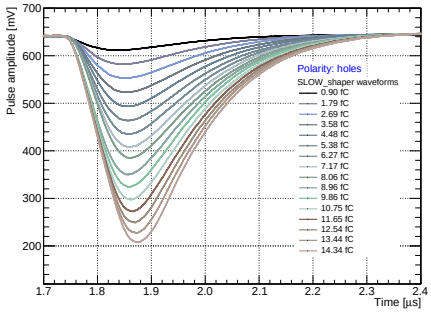

Figure 2: Waveforms for Slow shaper.

First, communication with and configuration of the ASIC were established. Afterward, the analog waveforms were acquired using 1.5 GHz active probes connected to the test channels of the STS-XYTERv2.1. They were read out using a Tektronik 4054 oscilloscope. Using the internal pulse generator, pulses of different amplitudes were injected. The waveforms from shapers in a test channel are shown in Fig. 1 and Fig. 2 for polarities corresponding to holes.

The shaper's gain can be estimated, for the STS mode, by measuring the output signal amplitude. A first order polynomial was used to fit the data and extract the gain parameters. The values result in approximately 50 mV/fC and 30 mV/fC for the FAST and SLOW shaper, respectively.

Noise and stability in the STS-XYTERv2.1

To estimate the noise levels for the STS-XYTERv2.1, a voltage pulse scan was performed and the S-curves from all discriminators in every channel were recorded. The ADC noise levels were calculated as the average of all discriminators in the same channel. Results from the noise measurement are displayed in Fig. 3 for both polarities.

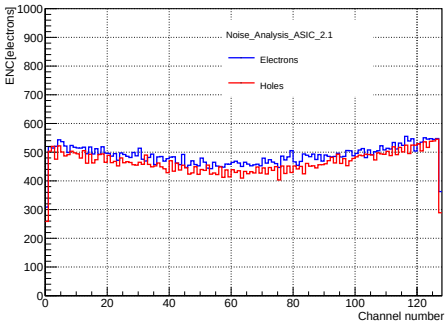

Figure 3: Noise for a single ASIC in prototype FEB-C.

From the figure, the noise measured for electrons is slightly larger than for holes, as expected. This is due to the contribution from the polarity selection circuitry (PSC), which is bypassed in the case of holes [1]. There is almost no difference in performance between odd and even channels.

Reliable long-term performance is considered to be an important parameter. In order to study the noise evolution over time for a single STS-XYTERv2.1 ASIC, measurements for electrons and holes polarities were taken every 12 minutes for approximately 72 hours. The results are illustrated in Fig. 4. Every point represents the average noise value among all the channels in the chip and the error bars indicate the standard deviation. Almost no variations can be distinguished in both polarities along the monitoring period.

Noise dependency on the input load capacitance

The noise of the pre-amplifier strongly depends on the input capacitive load. On the final STS detector, multiple

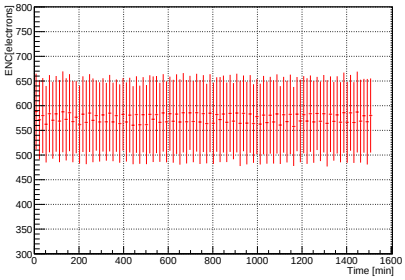

Figure 4: Noise stability for ASIC in prototype FEB-C.

combinations of sensor sizes [2] and cables will result in capacitance loads in the range of 12-40 pF.

In order to study the noise dependence on the capacitive load, a set of dedicated capacitor phantom boards was used. The two boards consist of simple ERNI connectors with 64 pins, where a set of low leakage C0G SMD9 capacitors ranging from 1 to 40 pF are soldered to the even channels. Every capacitance value is cross-checked using a Peak Tech 2155 LCR meter, in order to correct for parasitic values. The results are illustrated in Fig. 5. For the

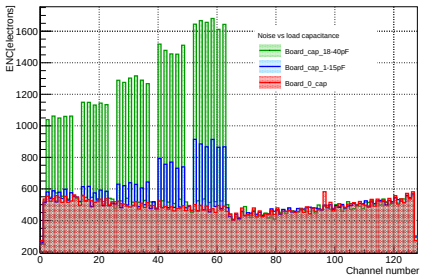

Figure 5: Noise as a function of the input capacitance.

measurements, the boards were attached to the first ERNI connector of the FEBs. Using the internal pulse generator, different charge amplitudes are injected at the input of the CSA. Output signals are read out on the dedicated counters of the ADC discriminators. A background measurement without capacitors was taken as reference (red line). The results show a strong dependency between the noise performance and the input capacitance of the system. The experimental data were fitted with a first order regression line, resulting in an average slope of 22 ENC(e-)/pF and 28 ENC(e-)/pF for electrons and holes respectively. Similiar results were obtained for previous version of the ASIC [3]. Discrepancies between electrons and holes are still under investigation.

Noise as a function of the peaking time

The design of the slow shaper allows to operate at 4 different peaking times. This feature is exploited to trade of between speed and noise.

In the slow shaper of the STS-XYTER, the selection of the signal peaking time is controlled via a 2-bit DAC. This register modifies the resistance values in the pulse processing chain that establishes the corresponding integration time. The output waveforms for all possible shaping times are shown in Fig. 6. Waveforms were collected with a Tektronik 4054 oscilloscope. The noise as a function of

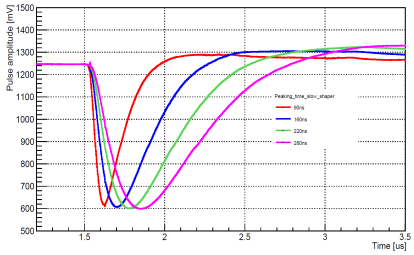

Figure 6: Waveforms for all possible shaping times.

the peaking time is shown in Fig. 7. These measurements were taken with the same ASIC, in two different configuartions. We can observe how an increase on the imput capacitance lead to an increase on ENC amont all differnt peaking times. First, a single ASIC was bonded on a prototype FEB-C. Second, the same prototype FEB-C was connected to a 6×6 cm^2 sensor via an ERNI conector. Every point represents the average among all channels, and the error bars illustrate the standard deviation. For the first config-

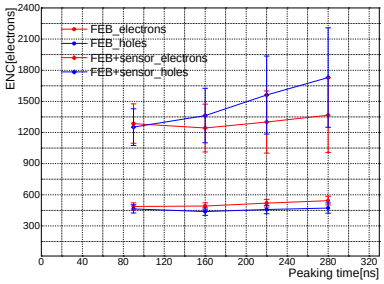

Figure 7: Noise as function of peaking time.

uration, there is almost no difference between all peaking times. For the second configuration, there is a difference in terms of noise performance and also a divergence between electrons and holes. An increase in input capacitance results in an increase of ENC among all different peaking times. The divergence between electrons and holes can be attributed to the contribution of the PSC, which is present in the electron processing chain.

References

[1] K. Kasinski et al., *STS/MUCH-XYTER Manual v2.02*

[2] H. R. Schmidt, J. M. Heuser et al.,*CBM Progress Report 2017, Darmstadt*, p. 16

[3] K. Kasinski et al., *Nucl. Instr. and Meth. A 908* (2018), 225-235.

Testing and optimisation of the analog part of the SMX 2.1

D. Dementiev[1], *I. Kovalev*[2], *I. Kudryashov*[2], *A. Kurganov*[2], *M. Shitenkov*[1], *and A. Voronin*[2]
[1]JINR, Dubna, Russia; [2]SINP, MSU, Moscow, Russia

Testing and optimization of a modern multichannel ASIC is not an easy task because such ASICs often have a number of variable settings for both analog and digital parts.

To optimise these settings, one needs to measure key characteristics of the ASIC in every point of the multidimensional phase space of its parameters and to choose an optimal point based on the requirements of the experiment.

A special test stand was built to measure the characteristics and to test the STS/MUCH-XYTER ("SMX") ASICs (Fig. 1). It allows carrying out measurements in both automated and manual modes[1].

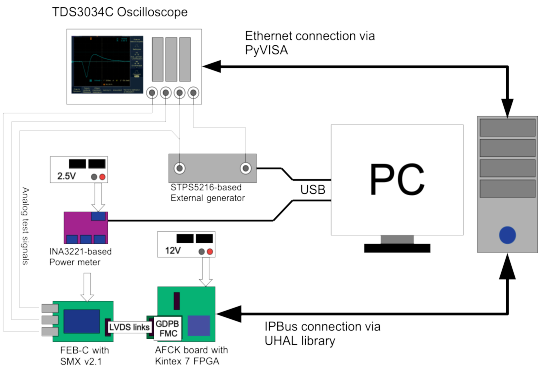

Figure 1: Simplified schematics of the test stand.

Software for the test stand was developed using Python 2.7 language. It mainly consists of communication interface implementations for the rest of the hardware: oscilloscope, current monitor and signal generator. The software also implements routines for the measurement of baseline, noise, signal shape for different amplitudes of input signals, and the power consumption of the ASIC.

Using this test stand, measurements of CSA characteristics for a single SMX 2.1 chip on a FEB-C board [1, 2] were conducted. The obtained data was used to determine optimal values of the following registers: CSA bias current (IN_CSA), CSA cascode and buffer currents (CAS_CSA, BUF_CSA), CSA bias 1V generator (CSA_BIAS_1V) and CSA FB resistor (RF_HL, I_FED).

First one needs to select most important characteristics of the ASIC which will be calculated from the measured data. Then the optimal values of the parameters should be selected to provide best possible values of these characteristics. For this work, the following characteristics were selected:

- Power consumption;
- Signal (from a particle of interest, in our case - MIP) to noise ratio;
- Dynamic range;
- Relaxation time.

Because the SMX chip will be used primarily in tracking systems, the signal-to-noise ratio is the most important characteristic of the ASIC, as it will provide better separation of single events from noise. Power consumption is also important in tracking systems, because a lot of chips will be closely packed together, which can lead to heat dissipation difficulties. Due to these reasons, obtaining the best signal-to-noise ratio with simultaneous minimization of power consumption were the main priorities of this work (Fig. 2).

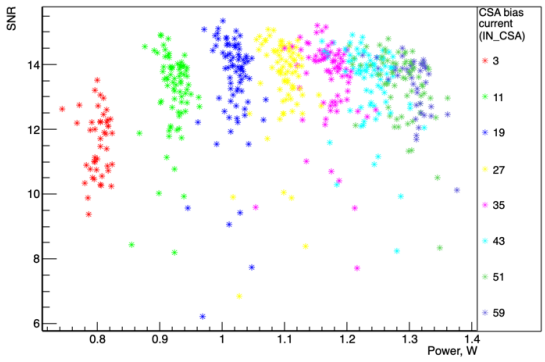

Figure 2: Signal-to-noise ratio and power consumption dependence on the CSA bias current register value.

The result of such an optimization of register values is (in parentheses - typical values provided in the manual): IN_CSA=19(31), CAS_CSA=3(3), BUF_CSA=7(3), CSA_BIAS_1V=19(27), RF_HL=0(1) and I_FED=24(7).

Optimization of PSC, shapers, ADC and discriminator parameters is being carried out at the time of writing.

[1]Work supported by RFBR grant 18-02-40047.

References

[1] K. Kasinski et al., SMX2 and SMX2.1 Manual v2.03, 2018

[2] M. Shitenkow, D. Dementev et al., *Test station with silicon baby sensor and readout electronics based on STS/MUCH-XYTER2 ASIC for in-beam tests at Nuclotron*, CBM Progress Report 2017, p. 37

Towards SMX2.2, final read-out chip for STS and MuCH

K. Kasinski, W. Zubrzycka, and R. Szczygiel
AGH University of Science and Technology, Krakow, Poland

STS-XYTER, or SMX is a family of Integrated Circuits developed for the CBM STS and MuCH detectors[1]. After extensive testing campaign [1], the development is heading towards the final architecture. The next revision, named SMX2.2 is currently being taped-out. This paper briefly summarizes the changes implemented in this IC revision. Both detector systems require thousands of SMX chips for their operation. The QA procedures require traceability of the IC performance starting from the wafer, through wafer-level characterization, stealth-laser dicing, complex procedure of microassembly with intermediate testing and calibration in the system. AGH is preparing for the wafer-level characterization task in terms of equipment (wafer-prober, digitizers, digital communication systems, wafer-probe card PCB etc.) and software-wise (MATLAB + python scripts on both Linux and Windows machines). For the purpose of this project a clean-room was designed and built in a dedicated room (Fig. 1). Before going to volume production (100 wafers), a pilot run is organized, where, 8 out of 12 wafers will be fabricated as typical (TT), while the remaining 4 will explore the process shifts of NMOS and PMOS transistors (FF, SF, FS, SS). The purpose is to prove the robustness of the design and also to train the wafer-level characterization software to achieve proper classification of the fabricated ICs.

Changes in the SMX2.2 include, but are not limited to:

- Fast reset of the charge-sensitive amplifier acts earlier and for shorter period of time to enable faster recovery of the baseline. This prevents usage of longest peaking times of slow shaper in conjunction with CSA reset.
- On-chip voltage monitoring ADC [2] enables measuring of VDDA, VDDC and VDDADC potentials now in addition to the VDDM, temperature sensor, CSA bias potential and any external potential connected to the pad.
- Layout changes around pads to minimize the risk of shorts between pad being wire-bonded and any top-metal structure.
- ESD: Integration of DIODE-based ESD protection at the CSA input pads. The study of the leakage current resulting from the previous, MOS-based ESD protection circuit were evaluated in [3]. The integrated circuit named ESD-CHIP was fabricated together with SMX2.1 and contained multiple variants of ESD protection circuit. Evaluation of its leakage current vs. applied voltage for various temperatures and ability to protect the CSA amplifier against standard ESD pulses lead to the selection and integration of thiese structure in the new ASIC
- ESD: Size of ESD protection at the LVDS I/Os is doubled to withstand the shutdown of detector bias.
- Bug fix: enabling read-back of new registers (col=17 through 22) in row=130 (global settings).

Various working documents are collected at [4].

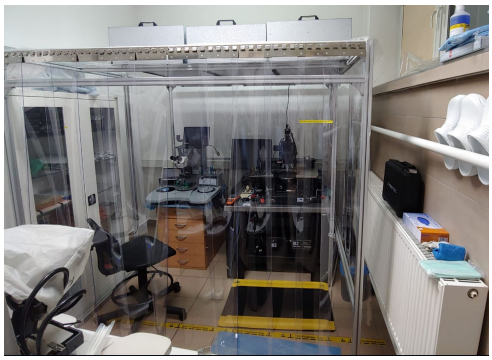

Figure 1: Wire-bonder and wafer-prober in a clean-room ready for SMX2.2 ICs.

[1] Work partially supported by Ministry of Science and Higher Education, Poland.

References

[1] K. Kasinski et al., *Characterization of the STS/MUCH-XYTER2, a 128-channel time and amplitude measurement IC for gas and silicon microstrip sensors*, Nucl. Instr. Meth. Phys. Res. A908 (2018), 225-235, https://doi.org/10.1016/j.nima.2018.08.076]

[2] W. Zubrzycka and K. Kasinski, *Biasing potentials monitoring circuit for multichannel radiation imaging ASIC in-system diagnostics*, Proc. 2017 MIXDES - Mixed Design of Integrated Circuits and Systems, 234–239.

[3] W. Zubrzycka and K. Kasinski, *Leakage current-induced effects in the silicon microstrip and gas electron multiplier readout chain and their compensation method*, Journal of Instrumentation, 13(4), T04003, https://doi.org/10.1088/1748-0221/13/04/T04003

[4] https://cbm-wiki.gsi.de/foswiki/bin/view/CBMXYTER

Study of adhesives for globtop and thermal interface during STS module assembly

S. Mehta[1], A. Wilms[2], C. Simons[2], R. Visinka[2], A. Lymantes[2], O. Maragoto Rodriguez[3], K. Agarwal[1], U. Frankenfeld[2], C. J. Schmidt[2], P. Kocon[2], M. Bajdel[2,3], and J. Swakon[4]

[1]Eberhard Karls Universität, Tübingen, Germany; [2]GSI, Darmstadt, Germany;
[3]Goethe Universität, Frankfurt, Germany; [4]IFJ PAN, Krakow, Poland

During the assembly of a module, several different kinds of adhesives are used at various steps. These are required for gluing the ASICs to PCB, shielding layers and spacers, applying globtop layers on ASICs and LDOs [1] and glue the FEBs to the L-shaped fins. Different glues vary in their characteristic properties, curing methods (thermal or optical) and their mechanical strengths. Also to use these glues in a high-radiation environment for several years requires radiation hardness and long term stability.

Thermal cycling of globtop material

To choose the globtop material for the ASICs, different adhesives were investigated namely, Polytec-2249, Polytec 2257, Dymax 9001 [2] and Dymax 9008 [3]. These adhesives were applied as globtop on FEB-Cs which acts as a safeguard for the ASICs. While all the adhesives under investigation are known to have sufficient working temperature range, the FEBs with different globtops were thermally cycled in BINDER MK53 climate chamber. The impact of repeated mechanical stresses following temperature changes were observed by setting up the minimum and maximum temperature of a cycle with the help of a LabVIEW program.

The LabVIEW program is prepared in such a way, that the number and duration time of each temperature cycles can be chosen individually. During each cycle, the extreme temperature value remains stable for 8 minutes. Before and after each measurement, a noise scan of the FEB was performed to see the effect of temperature on the ASIC. Our experience of thermal passive cycling (without powering the FEBs) with Polytec showed that by increasing the temperature we observed an increase in the number of channels which stopped responding in the ASIC and at high temperature of around 80 °C, ASIC stopped showing synchronisation. As an alternative to Polytec, DYMAX was chosen as the other candidate for the globtop. The same set of measurements were repeated for the FEBs with DYMAX as globtop keeping all the other parameters same to have a comparison with Polytec. As a result, DYMAX performed nicely with all the synchronized channels till high temperature up to 90 °C. To see the effect of globtop, a set of measurements were performed between a FEB with globtop DYMAX 9008 and a FEB without any globtop under the same conditions as shown in Fig. 1. In there, the x-axis shows the maximum temperature during the cycle where minimum temperature was kept constant to -10 °C for each cycle with duration time of 60 minutes. As can be seen there is no increment in noise for the FEBs with and without globtop till high temperature of 90 °C with all the synchronized channels.

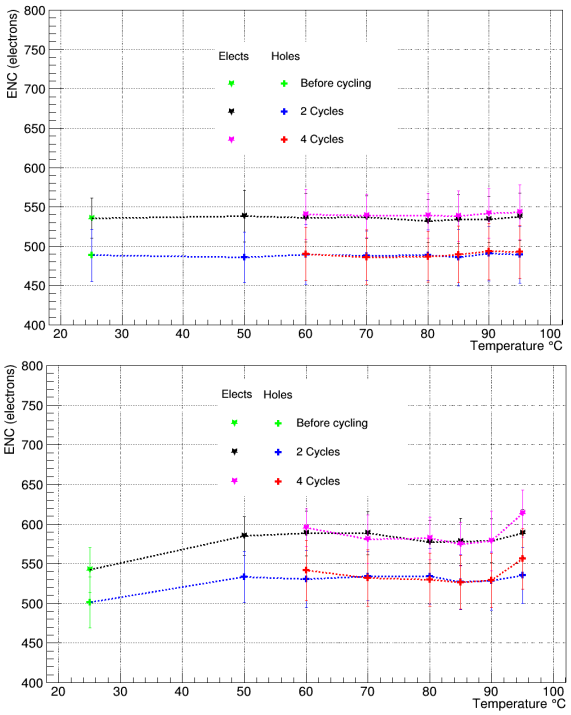

Figure 1: Temperature vs Noise Plots: a) FEB-C without globtop, b) FEB-C with globtop DYMAX 9008.

Irradiation studies

To study the radiation tolerance of the glues under ivestigation, DYMAX 9001 and 9008 were applied on two different FEBs and were irradiated at the Institute of Nuclear Physics in Krakow, Poland. The FEBs have been irradiated under 50 MeV proton beam with current of ∼50-60 nA which is comparable to the lifetime fluence of the STS. Each FEB was kept under exposure for 25 minutes with an integrated dose of ∼11 kGy. To see the effect of radiation on the glues, a noise scan of the selected FEBs was

performed before and after the irradiation as depicted in Fig. 2. The plots shows that the noise level before and after irradiation was nearly the same in both the cases and even after subsequent thermal cycling all the channels were responding nicely up to 90 °C.

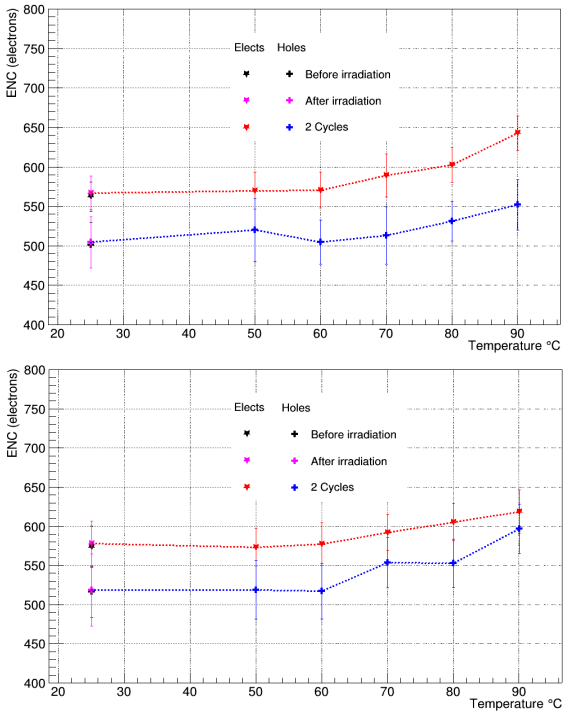

Figure 2: Temperature vs noise plots of FEB-C before and after the irradiation: a) DYMAX-9001 b) DYMAX 9008.

Resume on thermal cycling/irradiations

In conclusion, the observations after thermal cycling and irradiation studies indicate that both the DYMAX glue variants are suitable for the globtop on ASICs. The only drawback with DYMAX 9008 is that after applying it onto the ASICs it stays sticky till very long time which is not the case with DYMAX 9001. Also, the viscosity of DYMAX 9008 is lower than that of DYMAX 9001 so a dam is needed as an outer layer to ensure that it should not flow. During the beamtime at COSY in November 2019, and as well as the March-April 2020 mCBM beamtime, DYMAX 9001 was applied as globtop on ASICs and LDOs for the modules assembled. The results look reassuring. So, we plan to use DYMAX 9001 as globtop on the ASICs and LDOs for the STS modules. Further passive and active thermal cycling tests are ongoing to ensure that it meets our requirements.

Thermal glues

The last step of module assembly is the gluing of two FEBs to the L-shaped cooling fins before transferring the module to the storage, for testing, and finally for mouting it onto a ladder. For this purpose, thermally conductive glue with thickness not more than 250 μm is needed which will act as a thermal interface between the FEBs and the cooling fin as shown in Fig. 3. After some survey and learning from the experience of other experiments like ATLAS at CERN, a few suitable candidates have been chosen for the investigation of thermal interfaces, summarized in Table 1. To select the glue most suited for our purpose several tests like thermal and electrical tests, shear tests, irradiation hardness studies will be performed; the investigation is ongoing.

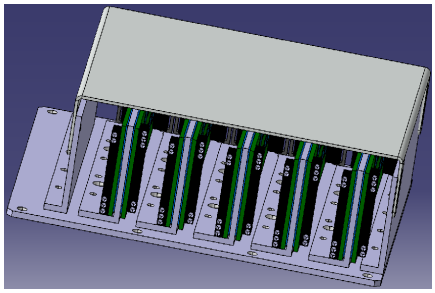

Figure 3: FEB box with FEBs glued to L-shaped fins

Table 1: Properties of different glues to test for the thermal interface between the FEBs and the L-shaped fin.

Product Name	Viscosity (Pa.s)	Thermal Conductivity(W/m-K)	Cure time (hours)	Operating temp (°C)	Density (g/cm³)	Electrical resistivity (Ω-cm)	Type	Comments	Reference
Stycast 2850 FT (Catalyst 23 LV)	5.6	1.02	16 – 24	-65 to 105	2.19	> 10^{15}	Epoxy	Tested by LHCb, NASA	https://lartpc-docdb.fnal.gov/0000/000059/001/stycas2850.pdf
Dow corning SE 4445 CV Ket-Gel	15	1.34	45 min @ 125 (°C) Can be cured at RT in ~ 24 hrs	-45 to 150	2.4	7 x 10^{15}	Gel based	Tested by ATLAS	Ellsworth Adhesives
Berquisite EA - 1805	60	1.8	10	-40 to 125	2.7	1 x 10^{12}	Epoxy		https://www.prweb.com/releases/2014/12/prweb12400905.htm

References

[1] C. Simons et al., CBM Progress Report 2018(2019), p.16

[2] Datasheet of adhesive DYMAX 9001, https://www.dymax.com/images/pdf/pds/9001-e-v30.pdf

[3] Datasheet of adhesive DYMAX 9008, https://www.dymax.com/images/pdf/pds/9008.pdf

Copper based Micro-Cables for STS modules

T. Blank, P. Pfistner, R. Speck, E. Trifonova, L. Eisenblätter, B. Leyrer, and M. Caselle
KIT, Karlsruhe, Germany

The development of copper micro-cables has been started to provide an alternative technology to Al-based cables for the interconnection of the sensor modules and the STS-XYter readout chips. As copper is used for the conductors vias and hence, multilayer cables can be produced. Therefore, only one copper cable is required the N- (P) side of the sensor to the STS-XYter instead of two, in case of Al-based cables. Additionally, fast Au stud-bumping and solder technologies can be used, which accelerates the production steps for the module [1, 2]. In this section, the progresses achieved for the cable development, the interconnection processes and the automated interconnection steps is reported[1].

Improvements in Cable Design and Assembly Processes

To reduce the capacitive coupling between the top and bottom layer, the copper traces were staggered, as shown in Fig. 1 [1]. However, this asymmetric layout resulted in a severe twisting of the cable after heating up the cable during soldering process of the STS-XYter chips to the cable (see Fig. 1). Hence, in version v8 the cable design was changed to be completely symmetric. After soldering of the STS-XYter chips the cable remains flat, as depicted in Fig. 2.

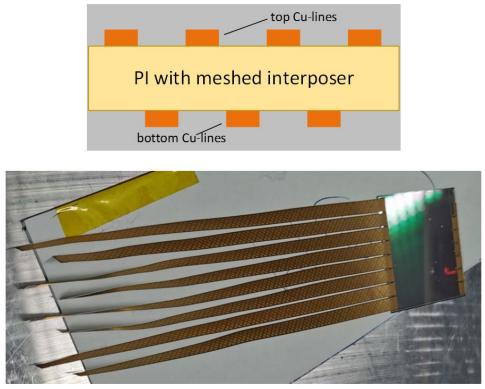

Figure 1: Top: Sketch of asymmetric cable layout; bottom: twisted cables after soldering on the STS-XYter chips and sensor.

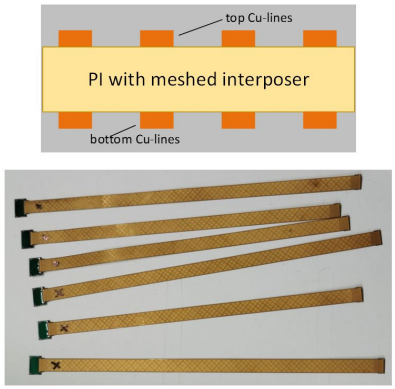

Figure 2: Top: Sketch of symmetric cable layout; bottom: cables are not twisted after soldering on the STS-XYter-chips.

Additionally, the width of the cables was changed on the sensor side as the nominal gap between two adjacent cables on the sensor at room temperature was designed to be 20 mum. However, during soldering process of the cables to the sensor the thermal expansion on the cable needs to be compensated. The measured Coefficient of Thermal Expansion (CTE) of the copper cable is about 20 ppm. Therefore, at a soldering temperature of 250 °C the copper cables with a width of 7404 μm expand by 37 μm. This expansion mitigated the bonding and soldering process on the cable, as the nominal gap between two cables is 20 μm, resulting in a possible overlap of the cables during the assembly. Thus, the cable width was downscaled by 41 μm in cable version v8. Furthermore, the small gap of 20 μm in prior cable versions resulted in severe difficulties to singulate the cables. The increase of a gap of 230 μm between two adjacent cables allows for an easy singulation of the cables from the production sheet by a laser (see Fig. 3). Finally, we changed the solder material from SAC305 to Sn42BI58. Sn42BI58 has a liquidus point of 138 °C instead of 220 °C of the SAC305. The lower melting temperature further reduces the effects of the thermal expansion.

The placement accuracy of the automatic cable was improved by modification of the mechanical fixtures of the optical reference marks. This modification ensures that the optical reference marks are now always aligned vertically with the camera objective. A slight misalignment of about only 2–3 degrees between the mark and the camera objective leads to a non-reproducible placement error when bonding the cable to the sensor. The misalignment-effect is illustrated in Fig. 4. Figure 5 shows the effects of a slight alignment error on the bonding position. The upper image of Fig. 5 shows an in the vertical direction misaligned cable. The displacement is about 15 μm. The lower picture of

[1]The text also appears in Technical Note CBM-TN-20002, section 6.8.

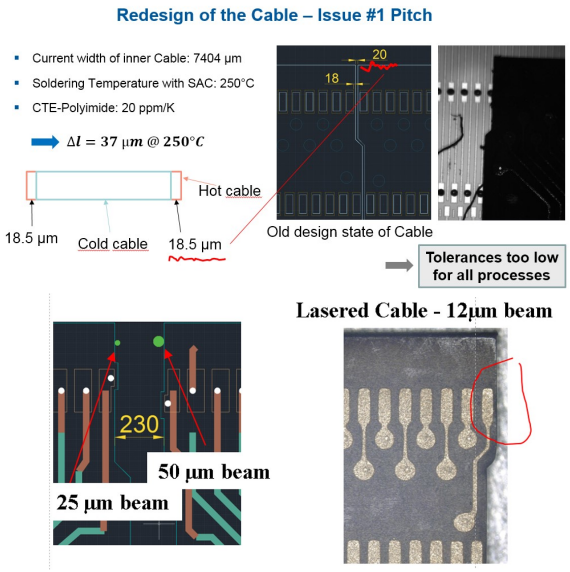

Figure 3: Top: The CTE and the small nominal gap between two adjacent cables of version v7 interferes with the soldering process of the cables on the sensor. Left: The design of the cable v8 with a larger gap for laser-singulation of the cables. Right: A well laser-singulated cable of version v8.

Fig. 5 shows a well aligned set of two cables on the sensor after the optimization of the mechanical fixture. Figure 6 shows the imprints of the Au stud bumps on the cable pads after the bonding process. They are perfectly centered on the pads of the cable.

The double-sided soldering process of the cables on the N- and P-side of the sensor requires a precise control of the temperature to avoid the de-soldering of the cables, which have been already soldered on the first side. Therefore, it would be beneficial to use two solder types with different melting temperatures. However, as the openings in the stencil correspond to the small pads of the sensor, solder paste with particle sizes of type #7 (5 μm to 15 μm), #8 (2 μm to 11 μm) or #9 (2 μm to 6 μm) are required. The combination of the specific requirement on the melting temperature of the solder paste and the particle size makes it difficult to find vendors offering these pastes. However, the process can be set up reliably by just using Sn42BI58, as described in in this section. Additionally, we improved the control of the amount of solder paste transferred during the printing process by changing from stainless steel stencils to fine-grained "Nanovate" nickel stencils. The nano particles in the "Nanovate" stencils allow for a better resolution of the paste from the stencil resulting a higher repeatability of the amount of printed onto the cable. The Nanovate stencil in combination with a variation of the openings (Fig. 7) mitigated the risk of short circuits between two pads.

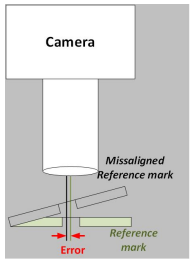

Figure 4: A misaligned reference mark results in an offset between the real position and the position detected by the camera.

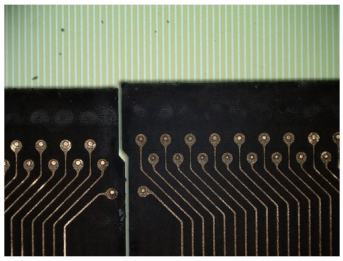

Figure 5: Top: misalignment of the cables bonded on the sensor; bottom: well aligned cables.

Figure 6: Perfectly centered imprints of the Au stud bumps from the sensor side in the solder depot of the cable.

Figure 7: Improved stencil design with variation in the stencil openings to reduce short circuits.

Production of a Dummy Module and First Operational Results

A first dummy module comprising one sensor, 16 Cu-cables compatible to the "micro cable unit 05 ladder type 16" specification with a length of LNSB = 172.3 mm, LPSB = 162.3 mm and 16 STS-XYter dummy chips has been built up. The module is shown in Fig. 8.

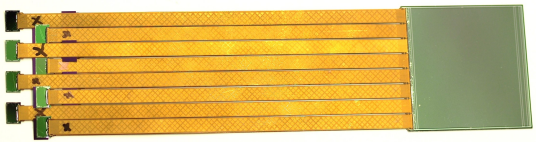

Figure 8: First copper module completely assembled with STS-XYters on N- and P-side.

First double-sided test modules based on the copper micro cable technology have been assembled at KIT. They comprise of one 20 cm copper micro cable per sensor side, two STS-XYTERv2.1 readout ASICs, two Front-End-Boards type C and a 6.2 cm by 6.2 cm CiS sensor. The test setup of the copper cable test module is shown in Fig. 9.

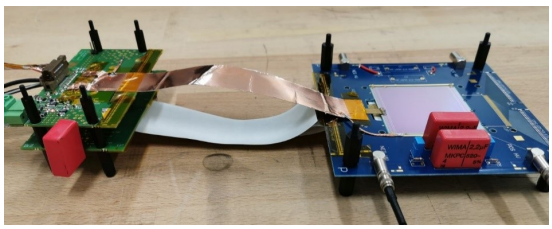

Figure 9: Double-sided test module based on copper microcables.

The modules assembled at KIT have been tested at the STS detector laboratory at GSI. The noise measurements have been performed by S-curve method. Figure 10 shows the measured ENC of the P-side of the test module. The noise level is uniform across all readout channels with a level of around 900 e^-. The increasing noise present at the edge channels is due to pickup of parasitic signals and can be removed by shielding of the micro cables. All channels are properly connected and the noise is very close to the expectations. More modules will be evaluated to confirm these first results. They indicate that from the perspective of system noise the copper technology is a suitable alternative to the aluminum TAB technology. Missing is the comparison with an Al-cable.

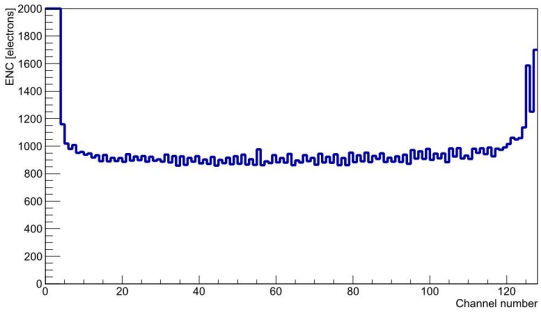

Figure 10: Measured ENC of the p-side of one of the test modules.

Next Steps

A complete working Cu-module will be fully assembled and both the electrical and thermo-mechanical test will be performed.

References

[1] T. Blank et al., *Investigation on low mass copper flex microcables for the STS detector*, CBM Progress Report 2016, ISBN 978-3-9815227-4-7

[2] T. Blank et al., *High density flex-cable and interconnection technologies for large silicon detector modules*, International Conference on Electronics Packaging and iMAPS All Asia Conference (ICEP-IAAC), DOI:10.23919/ICEP.2018.8374306

Front-end Board for the BM@N STS project

D. Dementiev[1], *A. Voronin*[2], *Yu. Murin*[1], *T. Lygdenova*[3], *A. Sheremetev*[1], *M. Shitenkow*[1], *and N. Sukhov*[1]

[1]VB LHEP, JINR, Dubna, Russia; [2]SINP, MSU, Moscow, Russia; [3]TSU, Tomsk, Russia

The BM@N STS project[1] [1] is being developed as a joint effort of JINR and CBM STS groups in the framework of the Russian-German Roadmap. The system is based on the CBM-STS type of modules, but with modified Front-End Boards (FEBs). The main constraints of the FEB design are very tight layout and connectivity, which are limited by the space available between STS stations and FEB-boxes. To provide more space for the power and data cables in the BM@N STS, it was decided to increase the distance between the stations by a factor two (up to 20 cm) relative to that foreseen in the CBM STS, and to design a new FEB with a modified geometry for easier integration of ladders into the mainframe. The main features of the FEB of BM@N STS are as follows:

1. Separate symmetries for the sensors' P and N sides;
2. Eight STS/MUCH-XYTER ASICs are staggered the same way as on CBM FEB-8;
3. Number of uplinks per one ASIC: 1;
4. LDOs are located in the bottom part of the PCB;
5. PCB size is 40*87 mm^2 with a thickness of 1.6 mm;
6. One edge-card connector SE18040[2] with 40 signal pins / 0.65 mm pitch and 8 power pins / 1.3 mm pitch;
7. AC-coupling capacitors for the signal lines are arranged in a 2D row near the connector.

A photograph of the prototype FEB is shown in Fig. 1. Since the connector SE18040 was not avaliable in stock, the first prototype of the board was produced with the same type of the connector but only 20 signal pins - SE10020[3]. The next version with a SE18040 connector is now being developed.

All interfaces for one module, including LV, HV-powering and data cables, are connected to FEBs with a FEB-panel. It is connected to both boards of one module and is fixed to the FEB-box. The lack of connectors on the FEB as well as a horizontal placement of AC-coupling capacitors allowed to minimize the height of the board and to increase the thickness of the FEB's cooling interface. The distance between two neighbouring boards was increased to 6 mm. That allowed placement of two SE408 connectors on the one FEB-panel. On the back side of the panel there is enough space for the placement of LV, HV and signal connectors, as well as a signal return capacitor. The FEB panel is now being developed.

[1]Work supported by RFBR grant 18-02-40047.

[2]Amphenol p.n. SE1804023111111

[3]Amphenol p.n. SE1002023111111

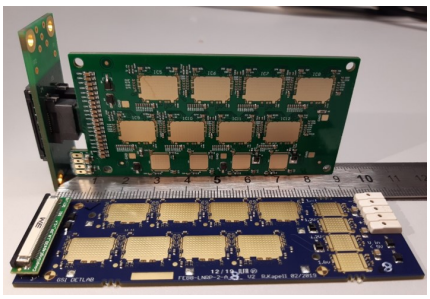

Figure 1: Prototype of the BM@N FEB in comparison with FEB8-2-LNRP-A2.

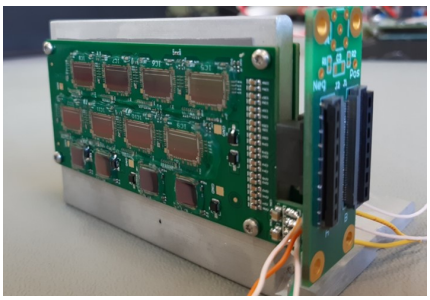

Figure 2: Two FEBs with a FEB-panel

Due to the power-connection scheme with a floating ground, the FEB should withstand the applied voltage between the FEB ground and the data connector. Breakdown tests were carried out with one board. The FEB withstood voltages from -450 V to +450 V at 20% air humidity.

The modification of the FEB-geometry allowed to increase the distance between FEB-boxes, which is crucial for the cabling, by up to 28 mm. The FEB-panel eleminates the need of the 90° cable bending and simplifies connection of the interfaces to the module. Signal integrity tests have shown that the data transmission even with 10 m cable is stable for clock frequencies up to 160 MHz [2].

References

[1] BM@N STS group, *TDR for the Silicon Tracking System as Part of the Hybrid Tracker of the BM@N Experiment*, https://bmn-wiki.jinr.ru/bin/view/Doc

[2] D.Dementev, M. Shitenkow, *Performance of STS-HCTSP with long transmission lines*, CBM Progress Report 2019

Performance of STS-HCTSP with long transmission lines

D. Dementiev and M. Shitenkow
VB LHEP, JINR, Dubna, Russia

The STS-HCTSP protocol was developed for the signal transmission between front-end readout electronics of the CBM STS and the GBTx core through AC-coupled lines, and is described in [1]. The protocol assures data transmission at 320 Mbps in uplink and 160 Mbps in downlink directions. Signal integrity depends on the quality of the signal transmission line, especially for applications with long cables. It is of particular importance to the BM@N STS project, as long data cable connections between FEBs and GBTxEMU boards, located in a radiation-safe environment, will be used. The data connection consists of two parts: inside and outside the STS enclosure. The length of the inner cables is less than 1 m, while the length of the outer cables is up to 10 m.

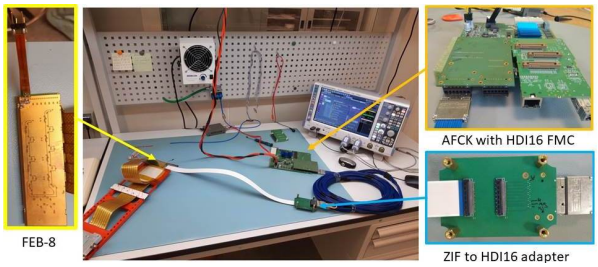

Figure 1: Photograph of the test bench.

SI tests[1] were performed for the signal transmission line consisting of the following parts:

1. AFCK with a dedicated FMC as a data processing board;
2. Twinax cables[2] with length 1/8/10 m;
3. FFC to twinax interconnection board;
4. FFC[3] cable of 1 m length;
5. FEB8-2_LPRN_B with SMX21.

A photograph of the test bench is shown in Fig. 1. Eye diagrams were measured at the following points. For downlink: at the FEB level after AC-coupled capacitors. For uplink: at HDI16 FMC at the level of AFCK. Examples of the eye diagrams for the uplink and downlink with the longest cable configuration are shown in Fig. 2. Analysis was performed with an R&S®RTO2000 oscilloscope 6 GHz, with two active differential probes. The waveforms were received during the SOS (Start-of-Synchronization) command generation. Measured parameters are defined as follows.

- Height: $(V_{top} - 3 \times \sigma_{top}) - (V_{base} + 3 \times \sigma_{base})$;
- Width: $(T_{cross2} - 3 \times \sigma_2) - (T_{cross1} - 3 \times \sigma_1)$;
- Rise time: from 10% to 90% of the top level of the signal and opposite for the fall time.

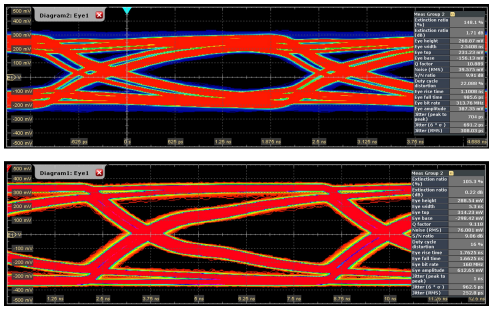

Figure 2: Eye diagrams of the uplink at 320 Mbps measured on the AFCK (top); and the downlink at 160 Mbps measured on the FEB after AC-coupling capacitor (bottom). Cables: 10 m twinax plus 1 m FFC cable.

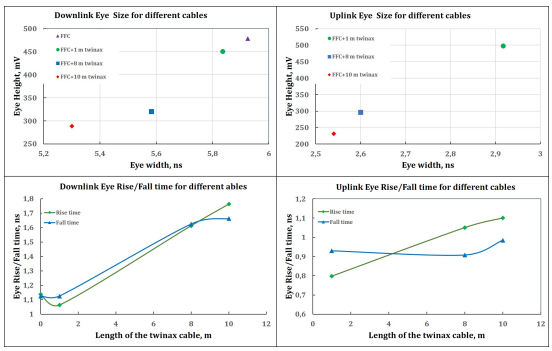

Figure 3: Parameters of eye diagrams for different types of cable connections. Height and Width of the eye (top figures). Rise and Fall time (bottom figures).

As shown in Fig. 3, the eye is closing with increasing cable length. However, even with 10 m twinax cables and 1 m FFC, the communication is stable. The Q-factor is exceeding 9 for all types of connectivity. It corresponds to the BER$\approx 10^{-19}$. The eye height for the long transmission line could probably be increased by changing the value of the termination resistor.

References

[1] K. Kasinski, et al., *A protocol for hit and control synchronous transfer for the front-end electronics at the CBM experiment*, Nucl. Instr. Meth. Phys. Res. A835 (2016) 66–73.

[1] Work supported by RFBR grant 18-02-40047.
[2] Samtec HDLSP
[3] Axon FDC100

Test of a fully integrated STS detector module in proton beam at COSY

J. M. Heuser[1], U. Frankenfeld[1], A. Lymanets[1], P. A. Loizeau[1], D. Emschermann[1], P. Koczon[1], O. Bertini[1], S. Mehta[3], C. J. Schmidt[1], H. R. Schmidt[1,3], J. Lehnert[1], A. Toia[4], A. Rodriguez Rodriguez[4], O. Maragoto Rodriguez[4], P. Pfistner[5], C. Simons[1], R. Kapell[1], R. Visinka[1], F. Nickels[1], K. Schünemann[1], P. Schweigert[1], and O. Vasylyev[1]

[1]GSI, Darmstadt, Germany; [2]FAIR, Darmstadt, Germany; [3]Universität Tübingen, Germany; [4]Goethe Universität, Frankfurt, Germany; [5]KIT, Karlsruhe, Germany

We report on the test of a prototype detector module for the CBM Silicon Tracking System, fully integrated and equipped with the complete front-end electronics to read out all sensor channels, carried out with high-intensity proton beam extracted from COSY, Research Center Jülich, in November 2019. The module integration onto a carbon fiber support ladder, the electrical supply through the final powering electronics, the read-out with the current data aggregation and data transport systems, as well the mechanical assembly of detector ladder onto a C-frame and its installation into a mainframe with close resemblance to features of the intended full-scale STS detector system marked the test an important project milestone. The results shown below contributed to concluding the ASIC Engineering Design Review in December 2019 and will give important input to the CBM module series production readiness procedure scheduled to take place in 2020.

mCBM experiment and dedicated detector tests at other facilities

The CBM experiment has entered a phase in which the main detector system test activity has been shifted to the mCBM ("miniCBM") [1] demonstrator experiment at GSI/SIS-18. mCBM is operational since late 2018. Initially being without explicit beam during SIS-18 recommissioning in December 2018, first beam delivery took place in March 2019, however limited to hours of parasitic beam from the HADES experiment as the main user then. A further beamtime for mCBM is taking place in Spring 2020, at the time of writing this report. The March 2019 mCBM beamtime yielded plentiful information from the combined operation of detector systems, including a miniature/demonstrator versions the of Silicon Tracking System, named mSTS [2]. The read-out was integrated in one full chain of data acquisition from the front-ends to the computing center Green Cube. Central aspect of the beamtimes is combined operation and data taking of the systems, allowing to study various correlations ranging from data rates, as function of beam intensity and target thickness, to timing and eventually track reconstruction. With beam intensities up to 10^8 Ag ions/s and collision rates up to 10 MHz, standard CBM operation conditions and high data rates > 2.5 GByte/s peak were achieved. Detailed detector studies took place but were naturally restricted to reaching configuration readiness. Specific detector investigations are therefore still well placed in different beam campaigns than mCBM, e.g., using the focused "pencil beams" at COSY rather the particle spray from SIS-18 beams directed onto a target, with the detectors being the object to be studied and not the reference detectors.

STS system test in proton beam at COSY

The test carried out in the JESSICA cave at COSY in November 2019 addressed a newly assembled STS module, alike the one shown in Fig. 1, comprising a further developed front-end electronics board (FEB-8) with the new ASIC version STS-XYTER v2.1 and new low-voltage regulation ASICs. This allowed the first operation of a fully functional and noise-optimized STS module in beam.

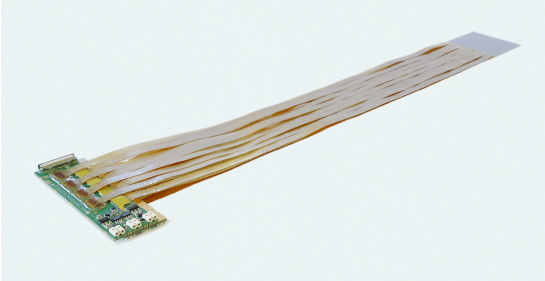

Figure 1: Detector module of the CBM STS as used in the test at COSY.

The module was mounted onto a carbon fiber support ladder, as described in [3] and installed on a C-frame in a mobile test station. For the beam time at COSY, a mSTS C-frame has been refurbished with a new ladder. The module of the type TL01 represents the longest module of mSTS, comprising one 6.2 by 6.2 cm^2 sensor from Hamamatsu fabrication, 45 cm Aluminum microcables, two FEB-8 with alltogether 16 STS-XYTERv2.1 readout ASICs. It has a wide shielding covering the sensor on both sides, and no cutouts for L-legs attaching the silicon to the carbon frame. A newly build mainframe was nesseary to match the beam hight at COSY. Inside, the ladder is horizontally arranged, as opposed to the vertical installation at mCBM. After the beamtime, the mainframe serves as a test box for mSTS C-frames since it can be used for all for units of the

mSTS. A view into the fully assembled system mainframe ready for the transport to COSY is provided in the photo of Fig. 2. One can distinguish the horizontally mounted detector ladder, the mass-reduced C-frame, and other components as the C-ROB data aggregating electronics, powering electronics, and a high-voltage filter box – all under shielding covers.

The system was operated with specific power regulating and distributing electronics and a full prototype CBM data-driven read-out chain, as also applied in mCBM, sandwiched in between two stations of a scintillating fiber hodoscope, its 64 channels per station with the same read-out as the silicon detector. The set-up on the beam table in the JESSICA cave at COSY is depicted in side-view shown in Fig. 3. In the front the chiller for water cooling of the read-out electronics in the detector system is seen.

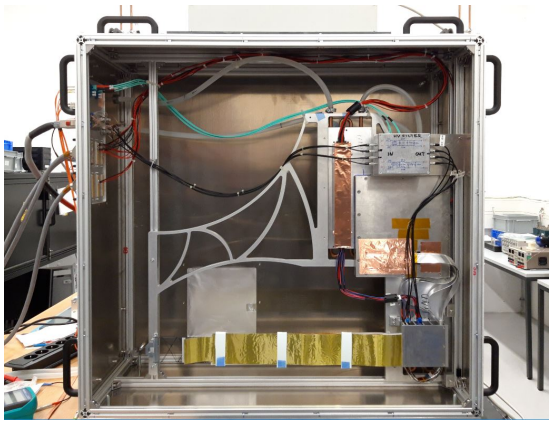

Figure 2: STS sytem assembled for the test at COSY.

Test results

During the beam campaign, we collected 26 runs of typically 5–10 minutes duration each, yielding 20–30 data (TSA) files, each of 1.9 GB size and comprising of the order of 1000 time slices (10 μs). Beam energy and momentum, respectively, remained constant at $E_{kin} = 1.92$ GeV, p = 2.7 GeV/c. We varied conditions of beam intensity, beam position and detector settings, that allowed us to measure various properties of the detector, and characterize them in different configurations. Figure 4 shows data rates as a function of time, given in number of recorded signals per second, in the whole detector, and separately for the p- and the n-sides of the module, as well as for the hodoscopes. The long beam spills of the COSY accelerator, followed by a short break, can be clearly identified.

The targeted STS system noise of around 1000 e^- ENC was demonstrated both during detector commissioning in the assembly laboratory at GSI and in the COSY beam environment (see Fig. 5). The measured signal is shown in Fig. 6 depicting the beam spot for one spatial coordinate and the signal distribution for one read-out ASIC, i.e. 128 channels, all in ADC units. Detailed analysis of the

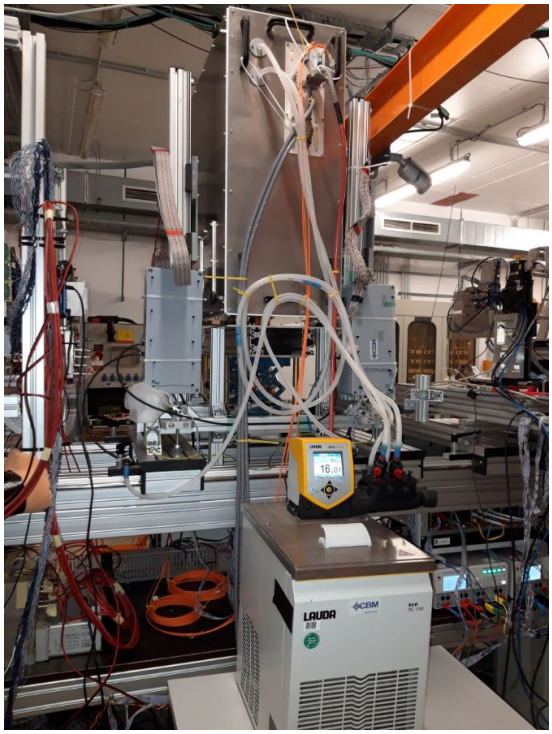

Figure 3: STS system set up in the JESSICA cave at COSY.

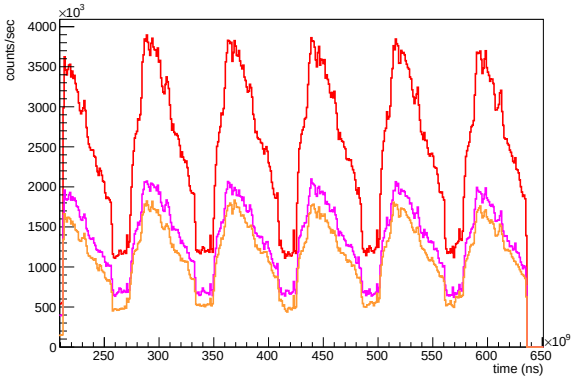

Figure 4: Data rates in STS module (p- and n-sides separately), and hodoscopes (line in red color) for a number of accelerator spills.

data taken is in progress to yield robust signal calibration and thus the signal-to-noise ratio, together with the particle detection efficiency in the small test system of STS module and the fiber tracking telescope.

The time calibration was done identifying a peak in the correlation $t_{STS} - t_{hodoscope}$. The distribution is shown in Fig. 7. The peak is very sharp and sits on a complex background; next to big "waves" (periods of about 300 ns), there are small peaks at periods of 25 ns from the COSY accelerator. Both STS and the hodoscopes were sensitive

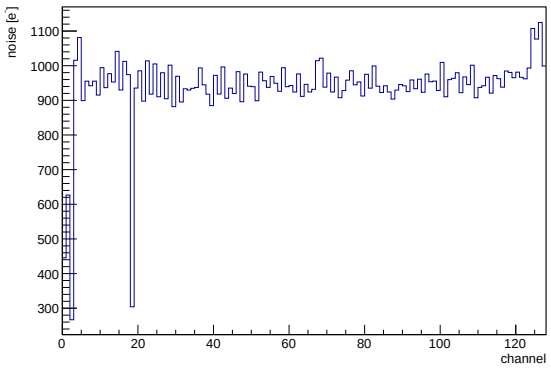

Figure 5: Noise in channels of one ASIC, given in units of electron charge. The measurement was done applying internal test pulsers in the electronics, and subsequent calibration.

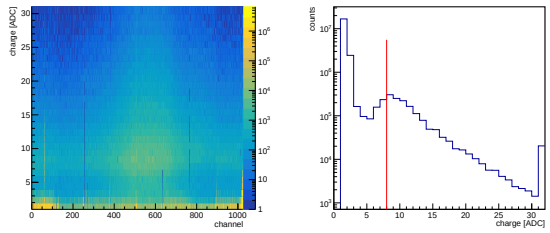

Figure 6: Beam profile seen in the channels of one sensor side (left), and signal distribution in one ASIC (right), all in ADC units before calibration.

to that 40 MHz noise. It was also noted that at high data rates, as a function of increased intensity, multiple peaks in the same time-slice appeared, which was followed by time-jumps, i.e. a sudden change in synchronization. At later times, this has been attributed to the sorting buffer and algorithm in the C-ROB firmware.

In order to improve the signal-to-noise ratio in the reconstruction of correlations of neighbouring signals (clusters) and then of clusters in the p- and n-side (hits), noisy channels have been masked. Moreover, the large noise in the even channels visible in the p-side, is removed by selecting signals with charge larger than 3 ADC.

After noise removal, clusters have been reconstructed by connecting signals from neighbouring strips. The time difference of signals in 2-strips clusters, shown in Fig. 8 separately for the p- and the n-side, demontrates a time resolution of few ns. This is an excellent resolution, considering that walk correction -which reaches about 20 ns for low charge signals, has not yet been applied. The signal distribution follows well a fit with a Landau function, see Fig. 9. A charge calibration in electrons is in preparation.

The hits from the STS module and the two hodoscope stations reconstructed in space are presented in Fig. 10. No

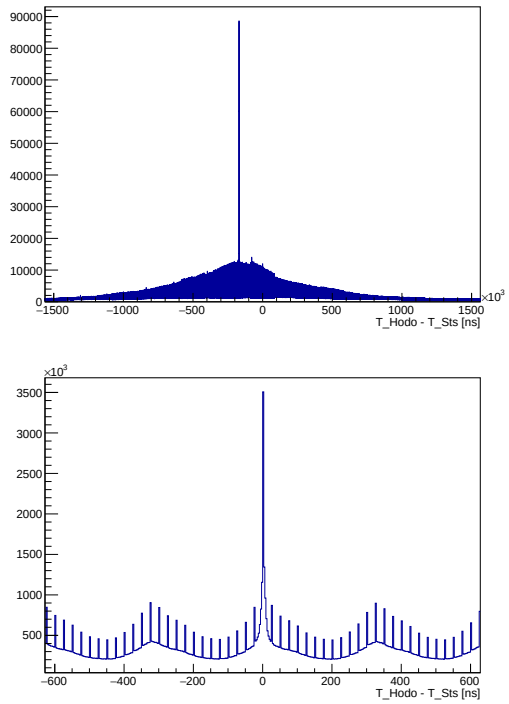

Figure 7: Time difference between data (“digi”) of STS and hodoscopes, shown for two time ranges.

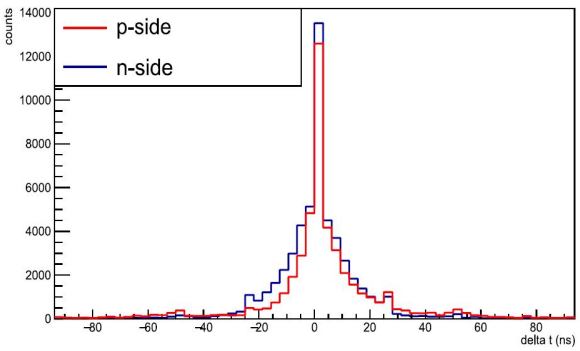

Figure 8: Time difference in digis of 2-strip clusters. The bin size is 3.125 ns. No time-walk correction applied yet.

corrections for spatial alignment have been applied, therefore a shift in transverse directions can be noticed when looking at the respective beam spots.

To understand the performance of the STS sensor, the coincidence with the hodoscope system has been studied. First the space correlation of the hits in the forward and backward hodoscopes has been analyzed: selecting the best time coincidence between two hodoscopes improves the correlation. The hits in coincidence are interpolated to calculate the expected position of the in the STS sensor. This is illustrated in Fig. 11. Then the hits in the STS are corre-

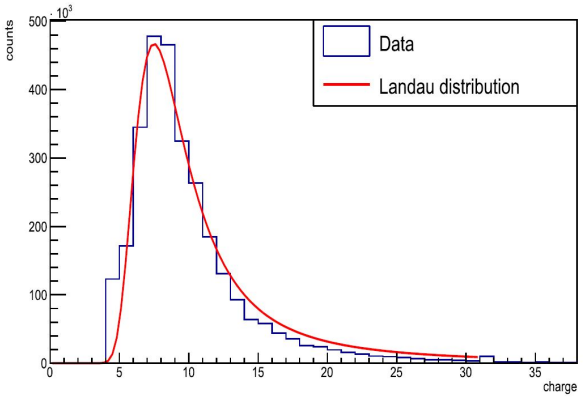

Figure 9: Fit of the reconstructed charge with a Landau function; low-noise cut applied.

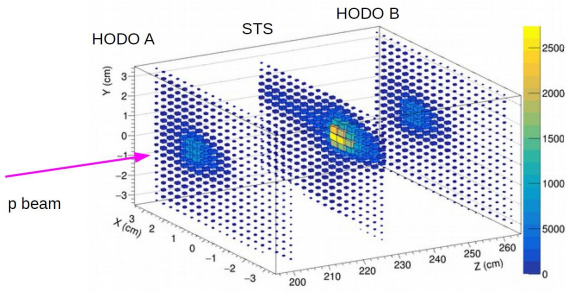

Figure 10: Reconstructed hit maps of the beam particles in the detector test system. No transverse alignment corrections have been applied yet.

lated with the expected interpolated hits. Figure 12 shows the space and time correlation: A sharp peak is visible on top of a broad background. The mean value is not centered at zero, since the STS sensor was not aligned with respect to the hodoscopes system. The resolution in X (≈ 0.07 cm), Y (≈ 0.03 cm) and t (≈ 6 ns) is narrow as expected. It is important to note that the signal time has not yet been corrected for walk effect, leading to an increase of the apparent time resolution.

Based on a simple straight-line trajectory reconstruction, and detector alignment not yet fully taking into account, a first attempt to determine particle reconstruction efficiency in the silicon detector has been made. While appearing very encouraging, in the vicinity of unity across large part of the area, the pointing accuracy of the simple tracking, or the noise treatment, is still to be improved in order to secure the error on the ratio STS hit/STS hit on track found. This is work in progress.

Conclusions

The first operation of a fully functional and noise-optimized STS module in beam has been carried out.

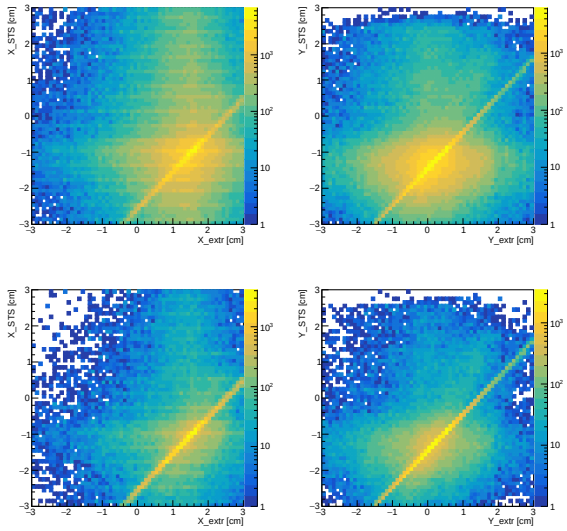

Figure 11: Correlation of digis of STS and hodoscopes in x (left two panels) and y (right two panels) coordinates.

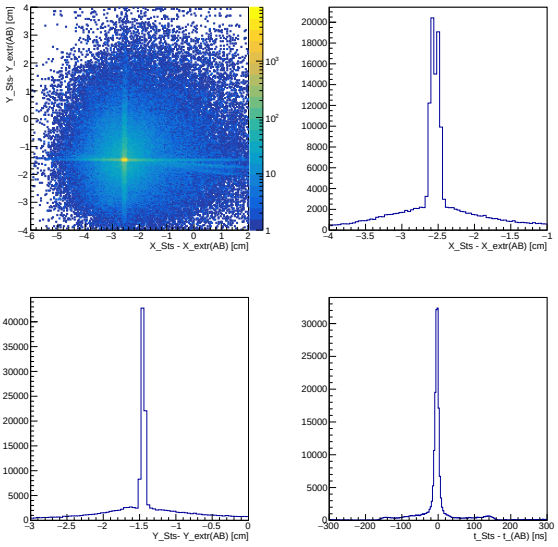

Figure 12: Extrapolation of straight-line tracks made from hodoscope two-dimensional hits to the STS module. Residuals in time and space at the silicon detector.

The targeted STS system noise of around 1000 e^- was achieved. The detector system proved being a great tool for characterization of the full CBM-STS electronics, read-out chain and the sensor. Scans of read-out threshold, beam impinging position and beam intensity have been performed. An excellent time resolution was demonstrated. The charge distributions show clear separation between

noise and proton signal peak. The beam spot reconstruction was achieved successfully. Correlation of hits in STS and the hodoscopes allow a first estimate of hit reconstruction efficiency. The COSY beamtime campaign was immensely helpful in commissioning the full readout electronic chain and online reconstruction software. First results have appeared, e.g. the time calibration, and steps to charge calibration. Much more is to come!

Acknowledgement

We acknowledge the kind support given by the Institute für Kernphysik at Research Center Jülich, providing beam and facilitating us to carry out the experiment.

References

[1] C. Sturm et al., *Start of mCBM Commissioning*, CBM Progress Report 2018, p. 190

[2] J. M. Heuser et al., *Assembly and commissioning of the mSTS detector for mCBM startup*, CBM Progress Report 2018, p. 31

[3] S. Mehta et al., *STS ladder assembly*, CBM Progress Report 2018, p. 26

STS carbon fiber ladders – series production in industry

U. Frankenfeld and J. M. Heuser
GSI, Darmstadt, Germany

Series production

A set of 50 pre-series carbon fiber ladders have been delivered end of 2018 [1]. The outcome was reviewed [2] and after discussion with the company ICM [3] the final order was placed. The complete production of 132 ladders has been delivered in three batches in summer 2019.

Metrology

Optical metrology was performed for a sub-sample of 20% of the produced ladders. The measurement were performed with a three axis measurement instrument equipped with a camera. Focus variation and pattern recognition techniques have been used to determine the position of the tube of the CF ladder between the winding knots [4]. The width of the knots has been measured to be up to 400 µm. For the assembly of the STS ladders [5, 6] the enlargement (Fig. 1) is the most important quantity and is defined as:

$$enlargement := \begin{cases} -(y - y_{nom}), y < 0 \\ y - y_{nom}, y \geq 0 \end{cases}$$

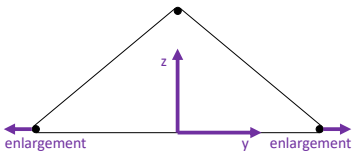

Figure 1: Definition of enlargements and coordinates.

Figure 2 shows the variation of the enlargement for the pre-series (black) and the improvement of the series production (blue). No outlier has been found. The larger variation in z will be evened during the assembly while gluing the sensor holding structures (L-legs) onto the ladder. To compensate the measured enlargement and knot width two sets of L-legs) with enlarged dimensions (y += 600 µm and y += 1000 µm) have been produced by the JINR team.

Central ladders

In addition 16 CF ladders with a cutout for the beam pipe are needed. The company ICM has performed finite element calculations for different realizations of the cutouts (Fig. 3) and produced test gluing. After finalizing the dimensions and tolerances three prototype ladders with a cutout will be ordered at ICM and are expected to be delivered before publishing this article. Metrology, load tests, vibration studies and sensor mounting close to the cutout will be carried out or investigated.

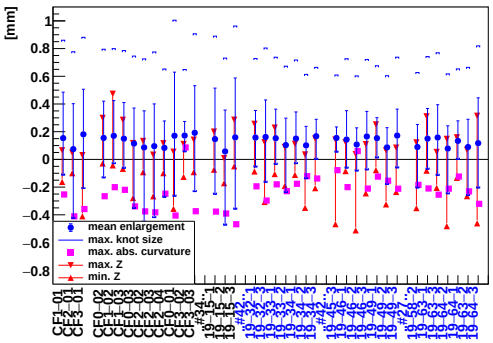

Figure 2: Metrology of 20% of the produces ladders.

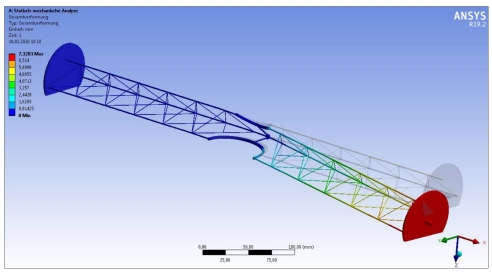

Figure 3: Example of a finite element calculation of one spezific realization of the cutout.

References

[1] J. M. Heuser, W. Niebur, and M. Faul, *STS carbon fiber ladders — pre-series production in industry*, CBM Progress report 2018, p.25

[2] J. M. Heuser et al., *Production Readiness Review for the STS Carbon Fiber Ladders*, CBM-TN-19006

[3] ICM-Composites, Weiterstadt, Germany; www.icmcomposites.de

[4] E. Lavrik, U. Frankenfeld, S. Mehta, I. Panasenko and H. Schmidt, "High-precision contactless optical 3D-metrology of silicon sensors," Nucl. Instrum. Meth. A **935**, 167-172 (2019) doi:10.1016/j.nima.2019.04.039 [arXiv:1812.00917 [physics.ins-det]].

[5] U. Frankenfeld et al., *STS Ladder Assembly*, CBM-TN-18011

[6] S. Mehta et al., *STS ladder assembly*, CBM Progress report 2018, p.26

First experience with the ladder assembly at JINR

D. Dementev, V. Elsha, and Yu. Murin
VB LHEP, JINR, Dubna, Russia

Ladder assembly at JINR is performed with the Ladder Assembly Device (LAD)[1]. The LAD with a set of fixtures was produced at PLANAR, Ltd. Enterprise (Minsk) and installed at the JINR site (see Fig. 1) at the end of 2019. It is equipped with an optical system, which is used for the monitoring of the sensor position in a horizontal plane and has an accuracy of 2 μm. For the alignment of the sensors it comprises different sets of sensor positioning tables with micro-screws and a lifting unit for the vertical displacement of the ladder sensor supporting CF truss. The device is installed on a heavy-duty diabase table to avoid vibrations of the LAD during operation. The LAD should provide the following accuracy of the sensor positioning:

X coordinate: $\pm$ 15 μm on 1200 mm along the truss;
Y, Z coordinates: $\pm$ 50 μm across the truss.

The assembly procedure consists of the following steps:

1. Gluing of L-legs to the sensors;
2. Carrying of the module with a transportation tool to the ladder assembly device;
3. Alignment of the sensor of the module and the cable leading to the corresponding FEB;
4. Steps 2-3 are performed for all modules of the ladder;
5. Putting the CF frame to the final position on top of the chain of sensors in between L-legs;
6. Gluing of all L-legs to the CF frame;
7. Fixation of micro-cables stack to the ruby ball positioning units at the rare ends of the ladder;
8. Mounting of FEBs on the cooling fins of the two FEB boxes of the ladder;
9. QA measurements of the ladder.

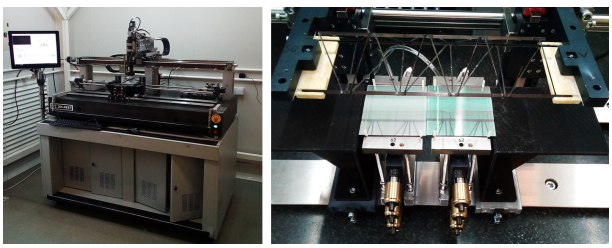

Figure 1: Photograph of the ladder assembly device installed at VB LHEP, JINR (l.h.s.); Photograph of the ladder mockup assembly process (r.h.s.).

[1]Work supported by RFBR grant 8-02-40113.

To test the device and tooling, the first mockup of the ladder with two 62 x 62 mm^2 dummy sensors was assembled, seen in Fig. 2. Before the assembly, positioning tables were installed in given positions, flatness was adjusted within 15 μm. Allignment of sensors on positioning tables was performed with dedicated micro-screws. Fiducial marks on sensors were aligned according to coordinates defined by positions of centers of ruby balls at the far ends of the ladder. After curing of the glue, coordinates of the fiducial marks on the sensors aligned on a ladder-line were measured. As shown in Fig. 3, the deviation of the X coordinate (perpendicular to the strips on the N-side) from the mean value is less than 8 μm.

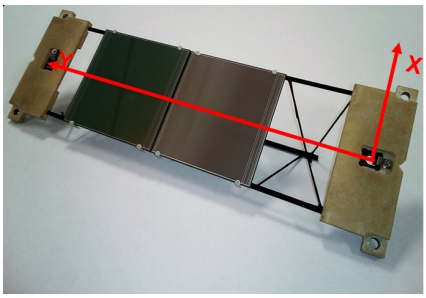

Figure 2: Photograph of the assembled mockup.

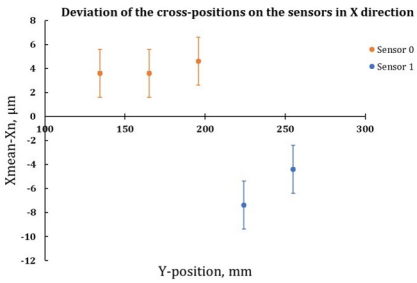

Figure 3: Measured deviations of X coordinates of the fiducial marks on the sensors from the mean value.

Further investigations are planned to demonstrate the workability of the whole assembly process with real modules. Also, modifications of the auxiliary tools and CF-frame crane are needed to adopt it to the version of ruby ball positioning unit of CBM STS ladders, which is slightly different from the one that is used in the BM@N STS ladder design. Metrology of assembled ladders is planned to be performed with the CNC coordinate measuring machine Mitutoyo Crysta-Apex S9206, which has already been procured and delivered but not yet installed at the assembly site.

Ongoing R&D for the STS Thermal Demonstrator

K. Agarwal[1], *R. M. Kapell*[2], *M. Kis*[2], *P. Koczon*[2], *P. Kuhl*[2], *S. Mehta*[1], *U. Möller*[2], *H. R. Schmidt*[1,2], *J. Thaufelder*[2], *and O. Vasylyev*[2]

[1]Universität Tübingen, Tübingen, Germany; [2]GSI, Darmstadt, Germany

This contribution describes the ongoing R&D to experimentally demonstrate the feasibility of STS's cooling concepts. The aim is to achieve this by building a thermal demonstrator comprising of up to 3 STS half-stations (all from Unit 01) under realistic constraints[1].

Silicon Sensor Cooling

Due to the expected irradiation damage, sensors will dissipate $\sim$ 6 mW/cm^2 at -10 °C. So they have to be kept at $\leq$ -10 °C to avoid thermal runaway & reverse annealing, by using forced N_2 cooling to ensure that no extra material budget is included inside the active detector geometry.

Preliminary tests have been conducted with gas nozzles on either sides of a ladder. Instead of real silicon sensors mounted on the ladder, an assembly of an aluminium plate with Kapton heaters was used as the heat producing source for this study.

The results obtained are shown in Fig. 1. These results have been extrapolated from room temperature to -10°C to represent the STS scenario. Given that one is limited by the gas velocity and the resulting vibrations, it can be inferred that the ambient temperature is the dominant effect determining the sensor temperature. Therefore, the temperature inside the STS thermal enclosure must be kept at $\leq$ -10°C in a controlled way, so that the remaining residual sensor heat could be removed by a low velocity gas flow.

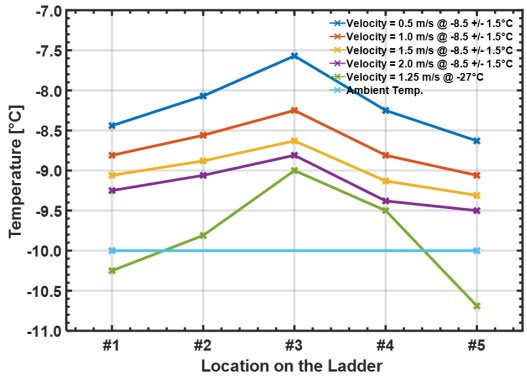

Figure 1: Variation of temperature along the ladder for different air-flow velocities and temperatures.

Please note that several other gas flow configurations with better test structures and its thermal and vibrational effects are under study.

Thermal Enclosure Walls

In order to avoid any outside heat and humidity to enter the STS environment, the walls of the insulation box will be up to 40 mm thick (carbon-fibre composite cladded insulating foam). Two additional features, used at several trackers at LHC experiments [2], will also be used (Fig. 2):

Cooling plates at -40 °C will be attached to the side walls of the enclosure to control the gas temperature inside the box. The temperatures on these plates is foreseen to be the coldest spot in the box so that it safely hosts any condensation outside the electronics area.

Kapton Heaters dissipating $\geq$ 100 W/m^2 at the outer surface of the walls to remove any condensation and keep the surface temperature above the dew point of the CBM cave.

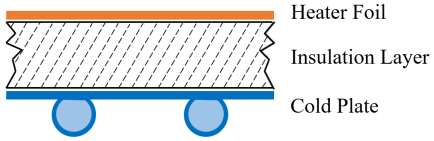

Figure 2: Cross-sectional schematic of the insulation panel.

Corresponding CFD simulations with the simplified STS geometry and realistic C-Frame temperatures showed that the maximum ambient temperatures around the beam pipe for the innermost sensors is around -17.5 °C.

Front-End Electronics (FEE) Cooling

FEE placed outside detector acceptance are connected to the silicon sensors via up to 55 cm long microcables and dissipate $\sim$ 40 kW. So the surface of the FEE enclosure, as seen by the sensors, should be $<$ -10 °C to avoid any heat transfer to the sensors.

Choice of Coolant

Upon intensive discussions at the *Cooling Conceptual Design Review* [3], it was concluded that the 3M NOVEC 649 Engineered Fluid is a better coolant option for the FEE Cooling than the Pumped Liquid-Circulation CO_2 because of the following reasons:

- Easier Commercial Manufacturing and Maintainence;
- High Volumentric Heat Transfer Coefficient;
- Low Global Warming Potential ($\sim$ 1);
- Radiation hardness up to 10 kGy.

Cooling Plate Optimisation

Another important conclusion from the CDR was that the NOVEC 649's flow velocity inside the cooling plate's copper tube is too high ($>$ 3 m/s) and is considered to be detrimental as per industry practices. This requires optimising the cooling plates for better thermal performance with lower flow velocity. Given that the length of copper tubes which could be winded within the plate is limited, a change in cooling plate technology is proposed from Press-Fitted Tube Channels to Milled Inner Structures. This R&D is done in collaboration with CoolTec Electronic GmbH[1]. Other option with Metallic 3D-Printing is also in consideration and isn't addressed in this report.

The CFD simulation results for the new baseline cooling plate (Unit 07) as performed by CoolTec Electronic GmbH are shown in Tables 1 and Fig. 3.

Power Dissipated	1100 W
NOVEC Inlet Temperature	-40 °C
Mass Flow	90 g/s
Maximum Flow Velocity	2.5 m/s
Maximum Temperature on the Cooling Plate	-24 °C
Total Pressure Drop	0.9 bar
Maximum Pressure Rating	5 bar

Table 1: CFD analysis results with NOVEC cooling
.

It must be noted that the optimisation of the FEB box and all its thermal interfaces is still ongoing [4]. Nevertheless, preliminary experimental and simulation results show that an additional temp. rise of $\sim$ 15 °C is introduced by the complete FEB box. This indicates that the maximum temp. on the ASICs with the parameters listed in Table 1 would be $\sim$ -9 °C, which is close to the targeted temperature of $\sim$ -10 °C.

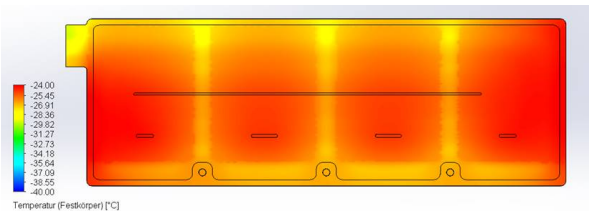

Figure 3: Temperature distribution on the Cooling Plate.

7.5 kW Cooling Plant

For the Thermal Demonstrator Project and the eventual STS integration procedure, it is planned to have a relatively smaller 7.5 kW cooling plant with most functionalities of the final 50 kW cooling plant. Therefore, a commercially available cooling plant is under design and construction with *compact Kältetechnik GmbH*[2] and *KKR Klima-Kälte-Reinraumtechnik GmbH*[3]. Main parameters of this plant are shown in Table 2.

Cooling Capacity	7500 W
Temperature Range	-40 ... +20°C
Max. Mass Flow	1125 g/s
Max. Operational Pressure	5 bar
Secondary Circuit Coolant	3M^{TM} NOVEC^{TM} 649
Primary Circuit Cooltant	Biphase CO_2

Table 2: Major specifications of the 7.5 kW Cooling Plant.

Dummy FEBs and Modules

Dummy FEBs were designed to mimic the thermal behaviour of the real FEBs (Fig. 3), by depositing copper meanders on the PCBs as the heat producing elements instead of using ASICs and LDOs. Such PCBs were manufactured by ILFA Feinstleitertechnik GmbH[4].

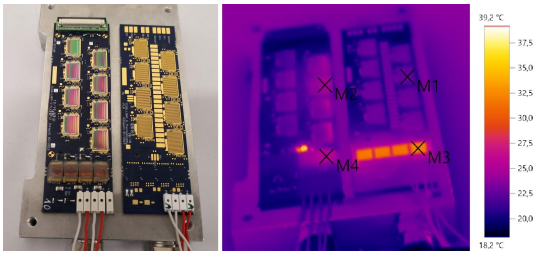

Figure 4: Temperature comparision: real / dummy FEBs.

Consequently, the first prototype of a thermal dummy module was also assembled (Fig. 4) and is currently under tests. Silicon power resistors are used to mimic the heat produced by STS sensors, by producing joule heat accross an Inconel layer (Ni-Cr Alloy; 200 nm) deposited on 300 μm silicon bulk (manufactured by Sil'tronix ST[5]) [5]. The microcables are mimicked by Polyimide-cladded Multi-Wire Copper Flexible Cables (manufactered by SUMIDA Flexible Connections GmbH) and are used to power and readout the temperature of the silicon power resistors.

Figure 5: Thermal Dummy Module.

[1]https://www.cooltec.de

[2]https://www.compact-kaeltetechnik.de
[3]http://www.kkr-gmbh.info
[4]https://www.ilfa.de
[5]https://www.sil-tronix-st.com

References

[1] K. Agarwal *et al.*, CBM-TN-18004 (2018)

[2] P. Petagna, Engineering Forum: Experiences from Cooling Systems for LHC Detectors (2008), https://indico.cern.ch/event/41288/

[3] CBM-STS Cooling Conceptual Design Review, 10 December 2019, https://indico.gsi.de/event/9671/

[4] S. Mehta *et al.*, this report

[5] E. Petit, Forum on Tracking Detector Mechanics (2017), https://indico.cern.ch/event/590227/

Sensor Alignment of the CBM-STS Detector Using Combined Sets of Targeted and Cosmic Muons

S. Das[1] *and H. R. Schmidt*[1,2]

[1]Eberhard Karls Universität, Tübingen, Germany; [2]GSI, Darmstadt, Germany

Abstract

The purpose of aligning a detector is to determine the accurate space coordinates and the orientations of all of its components. To achieve such a spatial precision ($\sim 10\ \mu$m) of all the components in a complex hierarchical detector like the Silicon Tracking System (STS), a track based alignment algorithm has been developed [1, 2]. In our previous reports [2, 3, 4] we had explained the task extensively for the unit and the ladder active hierarchies. This short report will address the sensor alignment of the STS and what additional strategies are employed[1].

Sample preparation

The STS geometry (version 16g) that we have used for the simulation, consists of 876 sensors. So, it is important to prepare a large sample of tracks for the alignment purposes. To be able to align the detector components (alignables) successfully using a track based alignment algorithm, each individual alignable (sensors in this case) with the limited active area, should have a decent track occupancy.

To fulfill the objective, 5 million muon tracks are generated from the regular target (T_0 at $Z = 0$ cm) and additionally, another target (T_1 at $Z = -10$ cm) is assigned (Fig. 1) upstream in 10 cm gap to T_0, to originate 5 million more new tracks. Further 3.7 million cosmic muons are used to complete the set of total 13.7 million tracks for the procedure.

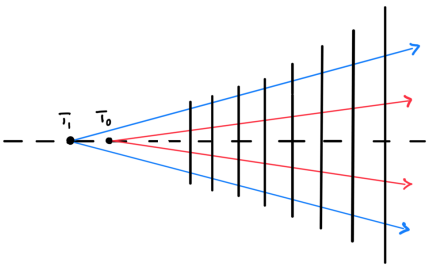

Figure 1: Two targets (T_0, T_1) within a gap of 10 cm.

Assignment of the constraints

The misalignment parameters are determined by the minimization of the track χ^2 with respect to misalignment parameters. In the χ^2 minimization, linear transformations like a shift of the complete detector leave the residual unchanged (*weak modes*). These linear transformations represent undefined degrees of freedom that have to be constrained, otherwise the alignment procedure has no unique solution.

The most general linear transformations in three dimensional space are described by twelve parameters:

- Three overall shifts D_x, D_y, D_z;
- Three scalings C_x, C_y, D_z;
- Three shearings S_{xz}, S_{yz}, S_{xy};
- Three rotations R_x, R_y, R_z;

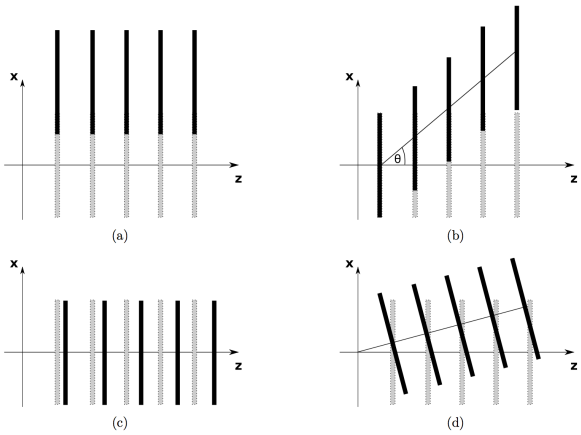

Figure 2: Example of undefined degrees of freedom that leave the corresponding track χ^2 invariant. (a) A shift D_x of the whole detector. (b) Shearing S_{xz} of the detector elements, (c) Scaling C_z along the z direction and (d) an overall rotation R_y of the detector. Figure taken from [5].

Eventually, the geometrical design of the detector already discards most of them out of context. But a few relevant parameters are still to be constrained for the same geomtery. Four such possible undefined degrees of freedom are illustrated in Fig. 2. The figure shows the xz view (applies to the yz plane as well) of five detector elements. The elements plotted in light grey define the nominal detector positions and changed positions are given in black.

In our case, as we plan to apply misalignment in the X and Y directions through translation, followed by a γ-rotation, allied to the Z axis, overall translations ΔX and

[1]This work is supported by the grant BMBF-05P16VTFC1

ΔY and overall γ-rotation, $\Delta\gamma$ are kept to 0 with respect to the global reference system. Additionally, two more constraints are applied by fixing the two target positions. Such a collection of constraints makes it sure to avoid any weak mode in the system and tests have been made to verify that by analyzing the eigen spectrum of the alignment parameters.

Realignment results

One toy misalignment scenario is proposed to test the sensor alignment. All the sensors are randomly displaced using a virtual method (i.e. instead of modifying the geometry, just modifying the hit position accordingly, during the track reconstruction step) by taking $\sigma_x = 50$ μm, $\sigma_y = 50$ μm for the translations along the X and Y axes, and $\sigma_\gamma = 100$ μrad for the rotation in the X-Y plane along the Z axis, using a Gaussian distribution of mean 0 and Z values are kept fixed throughout. The realignment results are given below:

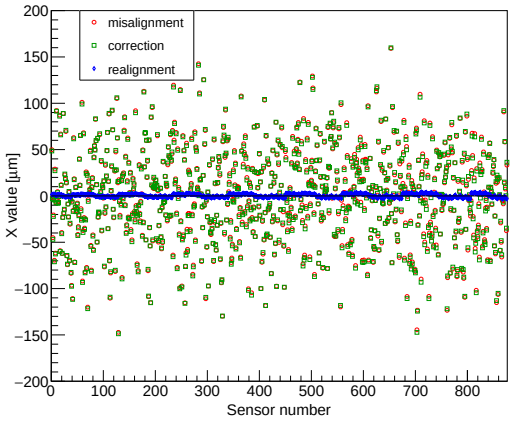

Figure 3: X directional misalignment correction.

Conclusion

From the realignment graphs (Figs. 3, 4, 5), it is clear that the result are within the desired limits: $\Delta X_{err} \leq 5\mu$m, $\Delta Y_{err} \leq 10\mu$m, $\Delta\gamma_{err} \leq 20\mu$rad. Although, some kind of micro patterns are visible on the graphs, but those are more like the non-influential mathematical artifacts of the system and are in well defined limits as mentioned above. So, this report concludes the study of the alignment of the STS in the linear regime and still there is a scope of improvement for the track pattern recognition method involved. Further multi-iterative based investigation can be made for the non-linear sector if the misalignment values come out to be very large during the mechanical mounting of the STS.

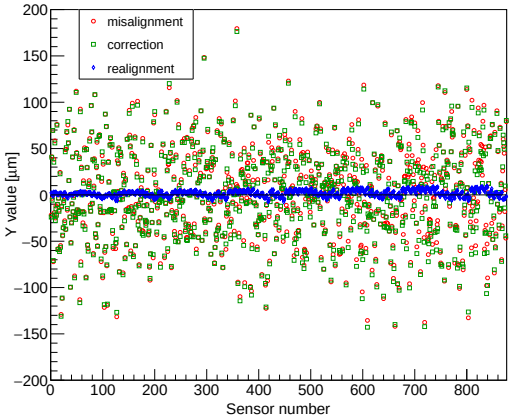

Figure 4: Y directional misalignment correction.

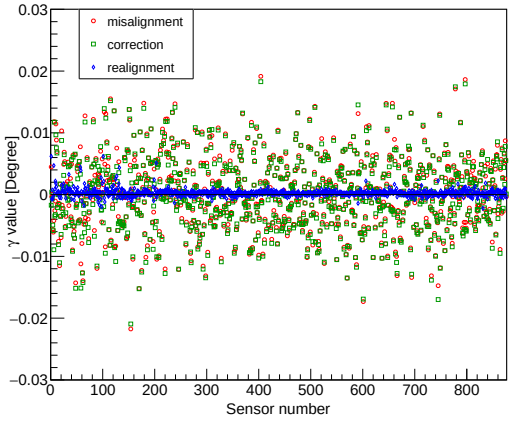

Figure 5: γ directional misalignment correction.

References

[1] V. Blobel, *Millepede II*, Institut für Experimentalpyhsik, Universität Hamburg (2007), http://www.desy.de/ blobel/mptalks.html

[2] S. Das, H. R. Schmidt, *Track Based Alignment Procedure for CBM-STS Using Millepede II*, CBM Progress Report 2017

[3] S. Das, H. R. Schmidt, *Ladder Alignment of the CBM-STS Detector Using the Cosmic Muons*, CBM Progress Report 2018

[4] S. Das, H. R. Schmidt, *Track based alignment procedure for the CBM silicon tracking detector*, J. Phys. Conf. Ser. 1390 012122 (2019)

[5] M. Deissenroth, *Software alignment of the LHCb outer tracker chambers*, CERN-THESIS-2010-063 (2010)

Z-Alignment of the STS Half Units Using Millepede II

S. Das[1] *and H. R. Schmidt*[1,2]

[1]Eberhard Karls Universität, Tübingen, Germany; [2]GSI, Darmstadt, Germany

Abstract

Z coordinate sensitivity of any tracking detector in stationary target experiments is quite poor because of the forward nature of the detector geometry. Therefore, the particle tracking can be challenging in order to obtain the real decay lengths from the decay channels and we mostly have to rely on Monte Carlo (or the ideal) Z values of the detector modules. In other words, the lack of sensitivity of the reconstructed tracks in beam direction implies that any presence of misalignment in the Z-direction remains unnoticed. So, it is obvious that the Z-alignment is a must during the alignment procedure of the STS[1].

Sample preparation

As the tracking sensors detect the signal in the X-Y direction only, because of their 2D-nature, we basically have to solve the Z-alignment problem by entrusting the X-Y residuals. Thus, selecting the right constraints is very crucial. And the best option is to use two fixed target positions for the particle production. Eventually, those two targets give two legitimate constraints as per as the Z-position is concerned. Additionally, fixing the overall Z movement of all the half units to $\Delta Z = 0$ with respect to the global reference system is enforced to avoid any weak mode.

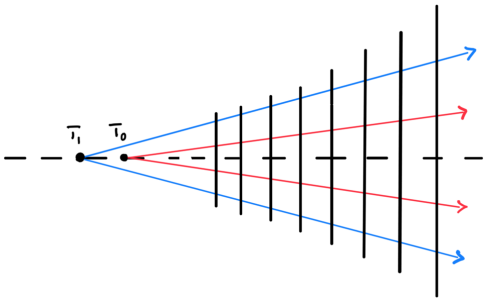

Figure 1: Two targets (T_0, T_1) in 10 cm distance are used.

The STS geometry (version 16g) that we have used for the simulation, consists of 18 half units. To fulfill the objective, $5 \cdot 10^4$ muon tracks are generated from the regular target (T_0 at $Z = 0$ cm) and additionally, another target (T_1 at $Z = -10$ cm) is assigned (Fig. 2) upstream in 10 cm distance to T_0, to originate $5 \cdot 10^4$ more new tracks. Further 10^5 cosmic muons are used to avert any space symmetry artifact that may appear from a single targeted tracks.

[1]This work is supported by the grant BMBF-05P16VTFC1.

Realignment result

One toy misalignment scenario is proposed to test the Z-alignment. All the half units are randomly displaced using a virtual method (i.e. instead of modifying the geometry, just modifying the hit position accordingly, during the track reconstruction step), translating by $\sigma_z = 100$ μm along the Z axis, using a Gaussian distribution of mean 0. After following through the alignment algorithm using Millepde II [1], the obtained realignment graph is given below:

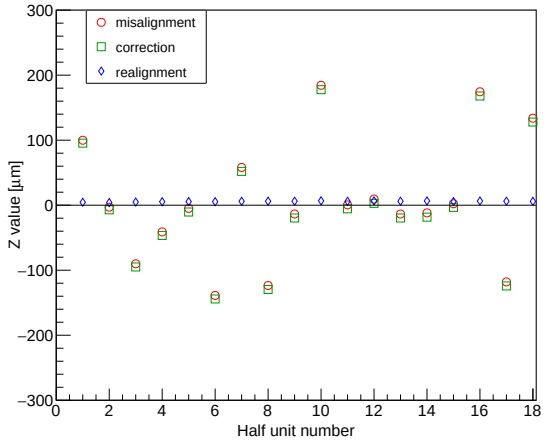

Figure 2: Z directional misalignment correction.

Conclusion

From the realignment graph Fig. 2 it is clear that the result is within satisfactory limit: $\Delta Z_{err} \leq 5\mu$m. And this method can be performed on the other hierarchies as well.

References

[1] V. Blobel, *Millepede II*, Institut für Experimentalpyhsik, Universität Hamburg (2007), http://www.desy.de/ blobel/mptalks.html

Ring-Imaging Cherenkov Detector

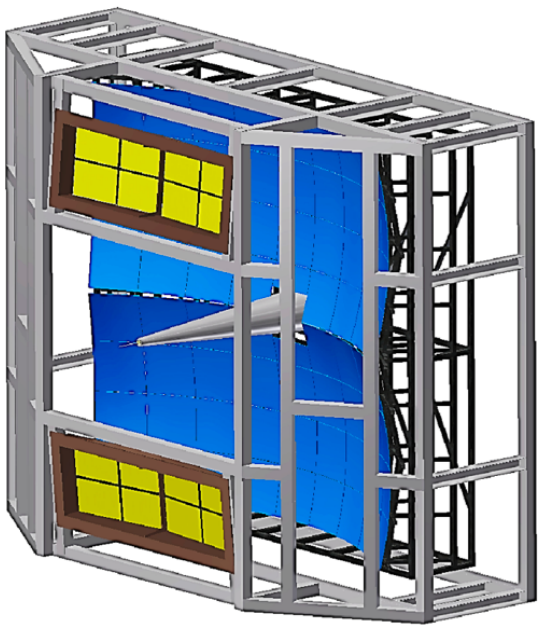

RICH summary

C. Höhne[*1,2], *K.-H. Kampert*[3], *C. Pauly*[3], *and the CBM RICH working group*

[1]Justus Liebig Universität Giessen, Germany; [2]GSI, Darmstadt, Germany; [3]Bergische Universität Wuppertal, Germany

The CBM RICH project has made substantial progress in various fields in 2019 as will be presented in this CBM Progress Report.

The greatest successes in 2019 in context with FAIR phase 0 (HADES, mCBM) were certainly the successful participation of the upgraded HADES RICH detector in the 4 weeks beamtime of HADES in spring 2019 and the successful construction, installation, and participation of a mRICH detector (see Fig. 1) in all mCBM campaigns starting in spring 2019. Both projects clearly validated the readout concept based on the DiRICH board combining very good timing information from a FPGA TDC with moderate amplitude information using ToT information. The full readout of 428 MAPMTs, i.e. nearly 28 000 single readout channels in HADES, was running very stably and at a high performance. Timing precision achieved is better than 220 ps which allows efficient suppression of non-event correlated noise. The ToT information proofed to be very valuable to reject signals resulting from crosstalk. Overall, ring reconstruction efficiencies beyond 99% are achieved which is a perfect basis for the challenging physics analysis of low-mass vector meson pairs. The successful mRICH operation has demonstrated that the intrinsically trigger-based trbnet readout from HADES can be integrated into the free-streaming DAQ concept of CBM. Time and spatial correlations of mRICH rings with the other mCBM detectors could quickly be identified. This first step is still based on the AFCK hardware and gave many valuable lessons on how to continue with porting the readout to the new CRI hardware platform; the development that has already been started.

Another important and well progressing aspect of the RICH development is the mechanical concept of the mirror wall as well as the conceptual design of a shielding box and the mechanical integration of the RICH camera into the overall detector setup. A prototype of the mirror wall has been built and 6 mirror prototypes were installed, aligned, and surveyed. Stability tests of an alternative pillar solution fabricated from carbon fibre are ongoing. The remaining mirror prototypes from the batch delivered from JLO Olomouc are used for lab tests with respect to reflectivity of different coatings as well as to global and local mirror distortions with respect to mirror mounts glued to the backside. QA routines to control the mirror production are being set up.

The operation of the HADES RICH detector also was teaching a lesson concerning cooling. Based on this experience, a full concept has been developed which is currently being tested in a specific prototype comprising one readout column operated in an insulated box. The current idea on cooling is already integrated in a mechanical concept of the RICH camera box that could smoothly be integrated into the overall RICH detector. An important aspect here is the size and design of a shielding box. Also this critical issue has seen great progress last year which resulted in a concept that seems to provide the necessary reduction of the stray field. Calculations to crosscheck the results are ongoing. In addition, the tests on MAPMT efficiency with respect to B-fields have been redone with the H12700 MAPMTs - so far the limits were still based on measurements with the former H8500 model. It seems limits can be somewhat released which eases the construction of the shielding box. In addition the RICH geometry has been changed to a set with 12° mirror tilt yielding to more space between RICH box and field clamps. With all these key ingredients, a full mechanical design of the RICH box with all details is expected to be finished in 2020.

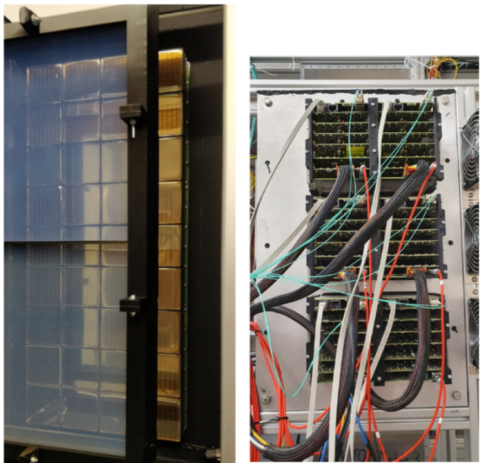

Figure 1: mRICH detector in mCBM; inside (left) with 2 aerogels and 36 MAPMTs and from outside (right) with all readout cards plugged in.

* claudia.hoehne@physik.uni-giessen.de

CBM RICH mirror supporting frame prototype testing

D. Ivanishchev[1], C. Höhne[2], A. Khanzadeev[1], N. Mifstahov[1], C. Pauly[3], E. Rostchin[1], Yu. Ryabov[1], V. Samsonov[1], O. Tarasenkova[1], D. Tyts[1], and A. Firsov[1]

[1]NRC "Kurchatov Institute" - PNPI, Gatchina, Russia; [2]Justus Liebig University, Giessen, Germany; [3]Bergische Universität Wuppertal, Germany

Intensive testing of the lightweight aluminum full-scale prototype of the mirror supporting frame for the CBM RICH detector created earlier [1] was continued. This year, the proposed procedures for mirror tiles gluing, their installation in the supporting frame and the stability of the complete mirror system were tested. For this, as a first step, four complete sets of small frames and mounts for gluing [2] and focusing the mirror tiles were produced, assembled and tested (Fig. 1).

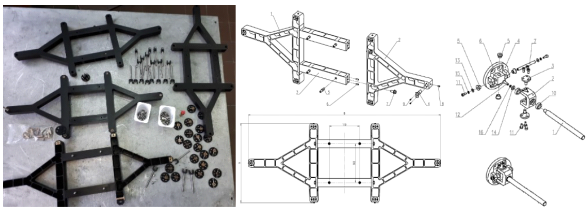

Figure 1: Four complete sets of small frames and mounts (left). Design drawing of a small frame and mounts (right).

Then, a special setup for gluing mirror tiles was designed and assembled (Fig. 2). Initially, flat mirror tiles were used to verify the procedure (Fig. 2a). Two small frames with two flat tiles each were glued and successfully installed in the prototype support frame. A special laser system was assembled to test the stability of the mirror system.

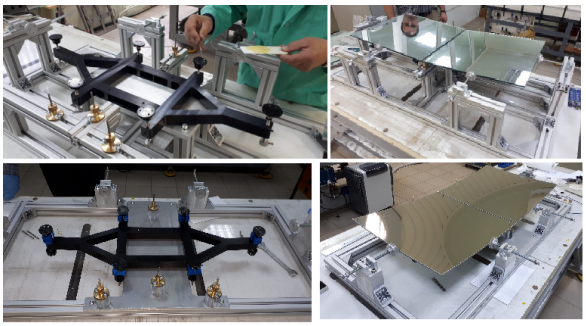

Figure 2: The gluing setup used for flat mirror tiles (two photos at the top), and the upgraded gluing setup used for spherical tiles (two photos at the bottom).

The laser was installed in the center of symmetry of the mirror system, three meters from the mirror surface. The laser light beam was reflected from the mirror tile and projected on a special screen. The center of the light spot position on the screen was measured every 10 minutes using a software system based on Labview. The results of such three months measurements are shown in Fig. 3c. Deviations of the center of the light spot were less than one millimeter at a maximum allowance of six millimeters. This corresponds to an angle of 0.33 mrad which is mainly related to temperature changes. The results indicate that the proposed design meets the requirements. At the next stage, we tested the gluing procedure for spherical mirror tiles which were similar to those that will be used in the real detector. Based on the previous experience, the design of the gluing setup was changed (Fig. 2b) to simplify the initial setup procedure. Three pairs of spherical mirror tiles were glued and installed in the prototype supporting frame (Fig. 3a).

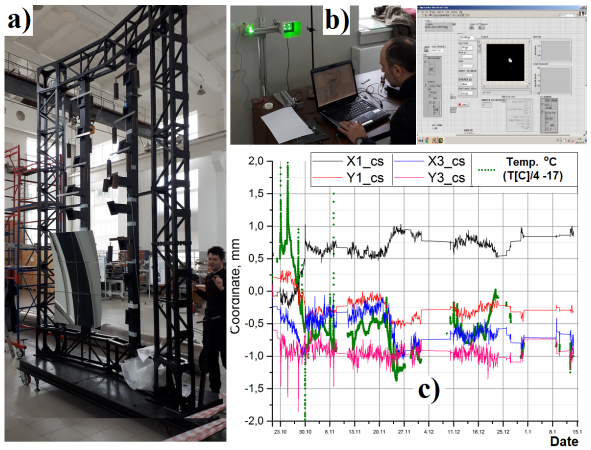

Figure 3: a) Prototype of the mirror supporting frame with six mounted spherical mirror tiles. b) Example of the light spot from the laser on the screen and a program interface for determining the center of a spot. c) Results of three months of measurements for flat mirror tiles (c): green dots - temperature, (X1,Y1) and (X3,Y3) - coordinates of the centers of the light spot on the screen from two mirror tiles.

We plan to glue another pair of mirror tiles after additional upgrade of the gluing setup. A special defocusing nozzle for the laser will be used to illuminate all the mirror tiles at the same time. Using the mount system, we can setup each mirror tile to obtain a separate spot on the screen and take measurements for all tiles simultaneously (Fig. 3c).

Thus, we are ready to test a complete set of components intended for use in the real detector. Tests will be started shortly.

References

[1] D.Ivanishchev *et al.*, CBM Progress report 2018, Darmstadt 2019, p. 40

[2] Ya.Berdnikov *et al.*, CBM Progress report 2017, Darmstadt 2018, p. 53

Stability measurements of a carbon fiber pillar prototype under load

J. Bendarouach[*1], *Y. Ryabov*[2], *and C. Höhne*[1,3]

[1]II. physikalisches Institut, Justus-Liebig-University, Gießen, Germany; [2]NRC 'Kurchatov Institute' PNPI, Gatchina, Russia; [3]GSI, Darmstadt, Germany

To ensure mechanical stability of the RICH mirrors and to optimize the material budget of the detector, the mirror supporting structure as shown in [1] was proposed and designed. A key component of this structure is the pillars, carrying two rows of mirrors, which are fixed via small frames allowing for mirror rotations. A first prototype consisting of two pillars made of aluminium was successfully developed [2] and the stability of a single test pillar under load was investigated [3].

To further improve the material budget of the detector, half a pillar made of carbon fiber was produced and is currently undergoing similar load tests. Figure 1a shows the measurement set-up. A supporting structure (partially seen in silver) was designed to support the carbon fiber pillar (in black) with minimal constraints.

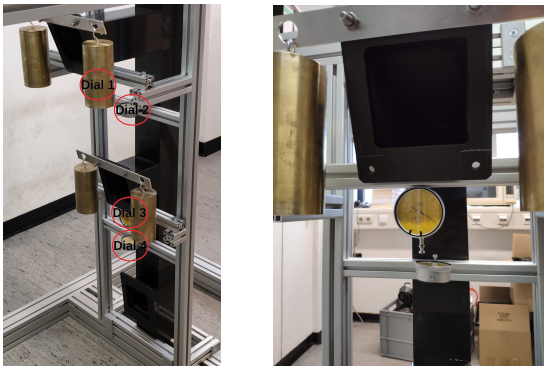

(a) (b)

Figure 1: Left: Test set-up for the stability measurement of the pillar and dial indicator numbering scheme. Right: Dial indicators 1 and 2 fixed on the upper arm.

Four weights (the golden cylinders on Figure 1a) were attached on each side of two arms of the pillar to reproduce the load constraints applied by the mirrors. Each weight is 4.5 kg, which corresponds to about 150% of the nominal load [3].

Four dial indicators were attached on the pillar and used to measure deformations with the increased load. They were given numbers as illustrad in Figure 1a. Two indicators were attached on the trunk of the pillar (2 and 4) and one on each arm (1 and 3). Figure 1b shows a closer view of dials 1 and 2. This configuration and the measurement method were chosen as they were the most similar to [3].

A first deformation measurement was conducted before and after loading the pillar with the weights. The measured deformations read on all four indicators are summarized in Table 1. The observed displacements are in agreement with the deformations observed during the loading of the aluminum prototype pillars [3].

	Dial 1	Dial 2	Dial 3	Dial 4
Preload	5.58	1.74	0.88	3.61
Afterload	5.83	1.53	0.99	3.15

Table 1: Pillar deformations (in mm) before and after loading.

The deformations of the pillar under load were monitored over a total period of seven months. The measurements are summarized in Figure 2. The evolution of the displacements of the carbon fiber pillar are also in agreement with the tests conducted for the aluminum prototype.

Two measurements per week were conducted during the first two weeks. After that a measurement was taken every week until measurement number 8. Measurements 9, 10 and 11 were read with a spacing of about one month, starting four months after measurement 8.

The displacements range between +10 and -40 µm until measurement 8. The maximal deformations were observed on the Dials 1 and 3, which are located below the two arms, indicating a higher pressure on the arms applied by the weights. The jump between measurements 8 and 9 is due to the fact that the whole setup had to be moved in the laboratory. However the values remain constant again from then on.

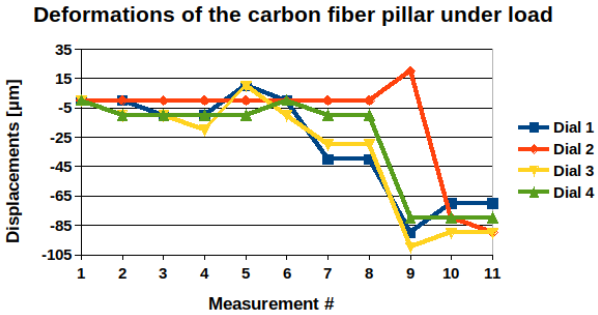

Figure 2: Evolution of the carbon fiber pillar deformations under load.

References

[1] Ya. Berdnikov et al., CBM Progress Report 2015, p.52

[2] Ya. Berdnikov et al., CBM Progress Report 2016, p.63

[3] D. Ivanishchev et al., CBM Progress Report 2017, p.53

*jordan.bendarouach@exp2.physik.uni-giessen.de

Magnetic field simulation, construction and cooling of the CBM RICH camera

*

D. Pfeifer[1]*, C. Pauly*[1]*, E. Ovcharenko*[2]*, and K.-H. Kampert*[1]

[1]Bergische Universität Wuppertal, Germany; [2]Justus-Liebig Unversität Giessen, Germany; [3]LIT JINR, Dubna, Russia

The photon detection system of the CBM RICH detector consists of two separate camera boxes, carrying the H12700 Multianode Photomultipliers from Hamamatsu, as well as all frontend readout modules. The MAPMTs are organized on backplanes, each backplane consisting of 3×2 MAPMTs on one side, and 12 DiRICH frontend modules plus power- and combiner module on the backside. Each camera box is surrounded by an iron shielding box in order to shield the MAPMTs from the magnetic stray field of the CBM dipole magnet by guiding the magnetic field lines around the MAPMT array. Significant progress has been made over the last few months towards a complete mechanical camera- and shielding box design, including a better defined interface towards the gas radiator box, a well defined interface between photon camera and shielding box, and an improved shielding of the magnetic stray field from the dipole magnet at the place of the photon detection plane.

Magnetic field simulations

The work on optimizing the shielding box design using Finite Element Methods (FEM) magnetic field simulations of magnet and shielding box has been continued, see also [1, 2]. The task of this shielding box is to reduce the stray field of the CBM dipole magnet in the region of the photon detection plane to values below 3-4 mT. The maximum tolerable field has been increased slightly based on new measurements of the H12700 MAPMT efficiency in magnetic fields (see [3]).

Many different iron shielding box versions with different geometries were generated and simulated using the COMSOL Multiphysics software package in order to identify the geometric parameters which play the most important role for the shielding performance. The largest influence is given by the thickness of the bottom plate of the shielding box and the height and width of the "wing", which is an integral part of the shielding box located underneath the bottom plate. This "wing" consists of massive iron and its shape is constrained by the requirement to not cut into the angular acceptance of particles produced in the target. Another important parameter is a maximum clearance between the shielding box bottom wall and the MAPMT sensors. The maximum distance is limited by the keep-out volumes reflecting the particle- and optical acceptance regions. Fixing the main mirror tilt angle to 12° allowed for some additional space in this region compared to earlier design iterations (still based on a 10° geometry). In addition, it turns out to be beneficial to leave a gap in the center part of the shielding box back wall, so that it can be manufactured out of non-iron material. Other parameters have only minor effects to the magnetic field. Based on detailed investigations of the interaction of the individual parameters, a geometry could be identified (as shown in Figure 1) that currently offers the best solution and is now considered to be close-to-final.

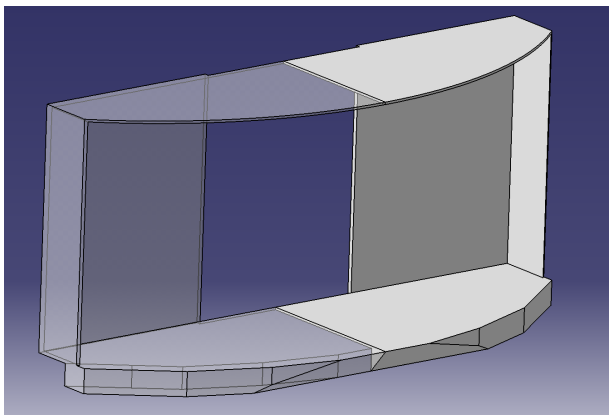

Figure 1: Latest design of the shielding box; the left side is shown slightly transparently in order to make the back- and bottom part visible.

The previous ANSYS simulation results of the old shielding box V1 geometry could be successfully reproduced using COMSOL. This geometry was then used as a reference model for all further simulations. Figure 2 shows a direct comparison of these simulation results (only the right half of the camera is shown). According to these simulations the B_z component, which is parallel to the beam axis, plays a critical role and contributes significantly to the total field B_{total}. The improved shielding box design reduces the magnetic stray field in particular in the previous "hot spot" region in the inner, middle part of the detection area, where the largest ring- and track density is expected. Together with the improved magnetic field insensitivity of the H12700 MAPMT, the shielding is expected to allow reliable operation of the MAPMTs, provided the stray field of the dipole magnet turns out as expected.

* Work supported by GSI and BMBF contracts No. 05P19PXFCA and 05P19RGFCA

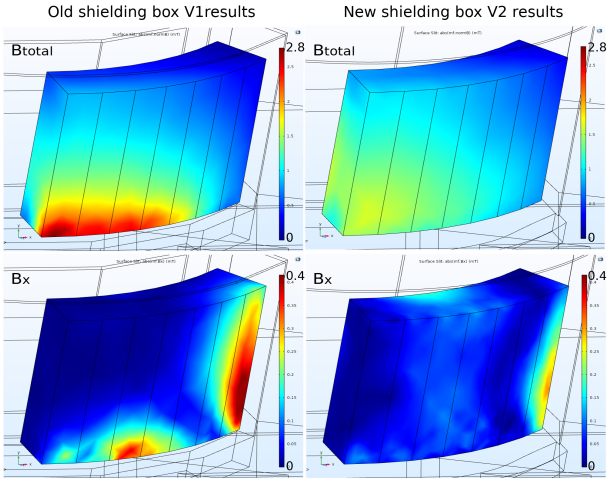

Figure 2: Comparison of magnetic field simulation results performed with COMSOL for previous (left) and latest (right) design of the shielding box. Field values given in mT. B_x is the field component parallel to the horizontal axis.

Mechanical design

The mechanical design of the shielding box is shown in Figure 1. It consists of relatively thin side top and bottom elements with a thickness of 10 mm and four back wall elements on each side with a thickness of 20 mm. The "wing" structure at the bottom is an integral part with dimensions of 103 mm in height and 100 mm in depth. The center part of the "wing" is chamfered matching the previously described keep-out volumes. The back wall of the shielding box is now flat, allowing for an easier integration into the radiator vessel, and also providing extra space for the camera box and its internal components.

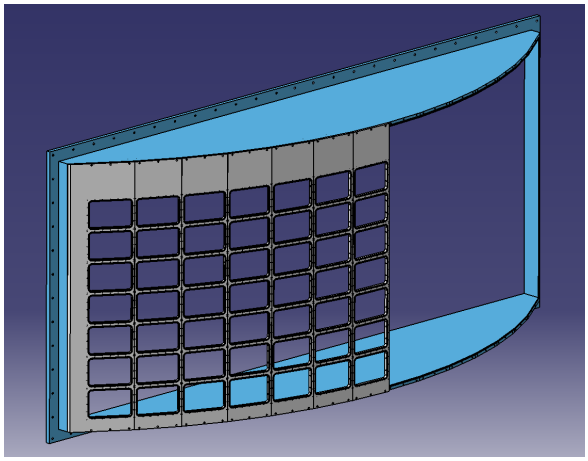

Figure 3: Camera box with flange interface (blue), and seven aluminum segments forming the curved front face carrying the PMT- and readout modules (grey).

The camera box (see Figure 3) will be constructed as an independent assembly part resting inside the heavy iron shielding box and being held in position by a surrounding flange. This simplify both the independent construction and testing of the camera box, as well as its installation into the pre-assembled RICH vessel. The precise curvature radius ($R = 1650$ mm) of the segmented front face is ensured by the upper- and lower walls, resulting in a cylindrical photocathode plane of radius $R = 1699$ mm, in good agreement with the simulation-based geometry optimization (see [5] for details). The front face will be made of individual aluminium elements ("columns"), joined together in a cylindrical shape, screwed and glued in order to be gas- and light tight. These aluminium columns carry the 3×2 MAPMT readout modules. To reduce the weight and to keep the effect of the magnetic field low, the camera box will be made of aluminium. The estimated weight of one complete camera is about 1000 kg, which includes all the components starting with the shielding box, camera box, MAPMTs and readout modules.

Cooling concept

The total heat dissipation per camera is up to 3 kW: about 100 W from the $\sim$ 500 MAPMT active voltage dividers and around 2.5 kW from the MAPMT readout electronics. Each camera system is a self-contained volume enclosed by the shielding box. Active cooling of the readout electronics is therefore a critical issue. Because of the strong temperature dependence of the MAPMT dark rate and instabilities occurring at higher temperatures (see [4]), particular care has to be taken to keep the temperature of the MAPMTs below about 30 °C . The MAPMTs are in good thermal contact to the individual module backplanes, and as such also to the electronic front-end modules, which are the main heat source. Thus, active cooling of the electronics and in particular of the backplane PCB, is a key issue. A sophisticated air cooling system has been designed, in which compressed cold air (50 - 100 mbar) is distributed via interconnected 3d-printed plastic masks (see Figure 5), situated between backplane and electronic modules. The masks serve at the same time as mechanical fixation for the individual front-end cards. The cold air-flow is directed towards the backplane-PCB to provide maximum cooling of the backplane and the MAPMTs which are mounted on the opposite site of the PCB. The air-flow then passes the individual electronic modules, providing cooling also to the electronics, before it flows out of the camera box. The cooling is designed as semi closed loop comprising a blower and a water-cooled heat exchanger located outside the camera box.

This approach has been tested using a single readout module with up to 12 DiRICH front-end cards attached. The concept of mechanical fixation of the electronic readout cards using similar 3d-printed masks was successfully implemented in the HADES detector upgrade, though without the additional air-cooling and distribution func-

tionality. For a more realistic test, a larger prototype is being setup now, consisting of a full "column" with 7 MAPMT backplanes and 84 DiRICH modules (see Figure 4). The prototype is enclosed by a thermally insulated box made of conventional XPS plates, preventing any heat exchange via convection to the outside, similar to the closed camera boxes, where the compressed air is the only coolant. Using this prototype we hope to obtain realistic and reliable results on the cooling performance of this concept.

Figure 4: Cooling system prototype with seven 3×2 MAPMT readout modules

In addition to air cooling, we started to investigate additional water cooling of the aluminium elements carrying the backplane modules (see [7] for some more details). The backplane PCBs have a gold-coated top layer, enabling good thermal contact between aluminium and PCB. The water cooling of the aluminium frame alone would be insufficient for the total heat load of 3 kW. However, used in combination with the air cooling it could help to further decrease the backplane- and thus sensor temperature, allowing higher operating temperature (and thus less cooling effort) of the readout electronics which can be operated at temperatures of 50 - 60 °C. According to current ideas, the water cooling would be realised by pressing two vertical aluminium water pipes on the outer edges of each of the aluminium modules (as shown in Figure 4).

Obviously, combining two cooling methods would increase the complexity of the system. On the other hand, it would provide redundancy in operation and would reduce

Figure 5: 3d-printed ABS plastic mask for direct backplane and indirect readout electronics air cooling (left to right; top, side and bottom view)

the demands of the air cooling. Moreover, the efficiency of air cooling increases with increasing temperature of the cooled object, here the readout electronics.

Extensive tests based on a prototype model of realistic scale are the next important step towards finalizing the cooling concept.

References

[1] P. Akishin et al., Design of a shielding box for the CBM RICH Camera, CBM Progress Report 2017, p.54

[2] E. Ovcharenko et al., Status of RICH magnetic shield simulations, CBM Progress Report 2018, p.44

[3] N. Weimer, et al., H12700 MAPMT efficiency dependence on B-field and incident angle, this report

[4] V. Patel et al., Temperature dependence of dark noise for H12700 MAPMTs, CBM Progress Report 2016, p.74

[5] I. Kres et al., RICH geometry optimization, CBM Progress Report 2016, p.64

[6] D. Pfeifer et al., Readout electronics cooling: concept and first measurements, https://indico.gsi.de/event/4759/session/14/contribution/137/material/slides/0.pdf

[7] D. Pfeifer et al., Camera box design and Cooling, https://indico.gsi.de/event/8628/contributions/42853/attachments/30712/38194/CbmCollaboration Meeting_20200326_RICH_camera_geometrie.pdf

H12700 MAPMT efficiency dependence on B-field and incident angle *

N. Weimer[1], *C. Pauly*[1], *J. Förtsch*[1], *and K.-H. Kampert*[1]
[1]Bergische Universität Wuppertal, Germany

The two CBM RICH photon detection cameras will placed in the vicinity of the CBM dipole magnet, where magnetic stray fields in the order of tens of mT are expected. Shielding boxes made of iron will be used to reduce the stray field to tolerable values of 1-2 mT in order not to spoil the single photon detection efficiency of the Hamamatsu H12700 MAPMT photon sensors. The design, and in particular the weight of the shielding boxes strongly depends on the maximum tolerable field at the position of the MAPMTs. So far, we assumed a maximum tolerable field of 1-2 mT, based on old measurements on the H8500 MAPMTs [1], a predecessor of the now used H12700 [2]. This very low value puts strong demands on the performance of the shielding box and motivated new measurements of the magnetic field effect of the new sensor.
Another factor which might reduce the sensor detection efficiency is the incident angle of photons hitting the MAPMT. In the geometry of the CBM-RICH, this angle can get rather large, up to $\sim 45°$.

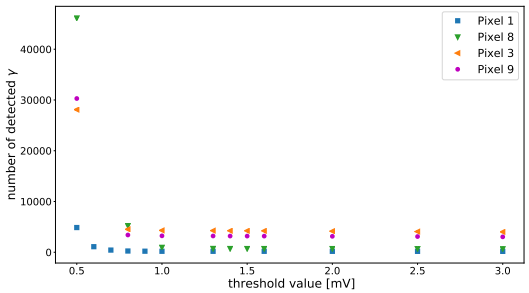

Figure 1: Number of detected photon pulses (for 50k generated pulses) as function of threshold. Below $\approx$ 1 mV an increasing contribution from noise is evident, above 1 mV in the plateau region the detection efficiency is only slowly decreasing with increasing threshold.

Using a dedicated laboratory setup, we have studied the dependence of single photon detection efficiency of H12700 MAPMTs on magnetic fields and as function of incident angle with respect to the PMT window.

The setup consisted of a laser pulse generator, producing regular light pulses guided to the MAPMT under test using a light fibre. The light intensity was damped such that on average a single photon was detected by the MAPMT in every 10th laser pulse. The MAPMT was connected to a digital oscilloscope that was triggered by the laser pulser to record the PMT response signal trace for each laser pulse for up to 3 pixels simultaneously. Each readout channel was connected either to individual MAPMT pixel outputs, or to the MAPMT dynode sum signal. All unused MAPMT pixel outputs were terminated with 50 Ω. Analysis of the recorded traces is done offline. A signal pulse above a certain threshold (in a fixed time window relative to the laser trigger signal) is counted as detected photon. The relative photon detection efficiency is then derived as the number of detected photons in relation to the total number of recorded laser pulses. The signal threshold was carefully chosen (offline in the trace analysis) based on Figure 1, showing the fraction of detected photons as function of threshold. For thresholds $\geq$ 1 mV, a plateau is reached with only little depencence on the precise threshold value.

Efficiency dependence on magnetic field

In order to measure the efficiency variation on magnetic field strength, the MAPMT was placed into a large Helmholtz coil with the field direction along the PMT axis (z-axis). The magnetic field was calibrated beforehand by a Hall probe placed at the location of the photo cathode. The variation of the MAPMT single photon efficiency was then studied as function of the field strength. A black plastic mask in front of the MAPMT window was used to illuminate only the pixels of interest.

The largest effect due to magnetic field is observed in the outer edge- and corner pixels of the MAPMTs. Figure 2 summarises the results for 7 individual pixels and for fields up to ± 8 mT (pixels are counted line wise starting with pixel 1 in the upper corner). All measurements are normalised to 100 % at zero field value.

We also tested the illumination of a single pixel only, and compared the readout of this single pixel with the readout of the dynode sum signal, as shown in Figure 3. Very similar efficiency behaviour is observed, suggesting that the loss in efficiency is not caused by a simple deflection of photo electrons towards neighbouring dynode channels. As a result, we find that the H12700 MAPMT shows a significantly higher field tolerance as compared to the H8500 MAPMT measured previously. In the inner pixel, hardly any effect is seen for the maximum applied field values.

Efficiency dependence on incident angle

In order to measure the angular dependence of the photon detection efficiency, a special PMT holder was con-

* Work supported by BMBF contract No. 05P19PXFCA

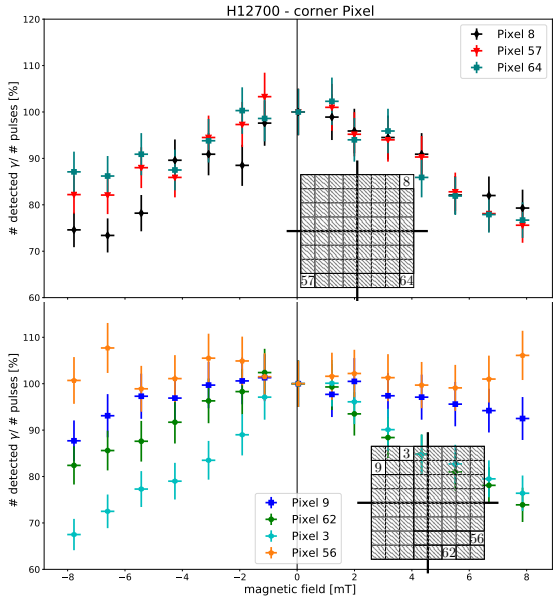

Figure 2: Single photon detection efficiency degradation of Hamamatsu H12700 MAPMT as function of magnetic field in z-direction (perpendicular to PMT window) for 3 corner pixels (top) and 4 outer edge pixels (bottom).

structed as sketched in Figure 4. Single photons from the the same light fiber as before were now projected onto a slit image of 3 mm width covering one of the middle rows of the MAPMT pixels. The MAPMT was then rotated in this holder along a rotation axis in line with the MAPMT window, such that the position of the illuminated slit stayed rather fixed on the PMT window. By rotating the MAPMT, incident angles from -80° to +80° could be realised, and for each given angle the fraction of detected photons (determined based on the dynode sum signal) is compared to perpendicular incidence. Results of this measurement are

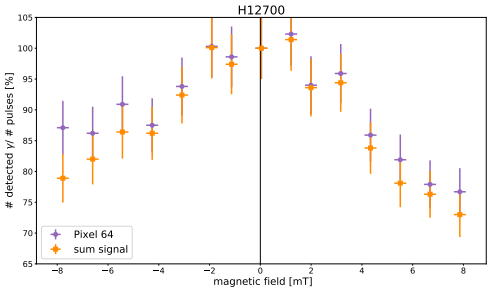

Figure 3: Efficiency variation of corner pixel 64 (all other pixel were masked) as function of magnetic field if the pixel is read out directly (magenta), and if the MAPMT sum signal is evaluated instead (orange).

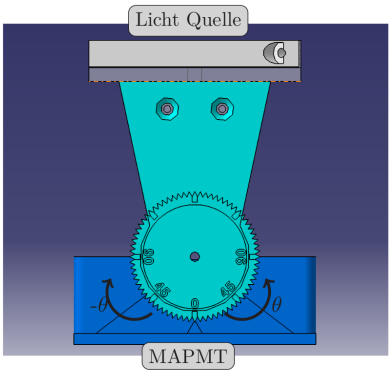

Figure 4: Sketch of the 3d-printed MAPMT holder, allowing for a rotation of the MAPMT with respect to the light source by +/- 80°.

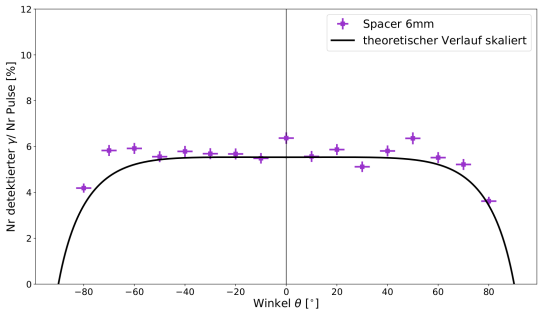

Figure 5: Relative variation of single photon detection efficiency with respect to the incident angle in the range of +/- 80° together with the theoretical expectation from pure Fresnel reflection on the glass surface (solid line).

shown in Figure 5, together with a theoretical expectation based on pure Fresnel reflection on the PMT glass window normalised to the data points, and averaging the horizontal and vertical polarisation components. For incident angles up to 70°, the detection efficiency is rather flat, in good agreement with the pure Fresnel reflection. More details on the incident angle measurements can be found in [3].

References

[1] C. Pauly et al., "Single-photon and magnetic field measurements on H8500 MAPMTs", CBM Progress Report 2010, GSI-2013-04801.

[2] J. Förtsch et al., "The new H12700 MAPMT for CBM RICH", CBM Progress Report 2014, GSI-2015-01521.

[3] N. Weimer, "Winkelabhängigkeit der Einzelphoton-Nachweiseffizienz eines Multianodenphotomultipliers", Bachelor thesis BUW (2019).

RICH geometry optimization

S. Lebedev[1], *E. Ovcharenko*[1], *and C. Höhne*[1,2]
[1]Justus Liebig University Giessen, Giessen, Germany; [2]GSI, Darmstadt, Germany

The current RICH geometry ($v17a$) was designed in 2017. It was optimized with respect to the electron identification and pion suppression [1]. However, one of the design issues is still open – the final design of the shielding box which protects the MAPMTs from the magnetic stray field. Our simulations showed that depending on the design the shielding box can significantly increase the number of background rings, mainly due to γ conversions. This in turn leads to a degradation of the RICH electron identification performance. The other problem is a possible shadowing of photons by the shielding box which reduces the geometrical acceptance in the inner part of the PMT plane. With these additional requirements one needs to optimize the RICH geometry again. One of the ideas is to move the PMT plane out of the magnetic field by rotating the mirror up to 15° (see Figure 1). This allows to reduce the material of the shielding box and gains more space between the RICH box and the magnet which helps to simplify the detector installation and maintenance.

In the optimization studies 3 mirror rotation angles were considered: 10° (same as $v17a$), 12°, 15°. For simplicity, let's tag these geometries as $m10$, $m12$, $m15$, respectively. The first simulation results showed that the RICH performance doesn't depend on the PMT plane radius thus all further simulations were performed with a fixed radius of 1697 mm. The following RICH geometry parameters were optimized (values are presented relative to the nominal position): **PMT plane rotation angle** [°]: 0, 3, 6, 9, 12, 15, 18, 21; **PMT plane Y(Z) shift** [mm]: -100, -75, -50, -25, 0, 25, 50, 75, 100. Combining all parameters one gets 648 geometries per one mirror rotation. Later in the text we refer to "PMT plane shiftY(Z)" as $shiftY$ and $shiftZ$, respectively.

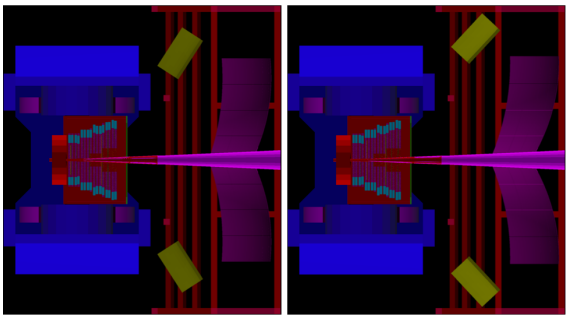

Figure 1: RICH geometries in the simulation with different mirror rotation angles: 10° (left) and 15° (right).

Each geometry was tested in several simulations: **1)** Geometry test with one e^- and one e^+ from the primary vertex (30k events). The main parameters to look at were: geometrical acceptance, B/A, dR, radius, number of hits in ring. **2)** Geometrical acceptance with ω-meson from Pluto at 3.5 and 8 GeV (1k events). **3)** RICH background test with UrQMD Au-Au central collision at 8 AGeV (1k events). The main parameters to look at were: number of hits per event, number of $e^{\pm}$ from γ conversion per event. **4)** Reconstruction performance test with 15 e^- and 15 e^+ per event from the primary vertex. The ring reconstruction efficiency approximately corresponds to UrQMD Au-Au central collision at 12 AGeV but statistics is much higher (5k events). **5)** Reconstruction performance test with UrQMD Au-Au central collision at 8 AGeV including 5 e^- and 5 e^+ from the primary vertex (1k events). The main parameters to look at were: ring reconstruction and STS-RICH matching efficiencies, electron identification efficiency and pion suppression.

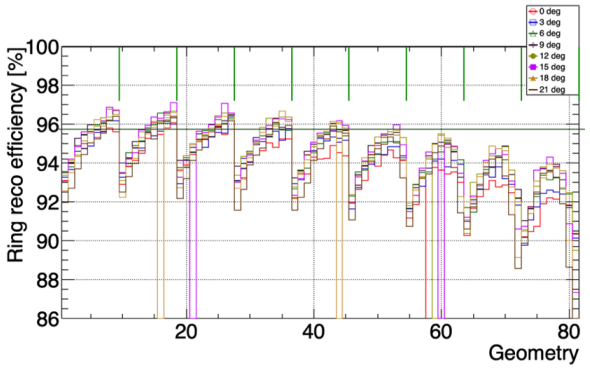

Figure 2: Ring reconstruction results for all tested $m12$ geometries. UrQMD Au-Au central collisions at 8 AGeV.

The results of the geometry comparisons are presented as 1D and 2D histograms. The 1D histogram shows integrated values of one of the tested parameters for each geometry. Each color represents a different PMT rotation angle. The vertical green lines correspond to 9 $shiftY$ geometries. Between each two green lines $shiftY$ is the same and includes 9 different $shiftZ$. In total, the X axis consists of 81 (9 $shiftY\times$ 9 $shiftZ$) values. Figure 2 shows an example of the 1D histogram for the ring reconstruction efficiency. The 2D histogram shows integrated values of the tested parameter for geometries with a fixed PMT rotation angle in dependence on $shiftY$ and $shiftZ$. Figure 3 shows the comparison of the ring reconstruction efficiency

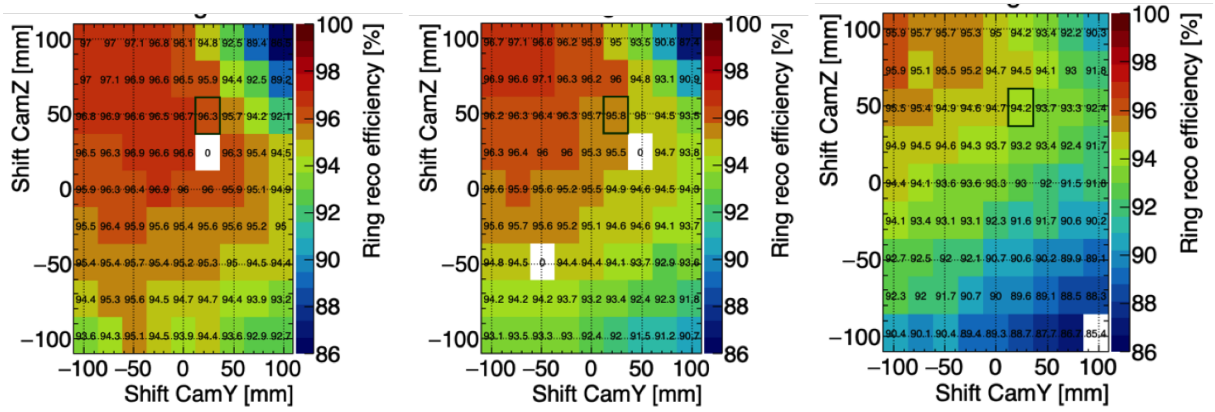

Figure 3: Ring reconstruction efficiencies for $m10$ (left), $m12$ (middle) and $m15$ (right) geometries. PMT plane rotation angle equals to 15°. UrQMD Au-Au central collisions at 8 AGeV.

for $m10$, $m12$ and $m15$ geometries as 2D histograms. The PMT plane rotation angle equals to 15°.

After detailed analysis and comparison of the obtained results and taking into account the RICH performance, magnetic field and technical issues, one reference geometry for each mirror rotation was selected which shows the best performance comparing to all tested ones. It turned out that the parameters for the reference geometries are the same for all mirror rotations. The parameters are the following: PMT plane rotation – 15°, $shiftY$ – +25 mm, $shiftZ$ – +50 mm. In Figure 2, the value for the reference geometry is shown with the horizontal line. In Figure 3 the reference geometries are marked with the black boxes. As an example of obtained results, the electron identification efficiency and pion suppression for the $m12$ reference geometry is shown in Figure 4.

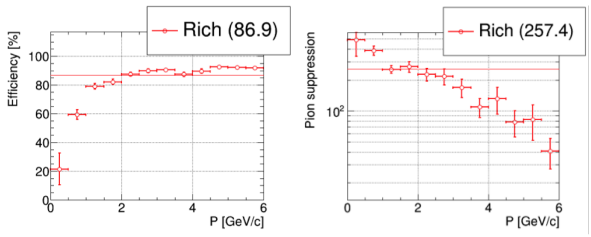

Figure 4: Electron identification efficiency and pion suppression for the $m12$ reference geometry. UrQMD Au-Au central collisions at 8 AGeV.

The comparison summary of the reference geometries for 3 mirror rotation angles is presented in Table 1. The results of $m10$ and $m12$ geometries look very similar. The difference in the reconstruction performance is 0.2-0.7%. For the $m15$ geometry the difference in the results is more pronounced, i.e. 2-3%. The RICH geometry with 12° mirror rotation angle is thus a good compromise between performance, magnetic field and technical issues and is thus the current proposal.

Table 1: The comparison summary of the reference geometries for 3 mirror rotation angles. Integrated numbers for reconstruction are presented for the momentum range 0 – 6 GeV/c.

$m10$	$m12$	$m15$
Geometry acc. with box generator [%]		
91.0	90.7	90.1
Geometry acc. Pluto ω at 3.5 GeV [%]		
49.2	48.6	47.2
Geometry acc. Pluto ω at 8 GeV [%]		
55.3	54.4	54.0
B/A		
0.94	0.93	0.92
dR.RMS [cm]		
0.294	0.317	0.363
Radius Mean/RMS [cm]		
4.92/0.286	4.97/0.322	5.07/0.384
Number of hits per electron ring		
29.26	29.48	29.9
UrQMD Au-Au central at 8 AGeV		
Ring reconstruction efficiency [%]		
96.2	95.7	94.4
STS-RICH matching efficiency [%]		
90.6	90.2	88.0
Electron identification efficiency in RICH [%]		
87.6	86.9	84.6
Pion suppression in RICH		
288	257	272

References

[1] I. Kres et al, "RICH geometry optimization', CBM Progress Report 2016 (2017) 64

QA tests (Radius of curvature and D_0) of 12 mirror prototypes

J. Bendarouach[*1] *and C. Höhne*[1,2]

[1]II. physikalisches Institut, Justus-Liebig-University, Gießen, Germany; [2]GSI, Darmstadt, Germany

CBM RICH mirrors are characterized by their reflectivity, their surface homogeneity (global and local) and their radius of curvature. To measure global homogeneity and the radius, an experimental setup had been designed, which aims at the measurement of the so-called D_0 value [1]. The setup is illustrated in Figure 1. A point-like laser source (b) is placed next to the nominal center of curvature of the mirror to be inspected. Its light is reflected by the mirror placed in a dedicated holder (a) into a CCD camera (c) placed next to the laser source. The laser-camera system is mounted on a stepper motor to determine precisely the distance laser/camera to mirror.

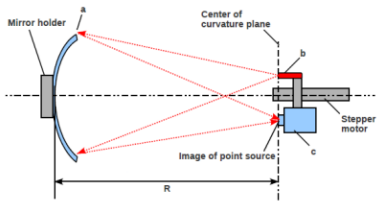

Figure 1: Experimental setup to determine the radius of curvature of the mirrors and the minimal D_0 value. Figure taken from [1].

For a given image, the D_0 measurement is defined as the diameter of the circle, which contains 95% of the total light intensity in the image. This technique was used to characterize the twelve newly produced prototype mirrors from JLO Olomouc.

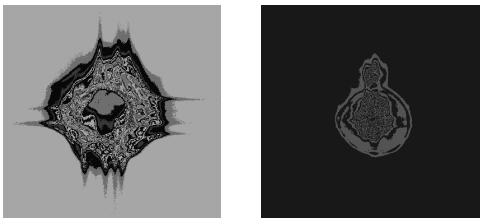

(a) (b)

Figure 2: Light spots viewed on the CCD camera. The mirror used here is labeled 'D019'. Left: Distance laser/camera to mirror of 3 m. Right: Distance of 3.007 m. Here D_0 is minimal.

The principle is the following. For a given mirror several D_0 values are measured with a varying laser/camera-mirror distance. The position for which the minimal D_0 is found corresponds to the mirror radius of curvature.

*jordan.bendarouach@exp2.physik.uni-giessen.de

Figure 2 illustrates two pictures taken for the mirror labeled 'D 019'. Figure 2a was taken at a distance of 3 m, corresponding to the nominal mirror radius of curvature. For this mirror, Figure 2b exhibited a minimal D_0 . Here the distance laser/camera-mirror amounts to 3.007 m. The camera used to obtain these results is an 'iKon-M 934' from ANDOR Technology. The laser source had a wavelength of 650 nm.

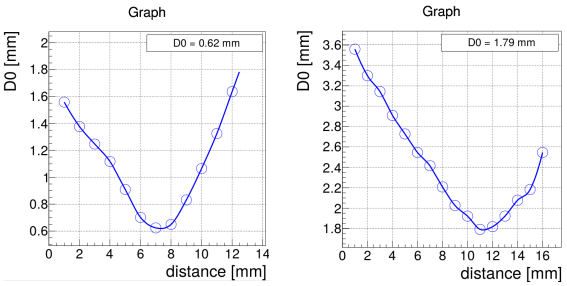

Figure 3: Evolution of D_0 with respect to the distance laser/camera-mirror for the mirror labeled 'D019' (left) and 'D014' (right). The x-axis starts at the nominal mirror radius of curvature of 3 m. The given D_0 values correspond to the minimal found at 7 and 11 mm.

Figure 3 shows the complete evolution of D_0 for the mirrors labeled 'D019' and 'D014'. One clearly sees a minimum reached for a distance of about 3.007 and 3.011 m, respectively. D_0 values depend on the threshold set on the figures and typically range between 0.5 and 2 mm.

This measurement was carried out on all mirrors delivered and the results are shown in Table 1. Overall the radii of curvature are slightly larger than the required 3 m. They fluctuate between +0.23% and +1.03% of the required value.

Mirror	Radius	Mirror	Radius	Mirror	Radius
D014_T4	3.022	D019_T2	3.007	D024_T3	3.021
D016_T1	3.031	D020_T1	3.013	D025_T1	3.015
D017_T2	3.024	D022_T3	3.016	D026_T2	3.014
D018_T1	3.022	D023_T1	3.011	D032_T1	3.023

Table 1: List of mirrors received from JLO Olomouc and their measured radius. For more details on the different mirror types, refer to [2].

References

[1] E. Lebedeva et al., CBM Progress Report 2011, p.37

[2] C. Höhne et al., ed. Technical Design Report for the CBM Ring Imaging Cherenkov Detector 2013, 215 p.

Development of a Ronchi test setup for the RICH mirrors*

C. Feier-Riesen[1], *S. Lebedev*[2], *and C. Höhne*[1,2]
[1]Justus-Liebig-Universität Gießen, Germany; [2]GSI, Darmstadt, Germany

A setup for Ronchi tests had been developed to determine the geometrical shape of the CBM RICH mirrors. The Ronchi test gives the local deviation of the curvature of a spherical mirror surface from an ideal sphere. The principle is quite simple: Light, that is emitted from a point source, is reflected by the mirror and passing a grid (a.k.a. Ronchi ruling), before it is detected by a camera. The setup is arranged such that the point source is placed approximately in the center of curvature of the mirror, while the grid and the camera are located slightly behind or in front of the center of curvature (see Fig. 1). If the mirror surface is perfectly spherical, the grid lines, that are projected onto the sensor, will appear as straight as the lines of the grid. If it deviates from an ideal sphere, the lines will be somewhat distorted (see Fig. 2). Depending on whether the grid is placed behind or in front of the center of curvature and depending on whether the surface is deeper or shallower than an ideal sphere, the grid lines can be bowed outwards or inwards. Due to the fact that the test is sensitive only for changes of the radius perpendicular to the grid lines, two images with different orientations of the grid (rotated by 90°) have to be acquired.

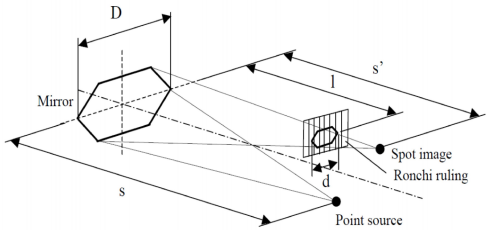

Figure 1: Setup principle of the Ronchi test [1].

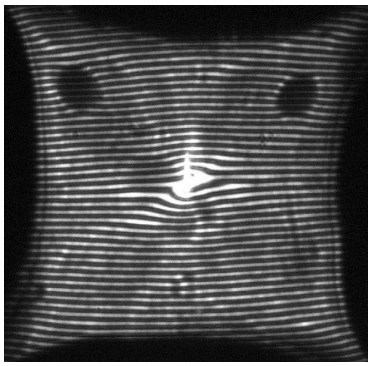

Figure 2: Image of projected grid lines from a CBM RICH prototype mirror.

Qualitative statements on the accuracy of the sphere can be made just by observing the course of the projected lines. A calculation procedure had been developed to enable quantitative determination of the deviation, based on the distortion of the lines.
In Fig. 3 an analysis of a CBM-RICH test mirror is seen. Pursuant to this evaluation the curve of the tested surface is slightly deeper than that of an ideal sphere, up to 3 mm at the centers of the edges. As seen in Fig. 2, the bands of the grid are bowed slightly outwards. According to literature, if the ruling is placed outside the center of curvature (as it is in this setup), outwards bowed lines indicate that the surface curvature is shallower than a sphere [2]. So further investigation have to be made to see if an error exists in the calculations or distance measurements or elsewhere. [3]

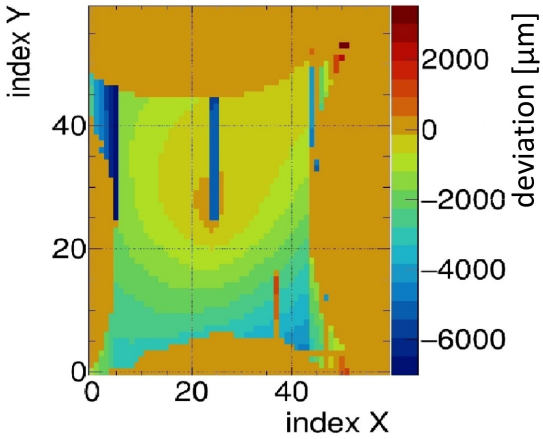

Figure 3: Quantitative evalutaion of deviations of the test mirror from an ideal sphere.

References

[1] Dissertation of Martin Laub: *Development of opto-mechanical tools and procedures for the new generation of RICH-detectors at CERN*; 2001

[2] PDF file of John Nichol: *The Ronchi Test*; downloaded at `https://nicholoptical.files.wordpress.com/2016/11/the-ronchi-test.pdf`

[3] Master's thesis of Cornelius Feier-Riesen: *Measurement of the local surface homogeneity of CBM RICH mirrors using the Ronchi method*; 2019

* work supported by BMBF 05P19RGFCA

Time over Threshold (ToT) cuts for optimising the signal information of MAPMT signals*

V. Patel[1], *C. Pauly*[1], *J. Förtsch*[1], *and K.-H. Kampert*[1]
[1]Department of Physics, University of Wuppertal

Protoypes of the CBM RICH front-end electronics were tested at the COSY test beam in autumn 2017 as final qualification before the start of mass production of components for the HADES RICH detector upgrade. Data taken with a proximity focusing test setup were analysed with respect to: Implementation of Time over Threshold (ToT) cuts, photon detection efficiency, timing precision, ring reconstruction, development of suitable calibration techniques, and verification of previous results obtained with the HADES RICH test box setup. In this article we focus on ring reconstruction parameters and timing precision / calibration, other topics have already been presented in previous reports [1, 2]

Ring Parameters

After initial tests of the reconstruction and calibration procedures the ring fitting algorithm was added to the analysis code, which is based on the Go4 framework. The implemented algorithm initially takes into account all hits within one event. Triggering of events was based on a coincidence requirement of hits in both layers of a scintillating fibre hodoscope located in front of the setup (see [1] for details of the setup). For each hit, the leading- and trailing edge times relative to the event trigger are stored. A geometry file linking the individual readout channel number to the X-Y position on the detection plane is implemented in the analysis. Usually one Cherenkov ring is detected per event (for each proton of the incident beam), with Cherenkov photons covering the 6 center MAPMTs of the detector plane. Quality of the ring reconstruction can be judged by the following observables or the width of their corresponding distributions:

- **ring center position:** The dimensions of the 3×4 MAPMT detection plane are approx. 15×25 cm^2 including a 5 cm gap in the center for the beam passing through. The reconstructed Cherenkov ring is expected in the center of this plane, at x=7.5 cm and y=12.5 cm.
- **ring radius:** The radius of the ring is about 6 cm according to a full Monte Carlo simulation of the setup.
- **dR of the ring:** Reconstructed Cherenkov photons will be scattered around the ideal, circular ring shape. The RMS value of the distribution of all individual distances of hits towards their corresponding ring is termed dR. A narrow distribution of all individual distances, and thus a small dR value, points to a sharp ring image, and thus improves the ring finding efficiency of the ring finder. Extra hits in the form of noise can spoil this dR value, as shown in Figure 1 and numbers given in Table 1

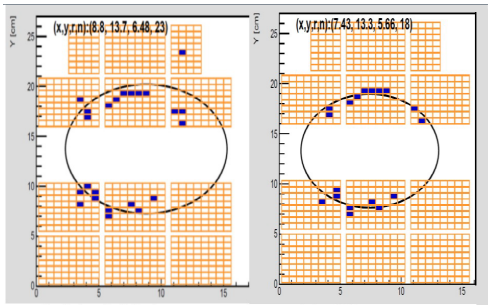

Figure 1: Go4 single event display showing the result of the ring finder / fitter, without (left) and with (right) additional ToT-cut for a signal threshold of 30 mV.

Parameters	X cm	Y cm	R cm	dR sigma	Nr. hits
no ToT cut	8.8	13.7	6.48	1.02	23
with ToT cut	7.43	13.3	5.66	0.81	18

Table 1: Effect of ToT cuts on ring parameters for a threshold of 30 mV. All geometrical parameters are in cm.

Timing precision

The main focus in the development of the DiRICH readout chain was on achieving precise leading- and trailing edge signal timing. On the DiRICH front-end board, the timing is measured by an onboard FPGA [5]. A main motivation for the test beam was to evaluate the performance of the DiRICH readout chain under realistic beam conditions. Initial tests of the analogue amplification- and signal shaping part of the readout chain in a test setup at GSI already showed promising results. A timing precision of 400 ps was measured using an oscilloscope replacing the FPGA TDC, which was not yet available at the time of these initial tests. The full TDC firmware became available only just in time for the COSY beam test.

Time offset calibration and timing precision were obtained applying the following iterative calibration procedure:

* Work supported by GSI and BMBF contracts No. 05P15PXFCA, 05P19PXFCA

1. For each channel, an individual Time-over-Threshold (ToT) cut is applied on all hits to suppress noise and cross-talk between pixels.

2. For each event, the ring finder finds the ring with all its corresponding hits. The average leading-edge time of all hits belonging to the ring is calculated.

3. This average ring time is subtracted from the individual hits in the ring, and the resulting offsets are histogrammed for each individual channel over the full data set.
   The width of these offset distributions is a measure of the channel-individual timing precision.

4. After analysing the full data set, the individual mean channel offsets are derived and stored in a data file.
   These (accumulated) values are used as channel offsets in the next iteration, thus improving the precision of the calculated mean time for each ring.

5. Step 4 is repeated for five iterations until no further improvement in sigma is observed.

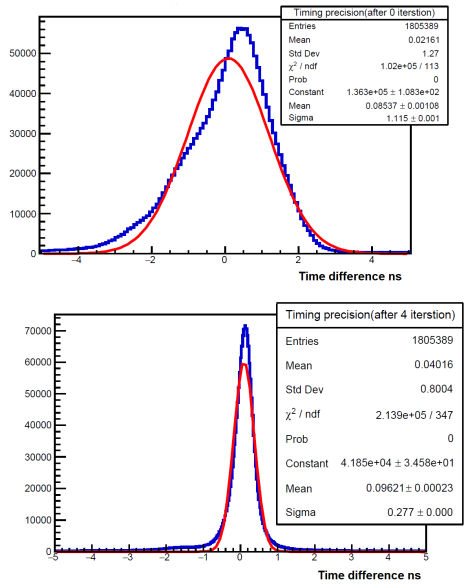

Figure 2: Top: Histograms showing the mean offset value distribution for all channels before first iteration (top) and after 4 iterations (bottom) for a signal discrimination threshold of 30 mV. The histogram (blue) represents the data together with a Gaussian fit (red).

Figure 2 visualises the improvement in timing precision, showing the variation of leading edge timing of individual hits with respect to the average time of hits in a given ring. Without offset calibration, the timing precision is limited by the channel-to-channel time offset variation. After properly calibrating these offsets, a timing precision of 277 ps (sigma) is achieved for the given discrimination threshold of 30 mV, corresponding to 650 ps FWHM (assuming Gaussian shape). The achievable timing precision is ultimatively limited by the Transit-Time-Spread of the MAPMT, which is in the order of 300 ps (FWHM) according to the manufacturer.

The resulting timing precision was studied as function of discrimination threshold as shown in Table 2. Optimum timing precision is achieved for thresholds $\leq$ 70 mV.

Threshold	sigma (ps)
30	277
40	265
50	299
60	293
70	272
90	273
100	297
120	311
150	330

Table 2: Timing precision as function of discrimination threshold.

Summary

The COSY beam test was crucial in understanding many aspects of the newly developed DiRICH readout chain, and paved the way for mass production of the electronic compones. The importance of Time-over-Threhsold cuts in order to clean the data and suppress capacitive cross talk could be demonstrated when using low discrimination thresholds. However, ToT cuts are useful only at low thresholds, at higher thresholds ToT cuts start affecting the efficiency of the detector (see [3]). With respect to timing precision, individual channel offset corrections turned out to be vital in achieving optimum timing precision. A corresponding calibration procedure was developed, and could be tested using the COSY data.
After calibration, a full system photon timing precision of 270 ps (sigma) or 630 ps (FWHM) could be demonstrated in the COSY data,which is already close (by a factor 2) to the inherent sensor timing precision. It is also similar to the result obtained in [4], giving a single channel timing precision of σ=260 ps using a different approach. This is already well sufficient for operation of the DIRICH readout chain under high rate conditions as expected in CBM.

References

[1] C. Pauly, "COSY testbeam for DiRICH qualification", GSI Scientific Report 2017, page 60.

[2] V. Patel , "First results from testbeam analysis", GSI Scientific Report 2017, page 64.

[3] V.Patel and M.Traxler, "The HADES-RICH upgrade using Hamamatsu H12700 MAPMTs with DiRICH FEE + Readout", JINST vol 13 (2018), p. 3038.

[4] A. Weber, COSY beamtime Data Calibration, Time Precision and WLS analysis, CBM Progress Report 2017, page 61.

FPGA based jitter measurements of different signal distribution methods with FPGA-TDCs

F. Zorn[1], *A. Weber*[1], *J. Michel*[2], *and C. Höhne*[1]
[1]Justus-Liebig Universität, Giessen, Germany; [2]Goethe-Universität, Frankfurt, Germany

Introduction

The CBM experiment is supposed to run at very high data rates in the future. Those require a good understanding of the hardware to ensure that a clear signal can be achieved. Therefore, it is very important to have a proper understanding of the DAQ hardware to guarantee minimal timing delays and clear signals.
In this Bachelor Thesis we investigated various transmission methods with respect to timing delays and jitter. This was mostly done with available HADES hardware. In addition the influence of high frequencies on RJ45 as well as KEL cables was measured.

Set-up

The measuring set-up uses two TRB3sc boards connected through a custom made board with KEL and RJ45 cables, as shown in Fig. 1. The master board is controlling the generated output signal, while the slave board is functioning as TDC.
The precision of the signals is expressed through a jitter which is here defined as the measured standard deviation which actually combines time precision and additional jitter.

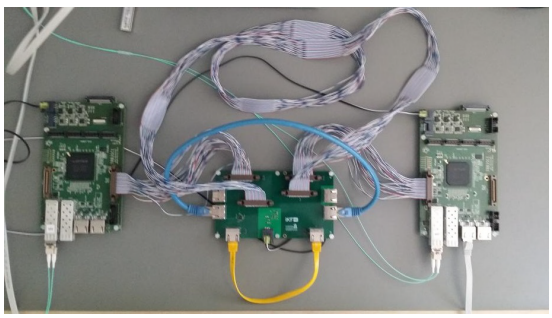

Figure 1: Measuring set-up showing connected master(left), custom(middle) and slave(right) board.

Three different aspects were investigated:

- **Influence of different cables**
  With a frequency of 50 kHz different KEL/RJ45 cable lengths and types and the resulting signal delay and precision was measured. Cable length ranging from 0.25 m to 50 m as well as insulated and uninsulated cables were tested.
- **Influence of high frequencies**
  To investigate the susceptibility of cables to crosstalk an additional 125 MHz clock was set to run on one channel at a time. Every other channel was run on 50 kHz. This was done for multiple channels taking the custom board signal distribution into account.
- **Influence of signal delays**
  For this the measurement channels on the KEL connector have all been set up to have a delay of 10 ns to the neighbouring channel.

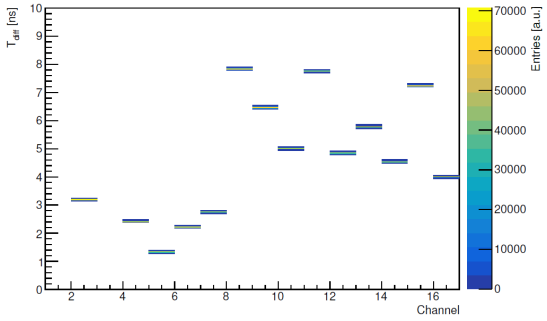

Figure 2: Example measurement without any additional influences showing the standard deviation as time difference to a reference channel 3 of all remaining channels.

Results

Results for the first measurement show that the jitter increases with RJ45 cable length, excluding the jitter caused by the inherent delay due to longer cables. The effect is further increased with cables rolled up compared to cables rolled out.
In addition, providing one channel with a high frequency showed a significant increase of the jitter on neighbouring channels, with the effect being less significant for RJ45 cables and more dominant in KEL cables.
At last, it was shown, that an increased artificial delay of the signal generates a jitter on the delayed channel, which is connected to the first finding working with different cable lengths.

References

[1] F. Zorn, “FPGA based jitter measurement of different signal distribution methods with FPGA-TDCs”, September 2019, JLU Giessen

mRICH status and first data analysis*

A. Weber[1], *T. Gessler*[1], *S. Lebedev*[1], *E. Ovcharenko*[1], *and C. Höhne*[1]
[1]Justus-Liebig Universität, Gießen, Germany

The mRICH detector setup

The CBM RICH team developed a small size prototype RICH detector based on the final readout electronics of the CBM RICH detector and is participating in the mCBM experiment. The mRICH detector is build from 2×3 DiRICH backplanes, corresponding to 36 Hamamatsu H12700 MAPMTs and 72 DiRICH boards. Two $20 \times 20 \times 3$ cm^3 aerogel blocks in front of the MAPMTs are used as the radiator material. The mRICH is mounted behind the mTOF detector and uses newly developed DCDC-converter boards for the low voltage power supply.
The readout of the mRICH setup is based on TrbNet and uses the standard DiRICH Firmware. The combiner boards run an online calibration for the TDC finetimes. The data from the combiner boards is combined by a hub on a trb3sc that sends the combined data over UDP to the mRICH AFCK. The trb3sc hosts in addition the central trigger system (CTS) that is used to generate a trigger message for each microtimeslice. Based on the trigger message all data in the front end buffers from the last trigger on is sent out.

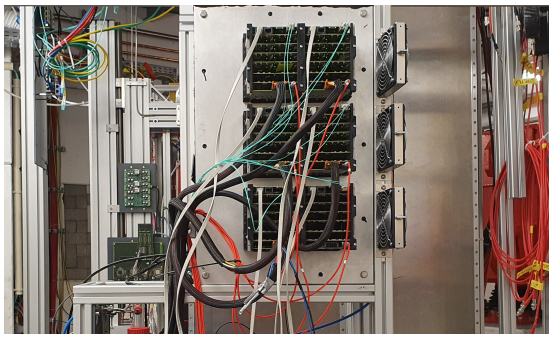

Figure 1: The mRICH detector in the mCBM Cave. The picture shows the readout electronics with the fiber connections, high voltage, low voltage cabling and the trigger distribution.

mRICH results

The mRICH detector was used in several beamtimes of mCBM and showed a reliable behaviour. The following results are based on the beamtime in December 2019 (run 384).
On the free streaming data from the mCBM detectors an event building with the trigger conditions of a fixed 200 ns time window, 1 Digi in T0, 10 Digis in mTOF and 10 Digis in mRICH is applied. The crosstalk in mRICH is reduced by the application of a Time-Over-Threshold (ToT) cut, after a ToT-calibration was generated and applied during unpacking. The ToT of mRICH hits is allowed to be between 23.7 ns and 30 ns.

As the mCBM detectors have to be synchronized in time, it is important to correct for any existing offsets in the timing between the detectors. The mRICH detector is corrected for an offset of -280 ns. No jumps or changes in this correction are found during data taking. Figure 2 shows the corrected timing between the mRICH and the T0 detector, that is by definition the reference detector for all subdetectors of mCBM.

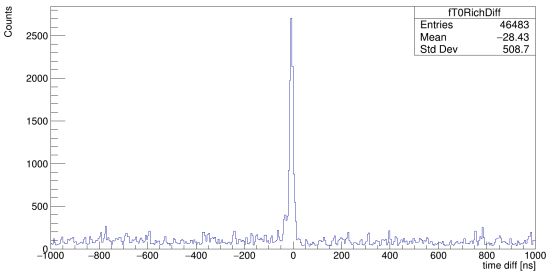

Figure 2: Timing distribution of the digis between T0 and mRICH after application of a time correction.

Figure 3 shows the data stream of three mCBM detectors which reproduces nicely the spill structure of the SIS18 Ar beam @ 1.7 AGeV. In addition, the number of reconstructed RICH rings is drawn. The number of RICH rings matches perfectly the spills structure and even the differences in the amount of rings matches the differences in the spill intensity.

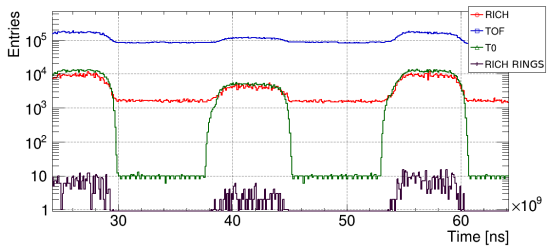

Figure 3: mCBM detector digis and reconstructed mRICH rings over time.

* Work supported by BMBF 05P19RGFCA.

As the mRICH was not fully operational in 2019, something that changed in March 2020, the acceptance is limited to 44 DiRICHes distributed as shown in Fig. 4. The hits are distributed as expected from simulations. The right figure shows the distribution of reconstructed ring centers. The middle of the detector is free of rings due to the separation between the two aerogel blocks. As the positions in the figure are in global coordinates, this already shows a nice alignment in the Y-direction of the detector.
The ring centers also seem to form a three row structure. It tends to be in-between two MAPMTs.

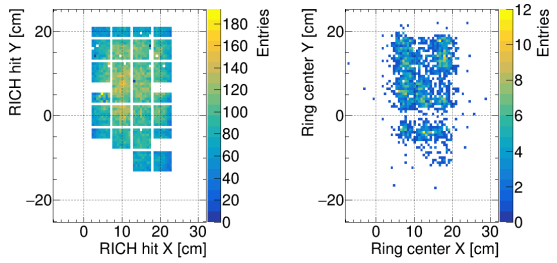

Figure 4: Distribution of mRICH hits (left) and mRICH ring centers (right) after event building and ToT-Cut.

Before ring finding and further analysis the digis have to been cleaned up, resulting also in a more homogenous distribution of hits. This is done mainly by the reduction of crosstalk due to the applied ToT-cut. Figure 5 shows the ToT distribution of digis (left) as well as of hits (right). The small peaks in the digi distribution are produced by a DiRICH with slightly too low gain, resulting from a too low voltage on the 1.1 V line. The ToT distribution of the mRICH detector shows a double peak structure. The left peak is resulting from crosstalk in the MAPMTs. The right peak, which is clearly larger, is mostly related to real hits. As each DiRICH channel has a slightly varying ToT distribution due to the routing of the FPGA firmware, the complete ToT distribution of each channel of the mRICH is shifted such that the main peak is located at 25 ns by the application of a ToT-calibration. As this distribution is hardware related, the differences between the same channels of different DiRICHs are relatively small and the distribution is not changing over time.

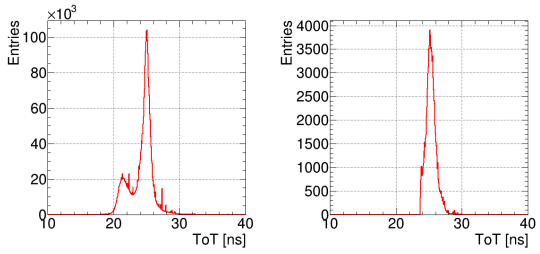

Figure 5: Time-over-Threshold distribution of RICH digis (left) and hits (right). The hits are created after event building and ToT-Cut application.

The RICH ring finder from the standard CBM RICH detector is currently used to find the rings from hits in the reconstructed CbmEvents. The ring radius distribution is shown in the left distribution of Fig. 6. Most of the reconstructed rings have a ring radius of about 3.5 cm. This value matches the expectations from simulations for electrons quite well. The right plot of Fig. 6 shows the number of hits per reconstructed ring. Most of the rings have around 13 hits. This distribution deviates from the simulations slightly as it is sharper than expected. Simulations show rings with higher number of hits. This needs further investigation.

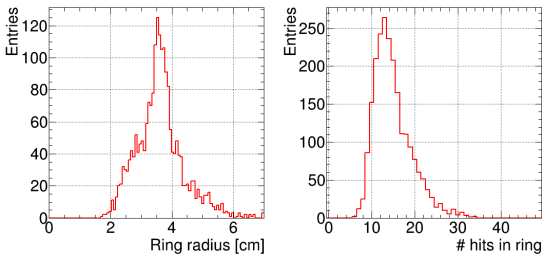

Figure 6: Left: ring radius distribution of reconstructed rings. Right: Number of hits in ring.

The mRICH detector finds very clean events with nice rings as found in the hit distributions shown in Fig. 7. In contrast to the CBM experiment, the mRICH detector is positioned in the particle stream. This leads to particles travelling through the MAPMTs and producing hits in the MAPMT matrix. For mRICH, this gives a unique footprint of the particle creating the Cherenkov ring in the center of the ring. On the one hand, this is a nice additional information for the correctness of a ring fit, as the ring center is matching this inner hits, on the other hand this makes it more difficult to separate double rings or even to fit small rings of just a few centimetres.

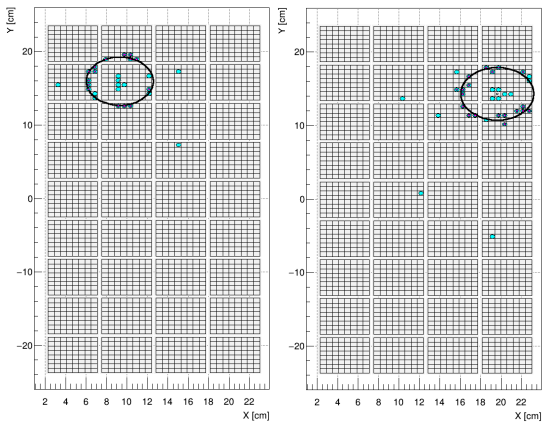

Figure 7: Two single event displays of the mRICH detector. The cyan coloured points show the hits in the detector. The hits with purple points inside are hits matched to the ring.

For a more robust ring finding in mCBM, the ring finder has to be retrained for such signatures hopefully improving the ring finding in the future. Nevertheless, the ring finder already gives nice results. Comparing the leading edge times of the hits in a ring to the start time of the reconstructed CbmEvent, the hits of a ring appear in the beginning of an event and show nicely the correct temporal alignment in the detector. Unfortunately, there is a probability that the start of a CbmEvent could also be triggered by background hits and therefore the time position of the rings could also be at different positions in the time distribution. Applying a leading edge cut on the data is possible but may not be efficient due to the loss of real rings.
The found rings in Fig. 8 are separated in different categories. Approximately half of the rings have no track near the found ring. Half of the rings have a track nearby but at least 5 cm away from the ring center and only a few rings have a track next to the RICH ring. This behaviour is also visible in Fig. 9. The track-ring distance peaks around 8 cm which corresponds to the green line in Fig. 8.

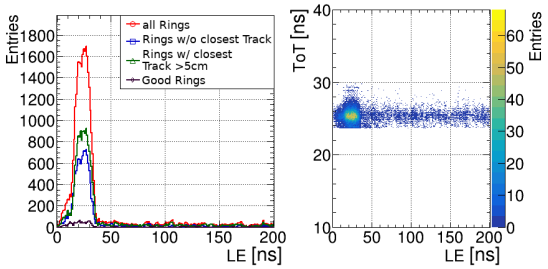

Figure 8: Left: leading edge distribution of hits in a found ring relative to the start time of an event. Right: Leading edge relative to start of an event against ToT for all hits in a ring.

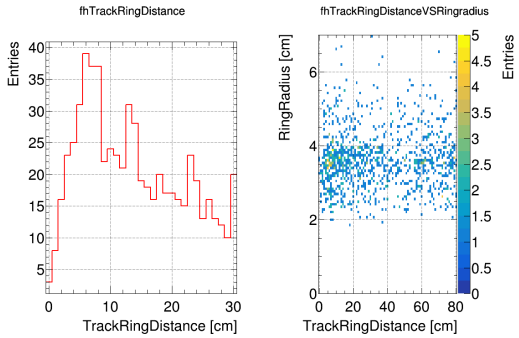

Figure 9: Left: Track-ring distance of RICH rings. Right: Ring radius vs. track-ring distance of the reconstructed track.

The hits located in the center of a ring are coincident in time with the hits of the ring of the same CbmEvent. This confirms that the hits in the middle are no random background noise. The number of hits in the center of a ring peaks around 4 hits and has a long tail to higher values.

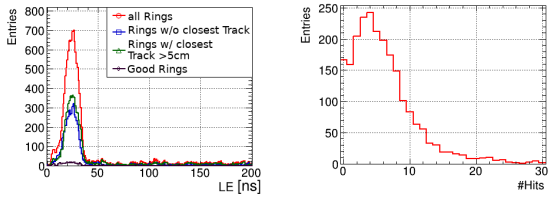

Figure 10: Left: leading edge distribution of hits in a found ring relative to the start time of an event. Right: Number of hits inside a ring.

To see a spatial correlation of the mRICH and the mTOF, hits from both detectors were taken separately for X and Y. Figure 11 shows the correlation between both detectors in X and Y. In X-direction the mTOF triple and the mTof double stacks are visible. The triple stack is located between approx. 0 to 30 cm in global coordinates. The mRICH is positioned in the center of the triple stack. As the double stack does not show any correlation, it proofs that the structure observed is really a correlation between the two detectors. In Y-direction the distribution is thinner in width and the overlapping of some modules is becoming visible.

The correlation is even visible when the reconstructed ring centers of RICH rings are plotted against the hits or even against reconstructed tracks.

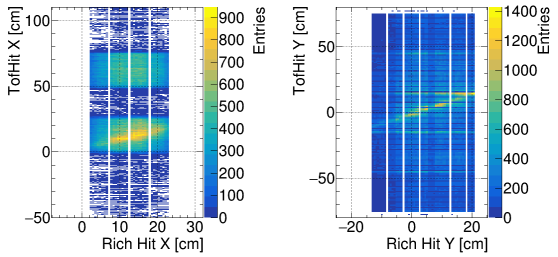

Figure 11: Spatial correlation between the mTOF and the mRICH in X- (left) and Y-direction (right).

The clear spatial correlation between the mTOF and mRICH as well as the time correlation shows the functionality of the full mRICH detector as well of the DAQ system developed for mRICH and thus for the full CBM RICH detector.

First evaluation of the upgraded HADES RICH during the HADES 2019 beamtime*

J. Förtsch[1], M. Becker[2], M. Dürr[2], M. Faul[4], J. Friese[2], C. Höhne[2,4], K.-H. Kampert[1], I. Kres[1], S. Lebedev[2], J.-H. Otto[2], J. Michel[3], V. Patel[1], C. Pauly[1], D. Pfeifer[1], E. Schwab[4], M. Traxler[4], and A. Weber[2]

[1]Bergische Universität Wuppertal; [2]Justus-Liebig Universität Giessen; [3]Goethe-Universität Frankfurt; [4]GSI Darmstadt

In the March 2019 HADES [1] beamtime, the upgraded HADES RICH was used for the first time to identify electrons and positrons in Ag+Ag collisions at 1.58 A GeV and at a triggered event rate of 16–18 kHz. A total of 15.3×10^9 events could be recorded, demonstrating the successful operation of the HADES detector setup over the full 4 week beamtime. The new photon detector of the HADES RICH is comprised of 428 Hamamatsu H12700 MAPMTs using the DiRICH read-out chain, both of which will also be used in the CBM RICH detector. The gaseous RICH detector operates with C_4H_{10} as radiator gas and uses a spherical mirror to form Cherenkov rings projected onto its two staggered photon detection planes. The inner photon detection plane at $z = -80.9$ mm (with respect to the target) with rectangular dimensions of ± 371 mm, is slightly closer to the mirror than the outer photon detection plane at $z = -208.9$ mm. Both planes together approximate the focal plane of the spherical mirror. A more detailed description of the HADES RICH upgrade can be found in [2].

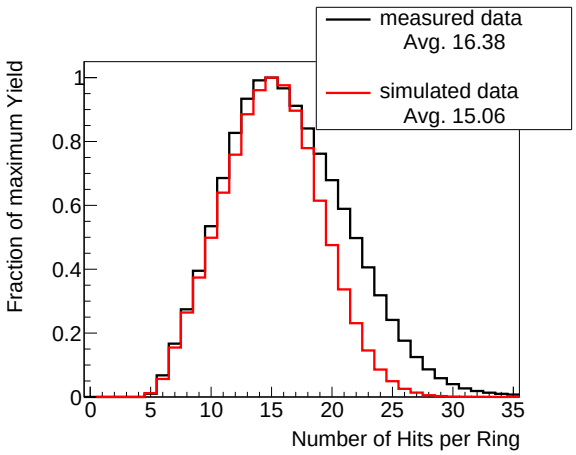

Figure 1: Number of hits per ring for measured and simulated data. Both distributions are scaled to the same maximum bin content. Here, hit stands for a registered photon after cuts.

One of the first parameters evaluated in the data analysis is the number of hits per ring. This distribution gives immediate feedback if the detector operates well above the average noise in the detector. In Figure 1, the number of hits per ring from measured data is compared to simulation. Here, the number of hits refers to registered photons after timing and time-over-threshold cuts. Given the average of 16 registered photons per ring, it is evident that most of the rings are easily reconstructible. This statement is further supported by the findings regarding the ring reconstruction efficiency presented in [3]. Moreover, the congruent distributions of measured and simulated data demonstrate a good understanding of the detector. Differences in the distributions tails towards higher number of detected photons per ring can be explained by misidentified nearby double rings. Those double rings which were reconstructed as one single ring with a higher number of hits associated were not accounted for in this simulation.

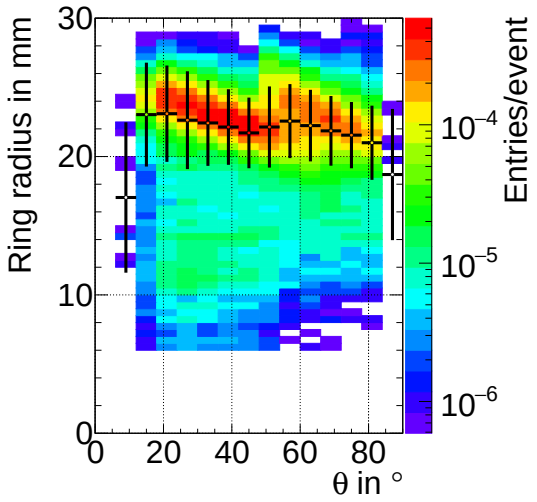

Figure 2: Reconstructed Cherenkov ring radius as a function of polar angle θ for rings associated to particles. The points indicate the average radius per bin in θ with the error bars representing the standard deviation.

The radius of the Cherenkov rings is another interesting feature one can assess. Two distinct aspects are expected to be seen in the ring radius distribution in dependence on the polar angle θ: Firstly, a jump in the mean ring radius at $\theta \approx 50°$, where the x,y-positions of the staggered RICH photon detection planes intersect. Secondly, a

* Work supported by GSI, BMBF contracts No. 05P19PXFCA and 05P19RGFCA, and the TRB working group

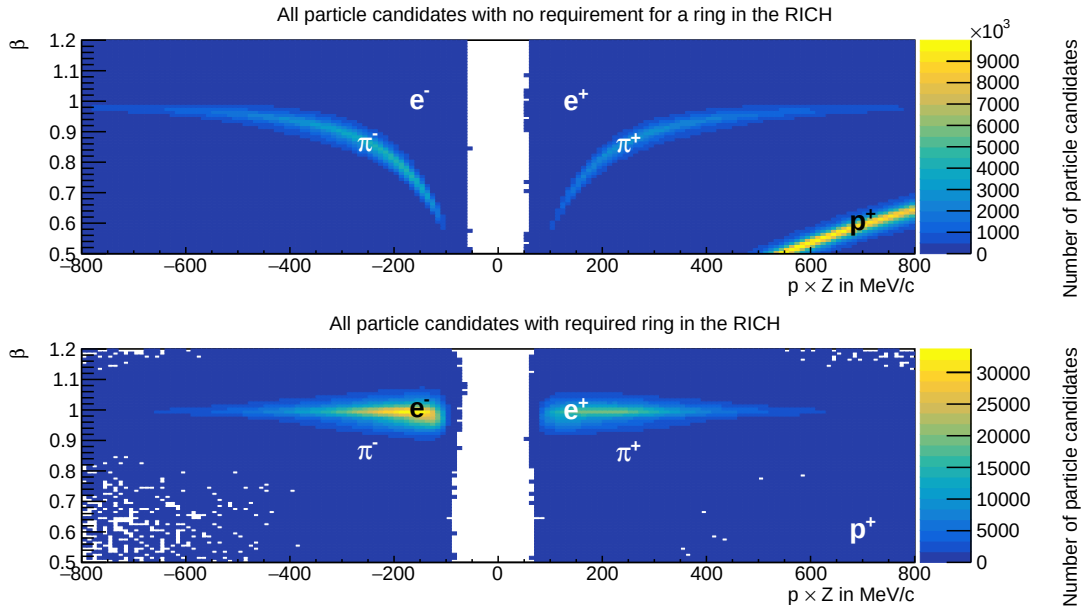

Figure 3: Velocity (β) versus momentum distribution times charge with (bottom) and without (top) requiring a Cherenkov ring in the RICH detector. Rings are fitted after applying strict cuts on the hit timing and time over threshold for each individual hit. In addition, rings are selected to have radii between 17 mm and 30 mm. Indicated in white and black letters are the different particle branches.

slow decrease in the ring radius with increasing θ due to the geometrical approximation of the real optical focal plane. Both of these features are visible in the measured ring radii distribution shown in Figure 2. From this plot one can extract the average ring radius to be 23 mm. Also this value is consistent with simulations. A more detailed discussion (together with an estimate on the timing precision) can be found in [4]. A radius cut from 17 mm to 30 mm thus allows to reduce background of falsely fitted rings, especially in the inner region of the detector ($\theta < 50°$).

The successful operation of the upgraded RICH detector is also seen in the reconstructed velocity-vs-momentum distribution. As the RICH detector is blind to all hadrons at the given collision energy, hadrons can be rejected by requiring matched RICH rings for reconstructed particles. This behaviour is clearly seen in Figure 3, where the proton- and $\pi^{\pm}$-branches are strongly suppressed so that only the electron- and positron-branches persist in the velocity-vs-momentum distribution.

In summary, the upgrade of the HADES RICH detector successfully enhanced the HADES detector capabilities. First performance data look very promising and confirm the path chosen for the CBM RICH design and construction.

References

[1] G. Agakishiev et al. [HADES Collaboration], "The High-Acceptance Dielectron Spectrometer HADES", Eur. Phys. J. A 41 (2009) pg. 243, doi:10.1140/epja/i2009-10807-5.

[2] C. Pauly et al., "The HADES RICH detector - getting ready for first beam", CBM progress report (2018) pg. 198, http://repository.gsi.de/record/220128.

[3] J. Förtsch et al., "Ring reconstruction efficiency for the upgraded HADES-RICH detector", CBM progress report (2020), this report.

[4] J. Förtsch et al., "Fast readout and performance of the upgraded HADES RICH in heavy ion collisions", JINST 15 (2020) C03021, https://doi.org/10.1088/1748-0221/15/03/C03021.

Ring reconstruction efficiency for the upgraded HADES-RICH detector*

J. Förtsch †[1], *C. Pauly*[1], *and K.-H. Kampert*[1]
[1]Bergische Universität Wuppertal, Germany

The upgraded HADES-RICH detector enables high quality di-electron measurements in HADES and serves, as a FAIR-Phase 0 experiment, as proof of concept for the CBM-RICH detector. Both detectors will use the same sensors to equip the photon detection area as well as the same read-out electronics. A precise understanding of the performance of the HADES-RICH detector is therefore a key issue in moving forward towards the RICH detector in CBM. The already well established HADES experiment [1] gives the opportunity to study the RICH performance in concert with the other well understood HADES sub-detectors. These include the MDC-tracking stations, resolving the precise track position and momentum of the particles, as well as the TOF/RPC-setup, measuring β for electron selection. Both of these detectors have been in operation for more than a decade.

The ratio of reconstructed electrons in the RICH detector over the number of electron candidates reconstructed by the other sub-detectors is hereby the simplest estimate for the RICH efficiency. A main limitation in this approach of determining the RICH detection efficiency is the fact that not all electrons seen by the sub-detectors behind the RICH must leave a reconstructible trace in the RICH detector. Electrons being generated in the RICH gas, mirror, or even behind the RICH, would artificially reduce the derived efficiency and must therefore be rejected. To deal with this situation, we shall first concentrate on the ring reconstruction efficiency. For its determination, we require a "certain amount of photons" in the vicinity of an electron candidate reconstructed by other sub-detectors. Those electron candidates which were not reconstructed in the RICH detector but did produce enough photons to be reconstructed in principle then count negatively into the RICH ring reconstruction efficiency. We define "vicinity of a track" as the maximum ring radius (30 mm) plus an additional absolute angular difference of $4°$. A "certain amount of photons" can be understood as a threshold, above which the reconstruction of a Cherenkov-ring should have been possible. Recapitulating the method, one counts the number of electron candidates reconstructed by other HADES sub-detectors for which the RICH detected a number of photons above a certain threshold within the vicinity of the track, but a Cherenkov-ring was nevertheless not reconstructed. The efficiency derived this way needs to be corrected for uncorrelated background, which can be derived by counting the number of detected photons in a detector region (geometrically) uncorrelated to the track candidate. The uncorrelated background is retrieved by the so called RICH rotating technique: Here, for each unidentified electron candidate seen by other sub-detectors, the RICH is virtually rotated by $60°$ (one sector, see Fig. 2) to assess the number of hits in the vicinity of the now incorrectly placed electron candidate. This approach works as the amount of uncorrelated background in the RICH should only depend on the polar but not on the azimuth angle. The resulting background subtracted distribution for the number of photons in the vicinity of electron candidates is shown in Figure 1. Here, also the number of photons per

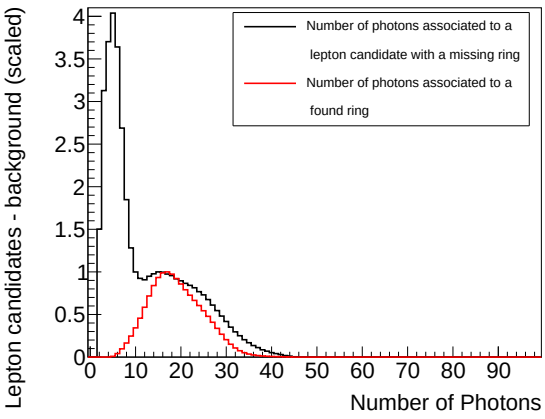

Figure 1: Distribution of number of photons per unidentified Cherenkov ring in the RICH (black) and per identified Cherenkov ring (red). Photons associated to unidentified Cherenkov rings are obtained by checking the vicinity of electron candidates identified by other HADES sub-detectors. The distribution of number of photons per unidentified Cherenkov ring is background subtracted, where the background is approximated via the RICH rotating technique. Both distributions are scaled to their maximum bin-value above 10 photons.

found Cherenkov ring produced by an electron is superimposed. Using both of those distributions one can then derive a final ring reconstruction efficiency. This is done by choosing a number of photons as threshold, counting all electron candidates with more photons near its vicinity (N_{Above}) for both, reconstructed ($N_{\text{Reco.}}$) and not reconstructed ($N_{\text{not Reco.}}$) Cherenkov rings. A factor of $\frac{N_{\text{Above, Reco.}}}{N_{\text{Reco.}}}$ is introduced so different photon thresholds have minimal

* Work supported by GSI and BMBF contract No. 05P19PXFCA
† j.foertsch@uni-wuppertal.de

impact on the resulting ring reconstruction efficiency. This factor gets lower the higher the threshold, as less and less photons reconstructed in real rings would lie above the photon threshold. This procedure results in the following formula to derive the ring reconstruction efficiency RRE

$$RRE = 1 - \frac{N_{\text{Above, not Reco.}} \left(\frac{N_{\text{Above, Reco.}}}{N_{\text{Reco.}}} \right)}{N_{\text{electron candidate}}}$$

$$= 0.992 \, \left({}^{+0.001}_{-0.003} \right)_{\text{syst}} .$$

Here, the systematic error is estimated by comparing the results for thresholds ranging from 10 to 25 photons in the vicinity of electron candidates. With this procedure to derive the systematic error, one includes both of the major contributing error sources: The first major contributor to the uncertainty of this result are close double rings, which can be found in the right tail of the number of photons in the vicinity of an unreconstructed electron candidate. This tail is not correctly approximated by the number of photons for reconstructed Cherenkov rings, as can be seen in Figure 1. This error contribution has increasing influence when choosing higher thresholds. The second major contributor are electron candidates being produced inside the RICH radiator, as those barely might emit enough photons to justify their contribution to the number of reconstructible electron candidates, especially for lower thresholds.

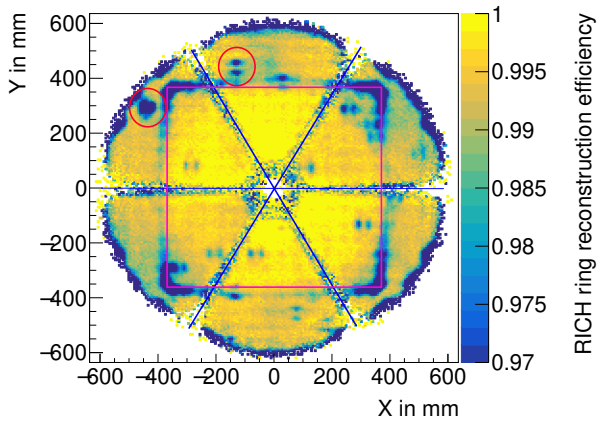

Figure 2: Spatially resolved ring reconstruction efficiency. The required number of photons for an identifiable Cherenkov ring for this plot is 10. Indicated with blue lines are the spokes of the HADES detector. Indicated with a pink rectangle is the transition between the staggered photon detection planes. Red encircled are two examples for failing read-out modules.

Using a threshold of 10 photons, the spatially resolved ring reconstruction efficiency is shown in Figure 2. It is obvious, that the ring reconstruction efficiency of the HADES-RICH is close to 100% in most of the detection area, featuring only very small spots with reconstruction efficiency $\leq 97\%$. Those small spots are for example the spoke regions (indicated with blue lines) of the HADES detector, where track-identification as well as ring reconstruction suffer due to shadowing, the outer rim of the RICH detector, where only partial rings can be reconstructed, and the transition between the staggered photon detection planes. This step between the photon detection planes follows a rectangular shape (indicated in pink) with its center at $(0, 0)$ and width $w = 371\,\text{mm}$. In addition to these areas with lower ring reconstruction efficiency caused by the geometry of the detector, one also finds several smaller areas with lower efficiency (examples are shown in red circles). Those areas are caused by broken electronic modules, where due to missing ring segments, the ring reconstruction efficiency is deteriorated.

References

[1] G. Agakishiev et al. [HADES Collaboration], "The High-Acceptance Dielectron Spectrometer HADES", Eur. Phys. J. A 41 (2009) pg. 243 doi:10.1140/epja/i2009-10807-5 [arXiv:0902.3478 [nucl-ex]].

Muon Detection System

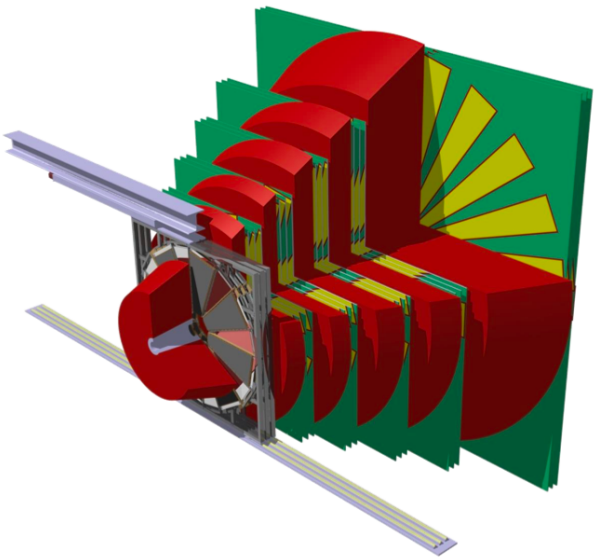

Muon Chambers (MuCh) for the CBM experiment at FAIR

S. Chattopadhyay
VECC, Kolkata, India

The Muon Chamber (MuCh) system of CBM is designed to study di-muons from various sources like vector meson decays and thermal radiation in pA and AA collisions at FAIR energies. The CBM-MuCh consists of five hadron absorber blocks of 60 cm, 20 cm, 20 cm, 30 cm and 1 m thickness, with tracking detector stations in between, placed downstream the target. The first absorber consists of graphite and concrete blocks pasted together and placed partially inside the dipole magnet. The other absorber blocks are made of iron. Placed downstream each of the first four hadron absorbers, racking station consisting of three detector layers are installed for tracking of muons and other charged particles. Behind the last 1 m thick absorber, the Transition Radiation Detector (TRD) serves as the last tracking station. The detector technology chosen for specific detector station depends mainly on the particle density at the respective locations. GEM detectors, that can handle high particle rates, is chosen for the 1^{st} and the 2^{nd} detector stations. Single-gap low-resistivity high-rate Resistive Plate Chambers (RPCs) are being investigated as candidates for the 3^{rd} and the 4^{th} station.
During last one year, extensive R&D has been performed on various fronts in building the CBM muon system. Teams from PNPI and VECC have been working on the MuCh mechanical design, including support structures, absorbers and detector mounting system along with services. While the PNPI team is responsible for building the super structure, its movement system and the absorbers, the Indian team is working on the design and fabrication of detector mounting systems and their movements. A report on the latest status of the job is included in this report (Fig. 1).

Another PNPI team is responsible for design and construction of the gas distribution systems of the CBM-MuCh. Two reports have been submitted to describe the design of the gas distribution and mixing systems for GEM and RPC, as they operate with two different gas mixtures.

The Indian team is responsible for the development of the tracking chambers. Two real-size GEM chambers suitable for the 1^{st} MuCh station have been installed in the mCBM experiment and took data under various conditions, e.g. for different voltages, target thicknesses, and beam intensities. Performance issues which have been discovered during the mCBM operation are being investigated by the VECC team. Several contributions have been submitted in this report to describe the results from mMuCh, including the investigations on the STS-XYTER ASIC, like calibration, performance studies, and read-out of a 10cm x 10cm GEM chamber. Apart from good time-correlation shown by the GEM hits with T0 and other detectors in the mCBM setup, hits from the GEM chambers are nicely correlated with the projected of TOF tracks on GEM coverage (Fig. 2).

R&D on RPC is being carried out using a 30 cm x 30 cm low resistivity bakelite RPC. The chamber is readout by a STS-XYTER based electronics that requires low-gain operation of the chamber. Several configurations of the pad-plane have been investigated, like the pad and strip read-out of different dimensions. One important aspect being looked into in detail is the cluster size and rate capability of the chamber.

Detailed investigations are under way concerning simulations, like the optimisation of materials in the 1^{st} absorber, the effect of surface thickness of the fifth absorber, and the segmentation and digitisation of RPC. Other software studies include the development of classes to relate electronic channels to detector co-ordinates, and to identify noisy cells. Several reports have been submitted on these topics.

There are unresolved issues that have come up during the mCBM operation of MuCh, like loss of links between GEM-FEBs and GBTX boards during high voltage and high intensity operations, lack of coverage of both the chambers due to less number of FEBs. Efforts are ongoing to resolve the issues and prepare mMuCh for data taking in the next campaign.

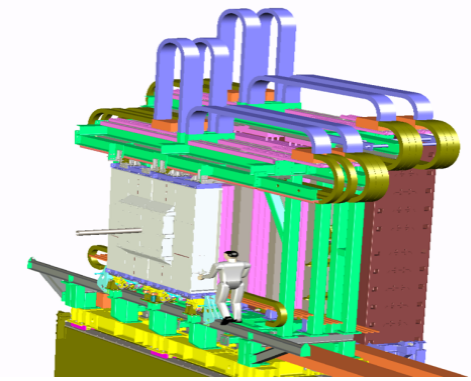

Figure 1: MUCH geometry design on superstructure

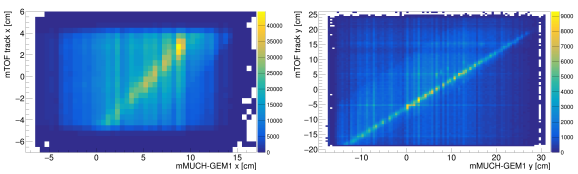

Figure 2: Spatial correlation between projected points from TOF tracks and MUCH hits in XX (top) and YY (bottom)

Response of mMUCH modules in the mCBM campaign 2019

A. Kumar[1,2], C. Ghosh[1], S. Chatterjee[3], G. Sikder[4], A. K. Dubey[1], J. Saini[1], V. Singhal[1], V. S. Negi[1], S. Chattopadhyay[2], and S. K. Prasad[3]

[1]VECC, Kolkata, INDIA; [2]HBNI, Mumbai, INDIA; [3]Bose Institute, Kolkata, INDIA; [4]University of Calcutta, Kolkata, INDIA

Two mMUCH GEM modules were tested in the mCBM campaign in March and November-December, 2019. The detector layout, it's FEB configuration and DAQ setup is the same as described in previous year's progress report [1]. A considerably higher acceptance acceptance could be achieved in March and then Nov./Dec. 2019, after resolving CROB-FMC connector and firmware issues. Additionally, a newer and improvised version of the STS-XYTER FEBs(v2.1) were used for Nov/Dec runs. Thus, in this report, we have discussed the results of the data acquired in the later half of 2019. The tests were carried out with Ar beam (of 1.7 AGeV) on Au target (0.25mm).

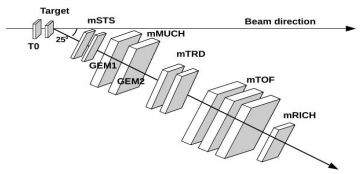

Figure 1: Schematics of the experimental setup of mCBM experiment for Nov./Dec.19 runs

The schematic of the experimental setup having all the subsystems is shown in Figure 1. The mMUCH modules were placed at a distance of ∼84 cm and ∼106 cm from the target position for the March setup. GEM2 was moved to ∼120 cm in Nov./Dec.

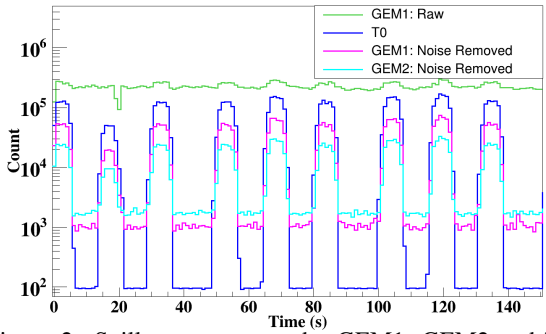

Figure 2: Spill structure seen by GEM1, GEM2 and T0 (diamond) detectors.

The distribution of mMUCH-Digis with time, is shown in the Figure 2. The spill structures from the GEM detectors is nicely correlated with those from T0 (diamond). The histogram in green represents the raw data from GEM1 without any noise removal. Based on individual pad-hit-rates during off-spill, ∼200 channels out of a total 2500, were identified as noisy, which were then masked, for further analysis. This noise-cleaned data for GEM1 is shown in magenta in the figure. A spill length of ∼7.5 s with a gap of ∼7.5 s and ∼12 s is observed.

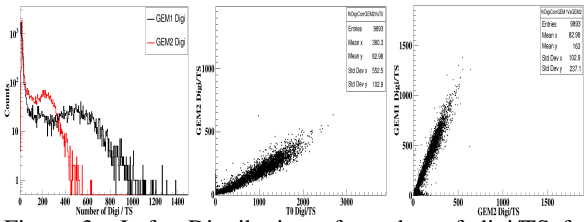

Figure 3: Left: Distribution of number of digi/TS for GEM1 and GEM2. Correlation in number of digi/TS between GEM2 and T0 (middle) and between GEM1 and GEM2 (right)

The distributions of number of Digis per time-slice(TS) after noise-removal, for GEM1 and GEM2 planes are shown in Figure 3 (left). The peak at the higher side of any spectrum corresponds to the on-spill case, while those close to the y-axis corresponds to the off-spill case. While GEM1 had almost full acceptance, GEM2 acceptance was about 70%; hence GEM1 counts are higher. The TS-wise digi correlation between GEM1 and T0 and those between GEM1 and GEM2 are shown in Figure 3 middle and right panels, respectively.

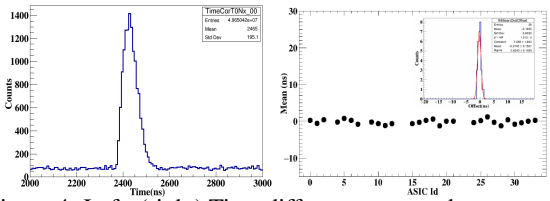

Figure 4: Left: (right) Time difference spectra between one FEB of GEM1 with T0. Variation of peak position (ns) after offset correction for all febs.

The time correlation plot for a particular FEB of GEM1 with T0 is shown in Figure 4 (left). Using Gaussian fitting, the peak position which represents the offset for this FEB is extracted, while the σ represents the time resolution. Different FEBs may have different time offsets which needs to be corrected, before any event reconstruction. Offsets of all the FEBs were thus determined. After correction, the measured mean offset for all the FEBs of mMUCH is shown in Figure 4 (right). These have a spread of about 0.6 ns.

Event reconstruction was also carried out. A run with low beam intensity ($\sim 6.7 \times 10^5 / spill$) was used. As a first approach, all digis in a time interval of 200 ns, with a selection criteria of having a minimum of 1 T0 and 6 TOF

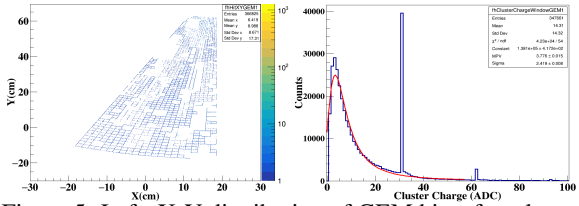

Figure 5: Left: X-Y distribution of GEM hits after clustering. Right: Cluster charge distribution for GEM1

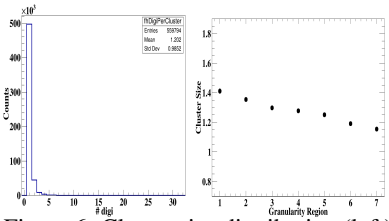

Table 1. Table for pad size at different granularity regions.

Granularity Region	Pad Size (mm)
1	~3.22 - ~4.55
2	~4.55 - ~6.22
3	~6.44 - ~8.49
4	~7.66 - ~10.09
5	~9.59 - ~11.40
6	~11.59 - ~14.02
7	~14.02 - ~16.97

Figure 6: Cluster size distribution (left) and its variation for different granularity regions (middle). Right: Pad size for different granularity regions.

counts, were combined together to form an event. Clustering and hit reconstruction of the mMuCh data were performed, as done in simulation. First, the digitized signals separated by less than 100 ns were members of one cluster. and then the nearest neighbours in space were clubbed together to form hits. A 2D X-Y hits-plot on GEM1 is shown in Figure 5(left). The cluster ADC distribution shown in the same figure is fit to a landau distribution. Owing to 5-bit ADC in the STS-XYTER, a significant amount of saturation is seen at bin (31). All the Febs were calibrated with a charge threshold of 6 fC. The detector gain thus estimated from these pulse-height distributions is plotted against a summed up GEM voltages in Figure 6,The cluster size distribution for GEM1 and its variation at different granularity is also shown in Figure 6. The average cluster size is observed to be $\sim$1.2 at a gain of about 3000. The readout consists of pads of varying sizes. The different granularity regions are divided as per shown in table 1. As we move towards higher pad size, the cluster size gradually decreases as expected.

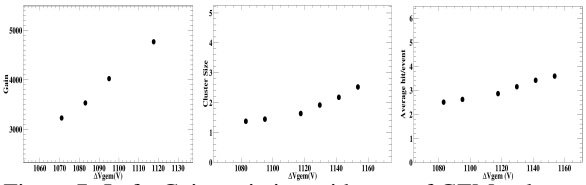

Figure 7: Left: Gain variation with sum of GEM voltages. Middle: Variation of cluster size with GEM voltage. Right: Variation of average hit per event with GEM voltage.

Data with varying GEM voltage were also taken and the corresponding gain variation is shown in Figure 7 (left). The variation of average cluster size (number of fired pads per hit) with GEM voltage is shown in the middle panel while the average number of hits per event with GEM voltage is shown in Figure 7 (right), which appears to saturate at higher voltages.

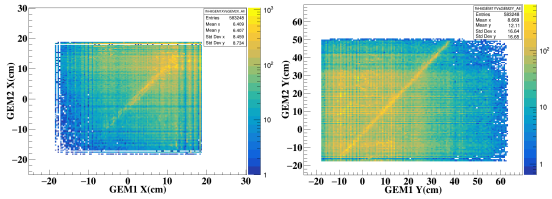

Figure 8: X-X(left) and Y-Y(right) spatial correlation of hits between GEM1 and GEM2 planes.

The spatial correlation in X-coordinate and Y-coordinate between GEM1 and GEM2 planes is shown in Figure 9. We observe a prominent correlation line. Similarly, we looked at the spatial correlation between GEM and TOF planes and this is shown in Figure 9. A clearly visible correlation between the GEM and TOF system is observed.

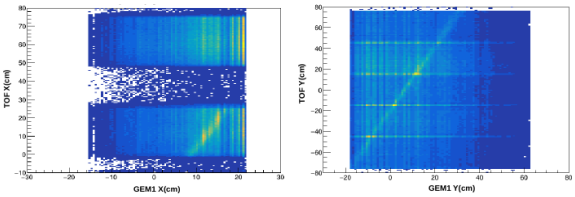

Figure 9: Spatial correlation of hits in X-coordinate (left) and Y-coordinate (right) between GEM1 and TOF planes.

Using the reconstructed events, a straight line track fitting using triple stack TOF module and two GEM modules has also been performed. The extrapolated X-Y distribution of tracks at z=0 planes is shown in Figure 10 (left). We observe that the centre is shifted from its original point (0,0), while the same in simulation with realistic coordinates was observed to be well centred at origin. So a translation in hit coordinates of TOF and MUCH was performed to align the detectors. The extrapolated X-Y distribution (Figure 10,right) is now observed to be as expected.

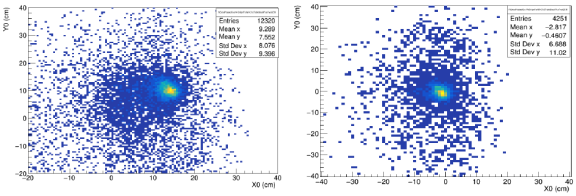

Figure 10: Extrapolated X-Y distribution of tracks at z=0 plane before(left) and after(right) alignment.

The detailed performance and track reconstruction using triple stack TOF and GEM module is under process.

References

[1] A. Kumar and et.al., “Installation, commissioning and testing of mMUCH modules in the mCBM experiment”, GSI Scientific Report 2018 (2018) 56

A Study of mMuCh Response at low and high intensity Pb+Au collisions at mCBM 2020

A. Agarwal[1], C. Ghosh[1], G. Sikder[1], S. Roy[2], S. Chatterjee[2], A. Kumar[2], E. Nandy[1], A.K. Dubey[1], V. Singhal[1], J. Saini[1], V. Negi[1], and S. Chattopadhyay[1]

[1]VECC, Kolkata, India; [2]Bose Institute, Kolkata, India

Large size trapezoidal GEM modules have been installed as part of the mMUCH subsystem in the mCBM experiment. The main goal is to study the detector response to the spray of particles originating from nucleus-nucleus collisions, that pass through our detector. Investigation on the rate capability of the detector is one of the most important goals in this study in mCBM. Two GEM modules participated in the mCBM campaign during March-May 2020, where Pb beams of 1.2 AGeV momentum collided on a Au target. In this report, we discuss the detector response at low and at high beam intensities, i.e. at $8X10^5$ ions/spill(Run-520) and 8 X 10^7 ions/ spills(Run-534), respectively.

Figure 1 shows the spill structures from the two GEM modules, diamond (T0) and Time-Of-Flight (TOF) detectors, for the low and high intensity runs. The GEM modules were operated at a voltage of 4600 V in both the cases. The gas mixture used was Ar/CO2 (70/30).

A 2D X-Y plot depicting the pads hit in GEM 1 is shown in Figure 2 for the two cases. The pallete gives us an idea about the individual pad hit-rates on the entire detector, looking upstream. The rate values are calculated by dividing the pad-hit counts by the length of the time-slice, to obtain the numbers in hits/second. The two runs have identical acceptance and the hit-density pattern over the detector surface also looks similar, with the obvious difference being the increased pad-hit rates for the high intensity case.

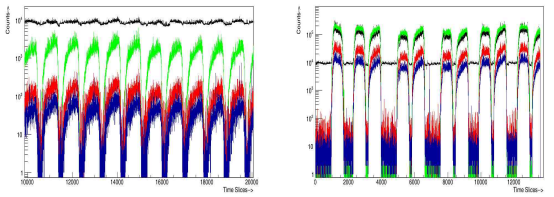

Figure 1: Spill Structure for Run 520 (Left) and Run 534 (Right) (TOF: Black,T0:Green, Gem 1:Red, Gem 2:Blue)

Figure 3 shows the time difference distribution between GEM 1 digis and T0, time-slice wise, for low and high intensity case. The peak of this distribution corresponds to the time-offset for the particular FEBs, with respect to T0. The satellite peak was a feature seen in group of runs taken during a certain period. This was not present in subsequent runs. The origin of these peaks were thought to be due to beam conditions however detailed it is not yet clear.

Offset study was performed for both low and high intensity cases for all Fee-Boards (FEBs). It is observed that FEBs from a given AFCK give a similar offset. No large

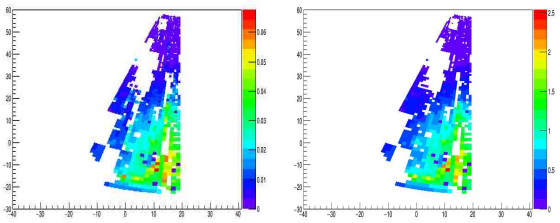

Figure 2: Pad hit rates for low(left) and high (right) intensity runs on GEM1.

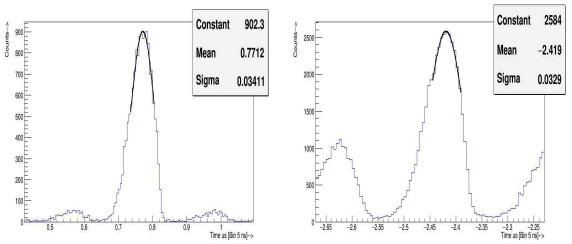

Figure 3: Offset in μs between T0 and Feb 0 for Run 520 (Left) and Run 534 (Right) in the beginning of the runs.

offset jumps observed in either of these runs.

The TS-wise digi correlation for GEM-T0 for the high intesity case is shown in figure 5 (Top Left). One can notice that T0 saturates at high intensities. However, the correlation for GEM-TOF (Right panels in the Top and Bottom) shows a linear behaviour. Bottom left figure conveys the linear behaviour between Gem 1 and Gem 2 for the same intensity run.

The average number of GEM 1 and GEM 2 digis per time slice for low and high intensity case is plotted in Figure 6. While a clear peak is observed in the number of digis per time slice for low intesity case, a rather wide distribution is seen for the high intensity run. It should be pointed

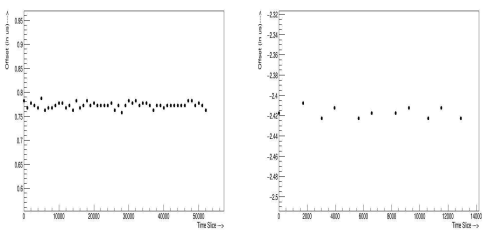

Figure 4: Offset in μs vs Timeslice for a particular FEB (FEB0) for low(left) and high(right) intensity case, respectively.

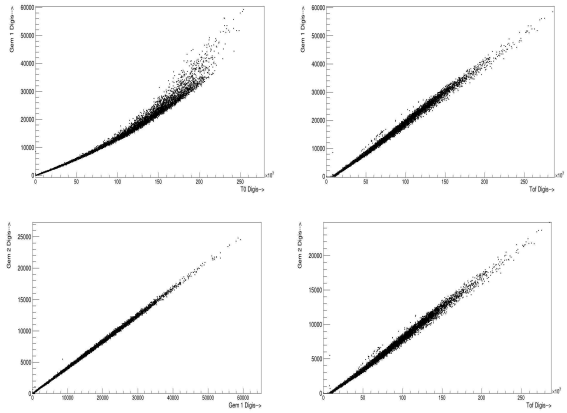

Figure 5: Gem1-T0 Digi Correlation (Top-Left), Gem1-TOF Digi Correlation (Top-Right), Gem1-Gem2 Digi Correlation (Bottom-Left) and Gem2-TOF Digi Correlation (Bottom-Right) for high intensity run (534).

out that this average number of digit include hits from both ON and OFF spill. For detailed analysis therefore, it is required that background at OFF-spil to be excluded for further analysis. We are in the process fo further investigations towards finding the rate estimate of hits during low and high intensity runs.

Data has been taken with thicker targets and also at few more different voltages. A detailed analysis of all this is underway.

During the campaign of mCBM in March-May 2020, mMuCh collected a huge amount of data in various configurations. The configurations include, pulser data, data at various voltages, varying beam intensity and two different target thickness. All these different configurations gave access to varying hit density and rate capability. Even though the runs were smooth during low intensity runs, high intensity runs even at nominal HV started showing that the link between a few FEB and AFCK got lost. We are in the process of detailed investigations, however, no definite solution is not yet found. We have also observed that such link loss results in change in offset time and requires corresponding correction. Even with a set of data with link break, we will be able to extract valuable information on the properties of the detectors from this dataset.

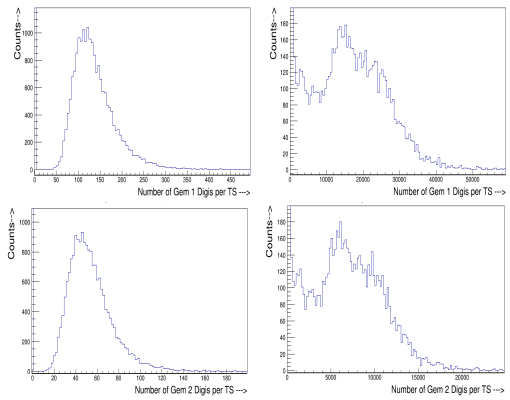

Figure 6: Number of Digis per TimeSlice for : GEM 1, Run 520 (Top-Left) and Run 534 (Top-Right); Gem 2, Run 520 (Bottom-Left) and Run 534 (Bottom-Right)

Implementation of Electronic FEB Id and channel Id for MUCH*

A. Sen† [1] *and V. Singhal*[2]

[1]Bose Institute, Kolkata, India; [2]Homi Bhabha National Institute, Variable Energy Cyclotron Centre, Kolkata, India

`CbmMuchAddress` is a 32-bit addressing scheme for uniquely identifying every MUCH channel. The generation of `CbmMuchAddress` for individual channel follows particular scheme. First 4 bits represent system information, next 3 bits represent station which varies from 0-5, next 2 bits represent layer (0-2), next 1 bit represents layer side information (frontside-backside), next 5 bits represent module (used 0-19 modules), next 8 bits represent sector (in phi angle) and rest 9 bits represent channel number. The angular acceptance of the detector spans from 5° to 25° and according to channel occupancy [1]. 1° and 2° segmentation and progressive geometry have been adapted for the first two stations of MUCH respectively. According to the availability of GEM foil size, each layer of 1st station has been divided into 18 modules. MUCH system is using STS-MUCH-XYTER ASIC readout for the individual pad. The ASIC contains 128 electronics channels (e-channel, for differentiation from the channel which is generated from simulation). First station's each module will contain 23×97 = 2231 pads, which requires at-least 18 Front-end Electronic Boards (FEBs) with one ASIC on it. During mCBM, 2 modules of GEM detector, equivalent of 1st station of MUCH, have been configured according to the availability of FEBs and both modules could not be fully populated [2]. During the simulation, a need has arisen that each channel which is connected to `CbmMuchPad` should provide information about physically connected FEB and corresponding e-channel.

For this requirement, FEB Id and Electronic Channel Id information have been implemented in the CbmRoot framework such that it can be utilized during the simulation. A class named `CbmMuchSegmentPar` has been created to implement the mapping between the channel and sector information of a module to the FEB id and e-channel id accordingly. Two getter functions in the `CbmMuchPad` has been implemented to extract the FEB Id and e-channel information accordingly. `CbmMuchSegmentPar` contains two 2D matrices. One matrix maps the FEB id, which varies from 0-17, and another maps the e-channel id from channel and sector information from `CbmMuchAddress`. Each `CbmMuchPad` has a unique `CbmMuchAddress` from which channel and sector information is extracted and using `CbmMuchSegmentPar` FEB-Id and e-channel information gathered. A macro to pictorially represent and draw the pad from the FEB and Channel information has been written. Also, the same has been used for mCBM data to compare with the simulation result. The MC points have been generated using transport macro. The PCB diagram obtained from the simulated data is shown in Figure 1. Different color represents the different FEB connection to associated e-channels and the FEB number is indicated according to the convention used in the mCBM.

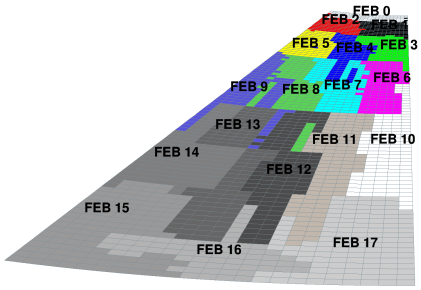

Figure 1: GEM Module pad layout with FEB and e-channel representation drawn from simulated digis.

Figure 2 shows the PCB from the mCBM data (run number 380 taken in December 2019) which is drawn using the address variable of `CbmMuchPad`. In Figure 2a the first GEM module is shown with all 18 FEB connected and in Figure 2b the second GEM module is shown with 6 FEB connected in it. In between blank space is due to non availability of FEB on those locations.

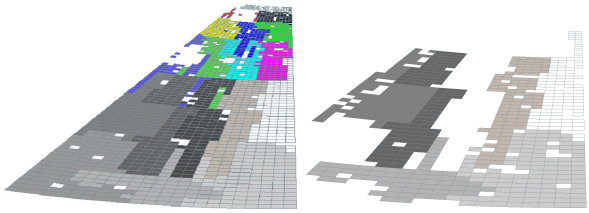

(a) GEM Module 1 (b) GEM Module 2

Figure 2: Pad drawn from mCBM data.

We would like to thank O. Sing, A. Seal, A. Kumar for their valuable suggestion and discussion.

References

[1] TDR for the CBM Muon Chambers, GSI-2015-02580, (2015)

[2] A. Kumar et al., CBM Progress Report 2018, p 51.

* Work supported by DST-INSPIRE and DAE (govt. of India).

† arindam@jcbose.ac.in

Optimization of RPC detector segmentation and charge threshold in 3^{rd} and 4^{th} MUCH Station

Ekata Nandy[1], *Omveer Singh*[2], *Vikas Singhal*[1], *Zubayer Ahammed*[1], *Partha Pratim Bhaduri*[1], *and Subhasis Chattopadhyay*[1]

[1]Variable Energy Cyclotron Centre, Kolkata, INDIA; [2]Aligarh Muslim University,AMU, INDIA

Introduction

MUCH system will be used for detection of dimuons originating from low (ρ^0, ω, ϕ, η), intermediate (continuum) and high (J/ψ) mass regions of dimuon invariant mass spectra [1]. MUCH in SIS100B configuration, consists of 4 absorbers and 4 stations. In first two stations, GEM will be used whereas, in 3rd and 4th stations RPCs will be used as an active detector components. For RPCs, we have considered sector shaped modules which are arranged in a staggered manner on both sides of the support structure. Each RPC module consists of 2 mm RPC gas (TetraFluorethan ($C_2H_2F_4$) 85%, Sulfurhexafluoride (gas composition: SF_6) 10% & 5% Isobutane (C_4H_{10}) sandwiched between 2 mm RPC glass. Each station has three detector layers. Detector layers consistes of several trapezoidal modules arranged together in a circular geometry. Each module has a length of 116 cm & 138 cm for the 3^{rd} & 4^{th} stations respectively. 1^{st} station has 16 modules,2^{nd} station has 20 modules. For 3^{rd} & 4^{th} station 18 & 20 modules respectively have been used. At present we are using 5° & 6° segmentation in 3^{rd} & 4^{th} station but the current segmentations give less efficiency and S/B in dimuon reconstruction and invariant mass distributions, respectively. So, we explored the possibilities of using finer detector segmentation with 1° and 2°. In addition, we studied the effect of charge-threshold parameter on RPC digitization. Presently we are using 30 fC charge threshold as default, we varied it to the 20 fC and 10 fC. Finally we compare our results for the above-mentioned choices of segmentation angles and charge threshold conditions. For this study we use much_v19b geometry tag version. The details of MUCH setup is shown in Fig. 1.

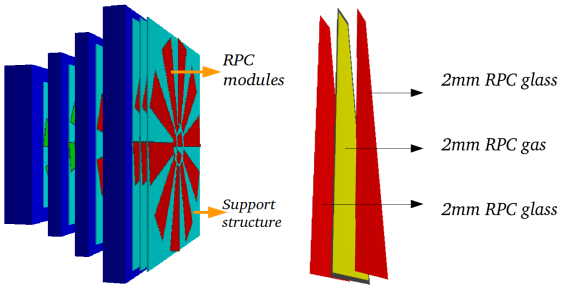

Figure 1: Arrangement of modules in staggered manner on both sides of a support structure. RPC module has been shown separately.

Segmentation study

Segmentation study with different angles have been done with SIS100B much_v19b geometry at 8 AGeV central Au+Au collisions with CBMROOT OCT19 release version. UrQMD has been used for background event generations and PLUTO for signal ω decaying to $\mu^+\mu^-$. Fig. 2 shows the granularity of detector pads for different angles. With smaller azimuthal angle granularity increases.

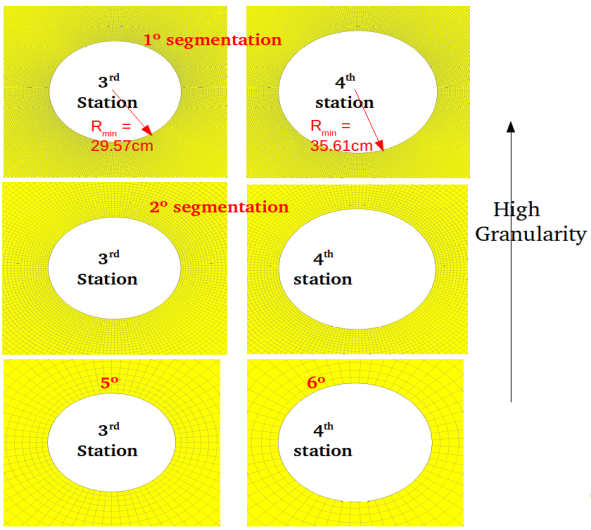

Figure 2: RPC detector segmentation with different azimuthal angle 1°, 2° in 3rd and 4th station and 5° in 3rd and 6° in 4th station

Details of segmentation

	Station	sectors/ layer	Pads/mod ule	Smallest pad size (cm)	Largest pad size (cm)	Modules/ layer	Module angle
1° segmen-tation	3rd station	92	2284	0.5161	2.492	18	20°
	4th station	91	2016	0.6216	2.950	20	18°
	Station	sectors/ layer	Pads/mod ule	Smallest pad size	Largest pad size	Modules/ layer	Module angle
2° segmen-tation	3rd station	47	602	1.032	5.003	18	20°
	4th station	46	532	1.243	5.822	20	18°
	Station	sectors/ layer	Pads/mod ule	Smallest pad size	Largest pad size	Modules/ layer	Module angle
5° & 6° segmen-tation	3rd station	19	114	2.58	11.63	18	20°
	4th station	16	64	3.729	16.61	20	18°
	Station	sectors/ layer	Pads/mod ule	Smallest pad size	Largest pad size	Modules/ layer	Module angle
1° segmen-tation	1st station	93	2714	0.3447	1.693	16	22.5°
	2nd station	91	2172	0.4361	2.106	20	18°

Table-1:Details of different segmentation angles

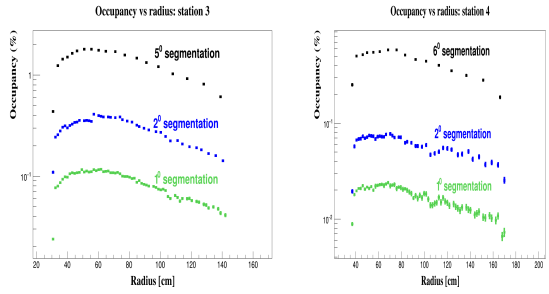

Figure 3: Occupancy distribution for 3^{rd} & 4^{th} station with different angles.

The details of segmentation has been mentioned in Table-1.

Fig. 3 shows the occupancy distribution in 3^{rd} & 4^{th} station with different segmentation angles, which shows with higher segmentation angle occupancy higher. Fig. 4 shows the invariant mass distribution of dimuons for signal ω embedded in background for different segmentation angles. We see for 1° segmentation invariant mass yield is maximum. This is because the high granularity of the detector pads increases the probability of seperation of nearby tracks. Table-2, shows the comparison of final efficiency and S/B of ω at 8 AGeV central Au+Au collision. We observed efficiency and S/B is slightly better for 2° segmentation and improves further for 1°.

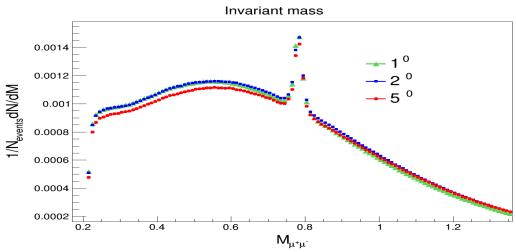

Figure 4: Invariant mass distribution of ω embedded in background at different segmentation angles

	ω Pair reconstruction efficiency (%)	S/B
5° & 6° segmentation	0.83	0.24
	2.4% ↓	
2° segmentation	0.85	0.24
	8.4% ↓	Efficiency & S/B increases
1° segmentation	0.90	0.26
		7.6% ↓

Table -2 : Efficiency and S/B of ω at different segmentation angles

Different charge threshold study

The readout planes of the RPC modules are segmented in pads. The procedure of distributing the MUCH points to pads, known as digitization involves the detailed procedure of implementing the response of the gas detector to the energy deposition inside the chamber. In this digitization process we have studied how does the change parameter gets reflected in the formation of digis. Presently 30 fC charge threshold has been used in simulation with dynamic range 100 fC, i.e, maximum charge limit is 130 fC [1]. However, RPCs can be operated at 20 fC as well. So we have simulated the final performance of detector at 20 fC and also at 10 fC charge threshold for both 1° and 5° segmentation.

Fig. 5 shows the dimuon invariant mass distribution of signal ω + background at different charge threshold values for 1° and 5° segmentation. Table-3, shows the efficiency and S/B of ω for different cases and we observe efficiency highest for 1° and 10 fC threshold conditions.

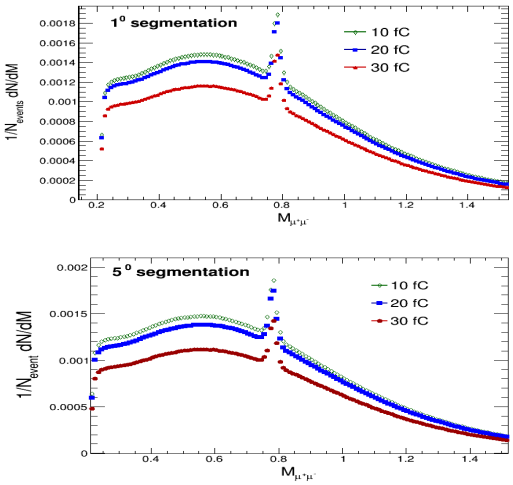

Figure 5: Invariant mass distribution of ω embedded in background at 1° and 5° segmentation for different charge threshold.

With 5° and 6° segmentation (3^{rd} & 4^{th} station)	ω Pair reconstruction efficiency (%)	S/B
30fC	0.83	0.243
	20% ↓ Efficiency increases	4% ↓ S/B going down
20fC	1.00	0.236
	26% ↓	
10fC	1.05	0.233
Eff ~ 36 % S/B ~ 4%		
With 1° segmentation (3^{rd} & 4^{th} station)	ω Pair reconstruction efficiency (%)	S/B
30fC	0.90	0.261
	22% ↓ Efficiency increases	S/B going down
20fC	1.10	0.261
	25% ↓	
10fC	1.13	0.254

Table-3: Efficiency and S/B of ω at different segmentation angles and charge threshold

References

[1] Technical Design Report for the CBM : Muon Chambers (MuCh), CBM Collaboration, GSI, 190 S. (2015)

[2] CBM Progress Report 2018 "Implementation of RPC geometry and digitization in the 3^{rd} and 4^{th} MUCH station", E. Nandy et.al.

STS/MUCH-XYTER v2.1 calibration of various parameters and e-link monitoring for MUCH detector system*

G. Sikder[1], J. Saini[2], C. Ghosh[3], A. K. Dubey[4], A. Chakrabarti[5], S. Chattopadhyay[6], A. Bhattacharyya[7], and C. Schmidt[8]

[1,5,7]University of Calcutta, Kolkata, India; [2,3,4,6]VECC, Kolkata, India; [8]GSI, Darmstadt, Germany

The new dual gain STS/MUCH-XYTER is a 128 channel highly configurable ASIC with dedicated 5-bit flash ADC for each individual channel. This ADC have 31 comparators which can be trimmed for a particular reference voltage controlled by a 8-bit Digital to Analog Converter (DAC).All 32 steps of ADC for all 128 channels of ASIC needs to be calibrated for a desired input charge. An automated setup is developed at VECC for the calibration of ASIC for MUCH detectors. In this setup we have also compared internal charge injector in ASIC with an external charge injector and effect of bias parameters VrefN, VrefP and VrefT on the calibration. MUCH/STS-XYTER downlink synchronization is highly sensitive to the glitches in clock lines hence an online monitoring code was developed for the MUCH detector system to monitor the synchronization of these downlinks.

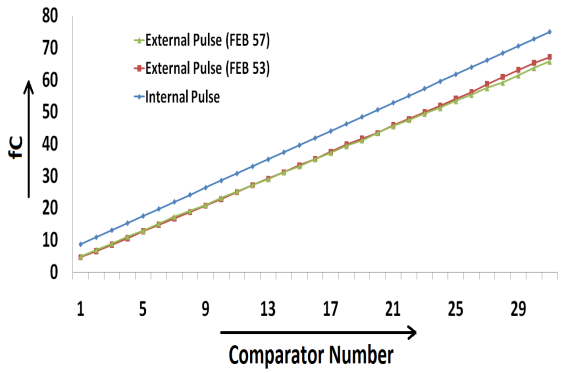

Figure 1: External vs Internal charge injector zeroth channel calibration plot for FEB 57 and FEB 53

Internal Versus external charge injector response of MUCH-XYTER 2.1

Test bench setup of VECC (reported earlier) is used to perform this study. For this study, 600 fF (MUCH mode) feedback capacitance setting along with other bias parameter settings of VrefN = 26, VrefP = 55 and VrefT = 180 was used. MUCH-XYTER was calibrated with internal charge injector ranging from 8.7 fC to 77.4 fC and trim settings were calculated for all 32 ADC comparators of a particular channel. Now with manual external charge injection was adjusted such that same trim settings were re-achieved. Figure 1 is the plot shows the charge injection versus channel number plot for both internal and external for the zeroth channel of two FEE boards. Calibration line derived from the internal charge injector is same for both the FEE boards but on comparing with the external injected charge, they shows variation in slope. As external charge injection setup is constant, the variation among the two ASIC indicates channel characteristics variation across the ASIC which may be either due to variation of internal charge injection capacitor or the pulse generator calibration. Detail study will be performed in future to study with more statistics to know the range of the variation.

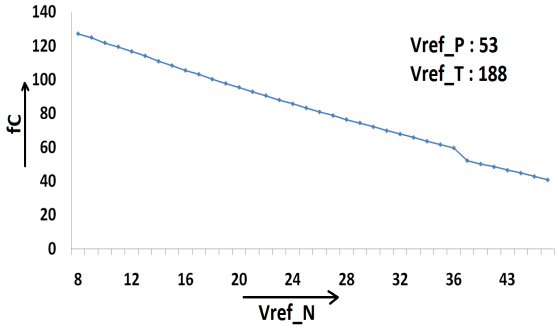

Figure 2: Varying threshold with respect to different VrefN

ASIC threshold with varying VrefN, VrefP and VrefT

The bias parameters VrefN, VrefP and VrefT not only controls the biasing of the ADCs but also have deep impact on the charge thresholds and dynamic range of the input channels of the ASIC. Here we only present the results of threshold effect with respect to VrefN, VrefP and VrefT on first comparator of input channel of the ASIC with varying one bias parameter at a time and keeping other two setting to their nominal values. Before these tests were performed, all the ADC of the ASIC was calibrated from range of 80 fC to 140 fC with linear step size of 2 fC keeping the other bias settings VrefN = 26, VrefP = 60 and VrefT = 188 using an External charge injector while CSA Feedback capacitor was kept at 600 fF. This setting was used for the testing RPC detector in high gain mode. Figure 2. shows

* Work supported by VECC, Kolkata (EHEP&A Group)

the threshold variation with respect to VrefN. This plot also shows the ASIC tunability for different 0th channel threshold.

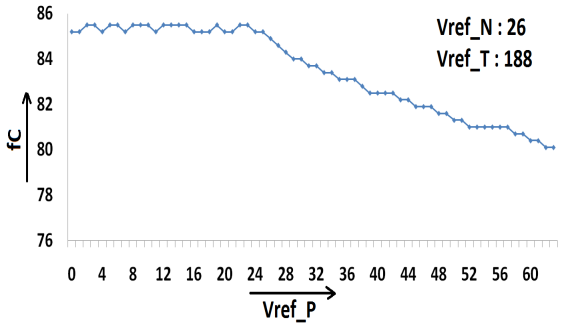

Figure 3: Varying threshold with respect to different VrefP

Figure 3. shows the threshold variation with respect to VrefP. Here the threshold change is in very limited range as compared to the VrefN. The reason behind this behaviour is the chosen starting range zeroth comparator threshold to 80 fC for this test. The results are exactly opposite if starting range chosen is 6 fC or lower instead of 80 fC.

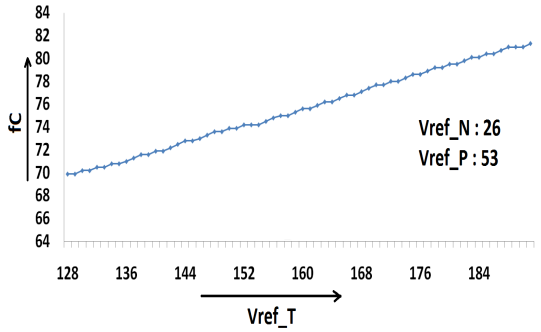

Figure 4: Varying threshold with respect to different VrefT

Figure 4. shows the the threshold variation with respect to VrefT. In version 2.1, this is designed for the fine tune settings hence variation is very low. The initial flat line indicates the saturation in the bias value and will lead to reduction in dynamic range, however detailed study is yet to be performed.

e-Link status Monitoring for MUCH Detector system

It was observed that any glitch introduced in clock line of STS/MUCH-XYTER will lead to synchronization loss in the downlink from CROB to FEE board. As a result, 1) there is no more communication possible with the ASIC, 2) each glitch is counted as an extra clock pulse to the counter of the ASIC leading to time offset in the data and 3) if the DAQ run cannot be started with such un-synchronized e-links. It is also seen that these glitches are observed more frequently with the higher detector HV and frequency increases with beam intensity falling on the detector. To know the heath of these downlinks, we have developed an online e-link monitoring code which can even store the timing information of event with resolution of few seconds which may be used at time of data analysis. Figure 5. shows a screen shot of the monitoring panel when running this code which shows few links stable while some are broken.

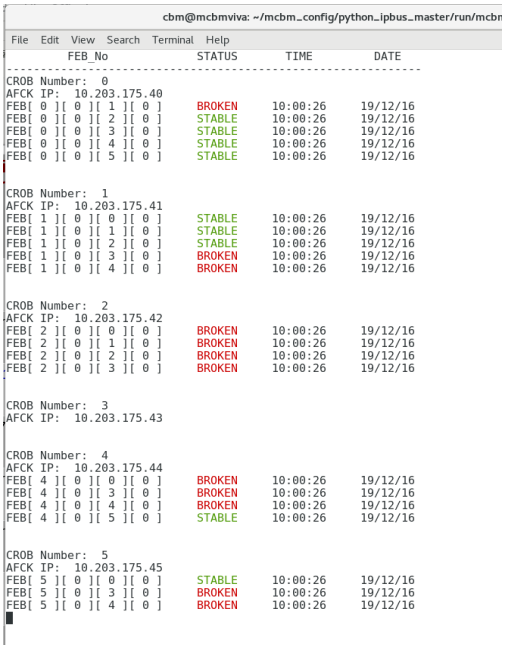

Figure 5: Online FEB Link Monitoring System for MuCH Detector

Future plans

A systematic study in MUCH mode on dynamic range with respect to the bias settings and effect of bias variation at different zeroth ADC comparator settings and effect of varying time constant settings of this ASIC will be done.

References

[1] K. Kasinski and R. Kleczek and R. Szczygie, "Front-end readout electronics considerations for Silicon Tracking System and Muon Chamber", Journal of Instrumentation, doi : 10.1088/1748-0221/11/02/c02024

Study of 10 cm X 10 cm GEM detector Characteristics using MUCH-XYTER v2.0 and v2.1 Asic

C. Ghosh[*1], *J. Saini*[1], *G. Sikder*[3], *A. Kumar*[1,2], *A. K. Dubey*[1], *and S. Chattopadhyay*[1]

[1]VECC Kolkata, India-700064; [2]Homi Bhabha National Institute, Anushaktinagar, Mumbai 400094; [3]University of Calcutta, Kolkata, India-700106

Triple GEM (Gas Electron Multiplier) detector will be used as MUCH (Muon Chamber) in CBM experiment at FAIR, to detect dimuons originating from the decay of low mass vector mesons [1]. CBM will operate at 10 MHz collision rate and the maximum particle density at the innermost part of the 1st station MuCh detector will be about 0.4 MHz/cm^2 [2]. Here we report the detailed test results of a 10 cm X 10 cm triple GEM detector [3] using MuCh-Xyter ASIC v2.0 and v2.1. The detector gap configuration used is 3-2-2-2 mm and the premixed Ar:CO_2 ratio has been used.

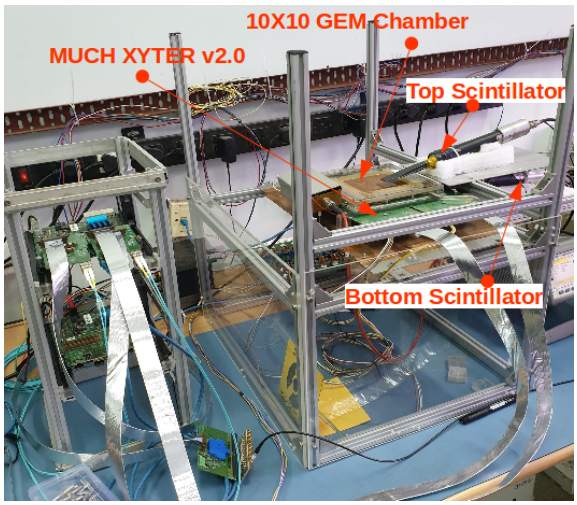

Figure 1: Lab setup with triple GEM detector

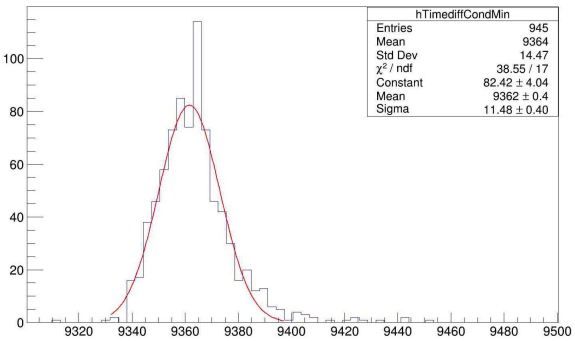

Figure 2: Time difference spectra with time diff (ns) in x axis and counts in y axis

Fig.1 shows the coincidence setup with a 10 cm x 10 cm triple GEM detector. Two scintillators with areas of 2 cm x 2 cm and 3 cm x 3 cm are used on the top and the bottom of GEM active area respectively for coincidence with cosmic rays. Data is recorded with MuCh-Xyter ASIC v2.0 and 2.1 separately and compared for various detector characteristics.

Cosmic ray events were recorded for 6 different high voltage (HV) starting from 4500 V to 5000 V in steps of 100 V. Fig.2 shows a time difference spectra between GEM hits and scintillator coincidence hits at detector voltage of 5000V. The detector efficiency and time resolution are extracted at all the above 6 voltages. Fig. 3 and Fig. 4 shows variation of detector efficiency and time resolution respectively.

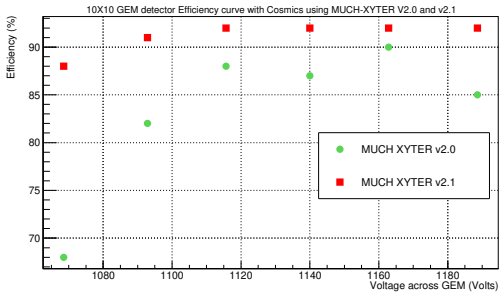

Figure 3: Variation of detector efficiency with summed voltage across 3 GEM layers

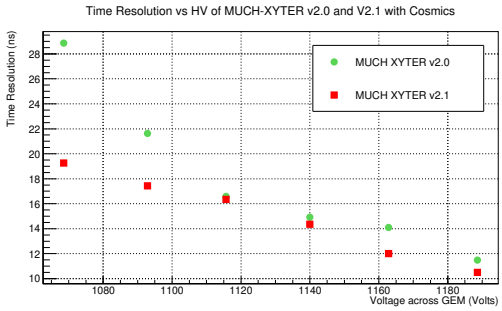

Figure 4: Variation of detector time resolution with summed voltage across 3 GEM layers

Fig.3 shows a decrease in efficiency with MuCh-Xyter-v2.0 at highest detector voltage, this may occur as v2.0 generates duplicate hits, so the actual hits get suppressed, thus reducing the efficiency. This bug has been fixed in v2.1, so

* c.ghosh@vecc.gov.in

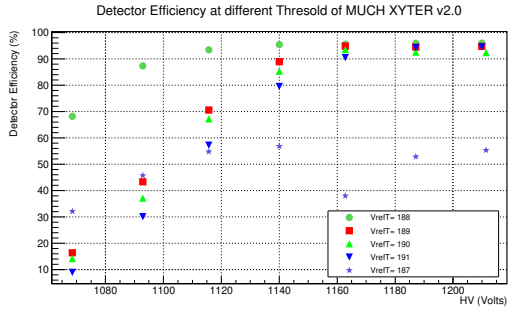

Figure 5: Variation of detector efficiency at different thresold VrefT for asic v2.0

we get expected efficiency at highest voltage also. Fig.4 shows time resolution improves with increasing voltage. v2.1 shows steady improvement than v2.0, which can be explained by the duplicate hits.

As the coincidence area is low ($\sim$ 4 cm^2) due to limitation in detector read out area so a high rate beta source (Sr^{90}) is used instead of cosmic rays to conduct some study on the variation of detector efficiency and time resolution with ASIC bias setting (VrefT).

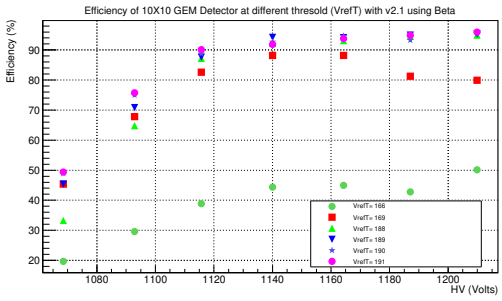

Figure 6: Variation of detector efficiency at different threshold VrefT for MuCh-Xyter-v2.1

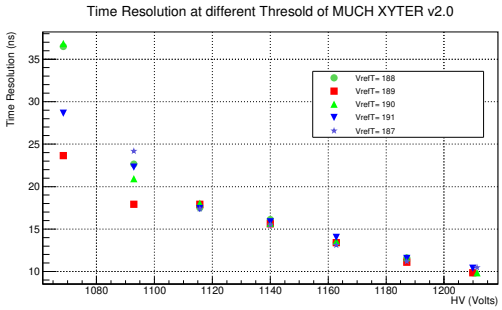

Figure 7: Variation of detector time resolution at different threshold VrefT for MuCh-Xyter-v2.0

From Fig.5 if we look at voltage 1140 V, it shows that VrefT=188 is optimal, above this data get suppressed and below this noise gets included, resulting in reduced efficiency. Although at higher detector voltage the efficiency value becomes nearly same except for VrefT=187. For MuCh-Xyter-v2.1 (Fig.6), no particular could be observed, but at higher voltages the efficiency values are almost same for different thresholds except at values like 166, 169.

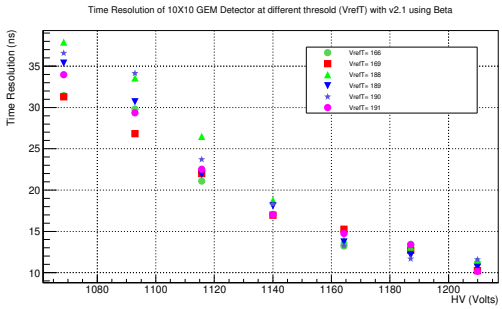

Figure 8: Variation of detector time resolution at different threshold VrefT for MuCh-Xyter-v2.1

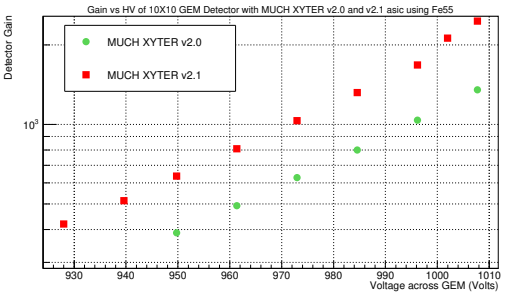

Figure 9: Detector gain variation with HV for 2 ASIC versions

Fig.7 and Fig.8 show that the time resolution doesnot follow any particular pattern with VrefT, at higher voltages the values coincide with each other.

Detector gain is measured with MuCh-Xyter-v2.0 and MuCh-Xyter-v2.1 using Fe-55 source at different HV setting, Fig.9 shows that v2.1 gives 1.6 times higher gain compared to that with v2.0. This gain variation may result from slight variation in the calibration trim file of both the ASICs at the time of calibration. Further investigations are ongoing.

References

[1] Technical Design Report for the CBM, Muon Chambers, November, 2014.

[2] A.K.Dubey et al., Nucl. Instr. Meth. A , 755 (2014) 62-68.

[3] A. Kumar et al., Proceedings of the DAE Symp. on Nucl. Phys. 63 (2018)

MUCH Mechanics Status

D. Ivanischev[1], A. Khanzadeev[1], R. Melnik[2], V. Nikulin[1], V. Samsonov[1], and O. Tarasenkova[1]
[1]NRC Kurchatov Institute, PNPI, 188350 Gatchina, Russia; [2]"OMP" Company, 192289, St-Petersburg, Russia

Introduction

MUCH detector of the CBM experiment is essentially a sequence of 5 absorbers with tracking stations between them located on the beam. MUCH shares the in-beam position with RICH detector, in order to achieve this, it sits on the movable Platform that should be able to displace the set-up from the operational (in-beam) position to the parking one (near the CBM cavern wall).

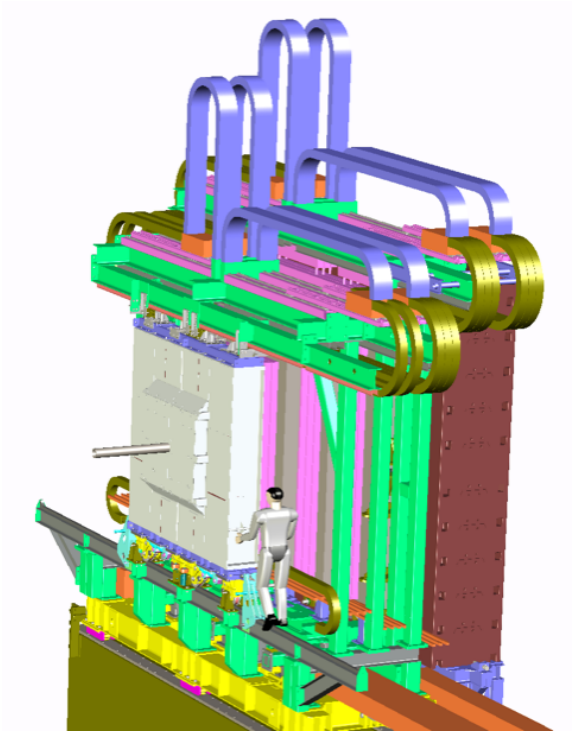

Figure 1: General view of the preliminary MUCH setup during installation of the Absorber 1. The supports for the Absorber 5 are not shown. The bent objects on top of MUCH are the chamber service carriers. The close cable carriers are extended to make possible extraction of the chamber layer in service position out of the gap between the absorber. The rear carriers are in the compact position, enabling RICH stand nearby.

The general view of the current MUCH setup sitting on RICH/MUCH Foundation is shown in Figure 1. The bent objects on top are the chamber service carriers.

Platform

MUCH Platform is shown in Figure 2. Several reasonable options for the Platform (long and short) and different displacement mechanisms (screw-nut, or rack-pinion, or hydraulic systems, moving along the rails or skidding). The optimal configuration consists of a welded frame, on the bottom of which roller carriages are installed. The roller carriages closest to the Absorber 5 have side rollers to take up the transverse loads during movement and an earthquake. The Platfrom is fixed to the Foundation at its extreme positions with the brackets. The Platform can be moved by means the hydraulic drive along the cogged guide from the operational (in-beam) to the parking (near the cavern wall) positions and back.

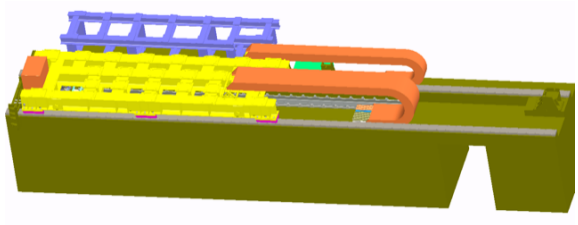

Figure 2: Standalone view of MUCH Platform.

The preliminary stress analysis proves its sufficient stiffness to sustain the loads from the detector.

Absorber 1

The Absorber 1 simulations [1] demonstrated that close to the optimal optimal detector performance can be achieved for the sandwich structure containing 28 cm of graphite with a density of 1.78 g/cm^3 and 30 cm of concrete with a density of 2.3 g/cm^3. its design could be seen in Figure 3. The small parts made of aluminum are permissible.

The aluminium-lead shield will be placed around the beam-pipe. The Absorber halves can be positioned along the beam with the tolerance of order ± 1 mm and can be moved aside to allow space required for the coupling of the beampipe parts at the STS wall. A 25 mm high step is introduced at the contact surface of the absorber halves in order to prevent direct passage of the particles through the clearance between the Absorber halves.

Basic structural elements of the Absorber fixation such as the platforms, rollers, brackets, adjustments and fixing elements are made of non-magnetic stainless steel.

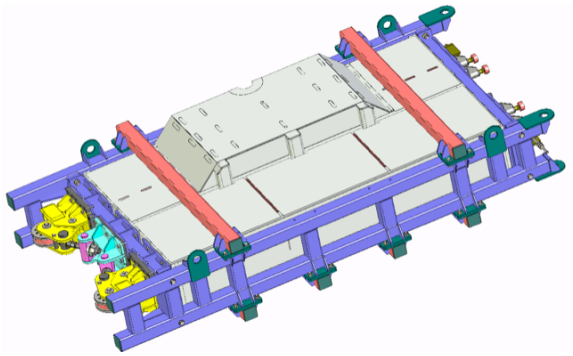

Figure 3: Right half of the Absorber 1 in installation-transportation tooling set.

Absorber 5

The Absorber 5 (see Figure 4) is the dismountable 1-m thick wall made of the cast iron blocks (density of about 7.2 g/cm^3) and sitting on its dedicated welded support. Welded racks are located on the sides of the Absorber to prevent tipping off a set of blocks during an earthquake.

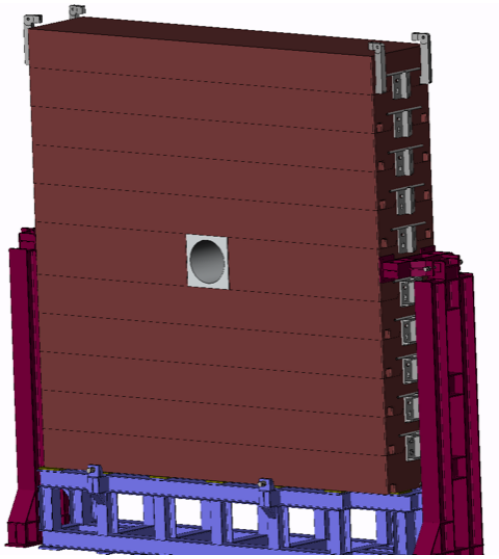

Figure 4: Standalone view of the Absorber 5.

The simulations [2] show low sensitivity of the Absorber performance to the machining quality of the blocks (the gaps of order 1 cm are tolerable). The machined tongue-groove joints ensure auto-centring of the blocks during installation and fixation against displacement along the beam direction in case of an earthquake. Blocks are fixed against displacement across the beam direction by means of side brackets. These brackets are also used for block positioning during the installation.

An aluminum shield to prevent the activation of the iron is fixed by means of steel plates screwed to the beam shield and a block.

Services

The tracking stations require for their operation considerable amount of different services — various cables, cooling and gas pipelines etc. These numerous cables and pipes do not allow disconnection and require careful handling during:

- The displacement of MUCH Platform from operational to parking positions;
- The displacement of each individual tracking chamber layer from operational to service position.

In order to organise these movements in a safe way the flexible cable channels will be used. The connection of the services with MUCH Platform will be done via two cable channels shown in right part of Figure 2.

The services come to the patch panels on the Platform and then distribute to the appropriate detectors. Three options for possible service distribution were studied. The variants when the services come directly from the Platform surface had severe problems due to width limitation of MUCH (6.4 m) and rater large bending radius of the services (about 300 mm). These options resulted to have poor access to the patch panels, difficulties with maintainability and repairability. An alternative version, where the services come from MUCH top (see Figure 1) has complications with installation of removable parts of the transverse beams, but these difficulties are resolvable.

Conclusions

MUCH mechanics is a complex system to be designed by Indian and Russian teams. The goal of the task sharing was to minimise possible interference and to exploit the best competence of each team: bulk mechanics for PNPI and chamber-related equipment for VECC. The Conceptual Design Reviews for MUCH Platform, the Absorber 1 and the Absorber 5 are recently submitted to the CBM Technical Management. Currently the concepts of the Superstructure and the Absorbers 2, 3, and 4 are under development. Essential dependence on the design of the tracking stations, especially their positioning and adjustment mechanisms and connection with services requires close collaboration between the PNPI and Indian designer teams. The recently organised MUCH mechanical integration meetings give good possibilities for the direct contacts between the designer team resolving the pending issues.

References

[1] O. Singh, *et al.*, Evolution of First Absorber in Muon Chamber, this CBM Progress Report

[2] S. Chatterjee, *et al.*, Optimization of fifth absorber of Muon Chamber (MuCh) for the CBM experiment at FAIR, this CBM Progress Report

Noise reduction and testing of a double gap RPC

V. K. S. Kashyap and B. Mohanty
School of Physical Sciences, National Institute of Science Education and Research, HBNI, Jatni 752050, India

Introduction

To achieve counting rate in RPCs for MuCh requirements, one needs to operate them at lower gain and average induced charges of $\sim$ 0.1 pC [1]. Detector and electronic noise reduction would be crucial to achieve this goal. Also, double gap RPC is one among the various modifications that can be done to improve the efficiency and rate capability of an RPC [1, 2]. By construction, the 2 gaps in a double gap RPC are independent of each other. Therefore, one gap would compensate for the inefficiency of the other. This will provide better efficiency for the double gap RPC as a whole at lower voltages and hence improve the rate capability since each gap would be working at a lower gain. Also, in case there is a problem with one gap, the RPC would still be able to function with the other.

Here, we report the tests done on a double gap normal glass RPC with $\rho \sim 10^{12}$ Ω cm bulk resistivity, operating with a standard gas mixture containing 95.2% r134a, 4.5% i-butane and 0.3% SF_6.

Experimental setup

A 30 cm $\times$ 30 cm double gap normal glass RPC is assembled as per the schematic shown in Fig. 1(a). It consists of two glass single gas gaps of identical dimensions with 2 mm thick normal glass electrodes and a gap thickness of 2 mm. Conductive coating of surface resistivity $\sim$1 M$\Omega/\square$ is applied on the electrodes. The readout panel is sandwiched between two gas gaps. The schematic arrangement of the gas gaps and the RPC is shown in Fig. 1(a). A schematic of the experimental setup is shown in Fig. 1(b). Readouts, scintillator telescope and electronics are identical to those described in [1]. Data from 3 strips (left, right and centre) are acquired as shown in Fig. 1(b).

Since the 2 gaps in the RPC are independent, it can be run in the single gap mode by switching either of the gaps off.

Noise reduction

The noise rate in an RPC is mostly due to electromagnetic interference and improper grounding. The readout electronics and the HV supplies were earlier connected to the main ground in a mix of daisy chain and single point schemes. We changed the scheme to a mix of multipoint and daisy chain with a thick conductor grounding scheme [3]. We constructed a Faraday cage around the RPC using alumimium foil to shield it from electromagnetic interference and observed a drastic reduction in the singles noise rate at low charge thresholds.

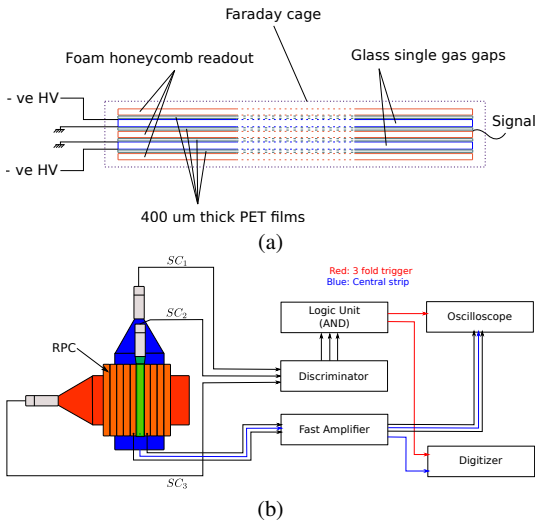

Figure 1: (a) Schematic of the double gap RPC. (b) Schematic of the experimental setup.

The singles noise rates (all signals crossing a set charge threshold) of the central strip for various thresholds before and after using a Faraday cage are shown in Fig. 2(a). The noise rate is reduced by a factor of 100 for a threshold of 50 fC and by a factor of 5 for a threshold of 25 fC. For a threshold of 200 fC there is no reduction. A faraday cage is very crucial for the reduction of noise in an RPC.

Double gap RPC test results and discussion

The comparison of efficiency, mean charge and cluster size for single and double gap configurations are shown in Fig. 2(b), 2(c) and 2(d) respectively.

One can see from Fig. 2(b) that the double gap configuration achieves around 5% higher efficiency compared to the single gaps at lower applied voltages. While calculating the efficiency, the signal detected by any of the 3 strips (OR) is considered as detected by the RPC.

From Fig. 2(c) it can be seen that the mean charge induced on the readout strip is also higher for the double gap configuration compared to the single gap. Since the induced charge gets added from both gaps in the double gap configuration, on an average it is higher compared to the individual gaps.

The average number of strips fired per muon trigger is

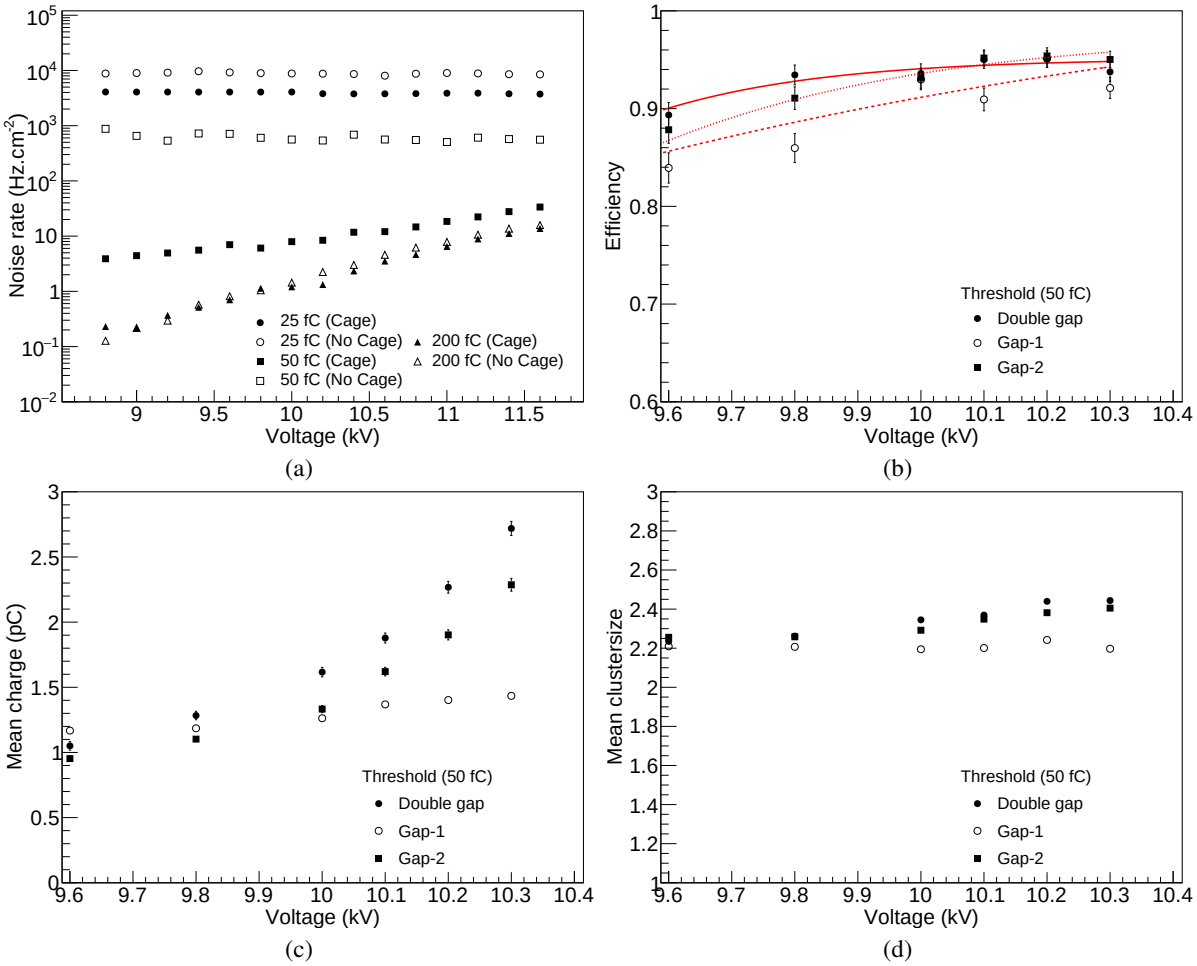

Figure 2: (a) Comparison of singles noise rate with and without Faraday cage at various thresholds for a single gap. Comparison of double and single gap RPC configurations: (b) Comparison of efficiency. The lines are sigmoid function fits to the data points (Double gap - solid, Gap1 - dashed, Gap2 - dotted). (c) Comparison of induced mean charge. (d) Comparison of average clustersize.

considered as the average clustersize. Looking at Fig. 2(d), the double gap configuration shows a higher average clustersize compared to single gap as expected. This is because the position of muon interaction can be slightly different in each gap.

Conclusion and outlook

A double gap RPC with normal glass electrodes has been tested. The results show that they provide around 5% improvement in the efficiency of the RPC at lower voltages and would be beneficial for operation of RPCs at lower gain to improve the counting rate. Further modifications in electrode dimensions and conductive coating surface resistivity may help reduce the clustersize.

We will be testing a double gap low resistivity glass RPC [1]. We also plan to test single and double gap RPCs made of low resitivity bakelite with different electrode and gap thicknesses to achieve the desired rate capability of MuCh. Tests with different frontend electronics are also planned.

Acknowledgements

We thank S. Chandra, O. P. Dash and S. Rout for their help in assembling the RPC and data acquisition. We thank the INO-RPC group at TIFR for providing us the conductive paint and readout panels to assemble the RPC. DAE and DST, Govt. of India are acknowledged for funding. BM also acknowledges the support of J. C. Bose National Fellowship of DST.

References

[1] V. K. S. Kashyap and B. Mohanty, “Characterization of a low resistivity glass RPC”, This progress report.

[2] The CMS muon project: TDR, CERN-LHCC-97-032.

[3] W. G. Duff, “Designing Electronic systems for EMC”, SciTech Publishing, ISBN: 978-1-891121-42-5

Characterization of a low resistivity glass RPC

V. K. S. Kashyap and B. Mohanty
School of Physical Sciences, National Institute of Science Education and Research, HBNI, Jatni 752050, India

Introduction

RPCs are being proposed as detectors for the 3rd and 4th stations of the CBM Muon Chamber (MuCh) subsystem [1]. Having excellent timing capability, RPCs have resonable position resolution and can typically handle count rates of the order of $\sim$ 1 kHz cm^{-2}. They are very good detectors for muons and the expected particle fluxes at the 3rd and 4th stations of the MuCh subsystem are $\sim$ 15 kHz cm^{-2} and $\sim$ 5.6 kHz cm^{-2} respectively for 8 AGeV central Pb-Pb collisions [2].

With modifications in the construction of RPC, usage of low noise electronics and lower gain operation, its rate capability can be improved. The rate capability of RPC is defined as

$$R_C = R/V = 1/\rho t\langle Q\rangle, \quad (1)$$

where $R_C = R/V$ is the rate per unit voltage drop, R is the particle (counting) rate, V is the voltage drop across the electrodes, ρ is the bulk resistivity of the electrodes, t is the total thickness of the electrodes and $\langle Q\rangle$ is the average charge produced in the gas for each count [3]. The average charge produced in the gas for each count in avalanche mode RPCs is $\sim$ 20 pC [3, 4]. If the permissible voltage drop across the electrodes is around 250 to 300 V, considering an electrode bulk resistivity of $\rho = 1.5 \times 10^{10}$ Ω cm (typical bulk resistivity of low resistivity bakelite and glass) and $t = 4$ mm, a rate capability of $\sim$ 1 kHz cm^{-2} is achieved. To increase the counting rate to MuCh requirements, one has to reduce the average charge produced in the gas gap per count indicating the operation of RPC at a much lower gain ($\langle Q\rangle \sim 2$ pC). In an RPC, the detected signal is the induced charge q on the readout as opposed to the actual charge produced in the gas. This charge is typically $\sim$ 20 times smaller than the charge inside the gas gap [3, 4]. Therefore, one needs to operate RPCs at induced charges of $\langle q\rangle \sim 0.1$ pC. One could also reduce ρ to increase the rate capability, but this would have adverse effect on the RPC position resolution. In this report, we present some results from the characterization of a low resistive glass RPC with $\rho \sim 1.5\times10^{10}$ Ω cm bulk resistivity. The glass has been developed by Tsinghua University, Beijing and supplied by Bjoptics, China. R & D on glass RPC is ongoing at NISER, Jatni in parallel to the ongoing activities using bakelite RPC at VECC, Kolkata.

Experimental setup

A 32 cm $\times$ 30 cm glass RPC made of low resistivity glass electrodes is arranged in coincidence with a scintillator telescope. The electrodes are 2 mm thick and the gap thickness is 2 mm maintained with the help of polycarbonate spacers. Conductive graphite coating is applied on the electrodes with a surface resistivity of $\sim$1 M$\Omega/\square$. Gas mixture containing Freon(r134a), *i*-butane and SF_6 is flown through the RPC at different concentrations with the help of a gas mixing system. The setup schematic is shown in Fig. 1. Signal readout is made of a polycarbonate honeycomb having foam filling with copper strips of 2.8 cm width and 30 cm length. The scintillator telescope consists of plastic scintillators SC_1 , SC_2 and SC_3 arranged as shown in Fig. 1. SC2 has a width of 4 cm and length of 30 cm. It is used to select particular strips. SC_1 and SC_3 are identical, have width of 20 cm and are 40 cm long. All the scintillators are 1 cm thick. Signals of all the detectors are processed using NIM electronics (for generating trigger, applying HV bias and amplifying RPC signals) and VME Digtizer and Digital Storage Oscilloscope (for analyzing RPC signals). A picture of the setup is shown in Fig. 2. Data from 3 strips of the RPC are collected as shown in the schematic. The digitizer has a Digital Pulse Processing firmware using which one can obtain the induced charge per event by integrating the signal pulse. The integrated charge of the induced pulses are corrected for the amplifier gain and detector strip impedence.

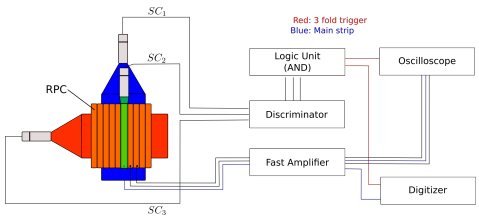

Figure 1: Schematic diagram of the experimental setup.

Figure 2: Picture of the RPC under test with electronics.

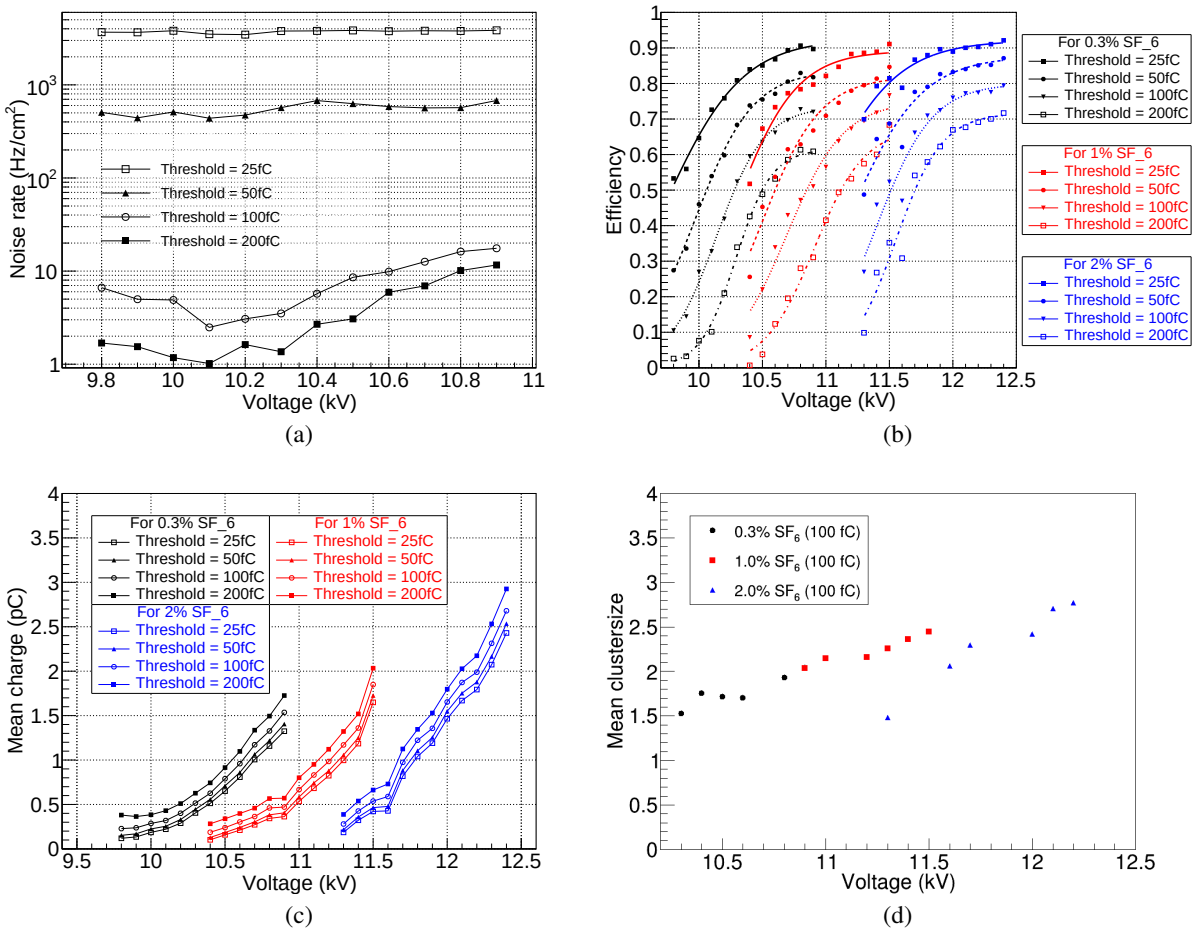

Figure 3: (a) Singles noise rate at various thresholds for 0.3% SF_6 gas mixture. (b) Efficiency at various thresholds. (c) Mean induced charge at various thresholds. (d) Average clustersize. Gas composition: r134a : i-butane : SF6 :: 93.5-95.2 (varied) : 4.5 (fixed): 0.3-2 (varied).

Results and discussion

Characteristic parameters of the RPC such as noise rate, efficiency, mean charge and clustersize are shown in Fig. 3(a-d). It can be seen from Fig. 3(a) that the pulses below a threshold of 100 fC are noise with very little variation as a function of voltage. We can reduce the noise levels by constructing a Faraday Cage around the RPC [5]. Looking at figures 3(b), 3(c) and Eq. (1), one can see that it may be possible to achieve a counting rate of $\sim 5\,\mathrm{kHz\,cm^{-2}}$ (mean induced charge $\sim$ 500 fC at 10.3 kV for 0.3 % SF_6 at 100 fC threshold) with an efficiency of 50-60%. In Fig. 3(d) the average clustersize or the average number of strips fired per muon trigger is plotted for different gas mixtures at different voltages. Looking at the plot it would be preferrable to use lower concentration of SF_6 for achieving better position resolution. The efficiency can further be improved by using a double/multigap geometry ($\sim 5-10\%$)[5], reducing the electrode thickness and better frontend electronics. We are doing further studies in these directions.

Acknowledgements

We thank S. Chandra and S. Rout for their help in assembling the RPC and data acquisition. We thank the INO-RPC group at TIFR for providing us the conductive paint, spacers and readout panels to assemble the RPC. DAE and DST, Govt. of India are acknowledged for funding. BM also acknowledges the support of J. C. Bose National Fellowship of DST.

References

[1] S. Chattopadhyay et al., eds. TDR for the CBM : Muon Chambers (MuCh), 2015, 190 S

[2] M. Mondal et al., CBM Progress Report 2018, p.63.

[3] G. Aielli et al., JINST 11 (2016) P07014.

[4] The CMS muon project: TDR, CERN-LHCC-97-032.

[5] V. K. S. Kashyap and B. Mohanty, "Noise reduction and testing of a double gap RPC", This progress report.

Gas system for the MUCH GEM detector

*L. Kochenda and P. Kravtsov**
NRC "Kurchatov Institute" PNPI, Gatchina, Russia

The primary purpose of the CBM MUCH Gas System (Fig. 1) is to provide Ar+30%CO_2 pure mixture to 0.2 m^3 MUCH detector at the correct differential pressure. The system operates nominally as a closed circuit gas system with the majority of mixture recirculation around the detector [1, 2, 3, 4] with the flow of 10 slpm (standard liters per minute) measured by FI7 flow indicator. The recirculation flow through the detector can be adjusted by the BMV2 bypass valve in the range of 0.2-2.0 slpm, measured with FT1 and FT2 flow transmitters, to exchange five detector volumes during 24 hours.

During normal operation a fresh mixture is added with the mass flow controllers MFC1, MFC2 in the range of 0.1-2 slpm. Both mass flow controllers are connected to each other as master-slave (MFC1-MFC2) to have a constant mixture content. To support the constant differential pressure measured by PT6 sensor in the range of 1-2$\pm$0.5 mbar, the control system will change the flow through the bypass loop and detector using the regulating electro valve REV1. If the differential pressure increases, the mixture flow through the compressor C3 bypass decreased by closing the REV1 valve, thus decreasing the PT6 pressure. This also slightly increases return pressure PT4 and finally main compressor outlet pressure. This leads to increasing of the exhaust mixture flow through the BPCV1. Thus the system withdraws exhaust mixture in case of differential pressure increase. Vice versa, in case of differential pressure drop, the flow through BPCV1 will be reduced by opening the bypass flow using the REV1 and PT6 pressure will be increased. The bypass valves BMV1, BMV2 and BMV3 are manually adjusted to enable the optimum flow rate through the bypass loop and the detector.

The pressure indicating switch PIS1 will operate SV8 normally open solenoid valve and compressors C1 or C2 (one is in operation, the second one is spare) to provide the interlock at low (0.5 mbar) and high (1.5 mbar) differential pressure levels upstream of the compressors in the case of REV1 failure. Two bubblers (B1 and B2) installed for additional protection of the detector from overpressure. The gas system can also operate in an open configuration for purging.

The purity and content of recirculation mixture is monitored using Carbon Dioxide, Oxygen and Humidity analyzers in three points: a fresh mixture, detector outlet and the mixture after the Purifier/Dryer. A fraction (up to 50%) of the recirculation mixture can be passed through the Purifier and Dryer to remove Oxygen and moisture. There is a possibility to check the gas purity with the analyzers after the purifier and dryer to determine their saturation. The Purifier is filled with active copper. Its operating and regenerating temperature is 493 K. Oxygen content after the Purifier/Dryer is about 2-3ppm. The Purifier regeneration is performed with Ar+5%H_2 mixture.

Dryer is filled with KA (3A) molecular sieves. Its normal operating temperature is 295 K. Water content is 3-5 ppm in Dryer's output flow at this temperature. The regeneration of the Dryer is performed at 650 K with Argon purging gas.

A distribution rack will supply two stations with the mixture using 16 capillary supply lines for the detector chambers (8 for the station 1 and 8 for the station 2). 16 return lines equipped with the bubblers (B3-18) and the pressure transmitters (PT7-22). The pressure transmitters will measure the pressure pulses from the bubblers to indicate a leak in the particular detector section.

The mixture flows through the stations can be adjusted by FI10 and FI11 flow indicators. Also, they may be stopped with the solenoid valves (SV9, SV10, SV11, SV12).

A computer driven data acquisition/control system [5, 6] monitors all of the process variables including the detector differential pressure stabilization. The computer system controls quantities, which fall outside of predefined limits, and initiates corrective action.

References

[1] L. Kotchenda *et al.*, STAR TPC Gas System. NIM **A 499** (2003) 703.

[2] L. Kotchenda *et al.*, PHENIX Muon Tracking Detector Gas System. NIM **A 578** (2007) 172.

[3] L. Kotchenda *et al.*, PHENIX TEC-TRD Detector Gas System. Preprint PNPI **2712** (2007).

[4] L. Kochenda *et al.*, CBM Progress report 2010, Darmstadt 2010, p. 31.

[5] P. Kravtsov *et al.*, CBM Progress report 2010, Darmstadt 2010, p. 32.

[6] P.Kravtsov and V.Trofimov, Multi-Channel Measuring Instrument for Slow Control Systems. Preprint PNPI-2723, Gatchina (2007).

* Kravtsov_PA@pnpi.nrcki.ru

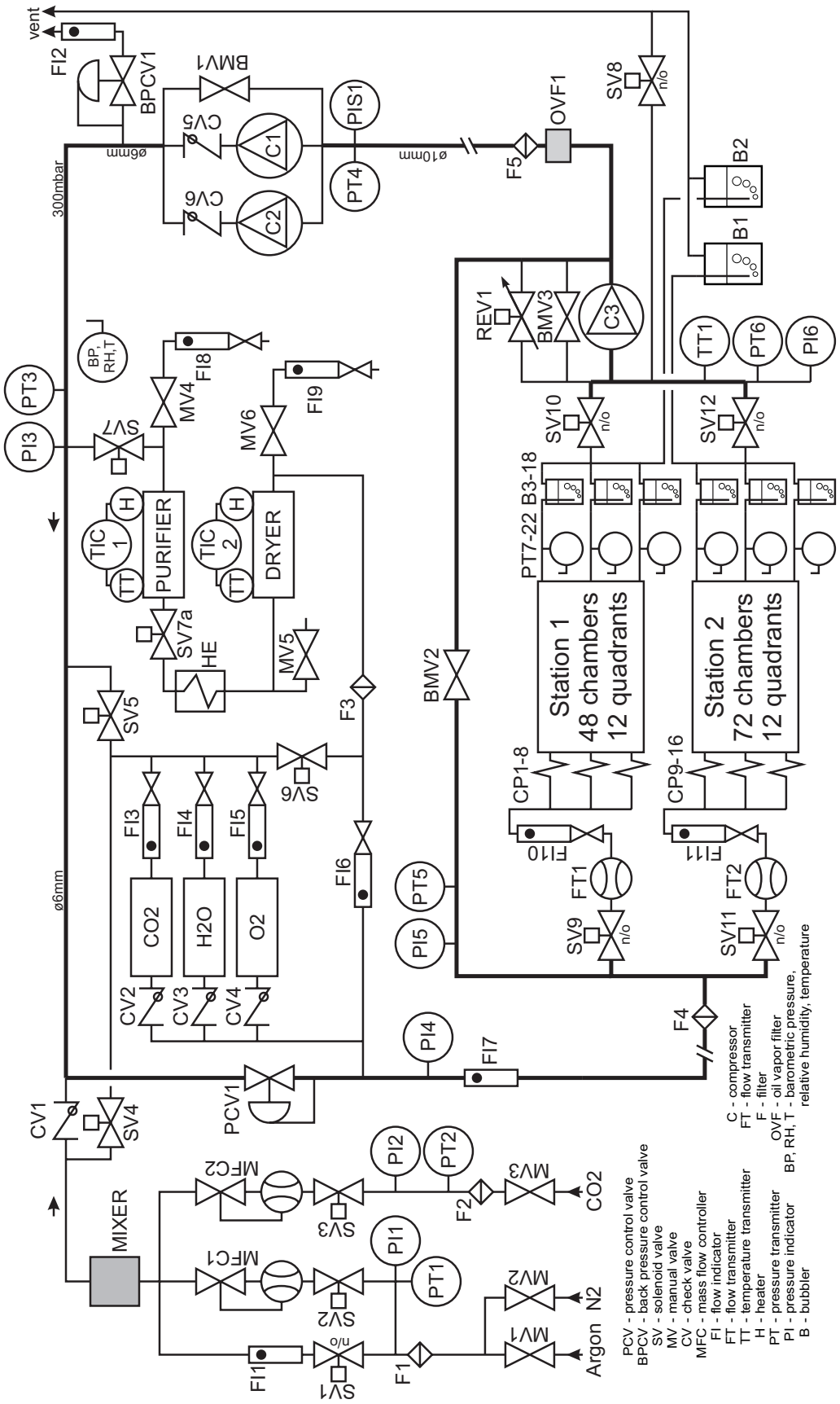

Figure 1: CBM MUCH GEM gas system diagram.

Gas system for the MUCH RPC detector

*L. Kochenda and P. Kravtsov**
NRC "Kurchatov Institute" PNPI, Gatchina, Russia

The primary purpose of the CBM MUCH RPC Gas System (Fig. 1) is to provide R134a + 4.5%iC_4H_{10} + 0.5%SF_6 mixture to the MUCH RPC detector at the correct differential pressure. The mixture content could be adjusted in the range: (88%-97%)R134a + (3%-7%)iC_4H_{10} + (0.2%-5%)SF_6. The system operates nominally as a closed circuit gas system with the majority of mixture recirculation around the detector [1, 2, 3, 4] with the flow up to 3 slpm (standard liters per minute) measured by FI9 flow indicator. The total volume of the RPC detector is 90 liters. The gas system can produce the dry mixture (0% RH) and the wet one in the range of 40-60% RH. The recirculation flow through the detector can be adjusted by the BMV2 bypass valve in the range of 50-1000 sccm (standard cubic centimeters per minute), measured with FT1 (FI10) and FT2 (FI11) flow transmitters (indicators), to exchange five detector volumes during 24 hours.

During normal operation a fresh mixture is added with the mass flow controllers MFC1, MFC2 and MFC3 in the range of 0.1-2 slpm. Three mass flow controllers are connected to each other as master (MFC1) and slaves (MFC2, MFC3) to have a constant mixture content. To support the constant differential pressure measured by PT7 sensor in the range of 5-10$\pm$0.5mbar, the control system will change the flow through the bypass loop and detector using the regulating electro valve REV1. If the differential pressure increases, the mixture flow through the compressor C3 bypass decreased by closing the REV1 valve, thus decreasing the PT7 pressure. This also slightly increases return pressure PT8 and finally main compressor outlet pressure. This leads to increasing of the exhaust mixture flow through the BPCV1. Thus the system withdraws exhaust mixture in case of differential pressure increase. Vice versa, in case of differential pressure drop, the flow through BPCV1 will be reduced by opening the bypass flow using the REV1 and PT7 pressure will be increased. The bypass valves BMV1, BMV2 and BMV3 are manually adjusted to enable the optimum flow rate through the bypass loop and the detector.

The pressure indicating switch PIS1 will operate SV15 normally open solenoid valve and compressors C1 or C2 (one is in operation, the second one is spare) to provide the interlock at low (1.0 mbar) and high (10 mbar) differential pressure levels upstream of the compressors in the case of REV1 failure. B1 and B2 bubblers installed for additional protection of the detector from overpressure. The gas system can also operate in an open configuration for purging.

The purity and content of recirculation mixture is monitored using Oxygen and Humidity analyzers in four points: fresh mixture, detector outlet, mixture after the Purifier/Dryer and the moisturizer. In the case of dry mixture production a fraction (up to 50%) of the recirculation mixture can be passed through the Purifier and Dryer to remove Oxygen and moisture. There is a possibility to check the gas purity with the analyzers after the purifier and dryer to determine their saturation. The Purifier is filled with active copper. Its operating and regenerating temperature is 493 K. Oxygen content after the Purifier/Dryer is about 2-3 ppm. The Purifier regeneration is performed with N_2+5%H_2 mixture. Dryer is filled with NaX molecular sieves. Its normal operating temperature is 295 K. Water content is 3-5 ppm in Dryer's output flow at this temperature. The regeneration of the Dryer is performed at 620 K with Nitrogen purging gas.

In the case of wet mixture production the Purifier/Dryer are not used. All recirculation mixture passes through the moisturizer. The part of mixture (up to 1000 sccm) will pass through the distribution rack and the detector.

A distribution rack will supply two stations with the mixture using sixteen capillary supply lines (CP1-CP16, eight lines per station). Sixteen return lines equipped with the bubblers (B3-B18) and the pressure transmitters (PT7-PT22). The pressure transmitters will measure the pressure pulses from the bubblers to indicate a leak in the particular quadrant.

Two mixture flows through the stations can be adjusted by FI10 and FI11 flow indicators. Also, they may be stopped with the solenoid valves (SV11, SV12, SV13, SV14). A micro compressor C3 will support the constant pressure, about 5 mbar, in the output manifold.

The gas mixture streams flowing through the bypass BMV2 and the micro compressor C3 are joined and pass through the oil vapor purifier OVF1 and HF acid purifier operated at room temperature. OVF1 is filled with the activated carbon, HF acid purifier is filled with soda lime. This purifier should be regenerated at 450 K with Nitrogen purging. All purification units are designed for continuous operation during the beamtime (2-3 months). Regeneration procedure should be planned between the experimental runs.

A computer driven data acquisition/control system [5, 6] monitors all of the process variables including MUCH RPC differential pressure stabilization. The computer system controls quantities, which fall outside of predefined limits, and initiates corrective actions.

* Kravtsov_PA@pnpi.nrcki.ru

References

[1] L. Kotchenda *et al.*, STAR TPC Gas System. NIM **A 499** (2003) 703.

[2] L. Kotchenda *et al.*, PHENIX Muon Tracking Detector Gas System. NIM **A 578** (2007) 172.

[3] L. Kotchenda *et al.*, PHENIX TEC-TRD Detector Gas System. Preprint PNPI **2712** (2007).

[4] L. Kochenda *et al.*, CBM Progress report 2010, Darmstadt 2010, p. 31.

[5] P. Kravtsov *et al.*, CBM Progress report 2010, Darmstadt 2010, p. 32.

[6] P.Kravtsov and V.Trofimov, Multi-Channel Measuring Instrument for Slow Control Systems. Preprint PNPI-2723, Gatchina (2007).

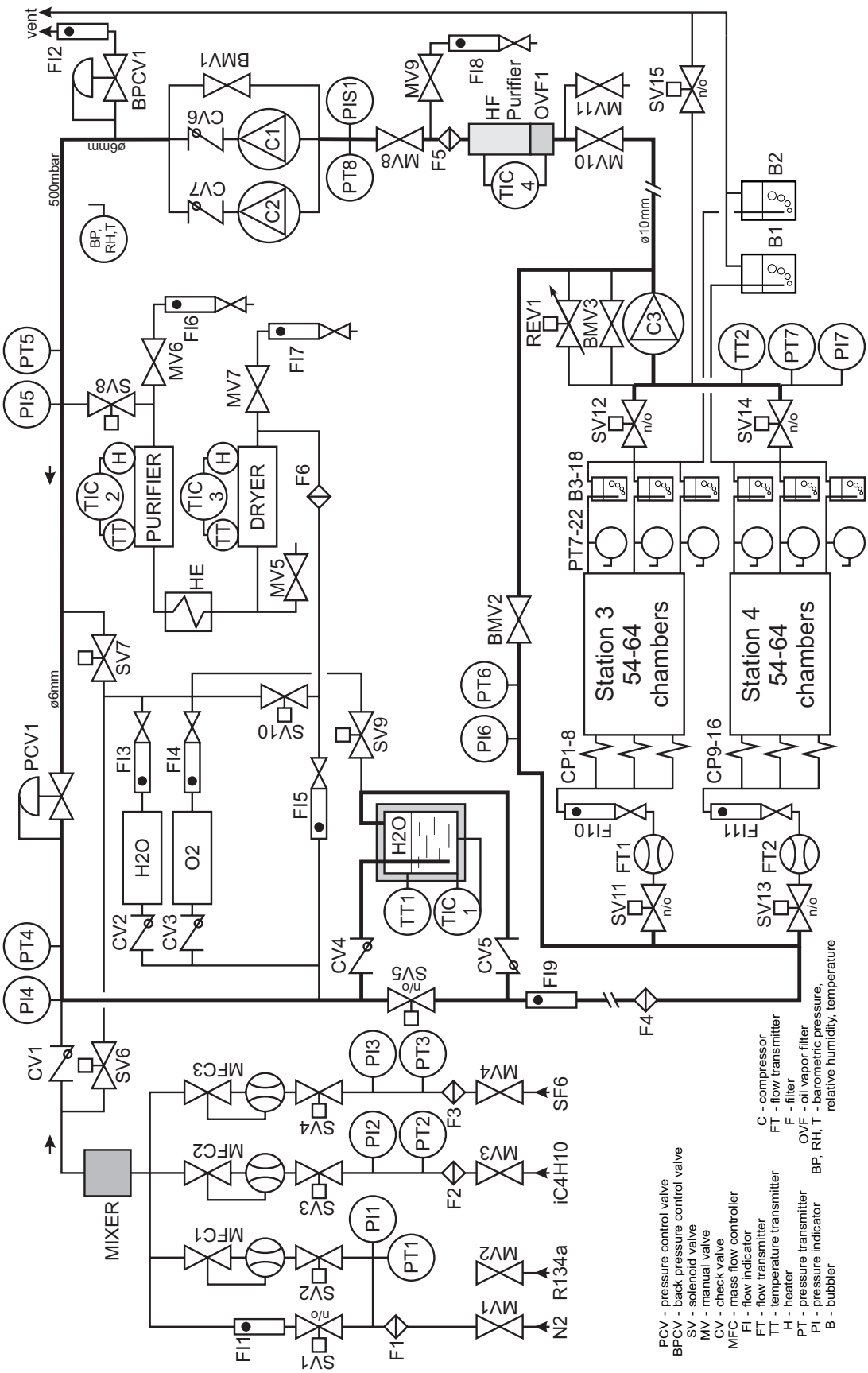

Figure 1: CBM MUCH RPC gas system diagram.

Crosstalk Study of a Low Resistive Bakelite RPC Prototype for the 3^{rd} and 4^{th} stations of CBM-MUCH

M. Mondal[*a], *J. Saini*[a], *R. Ganai*[b], *A. Sen*[c], *Z. Ahammed*[a], *and S. Chattopadhyay*[a]

[a]VECC, 1/AF, Bidhan Nagar, Kolkata, 700064, India; [b]Calcutta University, Kolkata, 700073, India; [c]Bose Institute, Salt Lake, Kolkata, 700091, India

Introduction

Resistive plate chambers (RPC) are planned to be used for the 3^{rd} and 4^{th} station of CBM-MuCh detector system. A single gap (2 mm) bakelite RPC detector of relatively lower bulk resistivity (4×10^{10} Ω-cm) has been tested using a strip readout and earlier version of STS-XYTER [1] readout at a cosmic ray setup at VECC and at the GIF++ beam test at CERN. The RPC electrodes used are same as has been used in ALICE muon trigger. The test results at GIF++ showed a larger cluster size than expected indicating higher cross-talks to the neighbouring strips. We report a series of studies performed at VECC on reduction of cluster size thereby minimising the crosstalk. Large size cluster could result from two sources, i.e., large avalanche size or crosstalk between readout strips/pads. In this work, we tried to optimize the later as for obtaining desired efficiency, avalanche size will be controlled by the required gas composition and applied voltage.

Setups of tested RPC

The RPC module was tested with two gas mixtures and various readout setup as discussed below. The variations are led by the reasons discussed later.

Gas-I Gas mixture ratio of R134a: iC_4H_{10} : SF_6 :: 95 : 4.5: 0.5. We also had a slightly different gas mixture of ratio 94:4:1, we include both these gas mixtures as Gas-I.

P1: A 10 cm $\times$ 10 cm readout panel with no ground plane and consists of pads of dimension 4 mm $\times$ 4 mm.

P2: A 30 cm $\times$ 30 cm pick up panel with 2.8 cm $\times$ 2.8 cm pads with a ground plane which was removed later. This pad size was driven by the results of simulation which showed that for optimum performance, the 3^{rd} station of CBM-MUCH RPC will require chambers of similar segmentation.

P3: A strip readout PCB of 30 cm $\times$ 30 cm size covered by 2 mm thick long strips. The reason for investigating with strips as comparison to pads has been discussed later.

Gas-II Gas mixture of R134a: iC_4H_{10} : SF_6 :: 90 : 5: 5. In this setup, P-3 readout with various configurations of strip grounding were used. This particular gas mixture was used so that the chamber could be tested in mCBM configuration where this gas mixture is available. However, it is known that SF6 plays a major role in avalanche formation and higher fraction requires higher voltage.

* m.mondal@vecc.gov.in

Results

In this study conducted at VECC, various options have been tried to reduce the noise to lower the threshold and operate the chamber at low gain and high rate. The requirement of lowering the gain is extremely important for running the system with a self-trigger electronics like STS-XYTER which is highly prone to noise. The main focus was to achieve optimum grounding scheme for reduction of noise. A low pass filter was also tried before the high voltage connection in RPC to block the AC noise. To reduce EMI noise, the chamber was kept in a closed Copper box. A common grounding scheme between the electronics, the shielding copper box and the readout plane has been implemented. A scheme was used where the ground plane was well separated from the signal plane thereby reducing the capacitance. As a result of all these efforts, the threshold could be reduced to 18 fC as opposed to 50 fC used at GIF++. In the results presented below, we have tried to operate the chamber at such a voltage so as to achieve 85% or higher efficiency for cosmic ray detection. Fig. 1 shows a typical distribution of cluster size for P-1 readout panel for the chamber operating at 9.6 kV, in which the mean goes upto 15 pads.

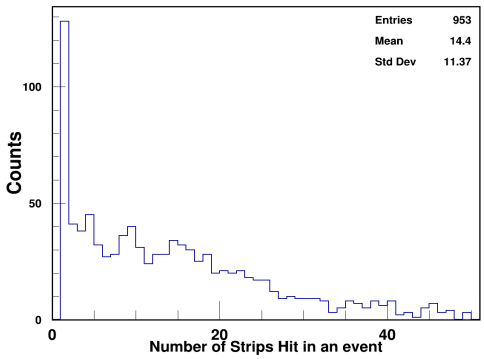

Figure 1: Cluster Size of RPC at 9.6 kV with P-1 Readout Panel.

Gas-I

P-1: For 4 mm $\times$ 4 mm pads, at 9.6 KV giving $\sim 86\%$ efficiency, mean cluster size is 15 pads thereby containing the cluster on an average in an area of 4 cm $\times$ 4 cm. It is evident that change in HV affects both the efficiency and cluster size as shown in Fig. 2 which shows a cluster size of 10 pads for an efficiency of 70%.

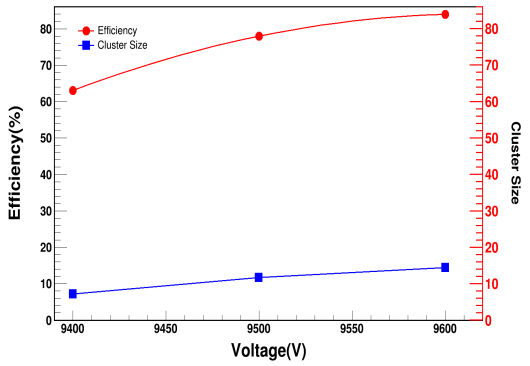

Figure 2: Variation of Efficiency and Cluster size with in voltage for Gas-I, P-1 Readout Panel (Threshold : 18 fC, 0.5 % SF_6).

P-2: In this case of larger pad size (2.8cm $\times$ 2.8 cm), reduction of noise allows a threshold of 6 fC. This has led to achieving an efficiency of 92.6% at 9.4 kV. Higher efficiency at similar voltage might be due to lowering the threshold. In this configuration, the cluster size obtained was of 14 pads thereby giving an even larger cluster of 14 cm $\times$ 14 cm size. Interestingly, for P-1 and P2 at similar voltages and both having pad geometry albeit different dimensions give almost similar cluster size in units of pads. This leads to a suggestion that the crosstalk might be dominated by the number of edges in the readout pad and not of actual size of the readout unit. We then decided to study a configuration of readout units of even smaller dimension i.e. smaller than 4 mm as was used in P-1. In that case, investigations with strips in place of pads might be more helpful as these small pads will lead to increase in the number of readout channels. We have therefore built a strip-based readout plane with strip width of 2 mm. In addition to the above, the connections of the nearby pads on the readout plane might not necessarily be the consecutive channels resulting in a pad further away to be affected by crosstalk. Strip readout might eliminate this possibility.

P-3 This setup was tested with 1% SF6. Based on pad-based studies mentioned earlier, the expectation is to have cluster contained in about 14 strips of P-3. Driven by such an expectation, we report here the results of P-3 in which two consecutive strips on both sides of a set of 13 strips have been grounded. This will hopefully confine the cluster within 13 strips unless it spreads even more further than two grounded strips.This configuration showed $\sim$ 85 % efficiency at 10 kV with a mean cluster size of $\sim$ 15 thereby spreading the cluster further than 3 cm. This result indicates the direction towards confinement of crosstalk driven by number of readout units rather than size of the units.

We have also grounded the effect of grounding the consecutive strips thereby also increasing the dead area under the trigger scintillator. The results remains inconclusive and requires further study. We plan to work on this Case-I, P-3 configuration in more detail.

Gas-II

We have studied the performance of the chamber using Gas-II mixture only with P-3 configuration. It should be noted that due to higher fraction of SF6, the voltage to be applied is higher for this gas mixture. For this configuration, threshold set was at 17-18 fC. We have got an efficiency of $\sim$ 81 % efficiency at 11.2 kV and a cluster size of 20 strips. This shows the spread of crosstalk horizontally up to 4 cm.

We wanted to study the effect of grounding strips which is expected to reduce crosstalk. We first tested by grounding the alternate signal strips. Even though it reduces the cross talk to 7 signal strips, however the efficiency reduces to 35 % mainly due to dead space introduced by the grounded strips. By increasing voltage, efficiency increases upto 88 % by making the cluster size upto 15 strips which effectively means very big clusters of upto 30 strips. It s therefore required to optimize the system with lower voltage and a better grounding scheme.

Summary

Different readout plane configurations have been tested with STS-XYTER ASIC to reduce the cluster size from a single-gap low resistivity bakelite chamber. Pad and strip geometries of different dimensions have been tested with cosmic rays using two types of gas mixture ratio. About 1% SF6 gives about 15 readout units (pad or strip) to attain an efficiency above 85%. The cluster size increases with increase in SF6 fraction at higher applied voltage. Preliminary results suggests cluster size to depend on the number of readout units and not on actual size. Further study is planned to obtain robust results and to finalise the configuration.

References

[1] Rafal Kleczek, *Analog front-end design of the STS/MUCH-XYTER2—full size prototype ASIC for the CBM experiment*, JINST **12** (2017) C01053.

[2] M. Capeans et al, *Systematic Study of RPC performances in polluted or varying gas mixtures compositions: an online monitor system for the RPC gas mixture at LHC*, CERN PH-EP-Tech-Note-2012-002.

Evolution of First Absorber in Muon Chamber

O. Singh[1], P. P. Bhaduri[2], E. Nandy[2], S. Chatterjee[3], S. Chattopadhyay[2], A. Senger[4], V. Nikulin[5], and N. Ahmad[1]

[1]Aligarh Muslim University, Aligarh, India; [2]Variable Energy Cyclotron Centre, Kolkata, India; [3]Department of Physics(CAPSS), Bose Institute, Kolkata, India; [4]GSI, Dharmstadt, Germany; [5]PNPI, Russia

The optimized design of the muon chamber (MuCh) detector system, for measurement of low mass vector meson (lmvm) at SIS100 energies, consists of four absorbers and four stations. Each station is a triplet of three detector chambers placed between two consecutive absorbers, to facilitate tracking and momentum dependent muon identification. The first MuCh absorber is placed inside the dipole magnet. It has a thickness of 60 cm and is made up of graphite to reduce the combinatorial background resulting from reconstructed mismatched tracks due to multiple scattering. Formerly, in muon simulation studies, the density of graphite was set equal to that of pure carbon, ρ = 2.26 gm/cm^3. However subsequently it has been realized that high density pure carbon is not available in bulk, making the design of the first MuCh absorber unfeasibility. Extensive simulations have been performed to look for alternative configurations of the first absorber. The basic constraint has been to look for materials which are cheap, available in bulk and at the same time restore the physics performance of the system in terms of di-muon detection. To ensure the later absorber materials are chosen such that the corresponding hadronic interaction length becomes equivalent to that of 60 cm high density graphite. After several iterations, it is finally decided to to use a composite structure of the first absorber with 30 cm low density carbon (ρ = 1.7 gm/cm^3) and 30 cm of Concrete (ρ = 2.3 gm/cm^3). This preferred choice keeps the physical thickness of the first absorber same as earlier and thereby keeps the overall design of the detector system unaltered. The old and new configuration of the first absorber are shown in Figure 1. The hadronic interaction length is though reduced due to low density carbon ($\lambda \propto \rho$). Concrete with advantage of technological and activation points of view has same density as that of high density carbon. However owing to less radiation lengths, the amount of multiple scattering (smaller radiation length leads to larger multiple scattering as they are anti-correlated) will be higher. For quantitative estimation of MuCh performance, with this new composite absorber, simulations are performed for central Au+Au collision at 8A GeV beam energy. Apart from the new geometry of the first absorber, some other changes are also incorporated during transport. To reduce the secondary electrons produced in the beam pipe, additional shielding (below the absorbers) are used around the beam pipe. In the old geometry, lead (Pb) is used as shielding material below the first absorber whereas, iron shielding is used for the rest of the absorbers. The opening angle of the hole in the shielding is 2.9 deg for all absorbers. In the new geometry, to reduce activation, 30 cm aluminum (Al) and 30 cm lead (Pb) is used for shielding below the first absorber and Al for the rest, in accordance latest design of beam pipe shields. The opening angle of the hole in the shielding is reduce to 2.5 deg for the first absorber.

Figure 1: First absorber of Muon Chamber. Left panel: 60 cm high density carbon (ρ = 2.26 gm/cm^3). Right panel: 30 cm low density carbon (ρ = 1.7 gm/cm^3) + 30 cm concrete (ρ = 2.3 gm/cm^3).

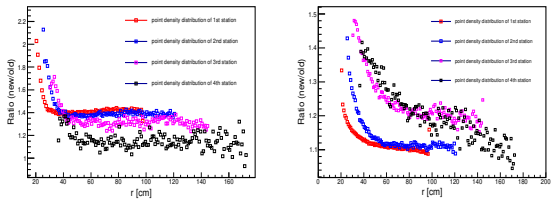

Figure 2: Radial distribution of MC point density on different MuCh stations for incident primary particles (left panel) and secondary tracks (right panel). For direct comparison, ratio of the point densities for new and old geometries are plotted.

To investigate the immediate effect on the performance of the muon detector chambers, we have first studied the radial distribution MC point density at all MuCh stations after the first absorber. Evaluation of particle densities is essential for calculation of particle rates on the detector chamber planes. To facilitate the comparison between the old and new geometry configurations, Figure 2 shows the ratio (new/old) of radial distribution of MC point density, separately for primary and secondary particles averaged over all the three layers for each station. An enhancement in point densities is observed for both primary and secondary particles in all muon stations, which could be attributed to the reduced absorption of the produced particles in the first absorber.

To study the feasibility of di-muon detection with new absorber design, we choose $\omega \rightarrow \mu^+\mu^-$ as our di-muon signal. The invariant mass spectrum for the ω signal and the combinatorial background for both geometries are cal-

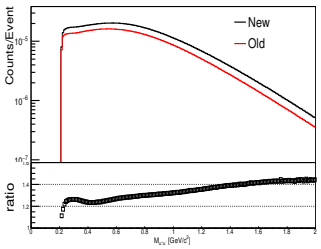

Figure 3: Di-muon invariant mass spectra of the combinatorial background for central Au+Au collision at 8A GeV with different configurations of first absorber.

culated. The standard di-muon analysis software within CbmRoot framework is employed for this purpose. For the analysis, a set of track quality cuts is applied to the reconstructed global tracks to identify the muon track candidates. A global track is selected if the associated STS hits ≥ 7, MUCH hits ≥ 11, $\chi^2_{Vertex} \leq 3.0$, $\chi^2_{STS} \leq 2.0$ and $\chi^2_{MUCH} \leq 3.0$. In addition, the di-muon combinatorial background is further reduced via application a 2σ cut in the plane mass-squared versus momentum provided by TOF detector. The invariant mass spectrum for the combinatorial background for both the geometries are shown in Figure 3. The corresponding values of pair reconstruction efficiency (ϵ_ω) and signal-to-background (S/B) ratio are calculated within a $\pm 2\sigma$ window around the signal mass peak and given in table 1. As evident from Figure 3, the combinatorial background increases in the new absorber by factor of 1.2-1.4, due to reduction in effective hadronic interaction length. The performance is around 8% worse in case of new absorber configuration (see significance ratio in table 1). Since the reduction in performance with this new absorber design is within 10%, as well as the particle rates on the chamber planes are within the acceptable limits, it has been decided to select the realistic new design as the latest MuCh configuration. The corresponding geometry file prepared in ROOT format is already committed to the repository with a tag version of `v_19c`.

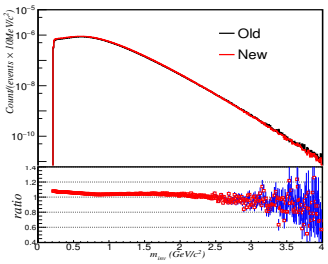

Figure 4: Di-muon invariant mass spectra of the combinatorial background for central Au+Au collision at 8A GeV with different configurations of the first absorber.

Geometry	Efficiency ω , %	S/B	Significance Ratio(w.r.t old)
`old`	1.11	0.229	1.0
`new`	1.13	0.189	0.92

Table 1: Reconstruction efficiency and signal-to-background ratio for ω meson in central Au+Au collision at 8A GeV for different first absorber configurations.

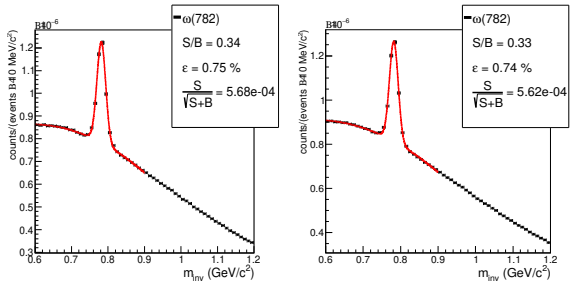

Figure 5: The di-muon invariant mass spectra of ω mesons in 8A GeV central Au+Au collision, for different configurations of graphite absorber: (left) 30 cm thick low density graphite and (right) 28 cm thick moderate density graphite.

In the meanwhile, extensive market survey of existing graphite samples indicates the availability of carbon blocks with slightly higher density of 1.78 gm/cm^3. In order to keep the hadronic interaction length same as that of 30 cm low density carbon, the equivalent physical thickness of this moderate density carbon block becomes 28 cm. This would lead to an additional 2 cm gap between the first two MuCh absorbers, which can be useful for MuCh service works for the detector chambers. To the study the effect on the MuCh performance, simulations have been performed with the reduced physical thickness of first absorber, made up of 28 cm block of carbon of density ρ = 1.78 gm/cm^3 and 30 cm block of concrete of density ρ = 2.3 gm/cm^3. The radial distribution of point density for primary and secondary particles are calculated. The new configuration with reduced absorber thickness has no additional effects on the point density for both primary and secondary particles. The reconstructed di-muon invariant mass spectra for ω signal and combinatorial background is calculated with the following the same analysis strategy as described before. Figure 4 shows the invariant mass spectra for the combinatorial background for two different physical thicknesses of the first absorber. The ratio of the two histograms is close to 1 which implies that there is no effective change in combinatorial background with the reduced physical thickness of the graphite absorber. The reconstructed invariant mass spectra in the ω mass (signal + background) region, is plotted in Figure 5. The corresponding values of pair reconstruction efficiency (ϵ_ω (%)), S/B and significance are calculated within a $\pm 2\sigma$ window around the signal peak and listed in dialog boxes. No significant change is observed in physics performance results.

Effect of absorbers surface tolerance on the Muon Chamber (MuCh) performance for the CBM experiment at FAIR

S. Chatterjee[*1], *O. Singh*[2], *P. P. Bhaduri*[3], *S. Chattopadhyay*[3], *A. Senger*[4], *and V. Nikulin*[5]

[1]Department of Physics, Bose Institute, Kolkata, India; [2]Aligarh Muslim University, Aligarh, India; [3]Variable Energy Cyclotron Centre, Kolkata, India; [4]GSI, Darmstadt, Germany; [5]PNPI, Russia

One of the major goals of the Compressed Baryonic Matter (CBM) experiment at FAIR accelerator complex in Darmstadt, is the measurement of di-muons ($\mu^+\mu^-$). The optimized design of the Muon Chamber (MuCh) detector system for identifying muons from the decay of low mass vector mesons (lmvm) (eg: ρ, ω, ϕ), at SIS100 energies, consists of one absorber made of 30 cm low-density graphite ($\rho = 1.7$ g/cm^3) and 30 cm concrete and three iron absorbers with thickness 20, 20, and 30 cm, and triplets of tracking detectors called stations behind each absorber layer. To cope up with the high particle density, Gas Electron Multiplier (GEM) detector will be used in the first two stations of the MuCh system. The particle density in stations 3 and 4 decreases substantially due to the absorbers, and detectors with low rate capability could be used. Our plan is to use low granularity Resistive Plate Chamber (RPC) detectors in the last two stations of the MuCh system. Accordingly, simulations have been performed with GEM-like detectors in stations 1 and 2 and RPC-like detectors in stations 3 and 4 [1]. The detector modules in each layer are trapezoidal in shape for both detector types. The readout pads are arranged in a r-ϕ geometry, where $\Delta\phi$ is 1 degree for the first two stations and $\Delta\phi$ is 5 degree and 6 degree respectively for stations 3 and 4, such that the radial size increasing with the radius. The simulated MuCh geometry is shown in Fig. 1. To account for the realistic material budget, 35 micron Copper and 3 mm G10 sheets are inserted on both sides of the active volume (3 mm Argon gas for GEM-like detectors and 2 mm RPC gas [1] for RPC-like detectors) of the detector chambers of all the stations. In addition, 1 cm thick aluminium plates are used to provide chamber support and required cooling to the detector electronics [2].

Recent investigations on MuCh mechanics revealed that it is difficult to attain uniform surface smoothness over the entire volume of the iron absorbers, which might affect the detector performance. Thus it is necessary to investigate the effect of surface tolerance of the absorber blocks on the overall di-muon reconstruction performance of the muon system. As a first step, four different geometry configurations have been considered where the thickness of the 2^{nd}, 3^{rd}, and 4^{th} absorber is varied. The thickness of the absorbers used in the simulation is the following, 60 cm - 20 cm - 20 cm - 30 cm (reference configuration), 60 cm - 19 cm - 19 cm - 29 cm, 60 cm - 18 cm - 18 cm - 28 cm and 60 cm - 17 cm - 17 cm - 27 cm. The overall thickness of iron absorbers is reduced by 3 cm in each step. The reconstruction of the omega mesons, in central Au+Au collision at 8 AGeV beam energy, is used for the comparison of different absorber configurations. The phase space decay of $\omega \rightarrow \mu^+\mu^-$ is simulated using the PLUTO event generator. The signal muon pairs are embedded into the background, generated using the UrQMD event generator. One ω ($\omega \rightarrow \mu^+\mu^-$) from PLUTO is embedded per event into the background. All the particles are transported through the entire CBM setup using GEANT3 transport engine.

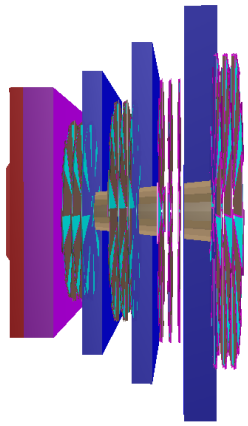

Figure 1: The optimized MuCh geometry. It consists of four absorbers and four detector stations. 1^{st} absorber is made up of 30 cm carbon (red part) and 30 cm concrete (purple). The rest of the absorbers are made up of iron (blue). GEM-like detectors are used in the first two stations and RPC like detectors are used in the last two stations. Detector modules are trapezoidal and arranged on the front and backside of the aluminium support structure.

The radial distribution of MuCh point density (number of Monte Carlo points per unit area per event), for primary and secondary particles, are shown in Fig. 2. As expected, no change is seen for station 1, as the thickness of the first absorber is kept fixed. For the rest of the stations, particle density monotonically increases with decreasing absorber thickness of the absorbers, for both the primary and secondary particles, due to reduced absorption. Around 30% increase in the primary and 50% increase in the secondary are observed when changing the absorber thickness from 60 cm - 20 cm - 20 cm - 30 cm to 60 cm - 17 cm - 17 cm - 27 cm. A similar trend is seen for the radial distribution of occupancy (fraction of fired pads) of stations 2, 3 and 4.

Finally, to test the effect on the signal reconstruction due

* sayakchatterjee@jcbose.ac.in

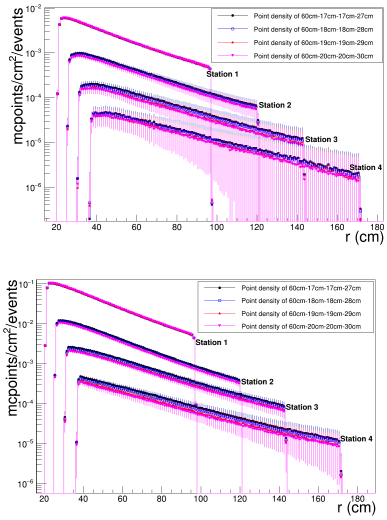

Figure 2: Radial distribution of MuCh point density of primary (top) and secondary (bottom) MC tracks for all four MuCh stations and for all the different absorber configurations.

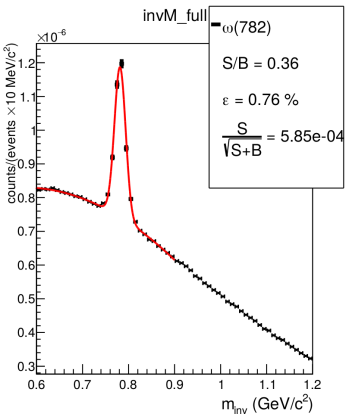

Figure 3: Invariant mass distribution with 60 cm-20 cm-20 cm-30 cm absorber configuration. One ω has been embedded per event.

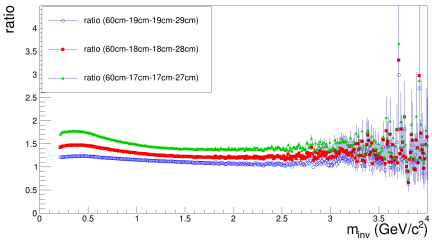

Figure 4: Ratio of combinatorial background with respect to 60 cm-20 cm-20 cm-30 cm absorber configuration.

MUCH geometry Configuration	ϵ_ω (%)	**S/B**	**Significance** $(S/\sqrt{(S+B)})$
60-20-20-30 cm	0.76	0.36	5.85×10^{-4}
60-19-19-29 cm	0.78	0.33	5.73×10^{-4}
60-18-18-28 cm	0.80	0.29	5.53×10^{-4}
60-17-17-27 cm	0.81	0.26	5.30×10^{-4}

Table 1: Reconstruction efficiency and Signal-to-background ratio for ω in central Au+Au collision at 8A GeV for different geometry configurations.

to surface tolerance, invariant mass spectra are calculated for all the four different geometry configurations, after full simulation and reconstruction. The latest muon software as available within the CbmRoot framework (CBMROOT TRUNK, Revision no. 15516), has been used for the analysis. A set of single track quality cuts are applied to the reconstructed global tracks to identify the muon track candidates. Reconstructed global tracks having associated STS hits ≥ 7, MUCH hits ≥ 10, TRD hits ≥ 1, $\chi^2_{Vertex} \leq 2.5$, $\chi^2_{STS} \leq 2.0$ and $\chi^2_{MUCH} \leq 2.8$ are selected as valid muon track candidate. The contribution of non-muonic tracks can be further reduced by applying 2σ cut on the reconstructed TOF mass. The signal is extracted from the embedded set of events by selecting oppositely charged muon candidate tracks on the event by event basis. The background is calculated using super event (SE) technique, where one muon candidate track is combined with all the other oppositely charged muon candidate tracks to calculate the combinatorial background. The invariant mass distribution of the reconstructed ω mesons along with the combinatorial background, for the nominal absorber configuration (60 cm-20 cm-20 cm-30 cm), is shown in Fig. 3. The pair reconstruction efficiency (ϵ_ω), signal-to-background ratio (S/B) and significance $(S/\sqrt{S+B})$, for all four different absorber configurations, are given in Table 1. As evident from the table, with decreasing absorber thickness, the pair reconstruction efficiency increases because of the less absorption of the signal muons but S/B decreases due to an increase in the background. Finally to study the effect of reduced absorber thickness over the full di-muon spectrum, in Fig. 4, the ratio of the combinatorial background over the entire di-muon mass range, for all the geometries to the reference geometry is displayed. In the low mass region ($m_{inv} \leq$0.5 GeV/c^2), sizeable enhancement is observed in the ratio and that may be due to the decay of pions since the air gap increases with decreasing the absorber thickness.

In summary, our studies reveal that reduction of the thickness of the iron absorbers, of the order of a few centimeters, would degrade the performance of di-muon measurements at SIS-100 energies. A surface tolerance of the order of a few millimeters might preserve the feasibility of di-muon detection.

References

[1] E. Nandy *et al.*, CBM Progress Report 2018.

[2] O. Singh *et al.*, CBM Progress Report 2018.

Effect of gaps on the fifth absorber of Muon Chamber (MuCh) for the CBM experiment at FAIR

S. Chatterjee[*1], *O. Singh*[2], *P. P. Bhaduri*[3], *S. Chattopadhyay*[3], *and V. Nikulin*[4]

[1]Department of Physics, Bose Institute, Kolkata, India; [2]Aligarh Muslim University, Aligarh, India; [3]Variable Energy Cyclotron Centre, Kolkata, India; [4]PNPI, Russia

One of the major goals of the Muon Chamber (MuCh) detector system at the CBM experiment at FAIR SIS100, is the detection J/ψ mesons in di-muon decay channel, in $p + A$ and $A + A$ collisions. MuCh is designed to have segmented absorber blocks and tracking stations placed in between two consecutive absorber blocks. For studying the low and intermediate mass region of the di-muon spectrum, four absorber and four detector stations will be used. The thickness of the absorber layers is 60 cm, 20 cm, 20 cm and 30 cm respectively where the first absorber is made up of 30 cm low-density carbon (1.7 g/cc) and 30 cm of concrete and the rest of the absorbers are made up of iron. For the J/ψ detection, an additional 100 cm absorber will be used at the end of the 4^{th} station. Hits after this thick absorber will be collected by transition radiation detector (TRD), which will be used as the trigger detector for J/ψ measurements.

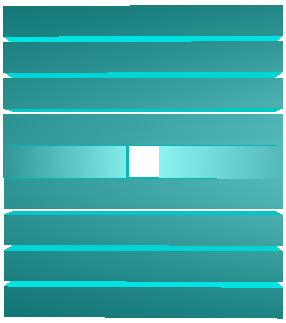

Figure 1: The 5^{th} MuCh absorber, made up of *cast iron*. The entire physical volume is divided into ten (10) blocks, out of which eight (8) blocks are of dimension 500×55×100 cm^3 and the two (2) opening blocks are of dimension 220×60×100 cm^3. The separation between the two successive absorber blocks is kept large for visibility.

In this report, our latest simulations corresponding to the realistic design of the MuCh fifth absorber is reported. The design dimension of the 5^{th} absorber is 500×500×100 cm^3 with an opening block of dimension 60×60×100 cm^3 for the beam pipe. Investigations related to MuCh mechanics revealed that due to the large volume of the absorber, it is very difficult to produce a monolithic iron block of the said dimension. As a viable alternative, two different geometry variants are considered for the MuCh 5^{th} absorber namely *cast iron* and *rolled iron* configuration. In the cast iron configuration, the entire absorber is made up of ten (10) iron blocks. Among the ten (10) blocks, eight (8) blocks are of dimension 500×55×100 cm^3 and the remaining two (2) opening blocks are of dimension 220×60×100 cm^3. In Fig. 1, a schematic view of the absorber geometry for the cast iron configuration is shown.

In the *rolled iron* configuration, the entire absorber volume is made up of fifty (50) iron blocks. Among these fifty (50) blocks, forty-four (44) blocks are of dimension 500×10×100 cm^3 and the rest six (6) blocks are of dimension 220×10×100 cm^3. In Fig. 2, the schematic view of the absorber plate with *rolled iron* configuration is shown.

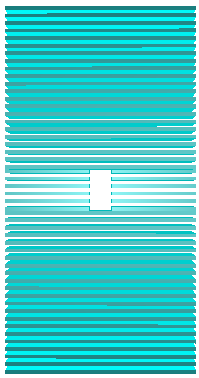

Figure 2: The 5^{th} MuCh absorber, made up of *rolled iron* configuration. The entire volume is divided into fifty (50) blocks, out of which forty four (44) blocks are of dimension 500×10×100 cm^3 and remaining six (6) opening blocks are of dimension 220×10×100 cm^3. The separation between the absorber blocks is kept large for visibility.

In both cases, the opening block of dimension 60×60×100 cm^3 along with an aluminium shielding is used with a 50 cm diameter hole for the beam pipe. A 3 mm gap is maintained throughout the simulation between the aluminium shielding and iron blocks to make the system more realistic. Due to the surface finishing, there may have some gaps between the iron blocks and that several gaps in between the absorber blocks are simulated with realistic MuCh set up including the 5^{th} absorber.

To investigate the effect of modular absorber design on the physics performance of the muon system $J/\psi \rightarrow$

* sayakchatterjee@jcbose.ac.in

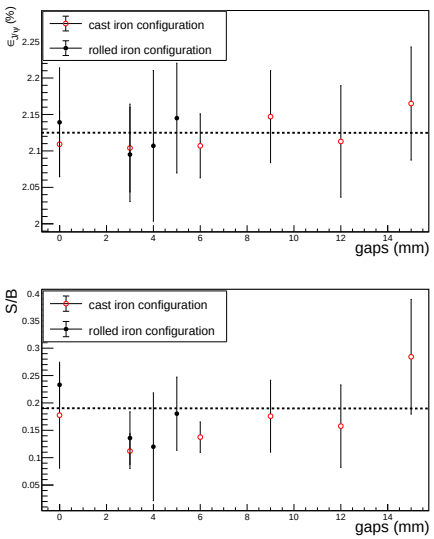

Figure 3: Variation of pair reconstruction efficiency (top) & signal to background ratio (bottom) with different geometry configuration and the gaps between the absorber blocks.

5^{th} **absorber configuration**	**Gaps b/w blocks (mm)**	$\epsilon_{J/\psi}$ (%)	**S/B**
cast iron	0.0	2.11(±0.04)	0.177(±0.10)
cast iron	3.0	2.10(±0.06)	0.112(±0.03)
cast iron	6.0	2.11(±0.04)	0.138(±0.03)
cast iron	9.0	2.15(±0.06)	0.179(±0.07)
cast iron	12.0	2.11(±0.08)	0.158(±0.08)
cast iron	15.0	2.16(±0.08)	0.284(±0.11)
rolled iron	0.0	2.14(±0.08)	0.233(±0.04)
rolled iron	3.0	2.10(±0.06)	0.136(±0.05)
rolled iron	4.0	2.11(±0.10)	0.120(±0.10)
rolled iron	5.0	2.14(±0.08)	0.180(±0.07)

Table 1: Reconstruction efficiency and Signal-to-background ratio for J/ψ in central Au+Au collision at 10 AGeV for different geometry configurations.

$\mu^+\mu^-$ is chosen as the di-muon signal. The updated muon software as available within the CbmRoot framework (CBMROOT TRUNK, Revision no. 15516), is employed to estimate the pair reconstruction efficiency ($\epsilon_{J/\psi}$ (%)) and signal to background ratio (S/B) in 10 AGeV central Au+Au collision, for different gaps between the absorber blocks. For each configuration, a total of 10^5 events are simulated. A set of track quality cuts are applied to the reconstructed global tracks to identify the muon track candidates. Reconstructed global tracks having associated STS hits $\geq$ 6, MUCH hits $\geq$ 10, TRD hits $\geq$ 3, TOF hits $\geq$ 1, $\chi^2_{Vertex} \leq 3.0$, $\chi^2_{STS} \leq 2.0$, $\chi^2_{TRD} \leq 3.5$ and $\chi^2_{MUCH} \leq 3.5$ are selected as valid muon track candidate, originating from the decay of J/ψ. The signal is extracted from the embedded set of events using the Monte Carlo (MC) information (mcpdg = ± 13 & GeantProcessId = KPPrimary). The variation in $\epsilon_{J/\psi}$ and S/B, due to different gap configurations are shown in Fig. 3 and respective values are tabulated in Table 1. Due to less statistics, the error bars are large and that is why it is difficult to conclude the effect of gaps on the pair reconstruction efficiency and S/B values. Work is under progress to simulate higher statistics, to reduce the statistical uncertainty and stabilize the obtained results.

References

[1] E. Nandy *et al.*, CBM Progress Report 2018.

[2] O. Singh *et al.* , CBM progress report 2018.

Automatized noise separation technique for mMUCH data

S. Roy[1] *and V. Singhal*[2]

[1]Department of Physics(CAPSS), Bose Institute, Kolkata, India; [2]Homi Bhabha National Institute, Variable Energy Cyclotron Centre, Kolkata, India

The primary aim of mCBM, a FAIR Phase-0 experiment at the SIS18 facility of GSI, is to develop, commission and to optimize the performance of the detector subsystems including the software chain and preparation of offline and online data analysis platform. Due to very sensitive self-triggered electronics high noise is a major problem in the data analysis therefore identifying and removal of the noise due to noisy channels is the first step towards time offsets correction between subsystems and then event building. This report is on development of an automatized technique to find out noisy channels in general for fixed target experiment and specific to mMUCH setup. mMUCH is comprised of 2 Gas Electron Multiplier (GEM) trapezoidal shaped modules in mCBM with around 2000 readout pads (channels) [1]. The spill structure or digi (hits) count rate with function of time obtained from the mMUCH in Figure 1(a) gives an insight of the volume of noise in data, as there is an observable baseline which is basically due to noisy channels of the detector's readout Front-End Electronics (FEB). In an ideal scenario the count rate baseline should be zero or in other words the detector should give no counts during off-spill. One method to identify good channels is to simply apply a threshold in the count rate from each channel during off-spill, such that when there is no beam, this count should be of order of zero. The count rate in channels vary with detector voltages and other electronic parameters that are subject to fluctuations and vary run to run. The main challenge is determining the threshold and it needs precise human intervention otherwise incorrect threshold may filter out a channel that is good and may lead to loss in data. To automatize the process of distinguishing noisy channels from good channels, two functions $f_1(x,y)$ and $f_2(x,y)$ where x and y are on-spill and off-spill counts respectively, has been used. This is done by comparing the channel count rates during off-spill as well as during on-spill. By selecting a cut in this ratio, we can separate noisy and good channels. To make the selection cut universal and run independent we took the normalised ratio:

$$ratio_{norm} = \frac{onspill\ count\ rate - offspill\ count\ rate}{onspill\ count\ rate + offspill\ count\ rate} \quad (1)$$

the value of this ratio will always be $\sim$1 for good channels and $\sim$0 for noisy channels which is shown in Figure 1(b).

Figure 2(a) is a 2D representation of the method in discriminating noisy channels. To make more precise similar ratio function of on-spill ADC and off-spill ADC value has been calculated for each channel. Figure 2(b) shows the average ADC values during on-spill and off-spill vs $ratio_{norm}$. This has also been considered for identifying true noisy channels. For instance we are using a cut like 0.6 in the $ratio_{norm}$ to mask the noisy channels.

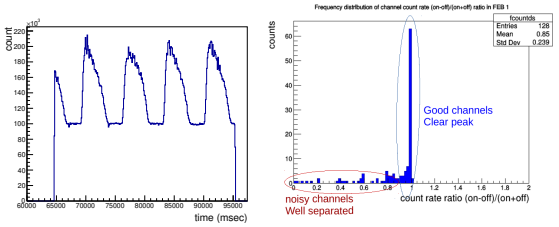

Figure 1: (a) Left: Spill structure of GEM1 (Run 143) (b) Right: Normalise ratio distribution of all channels

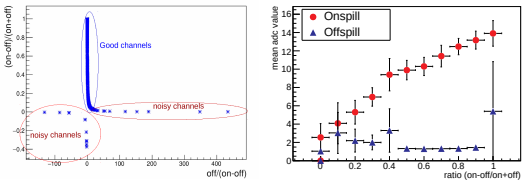

Figure 2: (a) Left: 2D plot representation of noisy channels separation method, (b) Right: Average ADC of the channels vs $ratio_{norm}$ during on-spill and off-spill

The discussed technique is used for March 2019, November 2019 and March 2020 mCBM beamtime data analysis and could successfully find out the noisy channels. The on-spill and off-spill regions in the data is determined using a cut in T0 (trigger) digis. It has been verified that the method works independent of detector biasing voltage. An automatized noisy channel detection method has been developed for the mMUCH detector and used for mCBM experiment data analysis. The same can be used for other subsystems where noisy channel is a big issue for identifying the signal. We are working on building algorithm to automatically select the cuts on T0 digis to define on-spill and off-spill timeslices which is input for the method.

We are thankful to Dr. S. Chattopadhyay, Mr J. Saini and Dr. A. K. Dubey for their valuable suggestions in this work. We would also like to thank Mr. A. Kumar, VECC and Mr. A. Seal for their help.

References

[1] A. Kumar *et al., Installation, commissioning and testing of mMUCH modules in the mCBM experiment, CBM Progress Report 2018*

Performance study of the first two stations of CBM MuCh cooling system

Sumit Kumar Kundu[*1], *Susnata Seth*[2], *Sidharth Kumar Prasad*[2], *Supriya Das*[2], *Sanjay Kumar Ghosh*[2], *Sibaji Raha*[2], *and Ankhi Roy*[1]

[1]Discipline of Physics, IIT Indore, Khandwa Road, Indore - 453552, Madhya Pradesh, India; [2]Bose Institute, EN-80, Sector V, Bidhannagar, Kolkata-700091, West Bengal, India

The Muon Chamber (MuCh) system of the CBM experiment is designed for the identification and tracking of muons which are produced from the decay of low mass vector mesons and J/Ψ in high energy heavy ion collisions in the beam energy range from 4 to 11 AGeV/c. The MuCh system consists of several segmented hadron absorbers interspaced with tracking stations. Each tracking station comprises of triplet detector layers. Sixteen and twenty Gas Electron Multiplier (GEM) detectors are proposed to be installed on the aluminium plates in each layer of the first and second stations, respectively. A single module of first and second stations is fitted with 18 and 15 Front End electronic Boards (FEBs), respectively, for the signal collection from the GEM modules. Each FEB produces around 3-4 W of heat during operation. As a consequence, around 7 kW heat is generated from the first two stations. This large amount of dissipated heat within a confined space results in the rise of temperature at the surface of the FEBs and at its vicinity. The FEBs used for the MuCh detector are very sensitive to temperature and have a favourable temperature range, i.e 20°C – 25°C, for their operation. The detectors for the first two stations of the MuCh system are GEM based as discussed earlier, and the gain of the detector is found to depend on the ambient temperature. The stable running of the detector and FEBs therefore requires a stable ambient temperature within the acceptable range which in turn demands the necessity of continuous draining out of the dissipated heat. A cooling system using demineralized water as a coolant is under investigation [1, 2, 3, 4] as a solution to the above requirement. In the present work, two different arrangements of the water distribution have been used to study the performance of the cooling system.

A test frame has been developed at Bose Institute, Kolkata using aluminium extrusion and plywood of size 244 cm × 244 cm for testing purpose. A setup of three modules (aluminium plate with water channel inside) as shown in Figure 1 has been used to study the cooling effect. Module 1, 2, and 3 are of thickness 6 mm, 12 mm, and 10 mm respectively and area 2883 cm^2, 4233 cm^2, and 4233 cm^2 respectively.

Heating elements that are 10 Ω resistors with flat surface were fixed at designated places of the FEBs to produce comparable amount of heat on the surface of cooling plates. To take the heat away, chilled distilled water was circulated through the water channels inside the modules from a water chiller using a submersible suction pump. The water level

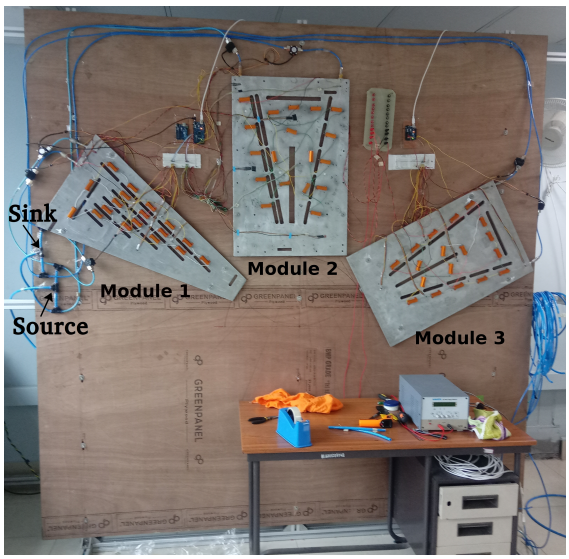

Figure 1: *Test setup of three cooling plates build at Bose Institute.*

of the chiller was kept at a height of 84 cm from the floor.

During the entire experiment, room temperature was maintained at 25°C. Each module was heated up until it achieved a stable maximum temperature (around 35°C). During this heating period, cooling was completely off. Chilled water of temperature in between 16.4 to 19.5°C was thereafter circulated until a stable lower temperature was reached. Note that, water from chiller was brought to the top of a plywood structure, at height of 250 cm, (denoted as 'source') before sending to the inlets of the modules. This is to simulate the position of the water source in the main CBM experiment which might be at a height of around 250 cm. Similarly, the outlet tube from each module was brought to the same height (denoted as 'sink') before sending back to the chiller. The temperatures at different positions on the surface of the cooling plate were measured with the help of six LM35 temperature sensors. The cooling performance study was carried out for the following two configurations of water distribution:

1) *Flow of water through three modules connected in series:* In this configuration, three modules were connected in daisy chain with outlets of the first and second modules connected to the inlets of second and third modules respectively. Therefore, inlet water temperature was expected to be different for each module. The heat liberated from the first module was expected to increase the temperature of

*phd1701151005@iiti.ac.in

water which was being used at the inlet of the second module and so on.

2) *Flow of water through three modules connected in parallel*: Each module had direct inlet from the source and direct outlet to the sink. This setup was made by using push-in pneumatic connectors and pneumatic polyurethane (PPU) tubes of 10 mm and 6 mm diameter.

The results from these two configurations have been shown in table 1 and 2. Comparison of the temperature

Module	Heat produced (W)	Temp. attained after heating (°C)		Temp. attained after cooling (°C)	
		Min.	Max.	Min.	Max.
1	72.5	30	33	20	22
2	78.2	29	31	23	25
3	82.2	33	36	25	27

Table 1: *Performance of cooling system when modules are connected in series.*

Module	Heat produced (W)	Temp. attained after heating (°C)		Temp. attained after cooling (°C)	
		Min.	Max.	Min.	Max.
1	72.5	31	35	20	22
2	78.2	29	33	23	26
3	82.2	31	34	20	24

Table 2: *Performance of cooling system when modules are connected in parallel.*

reached after cooling (from Table 1 and 2) shows that the cooling effect was similar for first two modules whereas it was improved for the third module due to parallel water distribution. In the view of developing a more realistic situation, the heating and cooling of the module were started simultaneously for parallel configuration. It was observed that a constant temperature can be maintained throughout the operation avoiding initial rise in temperature due to heating. Same experiment was repeated with source and sink at height of 130 cm (fig. 1) to see the effect of source height and no significant change was observed.

A realistic model of water distribution through the modules as shown in Figure 2 is being proposed for one layer of MuCh station where a 20 mm diameter blue colored tube, providing chilled water from both left and right sides, will be distributed to 8 modules by using a manifold distributor system of 6 mm diameter blue colored tubes in both sides. The outlet of 8 modules will be circulated back to 20 mm diameter red colored tube using a manifold reciever of 6 mm diameter red colored tubes. Use of remote control valve to control the water flow at inlet of each module is under consideration. A full setup as shown in Figure 2 is under preparation and will be installed and tested at Bose Institute, Kolkata for validating the performace of the cooling system before finalising the design for the real experiment.

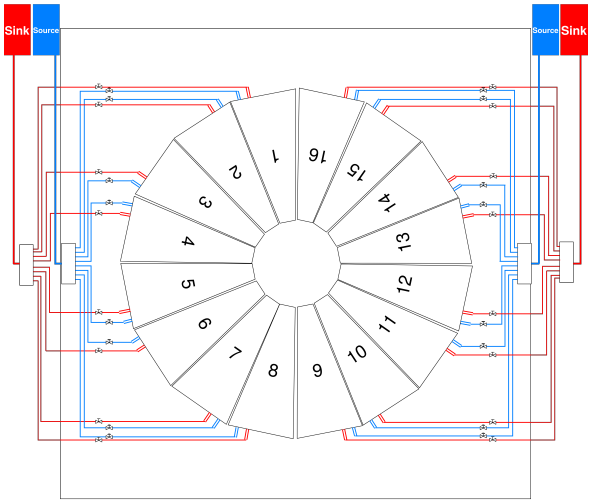

Figure 2: *Proposed model for first layer of first station.*

We would like to thank Mr. Jayant Kumar of VECC, and Mr. Subrata Das of Bose Institute for their help in building the plywood fixture for the test setup. Special thanks to Dr. Saikat Biswas of Bose Institute for his suggestions and fruitful discussions.

References

[1] Vikas Jain et al., DAE-BRNS Symp. on Nucl. Phys. **60** (2015).

[2] D. Nag et al., DAE Symp. Nucl. Phys. **61** 1096-1097 (2016).

[3] C. Ghosh et al., DAE Symp. Nucl. Phys. **62**, 1062-1063 (2017).

[4] D. Nag et al., Springer Proc. Phys. 203 893-895 (2018).

mCBM slow control system for mMUCH Detector

V. Negi, J. Saini, and S. Chattopadhyay*
VECC, 1/AF, Bidhan Nagar, Kolkata, 700064, India

Introduction

The mini CBM experiment, considered as FAIR phase-0 experiment and its results are very crucial for understanding the complication and performance of the full CBM experiment. This paper describes the indigenously developed Slow Control System for the mini-MUCH detector in mCBM experiment. The content mainly emphasizes on the reliable operations of the slow control system in the radiation environment. The system hardware, firmware and software were designed to mitigate any corruption of firmware at different levels. The system had been validated in the harsh environment of mini CBM experiment for more than 100 hours. Useful parameters were controlled and monitored for the entire data taking period.

mCBM slow control set up

All the hardware components of slow control system were subjected to accelerated life test with Gamma irradiation (acceleration factor 100000). The fault tolerance test had been conducted at BARC Mumbai with 14 Mev, neutron generator. The bulk damage and SEU cross section of 14Mev neutron is more than 1 Mev [1]. Dose rate during the experiment was approximately 1000 times of CBM dose rate. As shown in Fig1, mCBM slow control hardware comprise of four active control boards in mCBM experiment. There were two low voltage distribution boards which were powering thirty individual channels of two GEM detectors module, one sensor board which reads cave parameters (pressure, temperature and humidity). A master

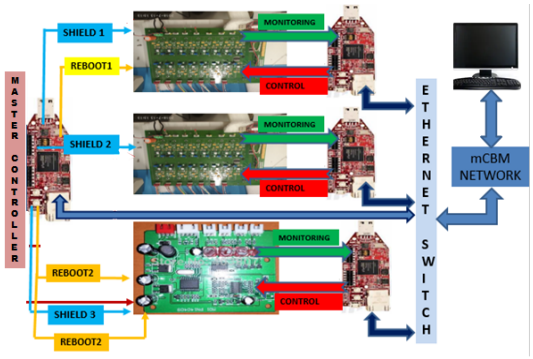

Figure 1: mCBM slow control Hardware.

FPGA board was placed outside the radiation zone which gives primary protection against SEUs. REBOOT and SHEILD are the primary output of master FPGA board. REBOOT take cares of periodic firmware scrubbing of secondary controller boards (FPGA Boards inside the cave). Once the initial configuration is done SHEILD electrically isolates the secondary controller boards from their respective hardware (LV and sensor boards). In this way radiation induced firmware errors were mitigated. All four boards were communicating to the much slow control server machine via dedicated mCBM network via UDP connection.

mCBM control and monitoring software

As shown in Fig2 Slow control machine talks to FPGA controller boards via UDP link. FPGA board activates SPI link and communicates with various channel of LV board individually via Control Multiplexer. Similarly FPGA controller allows us to get monitoring parameters (voltages, current of individual channel and other cave parameters like pressure humidity and temperature. Monitoring multiplexer selects the concerned channel and ADC digitized it and fetch it to FPGA via SPI link. Matlab based GUI

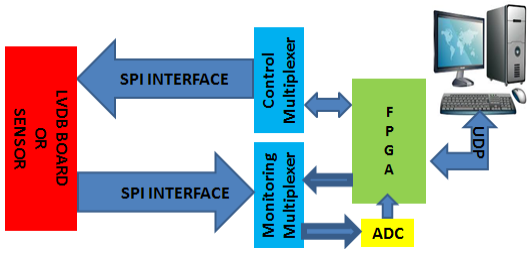

Figure 2: mCBM Data flow.

Application compatible with Linux and Windows were developed which requires no additional software installation. Successful and reliable monitoring, control and data logging of 2 LV-BOARDS (30 individual FEE boards) and one sensor board (Cave parameters humidity pressure and temperature) were done. Radiation hard firmware design had been developed and tested in the harsh environment of CBM experiment. No appreciable change in electrical parameter of any component was observed during this experiment.

References

[1] A. Vasilescu and G. Lindstroem, *Displacement damage in silicon, on-line compilation*.

* vnegi@vecc.gov.in

Correlation between mMuCh hits and projected mTOF tracks in the miniCBM setup

E. Nandy, V. Singhal, A. Aggarwal, A. Kumar, A.K. Dubey, J. Saini, C. Ghosh, V. S. Negi, S. Chattopadhyay

VECC, Kolkata, India

We report the analysis of mCBM@SIS18 data taken at GSI, Germany during March-May, 2020 with the realistic setup for each sub detectors; mSTS, mMUCH, mTRD, mTOF, mRICH and mPSD as shown in Fig.1. Data were taken for Pb^{206}, Pb^{208} & Bi^{209} at 1.075 AGeV with different intensities. We report here an analysis in which tracks formed by mTOF layers have been projected on one GEM chamber. This shows the ability to use GEM layer for tracking. A good spill structure is observed for MUCH, T0 & TOF as shown in Fig.2 indicating the frequency of beam on-and-off. As a first quality check, we obtain nice time correlations between two GEM chambers and with T0 as shown in Fig. 2(top) and Fig. 2(bottom) respectively. A time-based event reconstruction is employed to build events from the raw data. Very good spatial correlation is observed (not shown) between the hits from two GEM chambers and between GEM-1 and TOF which indicate coherent working of sub-detectors. Fig.3(top and bottom) shows spatial correlations in X and Y-coordinates, for GEM1 hits and TOF tracks projected at GEM1. The observed time and spatial correlations between detector subsystems demonstrate a first conceptual verification of the free-streaming DAQ system of CBM and of GEM chambers as tracking detector.

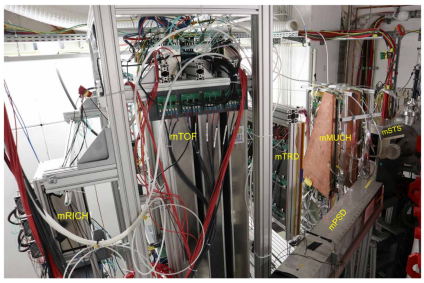

Figure 1: Photograph of the mini-CBM setup

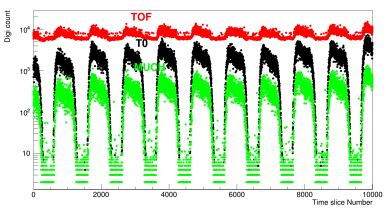

Figure 2: Spill structure by different subdetectors

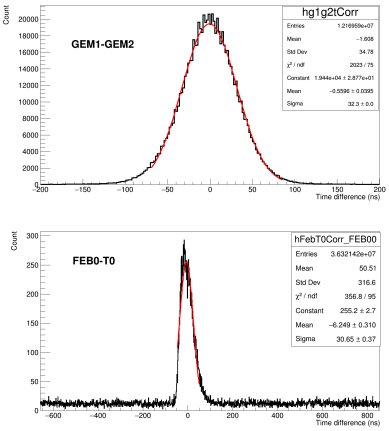

Figure 3: (top) Time correlation between two GEM chambers (bottom) time correlation between a GEM chamber and T0

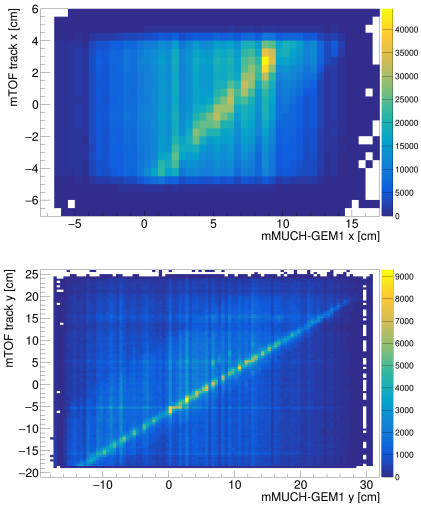

Figure 4: (a) X-X correlation between projected TOF tracks on GEM-1 with GEM1 hits (b) Y-Y correlation between projected TOF tracks on GEM-1 with GEM1 hits

Transition Radiation Detector

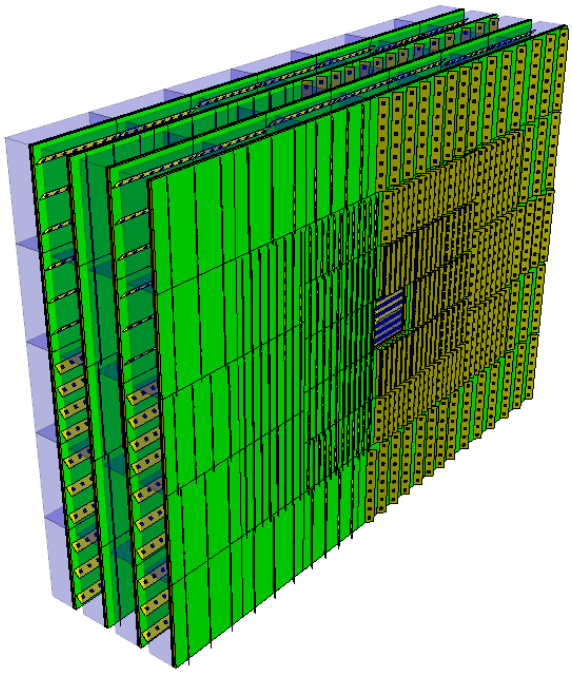

Summary on the TRD project

C. Blume[1] *and the CBM-TRD working group*
[1]Institut für Kernphysik, Frankfurt am Main, Germany

Introduction

The main task of the Transition Radiation Detector (TRD) is to identify electrons above momenta of 1 GeV/c and thus to extend the electron identification capabilities of the Ring Imaging CHerenkov (RICH) detector above momenta of $p \sim 5$ GeV/c. In this region the TRD should provide a pion suppression factor in the range of 10 – 20 at an electron efficiency of 90 %, in order to allow for a high quality measurement of dielectrons in the mass range from below the ρ and ω masses to beyond the J/ψ mass. Due to its capability to identify charged particles via their specific energy loss, the TRD in addition will provide valuable information for the measurement of fragments and thus be also decisive for the hypernuclei program of CBM.

These requirements can be fulfilled with a Xe/CO_2 based Multi-Wire Proportional Counter (MWPC) detector in combination with an adequate radiator. The default MWPC design is composed of a symmetric amplification area of $3.5 + 3.5$ mm thickness, complemented by a 5 mm drift region to enhance the TR-photon absorption probability in the active gas volume. This geometry provides also efficient and fast signal creation, as well as readout, with timescales below 250 ns per charged particle track. The performance of the detector is maximized by reducing the material budget between radiator and gas volume to a minimum.

The baseline design for the TRD at SIS100 will consist of one station, composed of four detector layers. It will be positioned between the RICH and the Time-Of-Flight (TOF) detector and thus will help to reduce the background in the TOF resulting from track mismatches by providing additional position information between RICH and TOF. The TRD will also be used as tracking station behind the last absorber of the MUCH detector in the muon configuration of CBM.

Detector module EDR

The outer detector modules (type 5 and 7) have been thoroughly evaluated in an engineering design review (EDR) on March 25th, 2020, at the IKP in Münster. While generally no critical issues have been found, several points have been identified where further simplifications and improvements might be possible. One important outcome of the review was the observation that state-of-the-art circulating gas systems, such as used for the ALICE-TRD, can provide gas pressure stabilities below 0.1 mbar variation. Such an environment would allow to construct the entrance window of the readout chambers, which is planned to be reinforced by a grid of carbon fibre ledges, with less material as currently foreseen, as the current design assumes variations of 1 mbar. Furthermore, the permeability of the entrance window foil to water might not be of real concern in terms of detector performance and ageing. However, it would increase the frequency with which the gas purifiers will have to be exchanged. An important aspect, which might require special attention are the capacitors in the HV filter boxes. Their capacitance should be chosen as low as reasonably possible and a thorough QA procedure needs to be established. Also, all materials used in the chamber construction should be tested with respect to their ageing properties and potentially further long term tests at the CERN-GIF++ facility should be foreseen.

Infrastructure

A detailed design of the TRD support structure has been made within the recent year. It complies with the space contraints imposed by the other detectors within the CBM setup and still allows to access every individual TRD layer for maintenance purposes. This is achieved by moving the inner frames, on which the layers are mounted, in x-direction, i.e. perpendicular to the beam direction, within the outer frame of the support structure. Single modules can then easily be installed or removed as they will be attached to the inner frame with a simple clamp mechanism. The outer frame can be moved as a whole along the z-direction, i.e. along the beam direction, in order to be able to position the TRD in different measurement configurations (e.g. electron and muon setup). The design of the support structure is described in detail in [1]. Ongoing work focuses on the routing of services, in particular flexible gas pipes, cable trays and LV bus bars.

While the external forces on the modules are taken care of by the inner support frame, the internal forces generated by the wire planes have to be absorbed by the frames of the individual modules. For the inner detector region this was recently addressed with mechanical stress simulations, based on the ANSYS™ framework [2].

Developments on the gas system have been taken up in the Münster group, based on the example of the gas system for the ALICE-TRD. So far, gas connectors have been designed and simulations on the resulting pressure distribution for within the different readout chambers have been performed. It is planned to setup a small test system in the laboratory to evaluate all components of the planned gas system.

Readout electronics

The readout electronics for the outer modules is based on the SPADIC chip, which has been developed at the ZITI in Heidelberg. About 16.000 ASICs of latest version SPADIC 2.2 have been produced in CBM-wide engineering runs, which in principle would be sufficient to equip the complete TRD. However, during extensive tests, in particular during the test beam at DESY in summer 2019, several issues have been identified which might require a further submission after some smaller design adjustments. Four of the SPADICs will be operated simultaneously on one Front-End-Board (FEB). The FEBs have been designed at the IKF in Frankfurt and are now available as prototypes. A description of the FEBs is given in [3]. The produced boards are currently being tested in the laboratory, as well as in the mCBM setup. New firmware for the readout has been written, which incorporates a newly developed micro-slice format and works within the AFCK based readout scheme. It has successfully been used during the DESY test beam and is further been developed during the mCBM run [4].

For the innermost modules the readout is supposed to use the Fast Analog Signal Processor (FASP) chip, developed for high data rates at the IFIN-HH in Bucharest. It will be operated on the newly designed FASPRO-FEB, which also provides the ADC. The I/O part will be handled by the additional Generic Event Time-stamping Streamer (GETS) board and will be implemented on radiation tolerant PolarFire FPGAs by MicroSemi. The development of this readout chain has been completed and tests are planned to evaluate its performance in a high radiation level environment and at high data rates.

Software and reconstruction

The digitization procedures for the TRD have been redesigned in the course of the recent year. They are now implemented for both configurations, rectangular pads in the outer chambers and triangular pads in the inner ones. Both digitizers include a detailed description of the response of the different electronics (SPADIC and FASP) and have been validated against test beam data. The new simulation software has also been prepared for 4D-reconstruction and now allows to investigate the hit reconstruction performance as a function of the mean interaction rate [5].

Another important ongoing study is addressing the performance of the inner detector region equipped with triangular readout pads [6]. This configuration provides a hit position resolution in two dimensions which is significantly higher than the one achievable with rectangular readout pads. It is now being evaluated what kind of improvements in the physics performance can be realized with this solution. The outcome of this study will be the basis of a planned addendum to the TDR technical design report, which is supposed to describe the high resolution design of the modules in the inner detector region.

Test beam activities and mCBM participation

In addition to these simulation studies, detailed analyses of recent test beam data have been advanced. Data from the 2017 test beam at DESY were investigated to obtain informations on the position resolution with an electron beam [7]. In 2019 a further test beam with two TRD modules was performed at the DESY electron beam. In addition to do a validation of the readout electronics, the aim of this campaign was to systematically characterize radiators of different thicknesses. First results of this study are presented in [8] and compared to simulation results. This study will allow to improve the simulation of the transition radiation (TR), which has to rely on a momentum dependent parametrization of the TR production. A detailed tuning of these parameters will be the basis of future simulation studies.

The TRD has already been part of the mCBM setup with two modules in the last year. However, due to manpower issues, the readout was not ready for a participation in the data taking at previous runs. Meanwhile, this problem has been solved and the TRD is prepared for joining the mCBM data stream in the 2020 run. In addition to many improvements in the hardware, a completely new firmware has been developed and a new message unpacker software has been implemented [4]. The analysis of the mCBM run will provide information on the operation of the TRD in a high hit rate environment and thus be an important reference for the production readiness review planned in 2020.

References

[1] P. Kähler and L. Wahmes, “TRD support structure and maintenance case”, this report.

[2] L. Radulescu et al., “Studies of mechanical stress for the high resolution TRD”, this report.

[3] F. Roether et al., “Update on the development of Front End Boards for the TRD”, this report.

[4] P. Raisig et al., “Preparation of the SPADIC 2.2 based readout of the TRD for the mCBM 2020 beamtime”, this report.

[5] E. Bechtel, “Recent development of digitization and reconstruction algorithms for the TRD with rectangular pads”, this report.

[6] A. Bercuci et al., “Reconstruction performance of high position resolution TRD, modelled in the CbmRoot framework”, this report.

[7] A. Puntke and P. Kähler, “Position reconstruction in DESY 2017 testbeam data”, this report.

[8] A. Meyer-Ahrens and P. Kähler, “Charge reconstruction in DESY 2019 testbeam data”, this report.

TRD support structure and maintenance case*

P. Kähler[1] *and L. Wahmes*[1]
[1]Institut für Kernphysik, WWU Münster, Germany

As the TRD is foreseen to be mounted on the cave rail system, we describe here the current planning status of the detector-carrying support structure and the mode of access to the TRD modules in possible maintenance phases between the annual beam times.

Inner support structure

The **inner part of the support structure** is carrying the single TRD modules and is located within the acceptance. The **four layers** are constructed with minimised material budget. The TRD will be installed from its single detector modules of 54 x 54 cm^2 or 99 x 99 cm^2, respectively, inside the cave into the layers of the inner support structure [1]. For efficient installation, a mounting clamp as shown in Fig. 1 is foreseen: the chambers are inserted towards the pre-mounted clamps and thereby already hanging safely, while being fully secured and adjusted in a second move. Subsequently, the radiator boxes are added with clasps onto the detectors.

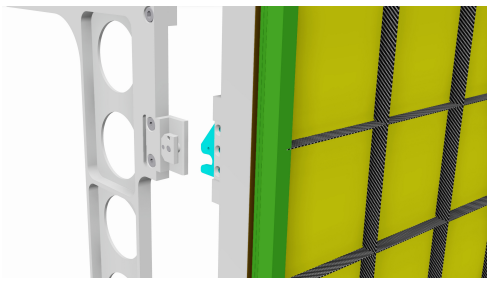

Figure 1: Mounting of a TRD module in specific clamp.

Also the routing of services and cables is currently being designed as part of the support structure. A full-size demonstrator sector of the inner support structure is available in Münster for this purpose.

Expected weight of one TRD layer carried in its inner support structure is up to 1500 kg. One empty layer of inner support structure accounts for 350 kg.

Outer frame and rail mounting

The four layers of the inner structure will be installed in rails (x-direction) inside an **outer support structure**. All sections, the four inner and the outer, are to be finished prior to detector installation. Outer and inner structure are installable with *cold* techniques. The outer structure is the actual, solid carrier of the overall TRD, standing on the cave rail system (z-direction). The full system is rendered in Fig. 2. Cave rail sliders enabling minor overall adjustment in y are subject of current discussion. Services will be brought to TRD in cable drags or comparable structures, ensuring the required flexibility for movement on the cave rails (z) and of detector layers in the inner (x).

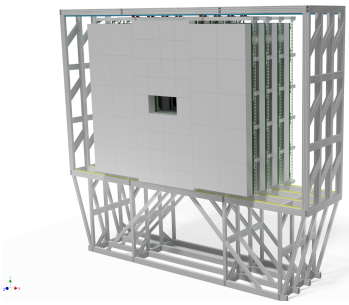

Figure 2: TRD in measurement configuration.

The weight of the outer structure (only) is about 5000 kg. With a movement system for the inner layers, an upper weight estimate for the full TRD is 12500 kg. Main source of uncertainties are services and cables.

Maintenance case

During the installation phase of single modules and completion of the cabling, but also to enable later maintenance, access to all parts of the detector system needs to be defined. Exchange of single TRD modules is supposed to be possible. The time frame for such access is during the annual beamtime break of CBM. Maintenance access is realised by movement of complete TRD layers against the others in x-direction. By moving a layer only in total, most of the cabling and Xe gas filling can be possibly preserved during such interventions. Maintenance configurations are shown in Fig. 3: by the aforementioned x movement, access to one or the other half of a layer is enabled. Workflows are being prepared, including the usage of scaffolds from front and rear of the layer.

References

[1] C. Blume and C. Bergmann and D. Emschermann, "The Transition Radiation Detector of the CBM Experiment at FAIR", Technical Design Report, FAIR, 2018

*Work supported by BMBF grant 05P19PMFC1.

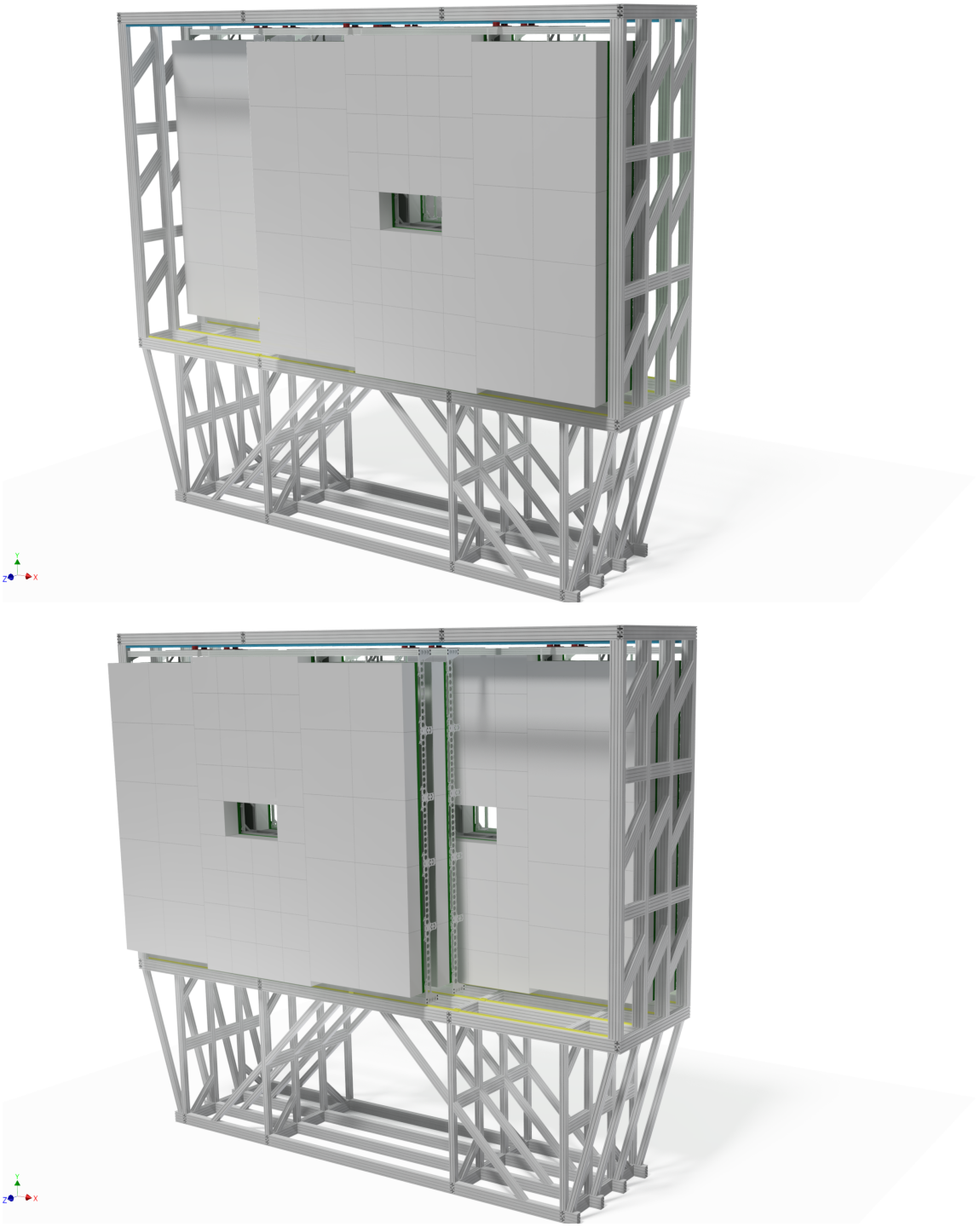

Figure 3: TRD in different maintenance configurations. Layers are shifted in total to enable access to detector modules.

Studies of mechanical stress for the high resolution TRD*

L. Radulescu[1], *A. Bercuci*[1], *M. Petrovici*[1], *and C. Schiaua*[1]
[1]National Institute for Physics and Nuclear Engineering (IFIN-HH), Hadron Physics Department, Bucharest, Romania

The alternative solution proposed for the inner part of the Transition Radiation Detector (TRD) wall, tagged as High Resolution (TRD-HR) [1], has to fulfil strict conditions in terms of construction and operation to accommodate high particle rate measurements with a minimum material budget. The light structure of the TRD-HR, on the other hand, has to support the stress induced by the multi wire cathode electrode with 100 cN/wire tension during construction, and due to the gas flow during operation. The mechanics of the flow is also subject to constraints as it has to be kept in optimal operation conditions (density, concentration, temperature, etc.) throughout time and space when irradiated with approx. 10^5 part/cm^2/s. In order to optimise the structure and its dynamics wrt. the above mentioned constraints, mechanical stress simulations, based on the $ANSYS^{TM}$ framework, were performed.

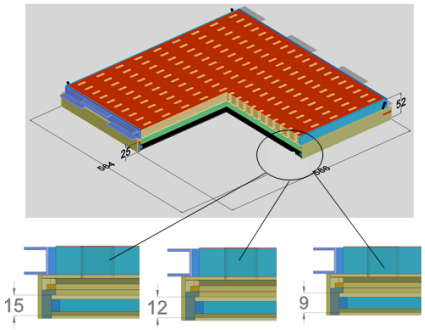

Figure 1: The chamber geometry and graphical illustrations of the parametric analysis for the entrance window mechanical structure.

The studies of the static chamber deformation during construction were concentrated on the following aspects: frame (see Fig. 2 left) and entrance window (see Fig. 2 right) deformations and wire tension variation. A parametric simulation was realised for different possible structures of the entrance window: w/o carbon fiber reinforcement on both sides of the honeycomb layer and for different entrance window thicknesses (see Fig. 1).

A 9 mm thick honeycomb sandwich structure for the entrance window surrounded by carbon fibers seems to be optimal in terms of minimal Transition Radiation (TR) absorption and gas gain variations. No significant variations in the wire tension were observed in the calculations after releasing the frame from the assembling support during construction.

* Work supported by Romanian Ministry of Research and Innovation NUCLEU Project Contract PN 19060103.

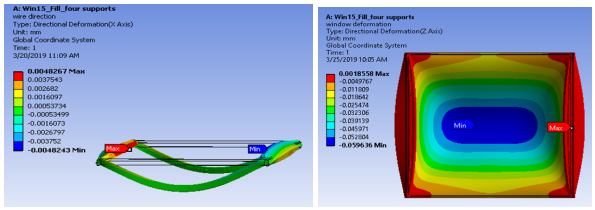

Figure 2: The deformation of the frame along cathode wires direction (left) and of the entrance window perpendicular to its surface (right).

The gas flow was simulated assuming rigid and fixed chamber walls. The boundary conditions were set such that a total inward mass flow of 6 l/h $ArCO_2$ was circulated at fixed normal output pressure. We have studied three configurations for the inlet/outlet geometries (see Fig. 3 left): linear distribution pipes for 10 inlets and 10 outlets, respectively (**a**), two parallel (wrt. pad plane) pairs of inlet/outlet (**b**) and two perpendicular (wrt. pad plane) pairs of inlet/outlet (**c**).

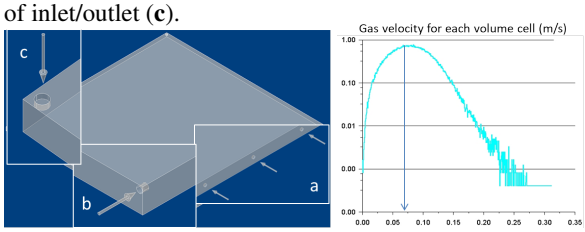

Figure 3: Three inlet/outlet geometries considered for the TRD chamber (left) and the distribution of gas velocities in the chamber (right).

We have recorded and compared the 3D-maps of the flow for the three configurations. No significant differences were observed for the given boundary conditions. A mean value of less than 0.1 m/s (see Fig. 3 right) was calculated for the velocity of the gas flow inside the chamber for all cases with an isotropic distribution.

Static and dynamic stress simulations were performed for the TRD chambers within the ANSYS framework. An entrance window geometry optimised in terms of performance and construction is proposed. An estimate of the mean gas flow velocity was given as input for a calculation of the burned-out gas ratio in high counting rates.

References

[1] A.Bercuci et al., "Reconstruction performance of High Resolution TRD", this report.

Update on the development of Front End Boards for the TRD*

F. Roether[1], *N. Bialas*[1], *C. Blume*[1], *D. Schmidt*[2], *S. Schreiber*[1], *P. Fischer*[3], *and R. Weihrich*[1]
[1]Institut für Kernphysik, Frankfurt, Germany; [2]IRI, Frankfurt, Germany; [2]ZITI, University of Heidelberg, Germany

The TRD will be read out by Front End Boards (FEB) which are currently being developed, tested and optimized at the electronics department of the IKF. The FEBs are equipped with Self-triggered Pulse Amplification and Digitization ASIC (SPADIC) chips [1], which were developed at ZITI and are the central component of the FEE.

The SPADIC 2.2

Each SPADIC has a single downlink for configuration and two uplinks for data readout. Version 2.2 implements an optimized message format compared to version 2.0, which allows for a higher data throughput. In addition, the new BGA package of version 2.2 made the development of a more compact FEB possible [2]. This is necessary due to tight space constraints on the back of the innermost detector chambers and to reduce the overall material budget of the TRD modules, as the FEBs will be mounted inside the active area of the detector. To decide if version 2.2 can be the final version or another iteration is needed, the ASIC has been tested in the laboratory and in a test beam campaign at DESY in 2019 [3]. It is further evaluated within the mCBM runs in 2020.

FEBs for mCBM

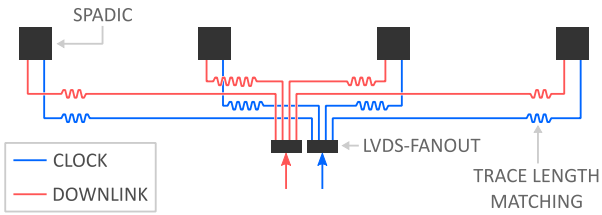

Figure 1: Schematic view of the signal distribution on the SPADIC 2.2 FEB.

On FEBs with multiple SPADICs the clock and downlink can be shared between the ASICs. For this purpose the clock and downlink are distributed via two LVDS fanout buffers (see Fig. 1). All trace length are matched to compensate for different signal propagation delays.

Even though the space constraints on the back of the large detectors for mCBM are less challenging in comparison to the most inner chambers in the final TRD design, the design goal was to develop a FEB that could also fit on chambers with the highest density. Thanks to the new

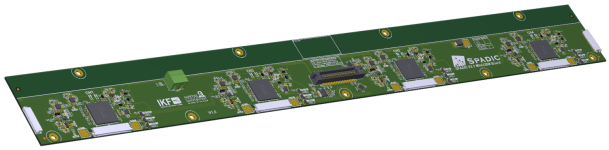

Figure 2: Rendering of the quad SPADIC 2.2 FEB used at mCBM.

BGA package it was possible to design a FEB with a width of only 33.75 mm (see Fig. 2). 12 FEBs were manufactured to populate the two TRD-chambers which are part of the mCBM-setup. The low voltage for operating the FEE is delivered by a Power Distribution Board (PDB). Each PDB is equipped with six radiation tolerant DC-DC converters (FEAST-MP). As of April 2020 the first chamber is installed at mCBM and runs successfully [4, 3].

Tests of SPADIC 2.2

As already mentioned, rigorous tests are needed to decide if the current version is suited for the final experiment. Early results hint at possible timing issues inside the ADC of some channels of the SPADIC. Further tests have to show if this behaviour can be fixed by an adjusted external circuit and if others unknown bugs exist. Furthermore, every ASIC needs to be individually tested before they are mounted on the FEB. For this a chip tester was designed by ZITI and an accompanying test software was developed at IKF.

References

[1] P. Fischer and M. Krieger., *Development of new SPADIC versions 1.1 and 2.0*, CBM Progress Report (2016) p. 109

[2] F. Roether et al., *Front end board development for the TRD*, CBM Progress Report (2017) p. 86

[3] A. Meyer-Ahrens and P. Kähler, "Charge Reconstruction in DESY 2019 Testbeam Data", this report.

[4] P. Raisig and D. Spicker, "Preparation of the SPADIC 2.2 based readout of the TRD for the mCBM 2020 beamtime", this report.

* Work supported by BMBF-grant 05P19RFFC1

Recent developments of digitization and reconstruction algorithms for the TRD with rectangular pads*

E. Bechtel[1]
[1]Goethe University, Frankfurt, Germany

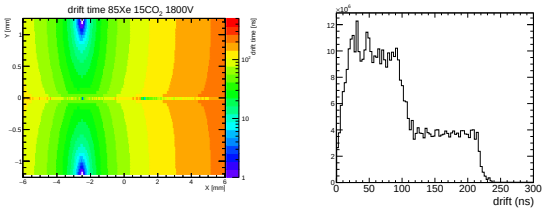

Figure 1: Left: GARFIELD simulation of the drift times in one TRD drift cell [1]. Right: Simulated drift time distribution for electrons from primary ionizations in the gas volume of the TRD.

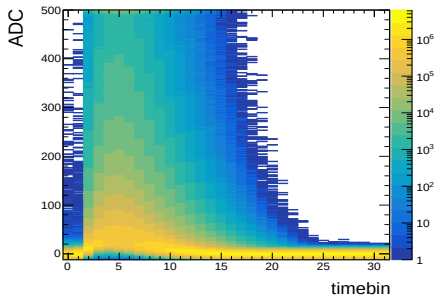

Figure 2: Distribution of simulated signal pulses in a central Au+Au collision at 12 A GeV, simulated with UrQMD.

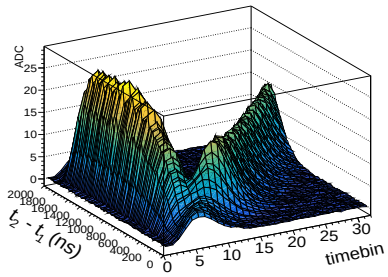

Figure 3: Signal pulses in a pile-up scenario with exactly two particles contributing to the signal. The times t_2 and t_1 correspond to the time of the closest electron cluster to the anode wire of the respective particle.

Front-end simulation

The latest version of the readout ASIC for the Transition Radiation Detector is the SPADIC version 2.2, which is now continuously tested with the available detector modules. One of the primary endeavors from the software side of the project was the accurate description of the front-end electronics in the simulation. Especially, precise simulations of high rate conditions are indispensable, since these conditions are currently still difficult to measure with a prototype setup.
The properties of the front-end electronics and the time evolution of the signal pulses were implemented at the beginning of 2019 and were further improved in the last year. The time distribution of the signal is heavily influenced by the time the electrons from the primary ionizations need to reach the anode wires. Figure 1 (left) shows the calculated drift times, which were obtained with a GARFIELD simulation. The positions of the primary ionizations are calculated by extrapolating the entrance point into the gas volume and randomly determining the ionization points according to the Bethe-Bloch formula. The simulated signal is resulting from a superposition of the individual electron clusters taking into account their respective distance in time, allowing for potential multi-hits in pile-up scenarios.

The implementation of the front-end electronics also provides a realistic description of the trigger logic. Any significant energy contributions are supposed to create a "self-trigger" in the respective readout channel, which then additionally forces the readout of the two adjacent channels to minimize information losses due to thresholds. Figure 2 shows the full distribution of signal pulses generated in the 10% most central Au+Au collisions of a 12 A GeV as simulated with UrQMD. The results include a stochastic (Gaussian) noise on each ADC sample, is visible as the broadening of the baseline at the bottom. Additionally, there is a crosstalk implementation, which assumes a signal sharing of 5% between neighboring channels. The time evolution of the signal in an inter-event pile-up scenario can be seen in Fig. 3. The z-axis shows the average amplitude of the simulated response and it can be seen that the second particle creates a distinct second maximum in the message provided the distance in time between the two particles is large enough.

Time evolution of the signal and rate effects

It is expected that pile-up scenarios with a time distance

* Work supported by BMBF grant 05P19RFFC1 and by HGS-HiRe.

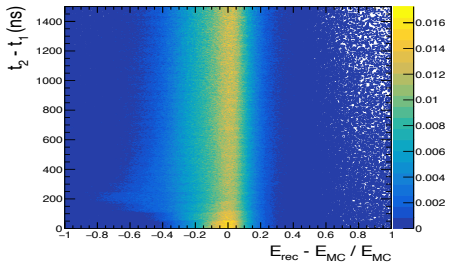

Figure 4: Energy resolution of a self-triggered signal pulse as a function of the time distance in a pile-up scenario of exactly two particles.

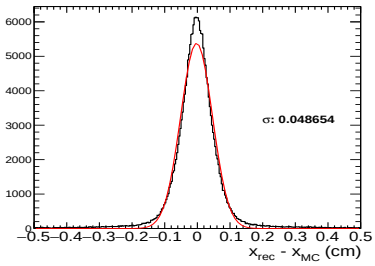

Figure 6: Resolution of the reconstructed position for the first detector layer as a function of the reconstructed position..

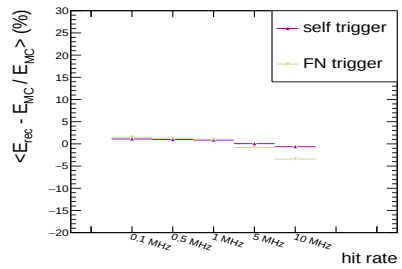

Figure 5: Mean relative difference between reconstructed and MC signal energy as a function of the mean interaction rate.

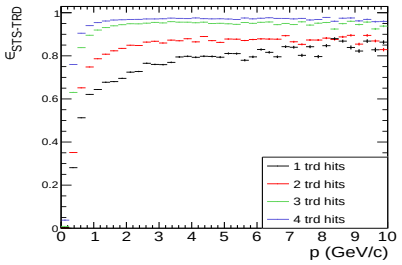

Figure 7: Efficiency of the matching between the track in the TRD and the track in the STS as a function of the momentum.

below 200 ns between the individual particles can not be separated by the multi-hit logic, which can be seen at the intersection at low dt= $t_2 - t_1$ in Fig. 3. Therefore, the energy resolution is expected to decrease for very large mean interaction rates. The energy resolution of self-triggered channels simulated with the new digitizer, for a multi-hit scenario is presented in Fig. 4 with the distance in time between the charged particles on the y-axis. The resolution decreases towards dt-values of about 250 ns, where the particles can not be separated properly any more. Further investigations of the multi-hit case are ongoing. Figure 5 shows the energy reconstructed for the simulated digis in the TRD in comparison to the reconstructable MC energy for a given channel as a function of the mean interaction rate and calculated separately for self- and forced-neighbor (FN)-triggered signals. The FN signals contain a smaller amount of deposited energy, which makes them more sensitive to small contributions from additional particles.

Hit reconstruction and track matching in the event-based mode

The total reconstructed energy of a given cluster is the sum of the energies in the contributing channels. The cluster time information is calculated as the average of all channels associated with this cluster. The time distribution between incoming events is calculated using a Poisson distribution in the digitization step. The position is calculated as the center of gravity of the charge distribution of the channels in the cluster. Due to the relatively large heights of the individual readout pads in the different module types (width=0.68cm, height=1.75-12cm), this information is always more precise in the direction along than across the pad rows. Therefore, square TRD modules are rotated by 90 degrees every other layer. The position resolution of the first detector layer can be seen in Fig. 6. The resolution, in the sensitive direction, is in the order of about 490 μm.

Since there is no four-dimensional tracking algorithm available yet, these simulations can only be done without inter-event pile-up in an event-based simulation procedure. After reconstructing the events, the matching between the reconstructed tracks in the TRD and the STS can be compared. Figure 7 shows the matching efficiency as a function of the particle momentum and the number of hits, which are associated with the track in the TRD. The efficiency drastically increases if at least three hits are found for the TRD track. The matching efficiency for tracks reconstructed in all detector layers is in the order of 98% above p $\approx$ 1.5 GeV/c.

References

[1] CBM TRD TDR , GSI-2018-01091

Reconstruction performance of High position Resolution TRD, modelled in the CbmRoot framework *

A. Bercuci[1], *V. Cătănescu*[1], *M. Petrovici*[1], *L. Radulescu*[1], *and C. Schiaua*[1]

[1]National Institute for Physics and Nuclear Engineering (IFIN-HH), Hadron Physics Department, Bucharest, Romania

For the inner 10 modules of the TRD (Transition Radiation Detector) wall of the CBM experiment, an alternative design is proposed with increased position resolution capabilities. Such device is thought to add lever arm to STS (Silicon Tracking System) in high multiplicity environments, yielding a more accurate track definition, pile-up resolution and a better matching with the ToF (Time of Flight). As the price for construction is driven mainly by the density of electronic channels per detection unit area, while for operation by the total data volume, our solution is bounded to keep such markers fixed wrt. default. The solution presented here achieves such goals by a qualitatively new design of the read-out electrode with heuristic implications for all detector observables. Effectively, we have traded some signal timing information for a two-fold read-out coverage of the active area.

The alternative solution for the inner zone of the TRD wall, tagged TRD-HR (High Resolution), was implemented physically and tested. Various reports were given elsewhere [1, 2]. Based on these data and FASP [3] based FEE electronic tests, we have implemented the new system in the CbmRoot framework. A "tracking" configuration was selected with Argon as the active gas and the anode voltage set to $U_{anode} = 1.95$ kV. A FEE signal threshold of $U_{thr} = 50$ mV produces a hit reconstruction efficiency above 99.7 % wrt. MC. The framework provides the environment to operate our system, namely the event-by-event mode (currently the only one available describing low interaction rates) and tracking based on STS-MVD seeding [4].

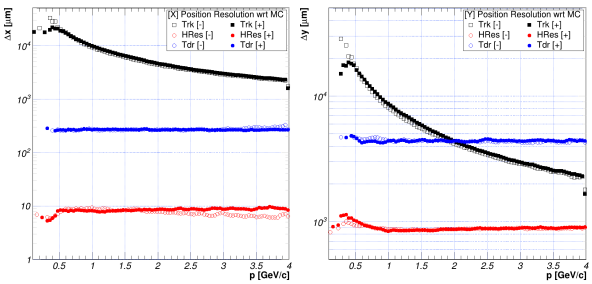

Figure 1: Position resolution wrt. MC at TRD entrance ($z = 441$ cm), for the horizontal direction (x - left) and vertical (y - right) for various tracking elements; the track model (black), the TRD-HR hit (red) and the TRD-TDR (blue), respectively, and for both negative (open symbols) and positive (closed symbols) charges .

* Work supported by Romanian Ministry of Research and Innovation NUCLEU Project Contract PN 19060103.

From a track definition perspective it is important to quantify the matching between the "framework" track and the corresponding TRD hit when this interaction is done first, i.e. in layer 0 of the TRD detector. The track parameters are saved $before$ being eventually updated by the TRD hit to preserve their independent state. The matching between track and hit was done using the associated MC-track as proxy which in turn was computed as the MC-track with maximum contributions to the STS hits attached to the track. In order to have an unbiased comparison the UrQMD particles were propagated also through the default setup (here tagged as TRD-TDR) and similarly processed. In Fig. 1 the results for the position resolution are summarized for the three tracking elements as function of particle momentum **p** and charge **q**. As the multiple scattering dominates at low **p**, the position resolution of the track exceeds $\Delta = 1$ cm in both x and y directions close to $p = 1$ GeV/c (black symbols in Fig. 1). The intrinsic position resolution of the default TRD is independent of **p** and **q** and levels at $\Sigma_{xy} = \sigma_x \times \sigma_y = 0.3 \times 4.3$ mm^2. For the HR solution a two orders of magnitude improvement is found on the $2D$ resolution at values of $\Sigma_{xy} = 10 \times 850$ μm^2 (see red symbols in Fig. 1).

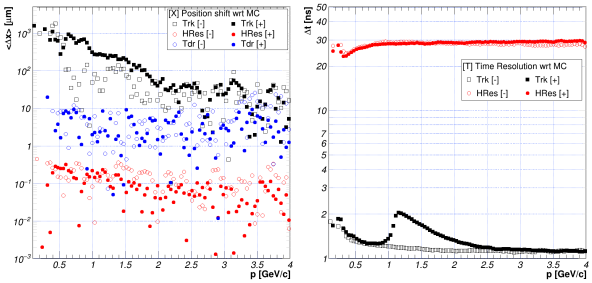

Figure 2: Absolute position shift on the horizontal direction (x) wrt. MC point in TRD layer 0 for the same elements as in Fig. 1 (left plot) and the time resolution at the same distance from target for the track model and TRD-HR hit (right plot) against MC info.

The mean values of the x residuals, the *systematic shift*, between MC and the three tracking elements mentioned above, are illustrated in the left panel of Fig. 2 as function of **p** and **q**. For **p** around 1 GeV/c values of $100 - 300$ μm are registered for the track (black symbols in Fig. 2), which are comparable with default TRD resolution and more than 10 times larger than the HR σ_x. Systematic shifts for TRD are of few μm for the default (blue) and tenths of μm for the HR solution (red symbols) around the same momentum range. To complete the image of track to TRD matching in

the right panel of Fig. 2 the estimated time resolution is given for the track model and the TRD-HR[1] wrt. MC. The system (detector and FEE) time resolution of 30 ns for all **p** and **q** obtained for TRD is a remarkable performance as the detector itself is slow, with intrinsic timing in the order of μs. The track time resolution is just above 1 ns at TRD level with a different behavior for the positively charged mainly driven by the abundant proton component.

The turning point between independent detection systems and unified particle trajectories in a CBM-like experiments is the tracking algorithm. Basically, for TRD, it implements a finding and a parameter update algorithm. The finding algorithm selects the correct hit from a candidate pool, while successful track update depends on both position and uncertainties to be correctly described by a linear error propagation model (pulls statistics). Time is a loose information in TRD wrt. track and therefore is hidden by large uncertainties but the position might impose strong constraints. The candidate selection criterion is the minimum χ^2 between track parameters and hit space-time position. Such algorithm should work best for cases where selector (track) and selected (hit) have comparable uncertainties and the systematic effects of both are smaller wrt. the average distance between the selected. For the HR case there are several orders of magnitude difference in spatial resolutions between the two and for the central regions also the second condition starts to fail. Additionally, the finding algorithm is sequential on track quality, best quality tracks being used first. As such, a double error possibility appears, in cases when a $mis-match$ is registered first, followed by a $not-found$ exception on the matched track due to (correct) hits being already used up previously on a (wrong) track.

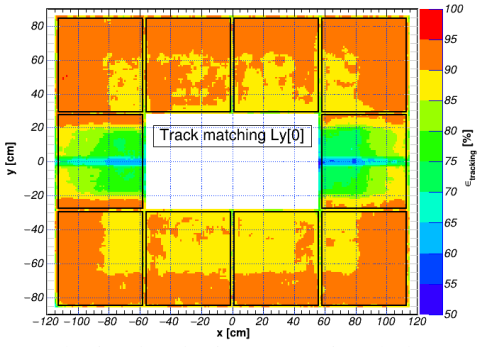

Figure 3: The fraction, in 5 % steps, of tracks in TRD layer 0 having TRD-HR hits attached as function of the corresponding MC point $x-y$ coordinates; structures not related to TRD geometry (chambers edges outlined by black squares) are clearly seen as sign of systematic effects between track and hit.

A synthetic view of the finding algorithm outcome is depicted in Fig. 3 in terms of its efficiency over the inner modules region of the TRD station 0. The color code represents the fraction of tracks having TRD-HR hits attached, in steps of 5 % for each location on the wall. Structures unrelated to the TRD wall geometry are seen in the figure as sudden changes in the efficiency values over short distances. Such structures are e.g. the outside border of $20-30$ cm width with $\epsilon > 90$ %, the 40 cm band extending around $y = 0$ with ϵ as low as 70 % or the dip around $y = 0$ with even lower efficiencies. Not presented here, but qualitatively similar, is the track matching efficiency for the default TRD solution.

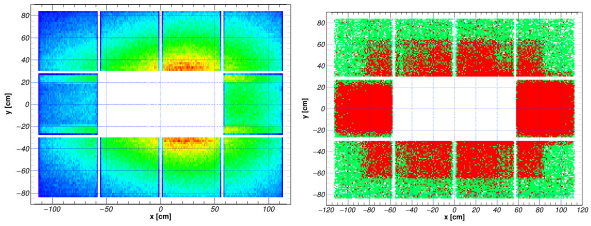

Figure 4: Yield of tracks at TRD entrance before updating with hit info (left) and of rejected TRD hits, although their χ^2 to track fulfilled the selection criterion (right).

In Fig. 4, causalities for the systematic structures observed in Fig. 3 and the subsequently low global efficiencies are searched in the $x-y$ dependence of two observables. The successfully to TRD layer 0 propagated tracks are shown in the left panel and the TRD hits rejected by the tracking algorithm with χ^2 values matching the selection criteria on the right. The two representations prove the tracking efficiency of CBM to be significantly lower in a 40 cm wide region centered around $y = 0$, while for the region marked in red in the right panel of Fig. 4, double tracks seem to be produced, which are randomly matched with TRD hits.

It has been shown that the STS/MVD seeding has quasi-blind spots around $y = 0$ and large areas of piled-up hypotheses which render the particle reconstruction efficiency map fragmented. On the other hand TRD-HR does not suffer from such geometric effects and has orders of magnitude better position resolution at a large lever arm from the target. Such observations suggest that the CBM tracking in particular and the physics program in general would largely benefit, if TRD-HR would be used actively in the tracking algorithm, i.e directly in the process of track seeding. The increase in combinatorics for track generation should be compensated by corrected non-uniformities in the efficiency map and by producing in general much larger track reconstruction capacities for the CBM experiment, especially in the hot region at low momentum.

[1]The time response is being currently implemented for the default TRD model.

References

[1] M. Petris et al., Nucl. Instr. and Meth., A732 (2013) 375.

[2] A.Bercuci et al., CBM Progress Report 2018 (2019) 87.

[3] A.Bercuci et al., CBM Progress Report 2018 (2019) 79-82.

[4] A.Bercuci et al., 35th CBM Collaboration Meeting, https://indico.gsi.de/event/10319/contributions/42879/attachments/30694/38179/TRD-HR-Tracking.pdf.

Position reconstruction in DESY 2017 testbeam data *

A. Puntke[1] *and P. Kähler*[1]
[1]Institut für Kernphysik, WWU Münster, Germany

Dataset for this analysis

Reported here is an analysis on data which have been recorded with TRD modules during a testbeam campaign at DESY in 2017. Detector modules of TRD type 8/2015, as used now in mCBM, with cathode pads of about 7.2 x 155 mm^2, have been crossed directly by DESY/TB22 electron beam of fix, but variable beam momentum [1].

While the main purpose of the campaign was to perform comparative radiator measurements, the dataset is used here to test position reconstruction of electrons along the beam axis. For this, data from three TRD modules with equivalent orientation (y-position reconstruction) are included, with z-positions at 0, 560 and 1120 mm. The radiator configuration was as follows: Layer I with the full PE foam foil radiator of 315 mm overall thickness, layer II and III with the 15 mm detector-near part only [2].

For readout, prototype version 2.0 of the SPADIC chip with 240 ns peaking time (1$^{\text{st}}$ order shaper) was employed, data transport via multiple parallel AFCK (synchronised to timing master) in "Simple-Microslice" mode. The self-trigger concept of this chip version was not yet optimised with respect to efficient reconstruction, e.g. displaced multihit-retrigger can occur within one channel of a charge cluster. Thus, careful recomposition of hit messages is required during clusterisation. In addition, a bug in the internal data handling of the chip was limiting the transmission efficiency of data, entailing the particular obligation to ensure the analysed dataset to be unbiased in what concerns the signal on adjacent pads. Anyhow, the data of this testbeam campaign are still valuable, e.g. with the electron beam being registered along multiple detector layers.

SPADIC signal clusterisation

To be able to process the hits of electrons in a TRD, SPADIC signals need to be grouped in clusters. The clusterisation algorithm for a TRD module to build a group of signals, i.e. a cluster, works as follows:

1. Select the earliest not already clustered signal. Add this *StartMessage* to the cluster.
2. Find a signal *CandidateMessage* with a time not more than 200 clock cycles later than *StartMessage*.
3. If *CandidateMessage* has a temporal distance less than 31 clock cycles to any signal which is already in the cluster and also there is yet a signal in the cluster with a channel difference to the *CandidateMessage* of less or equal than 2, add it to the cluster.
4. Go to step 2 and try to add another signal, otherwise the cluster is complete and called *hit*.

This implementation is stable against temporal segmentation of signals from a channel into many messages and against loss of signals from single pads in general, which is both present in data recorded with this SPADIC version.

The minimum of ADC values recorded at the start time of the cluster is subtracted from charge values as dynamic baseline correction. The y-positions of the clusters are calculated then with a centre-of-gravity method with the maximum ADC value of each involved channel as weight:

$$d = w \cdot \frac{\sum_{i=0}^{N-1} q_i \cdot (C_{\text{start}} + i)}{\sum_{i=0}^{N-1} q_i}, \qquad (1)$$

where w is the pad width, N the number of involved channels, q_i the charge-equivalent on channel/pad i inside the hit and C_{start} the left/lower starting pad. d yields the position (here: y) of the hit relative to the start of general pad counting.

Temporal alignment

The data streams of the three TRD modules included in this analysis were corrected for remaining time offsets of the early synchronisation algorithm. The time offsets have been determined by requiring maximum coincidence. The analysis is not prone to loss of epoch messages.

Grouping of coincident hits

To find tracks through the three TRD modules, the hits from the modules TRD0, TRD1 and TRD2 need to be matched. This is done as follows:

1. Select a hit which is not yet grouped and add it to the group.
2. Find a hit from the other modules which has a temporal difference of not more than 3 clock cycles and a position difference of not more than 1 channel to at least one hit in the group.
3. Add the found hit to the group and do not consider further hits in this modules' hit list.
4. Go to step 2 and try to add another hit, otherwise the group is complete and called *track*.

The algorithm is sketched in Fig. 1.

* Work supported by BMBF grants 05P16PMFC1 and 05P19PMFC1.

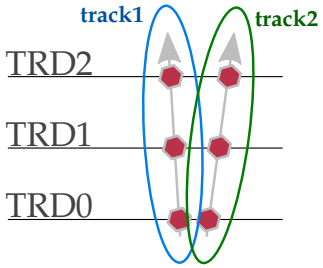

Figure 1: Sketch of grouping algorithm for simple tracking.

Spatial alignment

The three TRD-modules have been positioned perpendicular to the beam axis. Thus, deviations in the reconstructed y-positions within one track can be used for an alignment of the single modules in software as preparation for simple tracking implementations. In the following, only tracks which contain hits in all three detectors are considered. The distributions of the differences $y_N - y_0$ from the hit in TRD(N) to the corresponding hit in TRD0 have been evaluated. These distributions were fitted with Gaussian functions, resulting with the Gaussian mean values as spatial correction. Typical values are $y^{\text{offset}}_{\text{TRD1}} \approx 0.7$ mm and $y^{\text{offset}}_{\text{TRD2}} \approx 1.6$ mm. An example of these distributions after alignment is shown in Fig. 2. The origin of the non-Gaussian tails of the distributions is under investigation, also what concerns the contribution from Bremsstrahlung and beam divergence. Clearly visible is the broadening for the case TRD2-TRD0 due to additional multiple scattering in TRD1. The asymmetry in the distributions originates from detector acceptance effects.

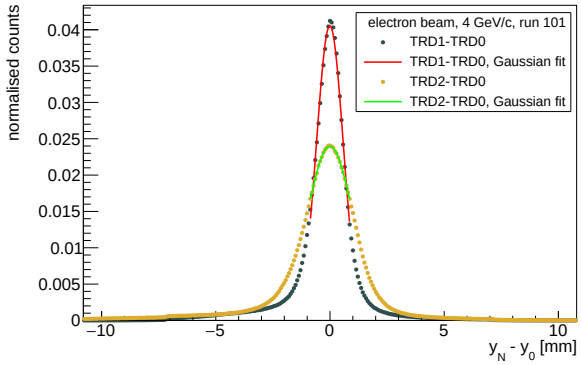

Figure 2: Spatially corrected distributions of differences $(y_N - y_0)$ from a hit in TRD(N) to the corresponding hit in TRD0 fitted with Gaussian functions. Normalised to area.

Position resolution

The width of the distributions $(y_N - y_0)$ can be used as measure for the detector position resolution. Nevertheless, a non-zero difference is expected not only from the detector not being a perfect system, but a broadening is also caused by small-angle scattering and Bremsstrahlung of the beam electrons. This already got visible in the comparison of $(y_2 - y_0)$ and $(y_1 - y_0)$ in Fig. 2: TRD2 registers a wider position distribution.

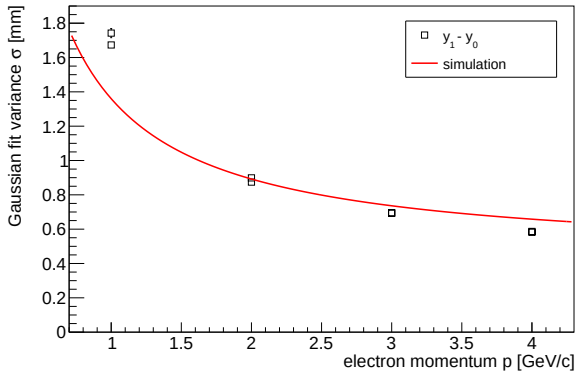

Figure 3: Gaussian variance σ of $(y_1 - y_0)$ distributions versus beam momentum for two data sets. Position resolution of both TRD layers contributes to σ as well as multiple scattering and Bremsstrahlung.

Small-angle scattering is less pronounced for particles with larger momentum p. Fig. 3 shows the Gaussian fit variances σ of $(y_1 - y_0)$ distributions for different beam momenta. Further shown is the expectation due to multiple scattering of electrons as calculated with the Highland-Lynch-Dahl formula for an assumed material budget of $X/X_0 = 2.1\%$, convoluted with the expected position resolution of 300 μm for each of the two TRD layers [3]. While similar shape of simulation and data is found, a deviation of the slope is visible. We note, that Bremsstrahlung is not yet included in the calculation.

Track reconstruction

Through coincident hit groups (tracks) which contain hits from all three detectors, linear fits were done, using their y- and z-positions. Further analysis based on such track fits is currently ongoing, e.g. beam divergence can be taken into account via track fit angles.

References

[1] F. Roether, P. Kähler et al., "Electron test beam campaign of the CBM-TRD at DESY", CBM Progress Report 2017

[2] P. Kähler and F. Roether et al., "The transition radiation detector in the CBM experiment at FAIR", Nucl. Instrum. Meth. **A958** (2020) 162727.

[3] C. Blume and C. Bergmann and D. Emschermann, "The Transition Radiation Detector of the CBM Experiment at FAIR", Technical Design Report, FAIR, 2018

Charge reconstruction in DESY 2019 testbeam data*

A. Meyer-Ahrens[1] *and P. Kähler*[1]
[1]Institut für Kernphysik, WWU Münster, Germany

DESY 2019 testbeam

From 18 August to 1 September 2019, the TRD group carried out testbeam measurements at DESY in Hamburg. Its main goal was the measurement of electron spectra (dE/dx+TR) with the TRD, depending on radiator thickness and electron momentum. Furthermore, the campaign served as a test of the candidate version for the final front-end ASICs, SPADIC 2.2. TRD prototype modules have been set up at DESYII beam line TB24, which is delivering secondary electron beam with variable beam momentum. During this campaign, momenta from 1 to 4 GeV/c have been chosen. The setup is shown in Fig. 1.

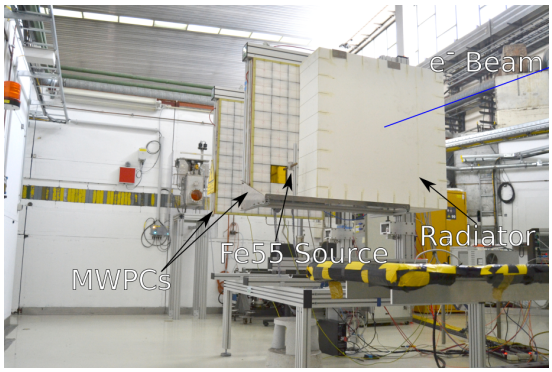

Figure 1: CBM-TRD setup used at the 2019 DESY testbeam: The front MWPCs was equipped with two SPADICs, enabling readout at the beam spot and at the position of the ^{55}Fe source.

The detectors have the default TRD wire geometry, and were operated with Xe/CO_2 (85:15). The anode voltage was set to 1800 V, the drift field was at the design value of 100 V/cm. According to Garfield calculations, these settings correspond to a gas gain of about 1500 [3].

Radiator comparison

Radiator boxes with thicknesses 10, 15, 20, 25 and 30 cm have been prepared to be inserted in front of the detector. These radiators are of same type as foreseen for the final CBM-TRD, i.e. consisting of 2 mm thick PE foam foil mats, housed in a Rohacell box which is open on the detector side. The carbon-grid in the detector entrance region was filled with 7 x 0.2 cm of additional PE foam foils, which is also in agreement with the final TRD design.

* Work supported by BMBF grant 05P19PMFC1.

Front-end electronics

The TRD modules were equipped with version 2.2 of the SPADIC ASIC, which is the candidate version for the final TRD readout chip. The analogue part of the chip features a 1st order shaper with the new shaping time constant of 120 ns. The forced-neighbour readout concept, which releases to send the signal values from adjacent cathode-pads in the same time window as for the self-triggered central pads, was hardened in SPADIC 2.2 for efficient data reconstruction: with the new "re-trigger protection", each channel is triggered only once to ensure compact message groups for fast clusterization.

Simulations

For evaluation of the recorded testbeam data, simulations of detector and radiators have been carried out. To simulate energy loss spectra of electrons in a TRD, a standalone simulation described in [1] has been adapted for the CBM-TRD. The parameters which have been used can be found in [2]. As the code simulates regular radiators, the irregular foam mats as foreseen for our TRD modules have been effectively parametrised in terms of a regular radiator. Simulated spectra for the used radiator thicknesses at an electron momentum of 3 GeV/c can be seen in Fig. 2. The simulated spectra show a clear trend for higher energy losses per electron for thicker radiators, caused by an increase of the TR yield with radiator thickness.

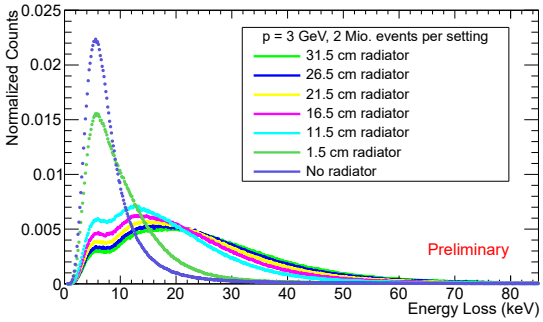

Figure 2: Simulated electron energy loss spectra (energy loss through ionisation + TR photons) for different radiator configurations at an electron momentum of 3 GeV/c. Each spectrum has been normalised by its area.

Calibration source

In parallel to the beam measurement, a ^{55}Fe source has been positioned in front of the detector and read-out with a SPADIC chip to monitor the gas gain. Usage of the corresponding data stream for calibration of the energy loss spectra is currently in preparation. A reconstruction of the energy deposition spectrum of the source measurement is shown in Fig. 3. The emissions of K-line de-excitations after decay to ^{55}Mn are reconstructed, fitted with a Gaussian function and calibrated to the known value of 5.96 keV ($K_{\alpha 1}$, $K_{\alpha 2}$, K_{β}). It was possible to optimise the reconstruction method in terms of energy resolution by requiring the lowest σ/μ of the Gaussian fit. We note, that noise contribution was observed during the measurements, leading still to a value of $\sigma/\mu = 15.6$ % with the gain setting of this measurement, while the design goal is about 10 %.

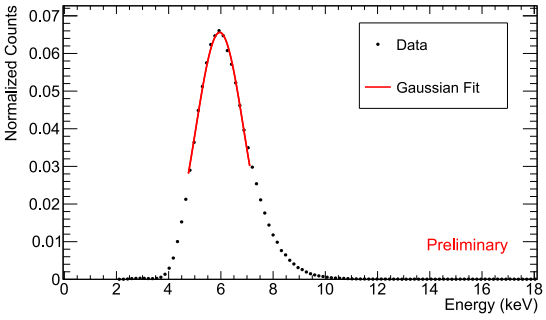

Figure 3: Spectrum from ^{55}Fe source. The main peak is fitted with a Gaussian function and calibrated to 5.96 keV.

Electron spectra

For reconstruction of the energy loss spectra with electron beam, the following procedure is employed: signals are filtered according to quality criteria aiming to exclude noise triggers. The maximum ADC value of accepted pulses is taken as charge equivalent, after subtraction of a fixed baseline. Following, clusterization of such digis from neighboured cathode pads with same readout time is performed. The charge of the cluster is the measurement of the energy loss. The reconstructed energy loss spectra for the different radiator configurations can be seen in Fig. 4.

Two selection criteria have been applied: i) Clusters with a width of two or less pads are excluded, as they are technically not expected by the readout concept and could miss a part of the deposited charge. ii) Clusters outside the well collimated beam spot were excluded.

In the spectra, a trend for larger energy losses for thicker radiators is clearly visible, which is in good agreement with the simulation (see Fig. 2). Exception is, that we see no significant differences between the 16.5 cm and the 21.5 cm radiators, while the trend for higher TR yield is still continued for thicker radiators, i.e. 26.5 cm and 31.5 cm. We assume a mix-up of the 15 cm and 20 cm boxes inadvertently occurring during radiator exchange.

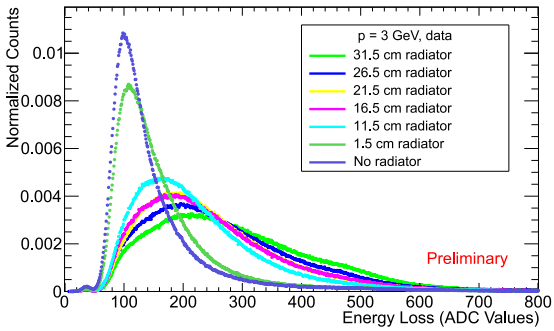

Figure 4: Energy loss spectra of electrons for different radiator configurations at an electron momentum of 3 GeV/c. Each spectrum has been normalised by its area.

Since no correction for signals exceeding the range of the SPADIC ADC with their maximum value was implemented in this analysis yet, a slight excess of the measured spectra at around 500 ADC units can be seen, which is not visible in the simulated spectra. This effect is in principle well known, and corrections are in preparation.

Discussion and outlook

Our goal is to compare the measured and simulated spectra on an absolute basis, using a calibration with the ^{55}Fe source. In first attempts, the measured spectra did appear at larger energy values and/or more narrow than the simulation, which is currently not understood.

This finding is subject of ongoing analysis. A possible bias introduced by the trigger thresholds seems excluded by comparison of data subsets, and also other checks did not provide explanations up to now. In a next step, the simulated spectra will be used as input for an existing full-system simulation of the CBM-TRD as described in [4].

Local gain variations will be investigated with existing ^{55}Fe source scan setups in the laboratory, as soon as front-end electronics will be available in sufficient number.

Overall, we note the already very good agreement of scaling with radiator thickness in simulation and measured data. We see this as validation of the simulations with the parametrisation for the irregular radiator.

References

[1] A. Andronic and J. P. Wessels. “Transition Radiation Detectors”, Nucl. Instrum. Meths **A666** (2012) 130.

[2] A. Meyer-Ahrens, “Sim. of TRD energy loss spectra for DESY”, 35th CBM Week, https://indico.gsi.de/event/10319/

[3] C. Blume and C. Bergmann and D. Emschermann, “The Transition Radiation Detector of the CBM Experiment at FAIR”, Technical Design Report, FAIR, 2018,

[4] E. Bechtel, “Recent developments of digitisation and reconstruction algorithms for the TRD with rectangular pads”, this report.

Preparation of the SPADIC 2.2 based readout of the TRD for the mCBM 2020 beamtime *

P. Raisig[†1], *F. Roether*[1], *P. Kähler*[2], *D. Spicker*[1], *and D. Schmidt*[3]

[1]Institut für Kernphysik, Goethe-Universität Frankfurt, Germany; [2]Institut für Kernphysik, WWU Münster, Germany;
[3]Infrastruktur und Rechnersysteme in der Informationsverarbeitung, Goethe-Universität Frankfurt, Germany

Introduction

After the integration of two large TRD modules into the mCBM experimental setup in 2018 [1], the required preparations for a successful data-taking in the 2020 mCBM campaign have been approached in 2019. Therefore, among other things:

- new front-end boards (see [4] for more details) with in total 24 of the revised SPADIC 2.2 per module were installed on the detectors
- firmware for the data processing boards (the AFCK) for readout of the SPADIC 2.2 chips via a CROB multiplexing layer was commissioned
- a software package was prepared which handles the unpacking and translation of data produced by the new SPADIC 2.2 for further analyses.

Detector setup

For the upcoming mCBM 2020 beamtime campaign, the already 2018 installed TRD modules have been fully equipped with a new version of readout electronics. SPADIC 2.2 features a faster shaping time of 120 ns in the analogue part and a newly designed message building block in the digital part with increased bandwidth efficiency in the uplinks. The mTRD setup consists of two detector modules with 768 readout channels each. A picture of one of the two TRD chambers with mounted front-end electronics is shown in Fig. 1. The front-end boards are visible in green. Every board carries four SPADIC 2.2 of which each is connected to 32 readout channels.

The modules follow the general chamber design as foreseen for the future CBM-TRD. The modules are mounted on the beam-table and are electrically decoupled. For operation of the detector, periphery and supply systems installed on-site were:

HV – The detectors are supplied with high-voltage for their amplification and drift field by HV modules which have been installed in an own rack in the general mCBM service area. The modules are free-floating and thereby decoupled.

LV – Also the LV supplies are separated. 12 V are transported into the cave and DC-DC converted with FEAST modules to the target voltage of the readout electronics. Necessary ground connections follow a canonical star topology.

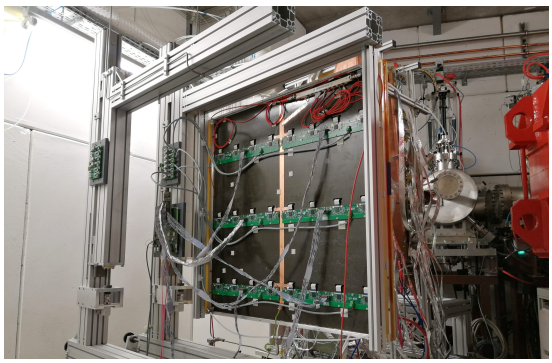

Figure 1: Rearview of one of the two TRD modules of the mCBM setup with SPADIC readout. On the back-side of the chamber 24 SPADIC 2.2 ASICs on six front-end boards are arranged in three rows. Each of these board rows can read two pad rows with up to 128 pads each.

Gas – For the operation of the mTRD detectors an Ar/CO_2 gas mixture is utilised, provided by the TRD gas mixing station. Further on an analysis station monitors the gas returning from the modules.

These systems can be controlled remotely. Measured values are available for live monitoring and fully logged.

DPB firmware

In preparation for the common readout in the mCBM setup the DPB firmware for the TRD has been implemented with the necessary data-preprocessing to generate microslices in accordance to the FLES specifications [6]. For this a message decoder was implemented which generates a SPADIC message container from the SPADIC message frames. The message container contains all the metadata of the hit message, i. e. the elink ID, channel ID, timestamp, hit type, multihit flag and the number of samples, as well as up to 32 ADC samples.

After that the message containers are sorted into their respective microslices. This is done through a time gating module which controls the data flow of the hit message containers. The hit messages of each elink are continuously passed through until the first message arrives which belongs to another microslice. Then the data flow is stopped

* Work supported by BMBF grants 05P19PMFC1 and 05P19RFFC1 and HGS-HIRe.

† praisig@ikf.uni-frankfurt.de

for that particular elink until all elinks received the first message of the next microslice. For more detail on the implementation see [5].

The sorted hit messages are then serialised into an efficient 64 bit format, packed into microslices and sent to the FLIB. The data-preprocessing as well as the microslice generation has been successfully tested during the 2019 DESY testbeam campaign [3].

Following the DESY testbeam campaign and in preparation for the mCBM campaign in the spring of 2020 the TRD DPB firmware was updated to support the CROB based readout of the SPADIC 2.2. The CROB features 3 GBTx ASICs with 14 uplinks each, therefore the data-preprocessing had to be modified from a total of 6 uplinks to 42 uplinks. In addition to the FPGA firmware, the control software had to be updated to support the GBTx firmware.

SPADIC 2.2 message unpacker

The SPADIC 2.2 message is a highly optimized container for the transfer of the raw information generated due to a registered signal on a channel ("hit message"). However, for further processing of the information the message needs to be unpacked and written into an analysis oriented container. For this purpose, a completely new SPADIC *unpacking* software was written. The new version not only suits the general format and data flow of mCBM [2], but also provides online-monitoring capabilities of the incoming data stream.

From regular hit messages the unpacker extracts information about the hit time, the trigger type, all forwarded ADC samples and whether this hit message follows directly to a previous signal ("multi-hit"). The package provides several modes of operation, varying between a focus on performance and debugging.

The software also translates the position information from the hit message into a global CBM address. The reconstruction is based on the channel ID in the local ASIC coordinate system and the ID of the ASIC in the global TRD coordinate system. While the local channel ID can directly be read from the SPADIC 2.2 message, the ASIC ID has to be reconstructed via the eLinkID and the ID of the AFCK. The mapping between the given information in the SPADIC 2.2 messages and the global channel addresses in the CBM address scheme is read from parameter files into the unpacker, which have to be prepared beforehand.

A first test of the software package took place at the DESY 2019 testbeam campaign [3]. One of the plots used to monitor the data quality online, is depicted in Fig. 2. The figure is a geometrical representation of a TRD chamber, where the x-axis represents the pad columns and the y-axis the pad rows while the z-axis displays the amount of hit messages on a given pad. In this case, a period of data recording during the DESY 2019 testbeam campaign was monitored. The distribution shows the expected values, since only two ASICs were mounted at the according positions. A detailed review of the DESY 2019 testbeam campaign can be found in this report [3].

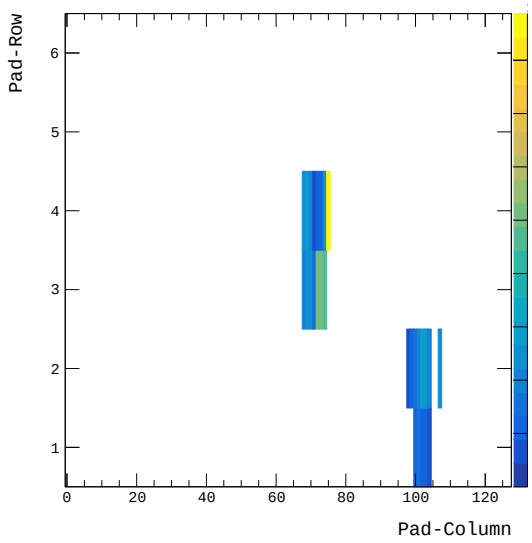

Figure 2: Hit distribution map of a TRD module, as provided by the online monitor part of the unpacking software package. This map corresponds to data recorded during the DESY 2019 campaign. While, the x- and y-axis correspond to the pad row and column of the chamber, the z-axis refers to the absolute number of hits on the given channel.

For the upcoming mCBM campaigns, the performance of the unpacker especially in terms of processing time will be subject to extensive tests. Further on, the set of provided figures for online data monitoring will be extended and optimized.

References

[1] C. Blume and the CBM-TRD working group, "Summary of the TRD project", CBM Progress Report 2018, *doi:10.15120/GSI-2019-01018*.

[2] C. Sturm, D. Emschermann and N. Herrmann for the CBM collaboration, "Start of mCBM Commissioning", CBM Progress Report 2018, *doi:10.15120/GSI-2019-01018*.

[3] A. Meyer-Ahrens and P. Kähler, "Charge Reconstruction in DESY 2019 testbeam data", this report.

[4] F. Roether, N. Bialas, C. Blume, D. Schmidt, S. Schreiber, P. Fischer and R. Weihrich, "Update on the development of Front-End Boards for the TRD", this report.

[5] D. Schmidt, "Firmware Development for the TRD Data Processing Board Prototype", Master's Thesis, Goethe-University Frankfurt, 2019.

[6] D. Hutter, J. de Cuveland, "The FLES Detector Input Interface", CBM Technical Note *CBM-TN-20002*.

Time-of-Flight Detector

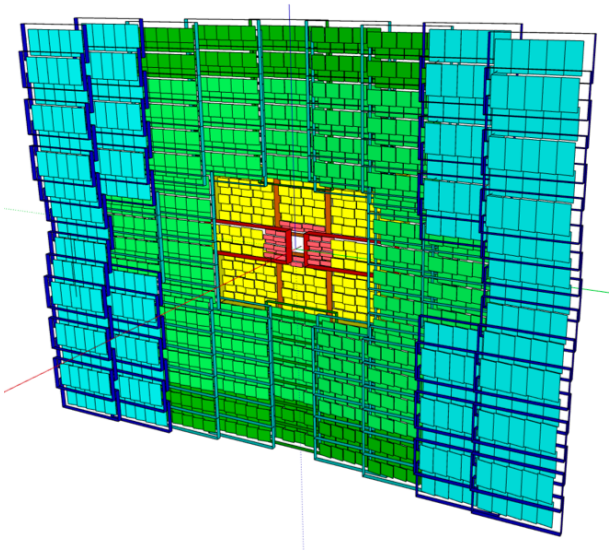

TOF - Summary

Ingo Deppner[1], *Norbert Herrmann*[1], *and the CBM TOF working group*
[1]Ruprecht-Karls-Universität Heidelberg, Heidelberg, Germany

The main activities in 2019 were focused on the operation of mTOF at mCBM [1] and eTOF [2] at STAR in the scope of the FAIR phase 0 programs but also on the detector R&D especially for the inner part of the CBM TOF wall and the Beam Fragmentation T0 Counter (BFTC). However, R&D on new resistive materials and gas mixtures were carried out as well.

The CBM TOF gas mixture consist of 90% R134a, 5% SF_6 and 5% iso-Butane with a total global worming potential GWP of about 2500. Due to new EU regulations which foresee a tremendous reduction of the emission of green house gases, the TOF group is assigned to find solution in order to do so. The current strategy foresees the recycling of the used gas without any emission in the atmosphere. An alternative solutions is the search of new eco-friendly gas mixtures [3] which show a comparable counter performance. The search of an alternative solution is also ongoing for the low resistivity glass [4]. Here a glass produced in a float process with a resistivity in the order of 5×10^9 was investigated. Even though the rate capability of this new material could be demonstrated the glass has the unfortunate characteristics that it changes steadily the resistivity with through-going accumulated charge which makes an R&D effort to use it in counters for the inner part of the TOF wall obsolete. However, the counter R&D for the MRPC1a - c prototypes foreseen for the high rate region is still ongoing as reported here [5, 6]. Based on the results obtained at mCBM and eTOF it can be concluded that the R&D effort on the MRPC2 and MRPC3 prototypes is finished and only minor optimization work is ongoing. As an example, a study on the relationship between the HV supply structure and the noise level on its nearest readout strip was performed with the outcome of an improved HV supply solution which will be transfered in the MRPC4 prototype as well.

The major attention in 2019, however, draw the TOF FAIR phase 0 program. eTOF at STAR started operation in Feb. 2019 with data taking of Au+Au events at $\sqrt{s_{NN}} = 11.5\,GeV$ with an eTOF efficiency of 85%. A damage of the FEE boards after several beam loss events required a major repair work. Data taking was continued in Dec. 2019 with the BES II RUN2020. Here a set of fixed target and colider runs could be taken (conf. Tab. **??**) until the experiment was shut down due to the Corona situation. First preliminary results from eTOF including the demonstration of its PID capability are presented here [2, 7].

The biggest effort, however, was put in mCBM in order to create the bases for upcoming TOF project milestones. In particular there is (i) the PRR for float glass MRPCs, (ii) the PRR for low resistivity glass MRPCs, (iii) the ASIC engineering design review (EDR) and (iv) the high voltage CDR. The first step in this regards was done in the Mach 2019 beam time obtaining valuable results as demonstrated here [**?**] and found its continuation in the beam time of March 2020 which will be the main subject in the next coming progress report. However, as an outlook we present in Figure 1 an event display showing a Pb + Au event obtained on April 2020 where 28 tracks could be reconstructed by mTOF. During this beam time rate and multi-hit conditions were realized that come close to the final CBM environment running at 10 MHz interaction rate. Such experimental conditions are essentially in order to prove the functionally of the full system.

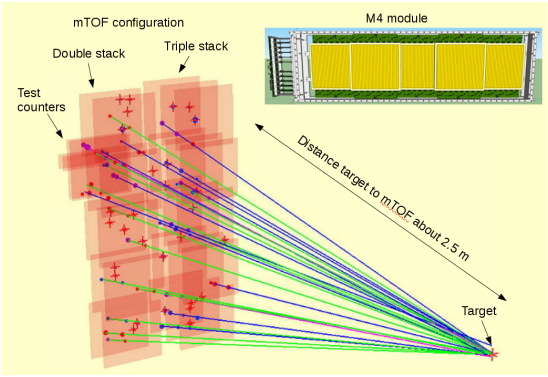

Figure 1: Event display of a high multiplicity Pb on Au event generating 100 hits in mTOF of which 28 tracks. 5 M4 modules are arranged in a triple and a double stack configuration in order to allow for tracking.

References

[1] Ch. Sturm *et al.*, CBM Progress Report 2019, this report

[2] I. Deppner *et al.*, FAIR phase 0, CBM Progress Report 2019, this report

[3] B. Wang *et al.*, CBM Progress Report 2019, this report

[4] X. Fan *et al.*, CBM Progress Report 2019, this report

[5] M. Petriş *et al.*, CBM Progress Report 2010, this report

[6] V. Aprodu *et al.*, CBM Progress Report 2010, this report

[7] P. Weidenkaff *et al.*, FAIR phase 0, CBM Progress Report 2019, this report

[8] Q. Zhang *et al.*, FAIR phase 0, CBM Progress Report 2018, this report

The test of MRPC with low resistivity float glass: 2019

X. Fan[1], Z. Liu[2,3], R. Beyer[1], J. Dreyer[1], R. Greifenhagen[1], D.W. Kim[5], R. Kotte[1], A. Laso Garcia[1], L. Naumann[1], K. Römer[1], D. Stach[1], C. Uribe Estrada[4], M.C.S. Williams[2,5,6], and A. Zichichi[2,6,7]

[1]Helmholtz-Zentrum Dresden-Rossendorf (HZDR), Dresden, Germany; [2]European Centre for Nuclear Research (CERN), Geneva, Switzerland; [3]ICSC World Laboratory, Geneva, Switzerland; [4]Benemerita Universidad Autonoma de Puebla, Maxico; [5]Gangneung-Wonju National University, Gangneun, South Korea; [6]INFN and Dipartimento di Fisica e Astronomia, Universita di Bologna, Italy; [7]Museo Storico della Fisica e Centro Studi e Ricerche E.Fermi, Roma, Italy

A new type of low resistivity float glass has been developed in CERN[1]. This glass is developed for high rate capable Multigap Resistive Plate Chambers (MRPCs). Therefore it could be an option for the Time-of-Flight (TOF) system of Compressed Baryonic Matter (CBM) experiment. During CBM experiments, MRPCs will be required to work at particle fluxes on the order of 1 to 5 kHz/cm^2 for the outer region and 5 to 25 kHz/cm^2 for the central region[2]. Thus, the rate capability is the key factor for the MRPCs in CBM TOF. The new low resistivity glass is developed as a commercial solution for increasing the rate capability of MRPCs, while maintaining the other key parameters like time resolution and efficiency. Samples of low resistivity glass is produced with a bulk resistivity in the order of $10^9\ \Omega \cdot cm$ and $0.4\ mm$ thickness with industrial standard. In the early tests in CERN, a 6-gap MRPC is assembled with low resistivity glass electrodes, and the efficiency reaches 90% at the flux of $90\ kHz/cm^2$[1].

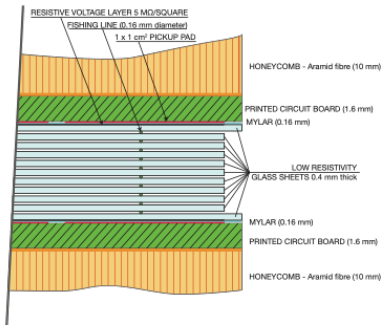

Figure 1: The geometry of 10-gap MRPC.

The MRPC is tested under high flux at the Electron Linac for beams with high Brilliance and low Emittance (ELBE) in Helmholtz-Zentrum Dresden-Rossendorf (HZDR) in Germany. The MRPC used in this test is a single-stack 10-gap MRPC with pad readout. The MRPC contains 2 outer glass electrodes with the area of $7 \times 9\ cm^2$ and 9 inner ones with the area of $5 \times 6\ cm^2$. The thickness of glass is $0.4\ mm$, the gap width is $0.16\ mm$. The detailed geometry of the MRPC is shown in Figure 1 The MRPC is tested under continuous single-electron beam of 30 MeV energy, and the beam spot at the MRPC is around $10\ cm^2$. The reference time is given by the RF from accelerator, and the flux and beam area are given by a set of scintillators.

The efficiency and time resolution scan of MRPC on dependence of the high voltage is presented in Figure 2 and Figure 3. The maximum efficiency of the MRPC amounts 97.0% and a time resolution of $36\ ps$ is accumulated at the voltage of $19.2\ kV$. A flux scan of the efficiency and time resolution is also operated, as shown in Figure 4 and Figure 5. While the flux of particles is tuned from $2\ kHz/cm^2$ to $200\ kHz/cm^2$, its time resolution degrades from $37\ ps$ to $60\ ps$, while the efficiency degrades from 97% to 95%. The high voltage is $19.6\ kV$.

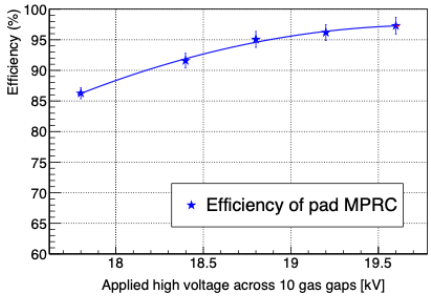

Figure 2: Efficiency as a function of high voltage

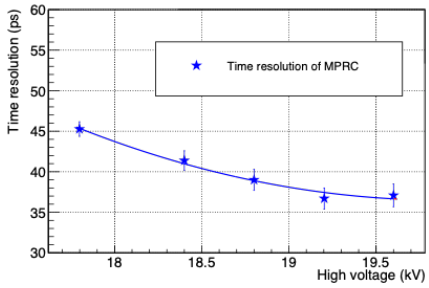

Figure 3: Time Resolution as a function of high voltage.

In the tests, it is discovered that the bulk resistivity will increase over time due to the current flow inside the glass sample. As it is possible that such effect will result in a reduction of MRPC performance, detailed researches are operated. It is found that the resistivity does not recover over relaxation (see Figure 6), but over reverse voltage (see Figure 7). The future application of low resistivity float glass in MRPC is also attached to the investigations of this effect. As a conclusion, the performance of MRPCs with low resistivity glass fulfills the requirements of CBM. Further long-term tests of MRPCs will be carried out in the

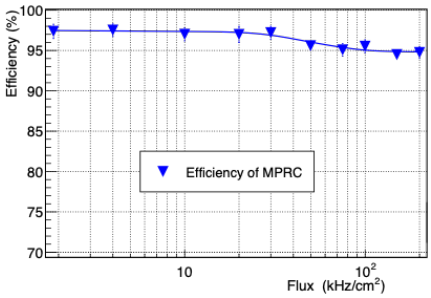

Figure 4: Efficiency as a function of flux.

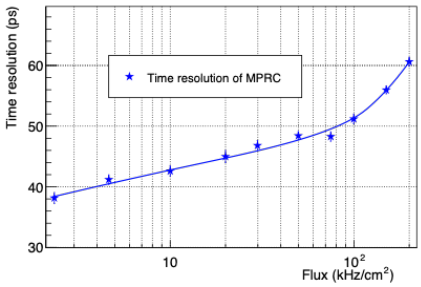

Figure 5: Time resolution as a function of flux.

year 2020 in CERN and HZDR.

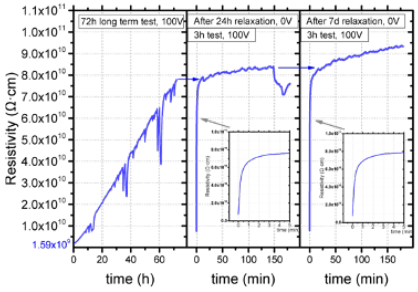

Figure 6: Bulk resistivity test with relaxation time.

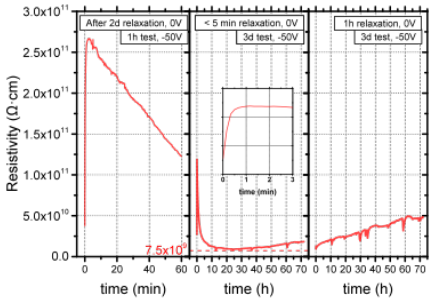

Figure 7: Bulk resistivity test with short relaxation and reversed voltage.

References

[1] Z. Liu, et al., MRPC detectors for ultra high rate applications[J]. NIMA, 2020, 959: 163483.

[2] I. Deppner, et al., The CBM time-of-flight wall: a conceptual design, J. Instrum.9 (10) (2014) C10014

Performance of CBM MRPC2 operated in ecological working gas mixtures *

Botan Wang, Yi Wang†, Dong Han, and Pengfei Lyu
Key Laboratory of Particle and Radiation Imaging, Department of Engineering Physics,
Tsinghua University, Beijing 100084, China

The 'F-gas regulation' [1] applied in 2015 aims at shrinking the production and emission of the Greenhouse Gas (GHG), which includes Freon (GWP = 1300) and SF_6 (GWP = 22800), the commonly used working gas components in MRPC operation. The uncertainty of the future usage of these gases has encouraged the development of gas circulation and recuperation system, and also, a lot of tests to find ecological gas substitutes [2]. For Freon, one of the most promising substitutes is HFO-1234ze (trans-$C_3H_2F_4$), and it is also regarded as a next-generation refrigerant, which indicates a good availability in the future. For SF_6, the searching work is started relatively later, and there is attempt given with replacements named 'Novec 4710' and 'Novec 5110' [4].

As a new molecule under study, it is reported that HFO-1234ze has a GWP value less than 1. Some of the ionization properties, such as ionization pair production and mean excitation energy, has been estimated by simulation methods [3]. Many existing experiments like ALICE, EEE, CMS that use RPC-type detectors have been testing the HFO-based gas mixtures, with wide types of components including iC_4H_{10}, SF_6, CO_2, He and Ar. A lot of results have shown good eco-gas performances with the existing RPC system, but at different working electric field [4]-[6].

The MRPC performance in ecological working gas mixtures has been an important issue in Tsinghua group, where the CBM-TOF detector MRPC2 (the former MRPC3a) has been developed and produced [7]. MRPC2 is a double-stack structure with 8 gas gaps and 32 readout channels. The width is 0.25 mm for a gas gap and 1 cm for a readout pitch (0.7 cm strip width + 0.3 mm gap). Working in 'standard gas' mixture, which contains Freon/iC_4H_{10}/SF_6 with a fraction of 90/5/5, the performance of the MRPC2 counters has fulfilled the requirements of the CBM-TOF system. The detection efficiency goes over 98%, and the individual time resolution is better than 60 ps.

The cosmic test system originally developed for the quality examination in MRPC2 mass production is used to test the detector performance in eco gas mixtures. This system uses three MRPC2 counters in test, PADI 10 as the Front-end Electronics, and TRB3 board for data acquisition. A 6-channel gas mixer is applied to flush the HFO-based working gas mixtures. For now, we have finished the performance test with the following gas mixtures and their fractions: (a) Pure HFO; (b) HFO/iC_4H_{10}/SF_6 90/5/5; (c) HFO/SF_6 95/5; (d) HFO/iC_4H_{10} 97/3; (e) HFO/iC_4H_{10} 95/5; (f) HFO/iC_4H_{10} 90/10.

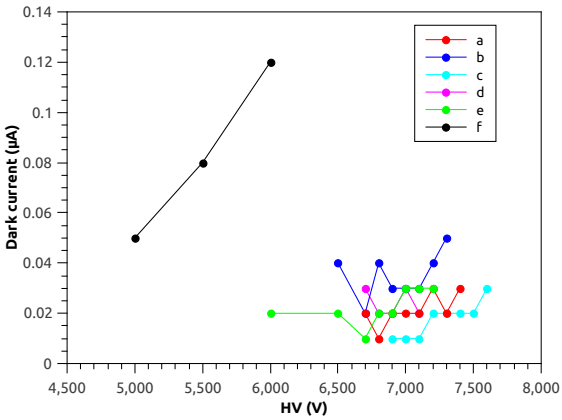

Figure 1: The dark current of the gas candidates.

For each eco gas mixture, the HV scan is carried out, and the corresponding efficiency, time resolution, cluster size and dark current of the tested MRPC2 are obtained. During the tests, the dark current has been monitored carefully to prevent detector damage at HV under these working gas with unknown characteristics. According to the operation experience under cosmic ray, HV is shutdown when the dark current of a counter goes over 100 nA, and the tested gas candidate will be abandoned. Figure 1 shows the dark current level with different gas mixtures, among which the candidate (f) can't reach the efficiency plateau under the dark current control. For other candidates, the efficiency and cluster size are shown in Figure 2. The efficiency is defined as the ratio of the coincident events of three counters over that of the two reference counters, and the cluster size as a reflection of the streamer fraction is the average number of the continuous fired strips in each event.

The working point for HFO-based candidates lies around 7 kV (140 kV/cm electric field in gas gaps), which is higher than 5.5 kV for the 'standard gas'. Adding the iC_4H_{10} will help decrease the working HV to some extent. And SF_6, due to its strong electronegative feature, will increase the working HV. From Figure 3, we can find that SF_6, with a very high GWP value though, plays an important role to a better time resolution. Further investigations should be taken to find an eco-gas substitute for SF_6.

Based on the results, we can make the preliminary suggestion that the best eco gas alternative for now is HFO

*The work is supported by National Natural Science Foundation of China under Grant No. 11927901, 11420101004, 11461141011, 11275108, 11735009, U1832118, and by the Ministry of Science and Technology under Grant No. 2018YFE0205200, 2016YFA0400100.
† yiwang@mail.tsinghua.edu.cn

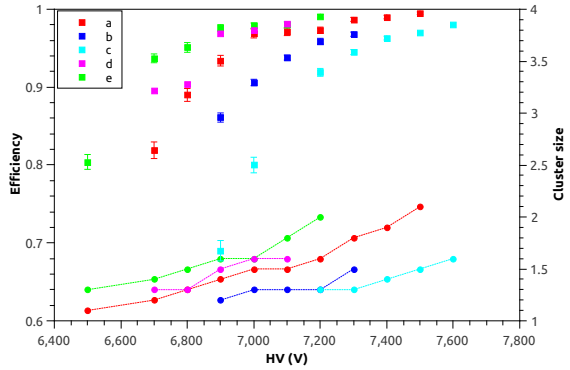

Figure 2: The efficiency (square dots) and cluster size (round dots) of the gas candidates.

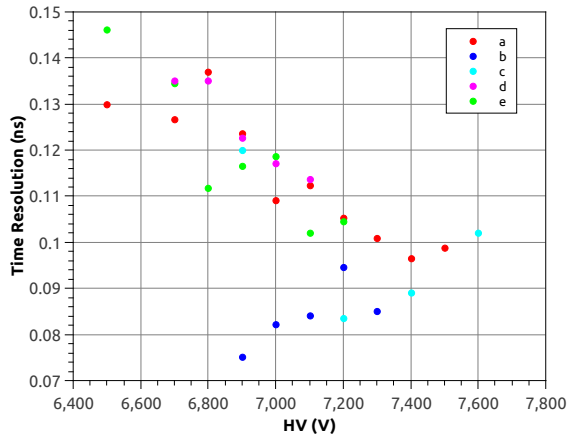

Figure 3: The fight-time resolution between the tested MRPC2 and reference in different gas mixtures.

with iC_4H_{10} at a fraction of 95/5 (mixture e in the plots). The efficiency can reach 97.4% at 6.9 kV, and the flight-time resolution is 115 ps (81.33 ps for a single detector). The GWP value of this gas mixture is as low as 1.2. The best time resolution at working point is obtained by the mixture of HFO/iC_4H_{10}/SF_6 with 90/5/5 fraction (mixture b in the plots). The efficiency at plateau is 96.8% and the time resolution is better than 90 ps.

The eco-gas cosmic test is still ongoing, and different fractions of the gas mixture and more components such as CO_2 and He will also be tested. These results would be very helpful to understand the potential ability to operate the CBM-MRPC counters with less environmental impact.

References

[1] European Commission. https://ec.europa.eu/clima/policies/f-gas/legislation_en

[2] M. Capeans, et al. NIMA. 845 (2016) 253-256.

[3] G. Saviano et al. JINST. 13 (2018) P03012.

[4] R. Guida et al. Talk on RPC2020. https://agenda.infn.it/event/19942/contributions/108497/

[5] A. Bianchi et al. Talk on RPC2020. https://agenda.infn.it/event/19942/contributions/108463/

[6] M. P. Panetta et al. Talk on RPC2020. https://agenda.infn.it/event/19942/contributions/108467/

[7] Y. Wang et al. JINST. 11 (2016) C08007.

Test results of high granularity MSMGRPC prototype for CBM – TOF wall*

M. Petriş[†1], *D. Bartoş*[1], *G. Caragheorgheopol*[1], *M. Petrovici*[1], *J. Frünhauf*[2], *I. Deppner*[3], *and N. Herrmann*[3]

[1]National Institute for Physics and Nuclear Engineering (IFIN-HH), Bucharest, Romania; [2]GSI Helmholtz Center for Heavy Ion Research GmbH, Darmstadt, Germany; [3]Universität Heidelberg, Germany

A new designed, assembled and preliminary tested MSMGRPC for the most demanding region of the CBM-TOF wall [1] was reported last year [2]. The strip pitch, the same for both HV and readout electrodes, is 9.02 mm. The 1.27 mm readout strip width leads to a transmission line impedance of $\sim$ 97 Ω, matched to the input impedance of the the front-end electronics. The high voltage strip width of 7.37 mm defines the granularity, taking into account the expected cluster size and the adjusted strip length of 60 mm (the CBM-TOF wall counters with the highest granularity). Two identical prototypes, 2 x 5 gas gaps of 140 μm gap size, were mounted one on top of the other in a gas tight and electromagnetically screened box.

Cosmic rays tests

The assembled counters were first tested in the detector laboratory of Hadron Physics Department from IFIN-HH using a gas mixture of 90%$C_2H_2F_4$+10%SF_6 and an electric field of 157 kV/cm (HV = 2 $\times$ 5.5 kV). In the experimental setup shown in Fig. 1, one counter was sandwiched between the top counter and the bottom plastic scintillator (10 cm length and 1.5 cm x 1.5 cm cross section). A front-end electronics (FEE) based on NINO chip [4] and a triggered data acquisition (DAQ) system equipped with CAEN TDCs were used for signal processing. A 3D view of the uniform cosmic-ray illumination across operated area (16 strips per counter) is shown in Fig. 2. For a 160 mV FEE threshold the estimated efficiency was of 95% with an average cluster size of 1.8 strips. A single counter time resolution of 64$\pm$9 ps was obtained after slewing corrections.

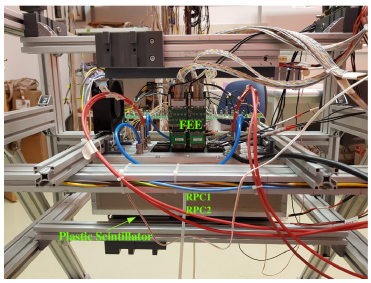

Figure 1: The cosmic ray experimental setup.

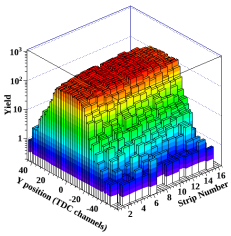

Figure 2: Cosmic ray hits distribution on the operated area.

In-beam tests

The prototypes were tested with reaction products (1.6A GeV ^{107}Ag beam incident on a Au target), in the mCBM test setup, in March 2019. The above mentioned prototypes were positioned in the experimental setup downstream relative to the counters developed for the outer zones of the TOF wall (Fig. 3 - left side). A diamond detector, positioned in front of the target was used as beam reference. The signals delivered by the detectors were fed into PADIX [5] FEE and processed by a free streaming DAQ equipped with GET4-TDCs [6]. For the estimation of the time resolution, one of the two above described prototypes was considered as reference (REF) and the other one as detector under study (DUT). The obtained system time resolution (includes the contribution of both REF and DUT counters) was of 78 ps. If an equal contribution of the two identical counters to the time resolution is considered, a single counter time resolution of 55 ps (including electronics chain contribution) is estimated. A lower efficiency obtained in the operation with the above mentioned free streaming readout chain, relative to the value obtained in the laboratory tests, is under investigation.

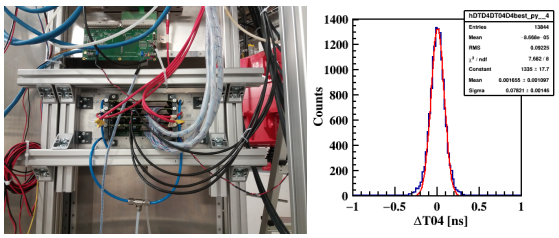

Figure 3: Position in the mCBM experimental setup (left). Calibrated time difference spectrum (right).

References

[1] CBM collaboration, N. Herrmann, ed., TDR for the CBM - TOF System. GSI, Darmstadt, 2014.

[2] D. Bartoş et al., CBM Progress Report 2018 (2019) 97

[3] D. Bartoş et al., Rom. Journ. Phys. 63, 901, (2018)

[4] F. Anghinolfi et al., Nucl. Instrum. Meth. A 533 (2004) 183.

[5] M. Ciobanu et al., IEEE Trans. Nucl. Sci. 61 (2014) 1015.

[6] https://wiki.gsi.de/pub/EE/GeT4/get4.pdf

*Work supported by Romanian Ministry of Education and Research NUCLEU Project Contract PN 19060103.

† mpetris@nipne.ro

Efficiency investigation of a high granularity MSMGRPC prototype for the inner zone of the CBM – TOF wall *

V. Aprodu[1], *D. Bartoş*[1], *G. Caragheorgheopol*[1], *M. Petriş* †[1], *M. Petrovici*[1], *L. Prodan*[1], *A. Radu*[1], *and V. Simion*[1]

[1]National Institute for Physics and Nuclear Engineering (IFIN-HH), Bucharest, Romania

The current design of the CBM-TOF inner wall [1] is based on double-stack multi-strip, multi-gap resistive plate counters (MSMGRPCs) with 2 x 5 gas gaps of 140 μm gap size, equipped with low resistivity glass electrodes. Their performances in terms of efficiency and time resolution, in direct beam tests or with exposure to reaction products over the full active area, in their operation in both triggered [2, 3, 4] as well as free streaming readout systems [5], recommend them as solution for the inner part of the CBM-TOF wall.

A double-sided MSMGRPC prototype, 2 x 5 gas gaps of 140 μm gap size, with the highest granularity (0.9 cm pitch and 6 cm strip length) of the CBM-TOF wall was reported in [6, 7]. A single counter time resolution of 67 ps

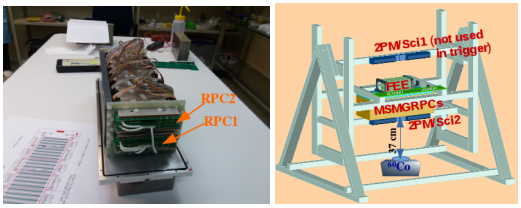

Figure 1: The two assembled MSMGRPCs mounted on the back panel (left). Experimental setup for cosmic rays and ^{60}Co source tests (right).

and a 95% efficiency were obtained in the cosmic ray tests. The counter signals were processed by a front-end electronics (FEE) based on NINO chip [8] and a triggered data acquisition (DAQ) system. In the operation in the mCBM setup in March 2019 with CBM - TOF FEE PADIX [9] and GET4 - TDCs [10], using a free - streaming readout, a lower efficiency was obtained. As a difference in the gains

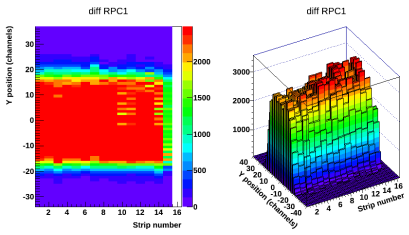

Figure 2: 2D (left) and 3D (right) plots of the mapping of the active area in a self-triggered mode, exposed to a ^{60}Co source positioned at 37 cm distance under the housing box.

between PADI and NINO FEE, (lower PADI gain) is the cause, an increase of the counter signal at the input of the PADI FEE is required. The solution was to assemble two new MSMGRPCs prototypes with an increased gap size of 200 μm and identical inner geometry and architecture for the high voltage and readout electrodes as of those reported in [6]. The two counters were first tested with cosmic rays and ^{60}Co radioactive source in the detector laboratory of Hadron Physics Department (HPD)/IFIN-HH. A gas mixture of 90%$C_2H_2F_4$ + 5%SF_6 + 5%i-C_4H_{10} was circulated through the counters at 4 l/h flow rate. For each counter 16 central strips were equipped at both ends with a FEE based on NINO chip [8].

The tests started with the mapping of the operated area, exposing the detectors to a ^{60}Co source (positioned at a distance of 37 cm from the detector housing box for an uniform exposure) and to the cosmic rays. The 2D and 3D plots (Fig. 2) of the hit distribution across the operated area, recorded in a self-triggered mode, show an uniform efficiency with pretty sharp edges at the ends of the strips, in radioactive source as well as in cosmic ray exposure.

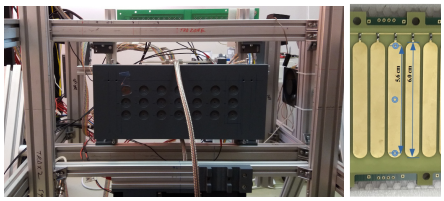

Figure 3: Multi-collimator mounted in front of the housing box (left). Exposed positions on a vertical column along the strips (right).

In order to investigate deeper the edge effects at both ends of the strips, due to possible electric field distortions in these zones, a multi-collimator made of Pb and fixed in a trovidur frame (Fig. 3 - left) was used. Each vertical col-

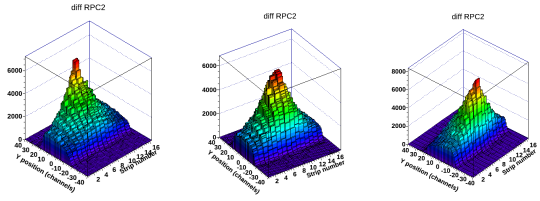

Figure 4: 3D - plots for the exposure of the active area to a collimated ^{60}Co source for up (left), center (middle) and down (right) positions along the strip.

umn of this multi-colimator has three colimators of 4 mm diameter distribuited along the strip length (Fig. 3 - right).

* Work supported by Romanian Ministry of Education and Research NUCLEU Project Contract PN 19060103.

† mpetris@nipne.ro

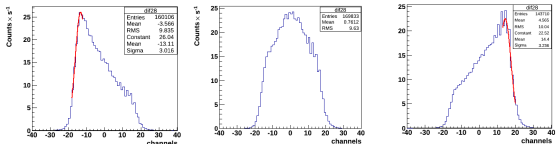

Figure 5: Position distribution for the exposure to a collimated ^{60}Co source for up (left), center (middle) and down (right) positions along the strip with the maximum yield.

As it is shown in Fig. 3 - right, the central one points to the middle of the strip, while the distance between the outermost two is 56 mm, (up and down, each one at 2 mm distance from the tip of the strip). Fig. 4 shows the 3D distributions of the hits over the operated area for each of the three described positions along the strips: up (left), center (middle) and down (right). The 1-D projections of these distributions (down (left), center (middle) and up (right)), along the strip with the maximum yield and normalized to the exposure time to the ^{60}Co source, are shown in Fig.5. The same value for the maximum of each of the three distributions confirms an uniform detection efficiency over the full length of the strip. Based on the position of the peaks in the yield of the distributions (Gaussian fits shown in Fig. 5) corresponding to 5.6 cm distance between the centers of the outermost collimators and the 0.025 ns/ch TDC calibration, a signal propagation velocity of 16 cm/ns is obtained.

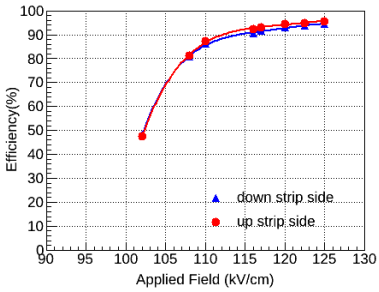

Figure 6: Efficiency as a function of field strength in the gas gap, measured with cosmic rays.

Further measurements addressed the quantitative estimations of the efficiency, cluster size and time resolution using cosmic rays. The counter called RPC2 (see Fig. 1) was sandwiched between RPC1 (positioned above RPC2 in the experimental setup) and the bottom plastic scintillator (10 cm length and 1.5 cm x 1.5 cm cross section), readout at both ends by photomultipliers and centered on the operated area, across the strips. The trigger signal for DAQ system was obtained from the coincidence of the signals delivered by the RPC1 and the bottom plastic scintillator. Due to the very low dark rate of both counters (less than 0.15 Hz/cm^2), in the performed measurements it was possible to operate the FEE at a very low threshold of 145 mV. The efficiency is estimated as the ratio between the number of coincident hits between RPC1, RPC2 and plastic scintillator and the number of coincident hits between RPC1 and plastic scintillator. Figure 6 shows the efficiency as a function of field strength in the gas gap. The working curve shows a 95% efficiency plateau at applied fields larger than 120 kV/cm (2 x 6 kV). Fig. 7 shows the average cluster size as a function of the value of one polarity of the applied high voltage, at the mentioned FEE threshold. The average cluster size, larger than two strips in the plateau region, could be due to the low value of the FEE threshold.

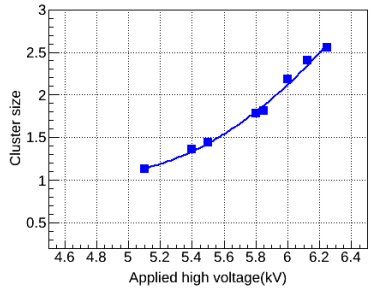

Figure 7: Average cluster size measured with cosmic rays.

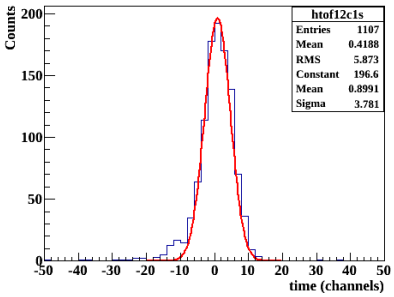

Figure 8: Time difference distribution between the two identical MSMGRPCs.

Fig. 8 shows the time difference between the two identical MSMGRPCs. The obtained single counter time resolution, if one considers equal contributions from each of the two identical counters, is of 67 ps for an applied high voltage in the efficiency plateau region.

The prototype performance was demonstrated in the laboratory tests and it is ready to be tested in the mCBM in-beam campaigns.

References

[1] I.Deppner et al., 2019 JINST 14 C09020

[2] M.Petrovici et al., 2012 JINST 7 P11003

[3] M. Petriş et al., 2016 JINST 11 C09009

[4] M. Petriş et al., Nucl. Instrum. Meth. A 920 (2019), 100.

[5] M. Petriş et al.,PoS ICHEP2018(2019) 663

[6] D. Bartoş et al., CBM Progress Report 2018 (2019) 97

[7] M. Petriş et al., this progress report.

[8] F. Anghinolfi et al., Nucl. Instrum. Meth. A 533 (2004) 183.

[9] M. Ciobanu et al., IEEE Trans. Nucl. Sci. 61 (2014) 1015.

[10] https://wiki.gsi.de/pub/EE/GeT4/get4.pdf

Update of the CBM-TOF inner wall design*

V. Duţă[1], *D. Bartoş*[1], *M. Petriş*[†1], *M. Petrovici*[1], *L. Rădulescu*[1], *and V. Simion*[1]
[1]1National Institute for Physics and Nuclear Engineering (IFIN-HH), Bucharest, Romania

The CBM - TOF inner - wall, covers a polar angle between 2.5^0 and $\sim 12^0$ of about 14 m^2 area around the beam pipe. The inner wall design was driven by the counting rate and the granularity requirements [1]. The anticipated counting rate for the inner zone is ranging from 30 kHz/cm^2 in the region of the beam pipe, to about 5 kHz/cm^2 at the largest polar angle mentioned above. A number of six versions for the architecture of the inner zone of CBM-TOF wall, from a cylindrical to a planar one, were investigated, each one in comparison with the others [3]. The current design is the result of the optimization in terms

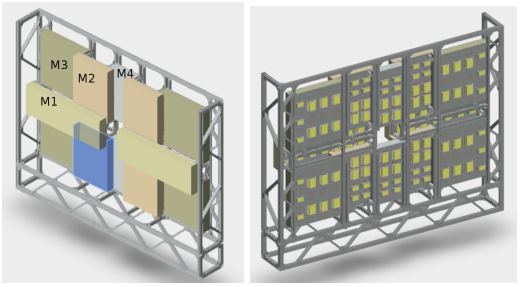

Figure 1: CBM-TOF inner wall architecture in the support frame: front,(left) and back (right) views.

of wall thickness along z direction, with minimum overlap between the counters as well as between the modules such to have a continuous coverage of the active area and optimization of the cost in terms of number of counters and electronic readout channels. All these constrains led to a modular concept defined by 12 modules of 4 types (M0, M1, M2, M3), staggered in z direction, such to obtain a continuous coverage of the active area. A mechanical frame is optimized in terms of material budget and precise positioning of the modules (see Fig. 1). The module M0

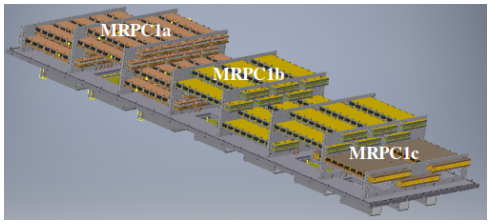

Figure 2: Counters mounted in module M0 with the mechanical supports fixed on the Al back panel.

positioned on the left side of the beam pipe, looking from the target position, can be translated up to 20 cm along the x axis in order to follow the beam bending due to the magnetic field, at different beam energies. A similar translation could be implemented also for the M0 module situated on the right side, if one considers measurements in which the polarity of the dipole magnet is reversed.

Based on the architecture of the MSMGRPC prototypes described in [2], the twelve modules were equipped with a total number of 470 counters which deliver a number of 30080 signals to the readout electronics. Inside a module the counters are staggered on four layers in z directions with a minimum overlap between them and continuous coverage of the active area, for a 8 m distance from the target. The mechanical supports which keep the coun-

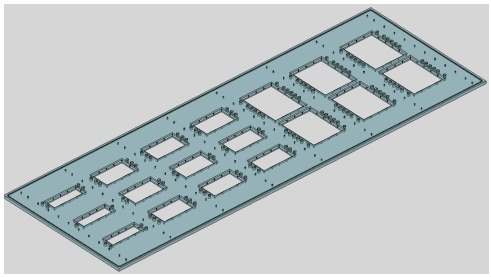

Figure 3: Architecture of the back panel of module M0.

ters in precise positions (Fig. 2) are fixed on an Al back panel of 12 mm thickness (Fig.3). Connectors soldered on both side of PCBs plates glued on the rectangular machined holes in the Al back panel (Fig.4 - left), transmit the signals from the counters to the readout electronics. All the feed

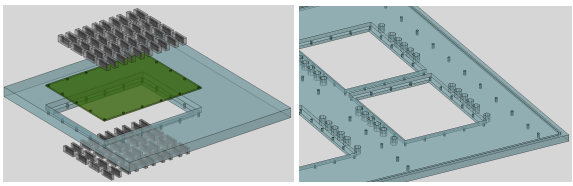

Figure 4: Zoomed view of the back panel:PCB plate with signal connectors on both sides (left), detail with the feedtroughs holes (right).

troughs for gas and high voltage connectors (Fig. 5 - green and orange connectors), mechanical supports for readout electronics and for mechanical implementation of the inner wall into the CBM experimental setup are worked out in the Al back panel (see the zoomed view of the back panel from Fig. 4 - right). The module is closed by a housing box made of a light composite material, electromagnetically screened

* Work supported by Romanian Ministry of Education and Research NUCLEU Project Contract PN 19060103.
† mpetris@nipne.ro

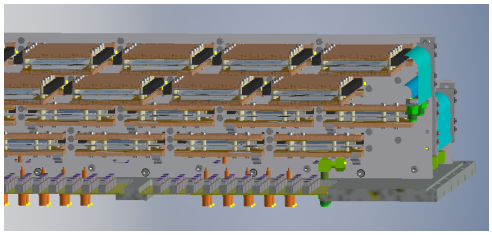

Figure 5: Cross section through a module; the gas (green) and high voltage (orange) connectors.

inside by a thin Cu layer. Each module contains up to three types of MSMGRPCs, with different granularities, depending on their position relative to the beam pipe. The 0.9 mm strip pitch is the same for all three counter types, their granularity being adjusted through the corresponding strip length of 60 mm (MRPC1a) [4], 100 mm (MRPC1b) [5] and 200 mm (MRPC1c) [6].

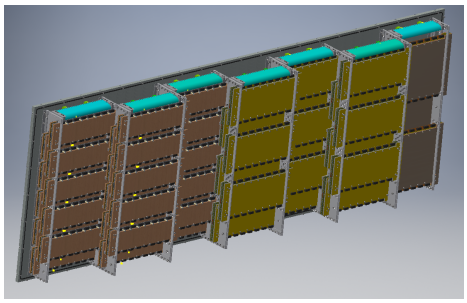

Figure 6: M0 module.

Module M0, shown in Fig. 6, is the most complex one. Its size is 2105 mm x 738 mm x 196 mm, being equipped with a number of 51 counters of all three types: 30 MRPC1a, 18 MRPC1b and 3 MRPC1c (see Fig. 2).

In order to be able to start its construction in the near future, we have to make sure that the back panel has enough mechanical strength, without any bending due to the weight of the mounted components and multiple mechanical machining. For this reason, dedicated mechanical strength calculations were performed in collaboration with the Department of Mechanical Strength of Technical University from Bucharest, using ANSYS software. The calculations took into consideration the design geometry of the module, the load of the module (taking into consideration the mass distribution) and the properties of the material of the back panel. In the performed calculations, mechanical stresses and strains, possible to appear in the horizontal position (corresponding to the position of mounting the counters in the module) as well as in the vertical position (as it will be installed in the TOF-wall) and during the transport and implementation in the experiment, were estimated. The maximum estimated deformation was not more than 340 μm and the maximum calculated stress was of 21 MPa, much smaller in comparison with 280 MPa yield stress of the material. Any possible significant irreversible deformation or bending were not evidenced by these mechanical strengths calculations.

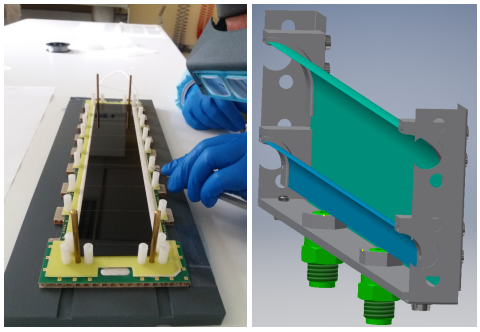

Figure 7: Left: Spacer distribution across the resistive electrodes. Right: Gas deflector.

For a proper operation of the counters of the CBM-TOF inner zone in high particle fluxes, a fast exchange of the gas mixture in the MSMGRPC gas gaps is important, taking into consideration the aging effects. In order to assure a fast refreshing of the gas, two technological solutions were implemented. The first one was carried out in the design of the MSMGRPCs where the spacers which define the gas gap size are distributed perpendicular to the long size of the resistive electrodes (Fig. 7 - left), along the strips, for a short path of the gas flow. The second one was implemented at the level of module design, where a gas deflector (Fig. 7 - right) will be mounted at the end of each column of counters. The gas deflector split the gas flow and force the flow in such a way that one half of the gas flow goes to the counters of one level and the second one to the counters of the second level (see Fig. 4). The seven deflectors are implemented on the side where the inlet gas connectors are mounted. They are shown in Fig. 6, in the upper part of the columns, in turquoise color.

The inner wall architecture and mechanical support presented above are on hold until a final decision on the type of material for the resistive electrodes [7] and gap size [8] will be made. Its integration in the full CBM-TOF wall (in an individual mechanical support or hanged on the outer wall support) is still under discussion.

References

[1] CBM collaboration, N. Herrmann, ed., TDR for the CBM - TOF System. GSI, Darmstadt, 2014.

[2] D. Bartoş et al., CBM Progress Report 2018 (2019) 97.

[3] L. Rădulescu et al. IBWAP 2016, Constanţa, Romania.

[4] M. Petriş et al., this progress report.

[5] M. Petriş et al., Nucl. Instrum. Meth. A 920 (2019), 100.

[6] M. Petriş et al., 2016 JINST 11 C09009.

[7] M. Petriş et al., 35^{th} CBM Coll. Meeting, 23 - 27 April 2020.

[8] M. Petriş et al., this progress report.

mTOF performance during beam tests in 2019*

Q. Zhang[1,2], *I. Deppner*[2], *and N. Herrmann*[2]
[1]Tsinghua University, Beijing, China; [2]Heidelberg University, Heidelberg, Germany

Here we report on results obtained during the mCBM beam time campaign executed in March 2019. The beam was composed of Ag ions with a energy of 1.58 AGeV impinging either on a 0.25 mm thin (interaction rate ≈1%) or on a 2.5 mm thick (interaction rate ≈10%) Au target. The beam intensity was tuned from 10^5 to 10^8 ions per second.

mTOF beam tests conditions

The mTOF setup is composed of 5 mTOF M4 modules grouped in a triple and a double stack and additional test counters as shown in Fig. 1. With the triple stack which is centered at 25○ with respect to the beam the MRPC2 prototype within the modules can be investigated by forming tracklets and using the outer modules (M1 and M3) as a reference. The test counters (MRPC3) which were located behind the double stack make use of the modules M4 and M5 as a reference. The gas mixture used at mTOF is the standard gas mixture foreseen for CBM and contains 90% $C_2H_2F_4$, 5% i-C_4H_{10}, and 5% SF_6. The total gas flow was 110 ml/min and was evenly distributed to in total 7 gas boxes. A slow control system based on EPICS was used to control, monitor and archive data from HV, LV power supplies and gas system.

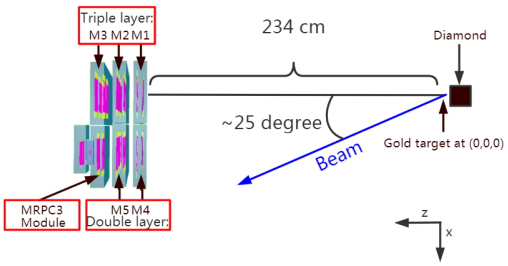

Figure 1: mTOF experimental setup used at mCBM in March 2019. M1 to M5 represent the mTOF modules grouped in a triple and a double stack. The other modules contain test counters.

Data-driven readout chain

Instead of the conventional triggered system, a new data-driven readout chain has been developed for all detector subsystems in CBM to meet the requirements from high-rate environment. The main feature is that self-triggered FEE delivers time-stamped data messages on activation of the respective detector channel [2]. The data sent by the FEE will be aggregated and transported to a high-performance online computer farm located in the Green IT Cube for data reconstruction and selection in real time. The read out components of mTOF are depicted in Fig. 2 [3]. The pre-amplifier discriminator (PADI X) has 32 channels on each board and the threshold can be set via slow control. The PADI boards are directly connected to the MRPC readout electrodes inside the gas box. The advantages of this configuration are the suppression of the electromagnetic induced noise from outside and the impedance matched transmission line from electrodes to PADI. The LVDS signals from PADI contains the time information in the leading edge and TOT signal width. Then the signals are digitized by TDC called GET4. A radiation hard ASIC called GBTx collects and combines data from 40 GET4 chips, sending them to the Data Processing Board (DPB), which is located in the DAQ room outside of the cave. The DPB concentrates the data from 6 GBTx boards and implements them into a data container with specific time interval. This process is called μ-time slice building. The μ-time slices from several DPBs are sent to the First Level event selector Interface Board (FLIB) where they are combined into time slices and stored on the hard drive for later offline analysis.

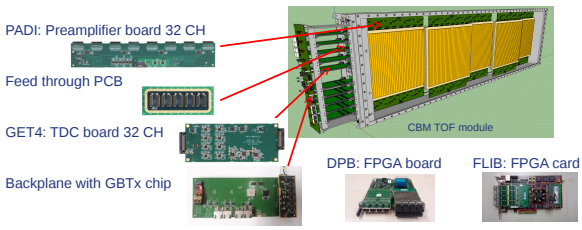

Figure 2: Readout chain of mTOF.

Preliminary results from mTOF beam tests

The analysis is based on subset of data from the 2019 beam time specifically on data from run 159, where the beam of 1.58 A GeV Ag ions hit the thin Au target(1% interaction probability). The beam intensity was around 2 × 10^5 ion/s reflecting in a charged particle flux of about 10 Hz/cm^2 on the triple stack counters. The HV of the five

*This project was supported by BMBF 05P15VHFC1.

modules was ± 5300 V (106 kV/cm) and the PADI threshold was set to -300 mV. A track-finding method was developed to evaluate the counter performance. The first step is to calibrate raw experimental data. This includes the calibration of position offset, time offset and walk. Fig. 3 shows the hit distribution of an exemplary counter after calibration with a clearly seen detection area (x-axis represents the strip number while the y-axis denotes the strip length of 27 cm).

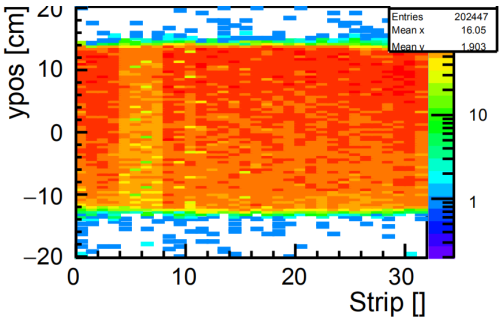

Figure 3: Hit distribution of an exemplary counter. The x-axis represents the number of readout strips (32 in total) and the populated area on the y-axis matches the strip length of 270 mm.

The next step in the performance evaluation is the formation of tracks starting from the diamond detector to all MRPC layers. The efficiency is evaluated by comparing tracks where all stations have a hit N_{Hit} with tracks where the counter under test is missing N_{Miss}. It is calculated by N_{Hit} divided by the sum of N_{Hit} and N_{Miss}. The obtained global efficiency of the exemplary counter (center counter in module M2) is determined to be about 92% as shown in Fig. 4. It is obvious that there is an under estimation of the real efficiency since the greenish band represents an area of missing hits which is caused by a synchronization mismatch in the epoch counter of the GET4. The true counter efficiency can be estimated by taking only the red part into account which amounts to above 95%.

An interesting feature of the tracking method is the possibility to visualize different vertexes as depicted in Fig. 5. Here, tracks neglecting the diamond counter are projected to the target plane. The main contribution comes from the target and the diamond counter (oval shape) while the right spot is generated by the beam exit window of the target chamber.

Conclusion and next steps

During the March 2019 beam time campaign several MRPC could be successfully tested. Out of 1600 channels from 5 mTOF modules, and only one channel was not functioning. The beam test results prove the feasibility of data-driven readout chain together with the tracking analysis method. However, a higher stability in the readout is

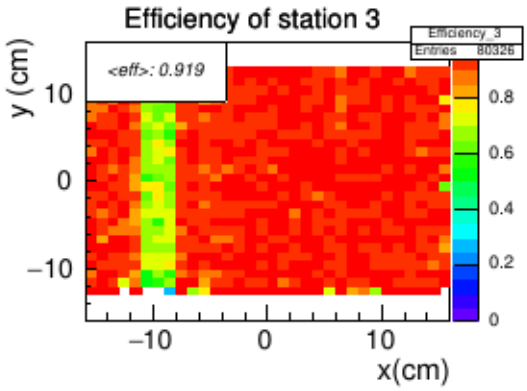

Figure 4: Global efficiency of the exemplary counter. The data loss caused by the readout spoils the true efficiency which is above 95%.

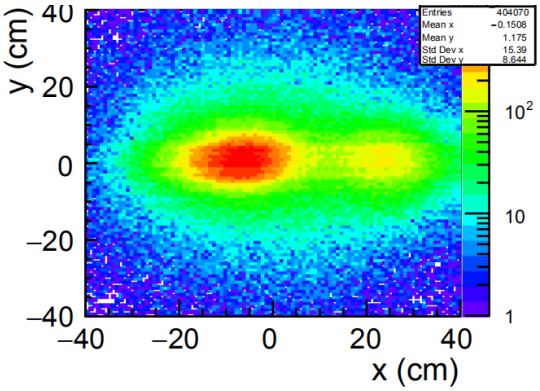

Figure 5: The intersection of extrapolated mTOF particle tracks with target plane. The left spot is generated by interactions with the target and the right less pronaunced spot is caused by the beam exit window of the target chamber.

needed in order to perform the targeted high rate tests in 2020. Those high rate tests are essential in order to accomplish the production readiness review. As for the mCBM experiment, combined data taking with other subsystems with the final goal of Λ reconstruction is the future aim.

References

[1] Q. Zhang, et al., CBM Progress Report 2018, p. 98

[2] V. Friese, "Simulation and reconstruction of free-streaming data in CBM", J. Phys. Conf. Ser. 331 2011, 032008

[3] The CBM collaboration, "A CBM full system test-setup for high-rate nucleus-nucleus collisions at GSI / FAIR", mCBM proposal 2017, p. 34

Considerations on the χ^2-matching between MRPCs in reaction data analysis*

C. Simon[1], *N. Herrmann*[1], *and I. Deppner*[1]
[1]Ruprecht-Karls-Universität Heidelberg, Heidelberg, Germany

In a successful series of MRPC prototype in-beam tests with heavy-ion reaction products the CBM ToF group has aimed at testing high-rate and low-rate counters under full-area load to get a complete picture of the detector performance to be expected under CBM conditions. The data analysis for a detector under test (DUT)—usually sandwiched between at least two additional MRPCs in the experimental setup—consists in first determining a selector hit or tracklet, respectively, which implies a passage of the underlying physical track also through the DUT and then matching to the reference prediction in the DUT plane $(x_{\mathrm{ref}}, y_{\mathrm{ref}}, t_{\mathrm{ref}})$ the nearest-neighbor (NN) hit on the DUT $(x_0, y_0, t_0$; if any) with the smallest chi-square,

$$\chi^2 := \left(\frac{x_0 - x_{\mathrm{ref}}}{\sigma_x}\right)^2 + \left(\frac{y_0 - y_{\mathrm{ref}}}{\sigma_y}\right)^2 + \left(\frac{t_0 - t_{\mathrm{ref}}}{\sigma_t}\right)^2 .$$

For the χ^2-method to be fully applicable the residuals Δx, Δy, and Δt between the predicted and the actual DUT hit should be predominantly Gaussian in shape. However, this assumption does not strictly hold under all experimental conditions. Intrinsic non-Gaussian response tails, for instance, reduce the χ^2-efficiency even in a single-track environment (e.g. with cosmics) where non-Gaussian response distortion by the interference of multiple physical tracks does not play a role. Also, the segmentation of the readout electrode leads to a rather discrete response in one dimension for small clusters and further causes a geometrical bias between reference counter(s) and DUT depending on their relative orientation. If the DUT is deficient in the selected spot, the NN approach still generates some match on a large-area counter in a multi-track environment. Imposing a χ^2-limit and extrapolating the actual χ^2-efficiency is inevitable under such constraints.

The ToF digitization scheme [1] allows for studying systematically the non-Gaussian response effects that necessitate a careful interpretation of the extracted DUT efficiency. For this report, a large-area float-glass prototype sandwiched between two high-rate prototypes, serving as hit selectors, is irradiated with an external particle flux of about $1\,\mathrm{kHz/cm^2}$ (mean external track multiplicity: ~ 1.2) originating from $19\,\mathrm{AGeV/c}$ Ar+Pb fixed-target collision secondaries. The simulated NN χ^2-distribution (cf. Fig. 1, left plot) with fitted weights σ_x, σ_y, and σ_t clearly shows a non-Gaussian tail beyond the set limit which is not accessible with the χ^2-method. To add another level of complexity, the performance of the float-glass DUT degrades as a function of time in spill (TIS; cf. Fig. 1, right plot).

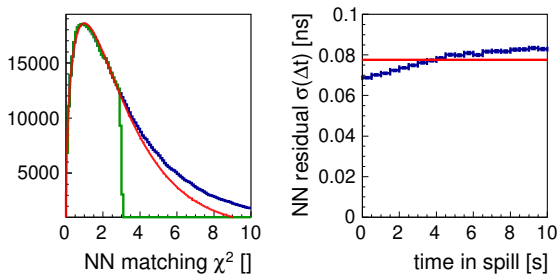

Figure 1: Left plot: Nearest-neighbor (NN) matching χ^2-distribution (blue curve) between the DUT and a reference MRPC including a fit (red curve) within a χ^2-limit of 3 (green curve). Right plot: Time-in-spill (TIS) evolution of the Gaussian sigma fit to the NN time residual Δt (blue curve). The horizontal red line shows the fit result for the TIS-integrated residual.

Under homogeneous single-track irradiation with $1\,\mathrm{kHz/cm^2}$ the counter yields a mean Monte-Carlo efficiency of $\sim 94\,\%$. This number cannot be reproduced in the reaction environment (cf. Fig. 2) with the χ^2-method. To study the χ^2-efficiency differentially as a function of TIS it is advisable to redetermine the TIS-dependent χ^2-weights along the axis.

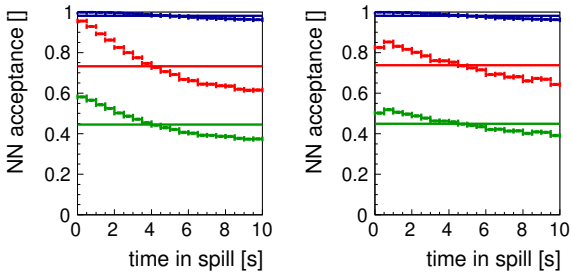

Figure 2: Total χ^2-matching acceptance (blue curve), extracted χ^2-matching efficiency share (green curve) at a limit of 3 (χ^2-CDF: $\simeq 60.8\,\%$), and extrapolated total χ^2-matching efficiency (red curve) as a function of time in spill (TIS). In the left plot, χ^2-weights were derived from TIS-integrated residuals; in the right plot, they were determined differentially for each axis bin.

References

[1] C. Simon *et al.*, CBM Progress Report 2018, p. 98

*This project was partially funded by BMBF 05P15VHFC1 and by EU/FP7-HadronPhysic3/WP19.

Calorimeters

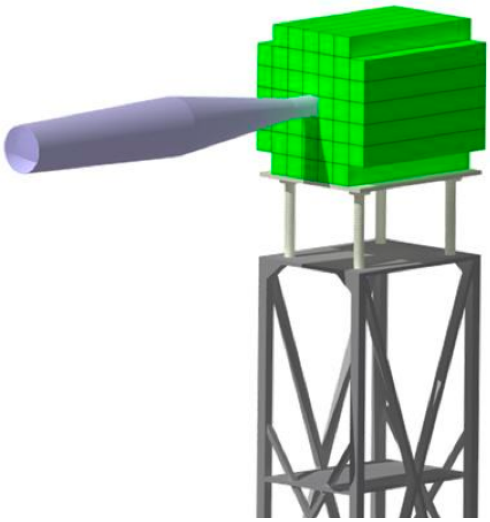

Progress in Projectile Spectator Detector project*

F. Guber†
INR RAS, Moscow, Russia

Status of the CBM PSD modules use in the external experiments during FAIR-phase-0

The CBM PSD project has substantial progress in 2019 in preparation to experiments in the framework of FAIR-phase-0.

Twenty of already constructed CBM PSD modules have been used for the assembly the new FHCal at BM@N experiment. The FHCal has been assembled and equipped with FEE and readout electronics and installed at the BM@N. The first tests on the cosmic muons has been done. The photo of the calorimeter is shown in Figure 1.

Figure 1: Left - front view of the BM@N FHCal. Right – the backside of the FHCal with installed FEE and readout electronics.

Another 13 PSD CBM modules have been used to upgrade the main PSD at the NA61/SHINE experiment at CERN. Here 4 CBM PSD modules with tapered edges are used at the center of the calorimeter to provide the beam hole $60 \times 60mm^2$ and another 9 modules are placed on the top and lateral sides of the calorimeter. The photo of upgraded main PSD is shown in Figure 2.

More details of the CBM PSD modules in these experiments can be found in [1]. First experiments at BM@N and NA61/SHINE are expected at the end of 2021.

mPSD@mCBM

At the end of 2019 and beginning of 2020 first tests to study of the mPSD response at mCBM up to top CBM interaction rates of 10 MHz and with the full free-streaming data acquisition system have been performed. The main goal was to test the mPSD prototype as a part of mCBM experiment to approve and verify the feasibility of the PSD readout concept. The mPSD prototype includes crucial

Figure 2: The upgraded NA61/SHINE mPSD which used 13 CBM PSD modules. First experiments at BM@N and NA61/SHINE are expected at the end of 2021.

parts of the readout such as Addon prototype board developed at INR RAS, and ADC FPGA readout board based on the ADC developed for PANDA ECAL. In this setup, Addon incorporated only the single-ended to differential converters and the necessary power systems. Photo of the assembled FEE setup is represented in Figure 3.

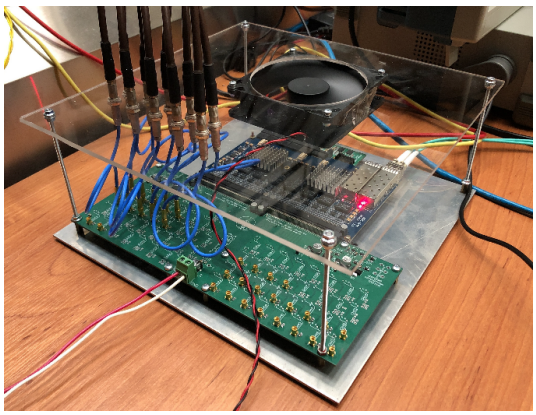

Figure 3: Photo of the ADC board assembled with the Addon board prototype.

The mPSD beam tests included all conceptual hardware, firmware and software parts, which will be used for final PSD@CBM setup. Signal transmission chain, ADC data processing on 80 Msps rate and GBT protocol functionality with clock switching procedure were tested. To check the synchronization of the data from the detectors, the time correlation graphs are constructed, Figure 4. An explicit peak in the distribution of the difference in the response time of the detectors T0 and PSD (time offset), located at about 200

* For the CBM PSD working group

† guber@inr.ru

ns, indicates the correlation of the data and serves to select beam events. Feasibility of the readout concept was proved and development of the full PSD readout system has been started.

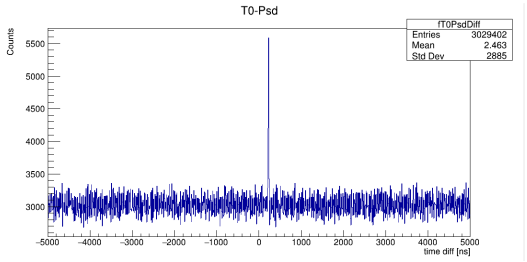

Figure 4: PSD-T0 correlation.

Status of SiPMs radiation hardness study

The Rez group continued in 2019 the study of the degradation of the Silicon Photo Multipliers (SiPM) response due to high neutron fluence (see V. Mikaylov et al. article in this CBM progress Report 2019 and [2]). Hamamatsu SiPMs MPPC S12572-010P are considered now as the best ones for the scintillator light readout at the PSD. These SiPMs were chosen due to small pixel recovery time allowing PSD to operate at collision rates up to 10^8 ions/s. Their small $10 \times 10 \mu m^2$ pixel size not only increases the calorimeter dynamic range, but also is presumably related to the better radiation hardness. It was shown that the single module energy resolution measured at different hadron energies at CERN test beams practically did not suffer from the radiation after irradiation up to 2.5 x 1011 n_{eq}/cm^2, which is the worst case scenario for a one year of the CBM experiment operation.

Status of preparation of the CBM PSD support platform

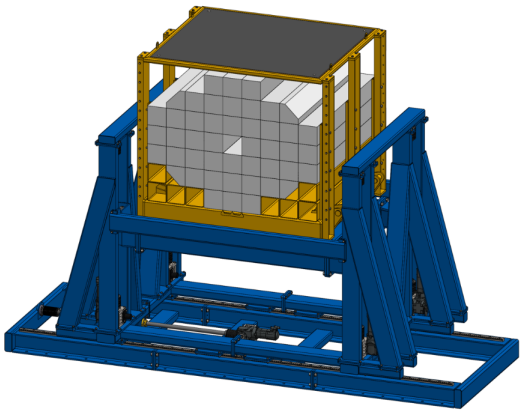

Figure 5: PSD CBM support platform.

Very important task performed with Czech group in 2019, was the construction of PSD support structure for the PSD CBM. The support platform, Figure 5, was fully constructed and will be shipped at GSI at 2020.

References

[1] F. Guber et al., Transverse and longitudinal segmented forward hadron calorimeters with SiPMs light readout for future fixed target heavy ion experiments, Nucl. Instrum. Meth. A958 (2020) 162728

[2] V. Mikhaylov et al., Characterisation of SiPM radiation hardness for application in hadron calorimeters at FAIR, CERN and NICA, JINST 15 (2020) No.02, C02005.

Extended study of Silicon Photomultipliers radiation hardness for PSD*

V. Mikhaylov[†1,2], *A. Kugler*[1], *V. Kushpil*[1], *S. Morozov*[3,4], *and O. Svoboda*[1]

[1]NPI of CAS, Řež, Czech Republic; [2]CTU, Prague, Czech Republic; [3]INR RAS, Moscow, Russia; [4]MEPHI, Moscow, Russia

Introduction

Silicon PhotoMultipliers (SiPM) are used for the scintillator light readout at Projectile Spectator Detector (PSD) [1]. The main issue of SiPM application is their degradation due to high neutron fluence that can reach up to 2×10^{11} n_{eq}/cm^2 per year of the experiment operation [2]. Multiple irradiation tests of SiPMs were conducted at the cyclotron of NPI Řež with a broad neutron spectra and total fluence in the range of $5 \times 10^{10} - 6 \times 10^{12}$ n_{eq}/cm^2.

The list of investigated SiPMs and their parameters, namely breakdown voltage V_{bd}, number of pixels N_{pix}, pixel pitch, gain, photodetection efficiency PDE, pixel recovery time $\tau_{recovery}$, pixel capacitance C_{pix}, quenching resistance R_q, difference between turn-on and turn-off voltage for the Geiger avalanche $V_{bd} - V_{off}$, are presented in table 1.

SiPM measurements in lab

Figure 1 presents dependence of SiPM electrical characteristics on fluence for the investigated SiPMs. Overvoltage V_{OV} = 1 V is used because highly irradiated Ketek and Sensl SiPMs reach 10 mA limit of electrometer supply right after 1 V. All the SiPMs follow the trend of linear dark current increase with fluence which is typically observed for silicon sensors. Dark current increased in up to 5 orders of magnitude for highly irradiated SiPMs which resulted in huge noise and power consumption. Breakdown voltages were extracted as maximum of $1/I_{dark} \cdot (dI_{dark}/dV_{rev})$, but its change after irradiation did not exceed 0.5 V.

SiPM quenching resistances were extracted from dark current versus forward voltage measurements as $R_q \approx N_{pix}/(dI_{dark}/dV_{forw})$. For fluence higher 10^{11} n_{eq}/cm^2 R_q seems to increase by up to 20 % for some SiPMs, for lower fluences it is below the measurement uncertainty of 8 %. Pixel capacitances were extracted from capacitance-voltage measurements as $C_{pix} \approx C_{par}/N_{pix}$ at 10 kHz frequency and bias voltage 1 V below V_{bd}. C_{pix} did not change after the irradiation for most SiPMs.

Signal to noise ratio was extracted from measurement of SiPM response to 10 ns LED pulses as $SNR = \bar{Q}/\sigma_{Noise}$, where $\bar{Q}$ is the measured signal charge. Figure 2 shows drastic degradation of measured charge and consequently SNR in up to 3 orders of magnitude after irradiation with high fluences. However, both old and new version of Hamamatsu 10μm SiPM after irradiation with Φ = 2.5×10^{11} n_{eq}/cm^2 exhibit signal to noise ratio above 10 which is considered to be sufficient for the calorimeter operation.

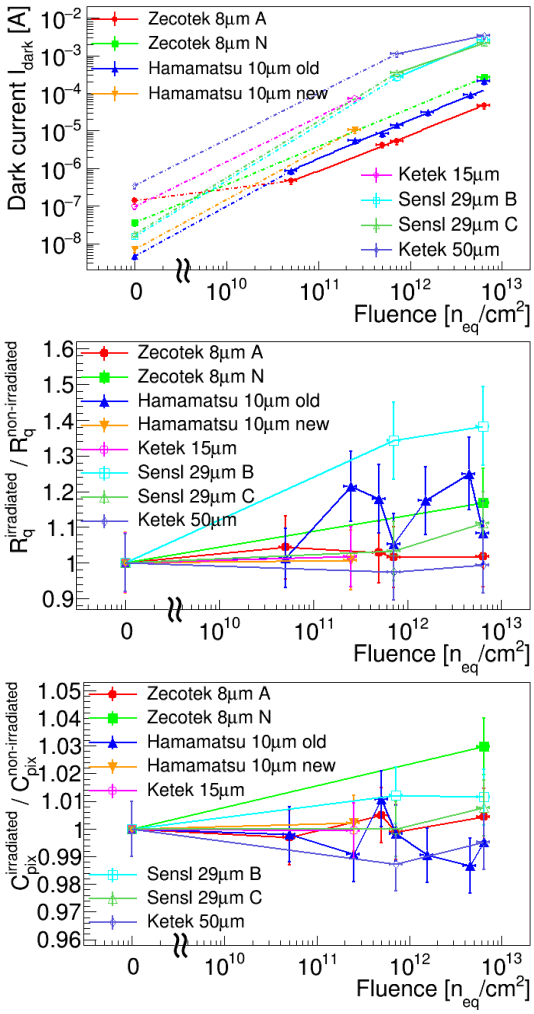

Figure 1: Dependences of dark current (top), quenching resistance (middle) and pixel capacitance (bottom) on fluence for different SiPMs at overvoltage V_{OV} = 1 V.

Dark current and LED response after irradiation directly depend on the pixel size, i.e. the bigger the pixels – the higher the dark current, and the lower are signal charge and signal to noise ratio. Detailed information on conducted measurements can be fond in our article [3].

*Work supported by Czech MEYS - LM2015049 , OP VVV - CZ.02.1.01/0.0/0.0/16_013/0001677

† mikhaylov@ujf.cas.cz

Table 1: Parameters of investigated SiPMs produced by various manufacturers. Most of parameters are typical and vary from sample to sample. All SiPMs have 3×3 mm^2 area. Values of C_{pix}, R_q and $V_{bd} - V_{off}$ are from our measurements.

	Zecotek MAPD		Hamamatsu MPPC		Ketek SiPM PM33		Sensl SiPM uF	
	3 A	3 N	S12572 -010P old	S14160 -1310PS new	15 -WB-A0	50	C 30020	B 30020
V_{bd}, V	64	88	67	38	27	23	25	25
N_{pix}	135000	135000	90000	90000	3600	38800	11000	11000
Pitch, μm	8	8	10	10	15	50	29	29
Gain	6×10^4	10^5	10^5	10^5	3×10^5	6×10^6	10^6	10^6
PDE, %	20	30	10	18	22	40	24	24
$\tau_{recovery}$, ns	2000	10000	10	10	13	2000	100	100
C_{pix}, fF	1.5	1.2	3.2	6.4	19.5	280	63	63
R_q, MΩ	2.7	2.7	2.7	1.6	0.74	0.42	0.4	0.48
$V_{bd} - V_{off}$, V	–	0.43	1.7	0.97	0.72	0.15	0.15	0.15

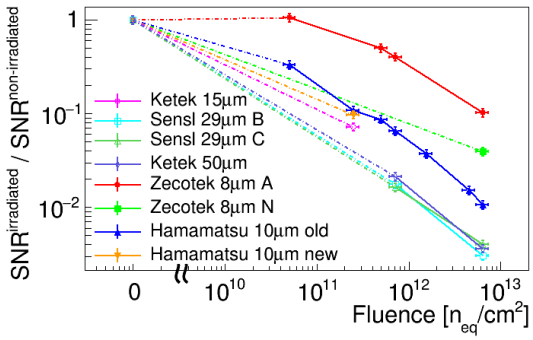

Figure 2: Dependences of signal to noise ratio on fluence for different SiPMs at overvoltage V_{OV} = 1 V.

PSD calorimeter performance

PSD single module response to proton beams was studied in the momentum range of 2 – 80 GeV/c. Module was consequently equipped with 3 batches of Hamamatsu SiPMs MPPC S12572-010P irradiated by 2.5×10^{11}, 1.6×10^{12} and 4.5×10^{12} n$_{eq}$/cm^2. These SiPMs were chosen for the superior radiation hardness and small pixel recovery time allowing PSD to operate at collision rates up to 10^8 ions/s. Their small 10×10 μm^2 pixel size not only increases the calorimeter dynamic range, but also is presumably related to the better radiation hardness.

Figure 3 shows that linearity of the calorimeter response did not suffer from the radiation. Only slight deterioration of energy resolution is observed after irradiation by 2.5×10^{11} n$_{eq}$/cm^2 which is the worst case scenario for a one year of experiment operation. Modular detector structure of CBM allows to exchange the most damaged SiPMs every year if necessary. Achieved results are as well of interest for MPD and BM@N experiments at NICA and NA61 experiment at CERN where very similar calorimeter design including the SiPM light readout is utilized.

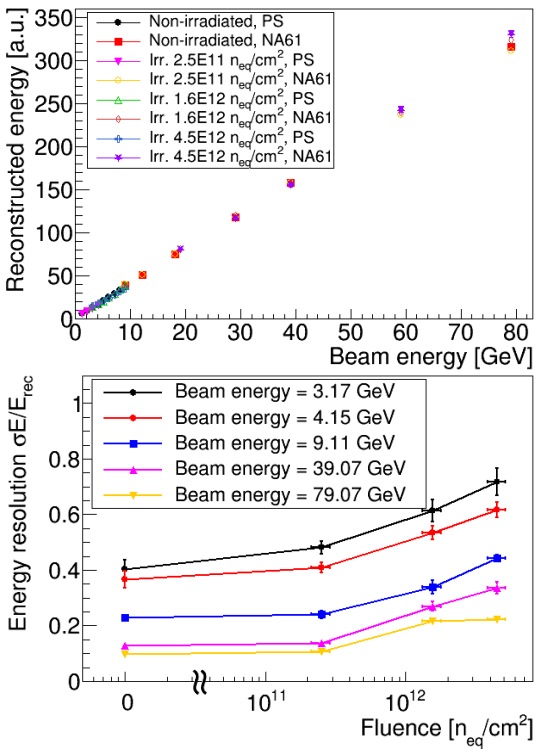

Figure 3: Energy linearity (top) and resolution (bottom) for single module equipped with non-irradiated and irradiated SiPMs. SiPMs were operated at overvoltage V_{OV} = 3 V.

References

[1] CBM collaboration, Technical Design Report for the CBM Projectile Spectator Detector (PSD), GSI Darmstadt 2015

[2] A. Senger, presentations at 29th – 32nd CBM Collaboration Meetings (2017 – 2018).

[3] V. Mikhaylov et al., Characterisation of SiPM radiation hardness for application in hadron calorimeters at FAIR, CERN and NICA, JINST NIM A 15 2 (2020).

Magnet

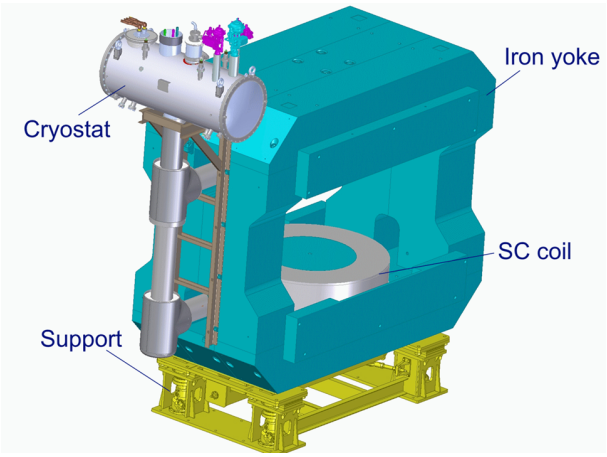

The superconducting dipole magnet of the CBM experiment

Peter Senger for the CBM magnet team
Facility für Antiproton and Ion Research

The Final Design Report of the CBM SC magnet has been approved in Dec. 2019 [1]. Six SC cables, each of about 5 km length, have been manufactured for three coils by the Bochvar Institute, Moscow. The insulation of the cable has started at VNIIKP in Podolsk in November 2019. Impregnation tests with a dummy coil are ongoing at BINP Novosibirsk. The iron blocks for the yoke have been purchased. A photograph of the cross section of the SC cable is shown in figure 1. The ratio of cupper to superconductor NbTi varies between 6.7 and 7.0 for the different cables produced. The total length of the cable in one coil is about 9 km, therefore, two cables have to be connected. Figure 2

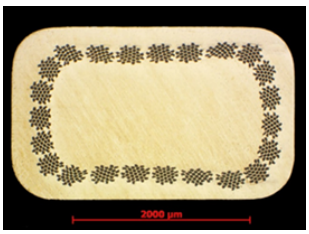

Figure 1: Photo of the cross section of the SC cable.

depicts the cross section of a mock-up coil after impregnation test. The coil is a 1 m long straight section, which was vacuum impregnated with an epoxy compound filled with Boron Nitride powder. The BN adapts the thermal expansion coefficient of the epoxy compound to that of copper in order to avoid cracks when cooling down. The next impregnation test will be performed with a round coil, like the final one, to provide more realistic conditions.

The cross section of the upper coil is shown in figure 3. The main components of the coils are superconducting cables, the copper and the stainless steel cases, the support struts, and the radiation shielding. The coil is indirectly cooled by liquid helium flowing in a tube at the outer circumference of the copper case around the coil. The single support strut is shown in figure 4. as a yellow ring. This cylinder will be made from glass fibre reinforced plastic, it reduces the deformation of the stainless steel plate due to the magnetic forces, with respect to the eight single struts of the former design. The eight titanium rods hold the coil when the magnetic field is switched off. The cooling of the superconducting coils of the CBM magnet is based on the thermosyphon principle. The liquid Helium, which has a temperature of 4.5 K and a pressure of 1.3 bar, goes from the cryostat down to the lower coil, then to the upper coil, and finally the helium returns to the top of the cryostat. The

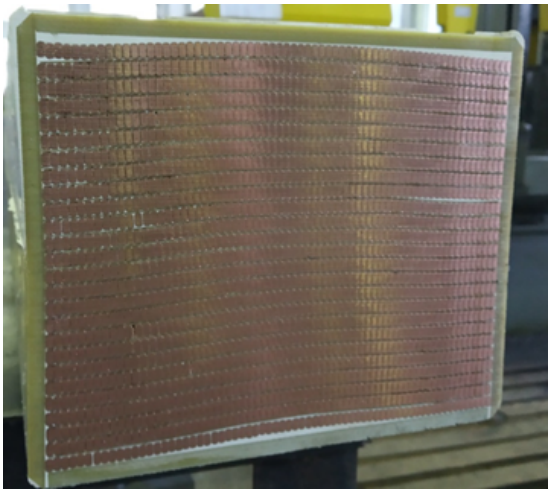

Figure 2: Impregnation test with a mock-up coil.

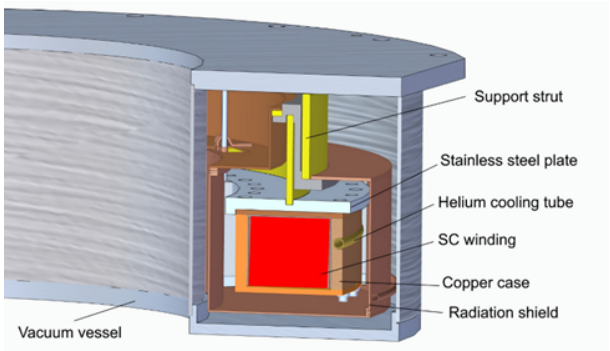

Figure 3: Cross section of the upper coil with the SC winding inside the copper case and the Helium cooling tube, the stainless steel plate the support strut, the radiation shield and the vacuum vessel.

cycle is driven by buoyancy, caused by the Helium bubbles created in the tube surrounding the coils. Therefore, these tubes have a slope of 1degree (see figure 4). The Helium flow is maintained by an additional heater located in the return tube below the cryostat. The cryostat, the Helium tubes, and the coils are enclosed in vacuum vessels as illustrated in figure 5. The cryostat is supported by liquid Helium via a transfer line of more than 30 m length, which is connected to the branch box located at the wall of the cave as shown in figure 6. The branch box distributes the liquid Helium coming from a cryo-plant to the CBM magnet,

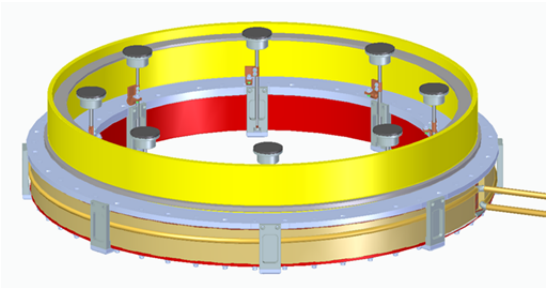

Figure 4: The upper coil assembled with the support strut and the titanium rods.

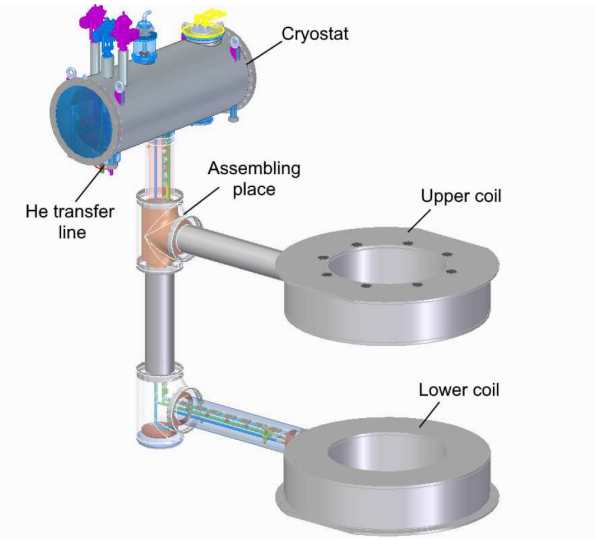

Figure 5: : Cryostat and vacuum vessels of the coils and the liquid Helium tubes.

and to the feed box for the HADES magnet. For cost reasons, the magnet yoke and the pole shoes will be assembled from steel plates of about 12 cm thickness as illustrated in figure 7, which depicts the ANSIS model of the magnet. The white lines indicate the gaps between the plates. For the calculation, a gap size of 3 mm was assumed. The color code refers to the magnet field strength. While the maximum field inside the magnet gap and the field integral does not depend on the lamination, the stray field increases for the horizontal lamination by about 25% compared to no or vertical lamination. Detailed calculations of the stray field in the region of the RICH photodetector including a shielding box are ongoing. If necessary, the horizontal yoke part opposite to the RICH may be produced as massive block, i.e. without lamination, in order to reduce the stray field.

Figure 8 depicts the support of the magnet, which allows to adjust and align the magnet in x, y, and z direction by $\pm$ 4 cm, and to rotate it along the beam axis by $\pm$ 2 degrees.

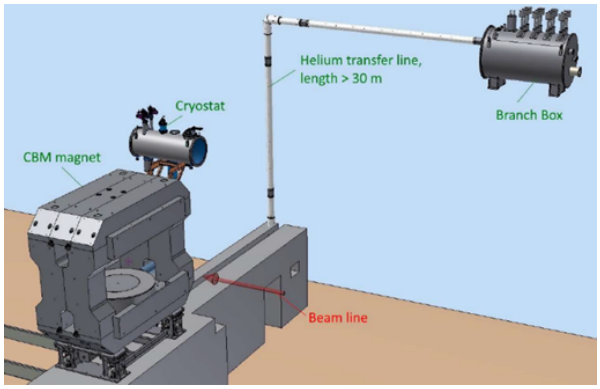

Figure 6: : General view of the CBM magnet including cryogenics.

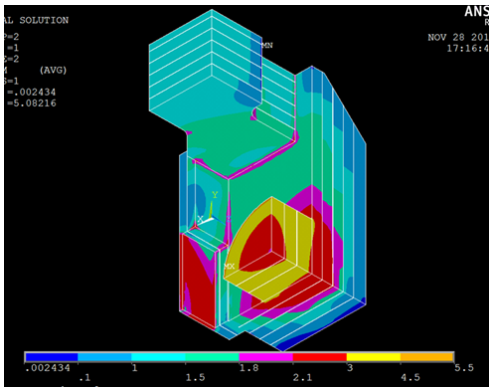

Figure 7: ANSYS model of 1/8 of the magnet, illustrating the horizontal lamination of yoke and pole shoe. The color code illustrates the magnetic field strength.

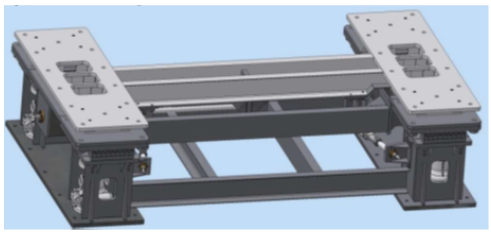

Figure 8: Support of the magnet yoke providing alignment (see text).

The next milestone of the magnet project is the Final Design Report in fall 2020. The construction of the magnet has partly already started, and will end according to schedule in fall 2022 with the Factory Acceptance Test.

References

[1] Final Design Report on the CBM magnet, https://fair-center.eu/for-users/experiments/nuclear-matter-physics/cbm/projects/magnet.html

3D- magnetic field calculations for the muon setup of the CBM experiment

P.G. Akishin[*1] *and V.P. Ladygin*[2]
[1]LIT-JINR, Dubna, Russian Federation; [2]LHEP-JINR, Dubna, Russian Federation

The CBM superconducting dipole magnet [1] with the enlarged vertical aperture of 1440 mm has to provide a vertical magnetic field with a bending power of $\sim$1 $T{\cdot}m$ over a length of 1 m from the target. One of the options of the CBM setup for SIS-100 includes a muon detection system (MuCH), which consists of one carbon and 3 steel absorber blocks and 4 tracking detector triplets [2] placed downstream the magnet. This report presents results of TOSCA [3] calculations of the magnitude of the magnetic field and the acting forces on the MuCH detector.

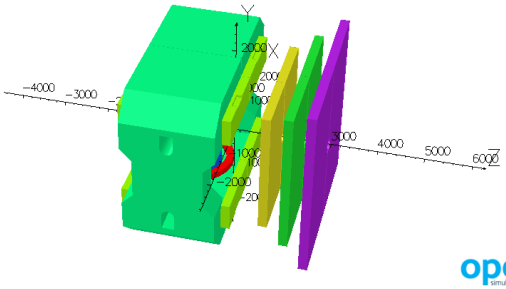

Figure 1: 3D model for CBM SC dipole magnet with MuCH system.

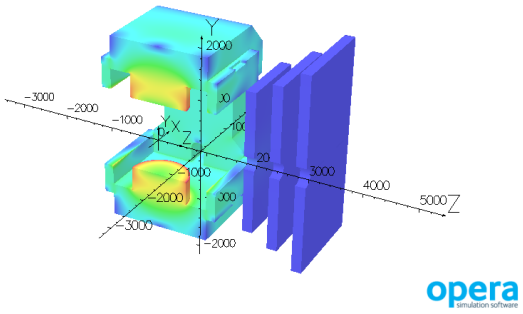

Figure 2: The CBM magnet saturation picture.

The 3D model of the CBM dipole magnet with 3 steel MuCH absorbers is presented in Fig.1. It is assumed that the first absorber is a carbon, and that the support structures of the MuCH system are made from nonmagnetic materials. Therefore, they are not included in the model. Two plane symmetries of the magnetic field have been taken into account, that allowed to reduce the number of unknown parameters. About $2{\cdot}10^8$ elements and $3.9{\cdot}10^7$ nodes have been used for $1/4$-th part of the model.

The magnet field saturation inside the CBM magnet is shown in Fig.2. The maximal field saturation is at the poles.

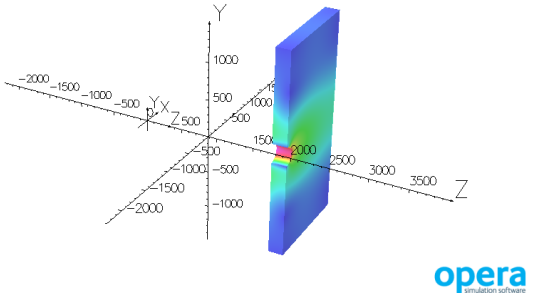

Figure 3: Magnetic field saturation in the 2-nd MuCH absorber.

The distribution of the magnetic field in the 2-nd (or 1-st steel) MuCH absorber is shown in Fig.3. The diameter of the hole in the 2-nd absorber is taken as 26 cm. The maximal value of the magnetic field of $\sim$0.25 T is in the center of this absorber. The Maxwell stress calculation of the force acting on the 2-nd MuCH absorber results in a value of $\sim$1095 N. The forces for the last 2 steel are negligible .

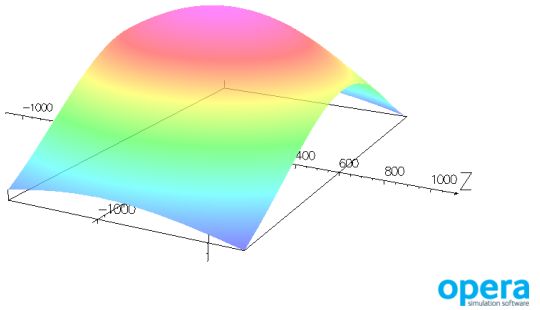

Figure 4: Vertical magnetic field component B_y distribution in the XZ plane at Y=0 mm inside the CBM magnet.

The total current through one coil is taken as 1.2 MA. The distrubution of the vertical magnetic field component B_y in the XZ plane at Y=0 mm inside the magnet is shown in Fig.4. The B_y distribution along the beam direction is presented in Fig.5. The maximal value of the B_y component is $\sim$1.1 T with the field integral of $\sim$0.9947 $T{\cdot}m$.

* akishin@jinr.ru

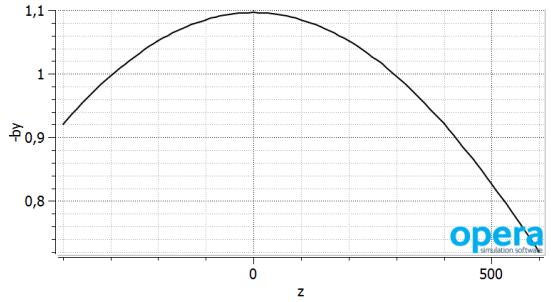

Figure 5: Vertical magnetic field component B_y distribution along the beam direction.

The 3D-calculation for the muon option of the CBM experiment at SIS100 [4] has been performed using the TOSCA code [3], and a 3D- field map for CBMRoot has been provided. It is demonstrated that the field integral is $\sim$1 $T \cdot m$. The Maxwell stress calculation has been used to evaluate the forces acting on the MuCH steel absorbers. It is shown that the forces acting on the 2-nd absorber is $\sim 10^3$ N, while they are negligiable for the last two absorbers. The next step can be the estimation of the forces acting on the support structures of the MuCH detector.

References

[1] The CBM collaboration, "Technical Design Report for the CBM Superconducting Dipole Magnet", GSI-2015-02000 (2013)

[2] The CBM collaboration, "Technical Design Report for the CBM Muon Chambers", GSI-2015-02580 (2015)

[3] J. Simkin and C.W. Trowbridge, "Three dimensional nonlinear electromagnetic field computations using scalar potentials", IEE Proc. B **127**, 1980, p.368

[4] T. Ablyazimov et al. (CBM Collaboration), "Challenges in QCD matter physics - The scientific programme of the Compressed Baryonic Matter experiment at FAIR", Eur.Phys.J. A **53** (2017) 3

Stress calculations for the CBM superconducting dipole magnet coils

Yu.V. Gusakov[*1], *A.V. Bychkov*[1], *and V.P. Ladygin*[1]
[1]LHEP-JINR, Dubna, Russian Federation

The design of the CBM superconducting dipole magnet with the enlarged vertical aperture of up to 1440 mm has been substantially updated with respect to the initial one as presented in the TDR [1]. A major difference is the structure of the superconducting coils.The vertical force on the coils is about 300 tons at a test current of 700 A. In the original design, the cold mass of the coil is suspended from the room temperature vacuum vessel by six G-10 struts of cylindrical shape, while in the last year two new designs have been studied in order to reduce the deformation of the coil: one suggestion was to increase the number of struts to eight, and the other one was to replace the eight struts by one single ring-shaped strut with the diameter of the coil. In the following, results of stress calculations are presented for eight cylindrical G-10 struts using the ANSIS code [2]. The geometry of the coil is shown in Fig.1. The structural model of a strut used for the ANSYS calculations is shown in Fig.2.

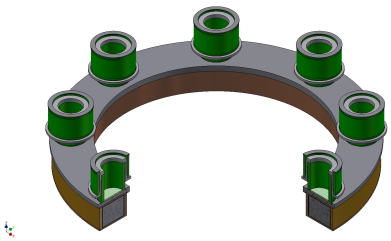

Figure 1: The coil with eight support struts.

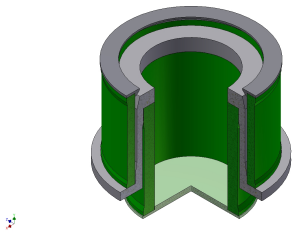

Figure 2: The structural model of a G-10 strut.

The ANSYS calculations have been performed in order to estimate the deformation, and the equivalent and shear stresses. The results of the coil deformation in the vertical direction are shown in Fig.3. The maximal deformation of the coil is $\sim$0.07 mm. The maximal values of the equivalent (von Mises) and shear (XY-plane) stresses are $\sim$64 MPa and $\sim$27 MPa, respectively. Their distributions for the coil are shown in Fig.4 and Fig.5, respectively.

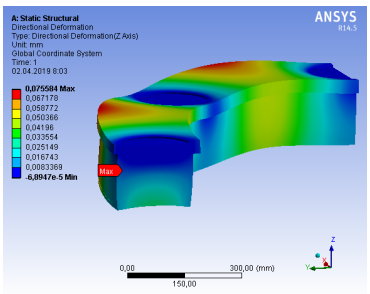

Figure 3: Deformation of the CBM magnet coil.

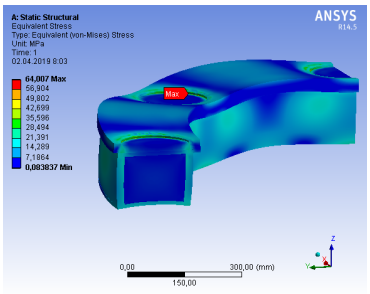

Figure 4: Equivalent stress of the CBM magnet coil.

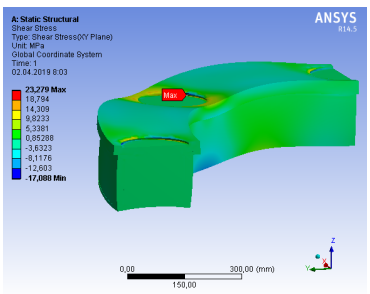

Figure 5: Shear stress of the CBM magnet coil.

References

[1] The CBM collaboration, "Technical Design Report for the CBM Superconducting Dipole Magnet", GSI-2015-02000 (2013)

[2] "Finite Element Simulation", http://www.ansys.com

* iourii.gusakov@cern.ch

Infrastructure

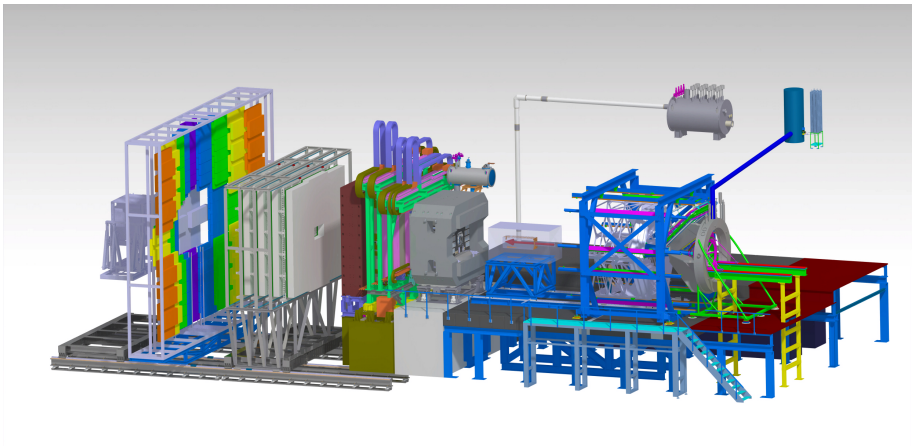

Rail System - baseline description

*P. Kuhl, P. Dahm, and M. Kiš**
GSI, Darmstadt, Germany

Description

Three downstream detectors (subsystems) of the CBM experiment are placed on the common rail system (RS): TRD, TOF, and PSD. The primary function of RS is to facilitate the movement of detectors along the beam axis in order to bringing them into required measurement position or during maintenance periods into service position. The second function of RS, that is anchored into ground floor, is to provide for the prescribed earthquake safety of above detectors. The positioning precision in movement direction is better than 0.1 mm determined by drive mechanics, while repeatability of positioning depends on implementation of position measurement device (laser) and drive mechanics. In vertical and horizontal direction positioning depends on actual implementation of rails which is typically less than 0.5 mm.

The RS comprises two rail pairs: inner and outer. Inner rails are 4 m apart and outer 8 m apart with nominal beam axis being in the middle of both pairs. Only inner rails are equipped with additional gear-racks for the drive mechanics. The PSD is placed on two inner rails while two other subsystems use all four rails. In order not to over constraining movement on four rails, the inner and outer rails differ in implementation; the inner rails are using the runner blocks (carriages), while outer rails are only supporting the weight.

Interfacing between RS and subsystems is facilitated with a connection plate (aka low platform aka sub-frame, concept drawing is shown in Fig. 1). The connection plate provides high precision joint towards the RS on one side and flexibility to the subsystem frame. Its construction provides required stiffness so that the installation tolerances for integration into the RS and for load distribution over the four (or two in case of PSD) rails are met. It also serves as a mainframe for the drive/engine installation.

* m.kis@gsi.de

Subsystem specific frame layouts

TRD comprises four identical layers of detector modules in a single frame. The frame is constructed in such way that each layer-half (left or right relative to beam axis) can be almost fully unfolded from the frame for installation or maintenance of detector modules while the frame depth (in beam direction) remains fixed.

TOF internal structure comprises two regions of detector modules referred to as inner and outer wall. The inner wall can be fully extracted and placed independently from the main TOF frame. In beam direction the inner wall is shifted beam downstream relative to outer wall so that the partially overlapping detector modules are fitted behind. The installation and servicing of detector modules requires scaffolding up- und downstream from the frame.

PSD is due to the beam deflection at its measurement position very sensitive to exact beam axis. Therefore the PSD frame allows for horizontal and vertical translation and limited rotation around its vertical axis. Different positions of PSD are taken into account for integration of the PSD frame onto the RS. The PSD frame is also providing support for the BFTC.

Dimensions

The rail system spans distance between the CBM dipole foundation and beam dump entrance of about 16.5 m which is approx. half of the CBM cave length. However, due to the MUCH/RICH foundation placed just behind the magnet foundation, only about 13 m is available for three downstream detectors. Assuming the depth of detectors 2.9 m for TRD, 2.0 m for TOF, and 2.5 m for PSD, only about 8 m is left for installation work on detectors. Consequently only one of the detectors can be installed/maintained at the given time.

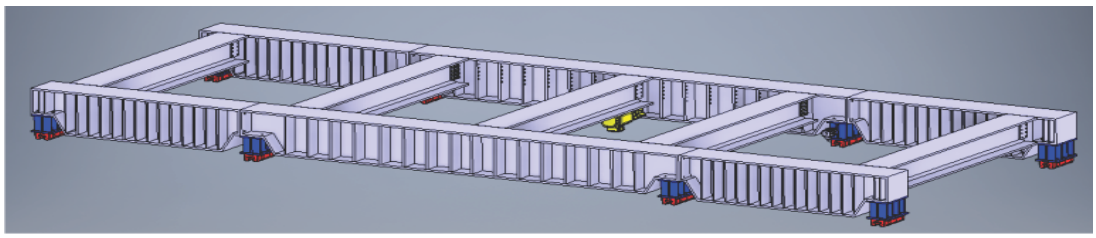

Figure 1: Concept of connection plate; each subsystem is placed on the sub-frame that is attached to the rail block-runners. The sub-frame also integrates the drive mechanics.

Upstream platform - new concept

P. Dahm, M. Kiš, and P. Kuhl*
GSI, Darmstadt, Germany

Upstream platform composition

The term upstream platform is used to denominate a composite platform structure that occupies upstream (relative to target position) area of the CBM experiment area E10. Main purpose of the platform is to serve as CBM dipole stand and HADES platform, but also to provide radiation shielding for the area under the platform that we refer to as service area.

The principal components of upstream platform are depicted in Fig. 1; the magnet foundation is a concrete block primary serving as support for the dipole and in addition as an anchor element for the iron support structure that are joined to it. The iron support structure is principal bearing element for the 60 cm thick shielding concrete blocks from which the platform is made. Because of weight of HADES ECAL system an additional iron support structure is placed under concrete blocks where its rails are laid out . Additional shielding blocks are placed on the ground floor next to the magnet foundation with an emergency exit cat-out to form a shielding wall against neutrons from the beam dump.

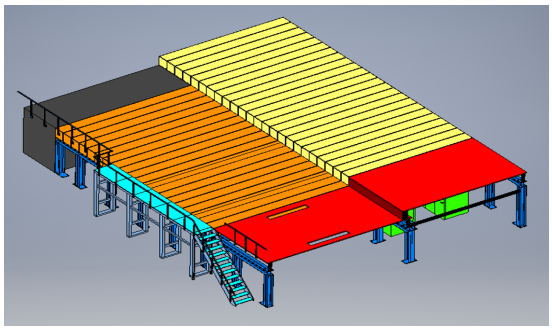

Figure 1: Upstream platform consist of: magnet foundation (dark gray), iron support structure (blue), shielding concrete (HADES side orange, service area yellow), and iron shielding plates (red).

The major difference in respect to previous design is a two level platform concept; height of the area under the beam axis (HADES area) is optimized to accommodate HADES detector and the area right to it is optimized for height of space underneath - service area. Since the magnet foundation is only concrete element that has to be cast on site, the whole installation process can be simplified. Please note that front part of the platform is not shielded with concrete but it is covered with iron plates; this allows for flexible installation of needed detector supplies in particular for HADES.

Since the radiation last imposed on STS during HADES experiments can be considerable, it is necessary to introduce an additional beam dump between the HADES and CBM dipole that we will be referred as HADES beam dump. Conceptually it is foreseen that the HADES beam dump is mounted only after HADES is prepared for experiment by using existing HADES ECAL rails for its placement. The beam dump comprises an iron core and concrete shell so that the overall weight is kept at about 20 t.

Layout of service area

Underneath the concrete shield the E10 service area has surface of about 90 m^2 which serves as installation space for 19-inch industrial racks 80 cm$\times$100 cm$\times$47 HU. The initial positioning allows for two rows of 12 (cf. Fig. 2) racks with enough space for installation from forward and backward. The water cooling can be installed directly to devices/crates placed within racks. Any kind of air-cooling is not foreseen because the whole installation is placed within a concrete shielding. The racks are primarily populated with PSUs of all subsystems. They can also be used for additional devices that need to be placed within the service area e.g. gas manifolds and ambient pressure controls. Dedicated Ethernet switch is also placed here (for DCS and Campus Network). Apart from the power cabinets (not shown) for power distribution, the magnet power supply and controls are placed in a vicinity of magnet foundation.

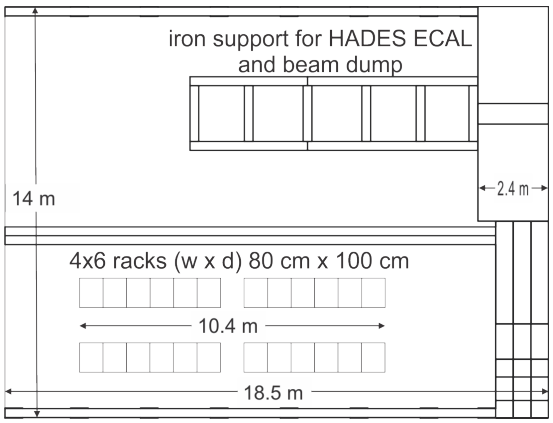

Figure 2: Service area top view; shown are two rows of racks and iron support for HADES ECAL.

* m.kis@gsi.de

Computing and experiment control rooms

*D. Emschermann and M. Kiš**
GSI, Darmstadt, Germany

Control room

The CBM experiment has made few iterations during shaping process of the control room. The initial version was substantially extended by completely absorbing the meeting room that does not exist any more. The overall surface of the control room is now about 155 m^2. In addition to experiment preparation room, it is the only place intended to be occupied by people during experiment running.

The overall layout anticipates two modes of usage i.e. experiment preparation and production running. It is envisaged that during production runs only limited craw can operate the whole experiment e.g. shift leader with DAQ and control crew members with subsystem-experts on call. On the other hand, during startup phase each subsystem has its own working space. In the layout presented in Fig. 1 each subsystem has two/three seats. Each seat is equipped with

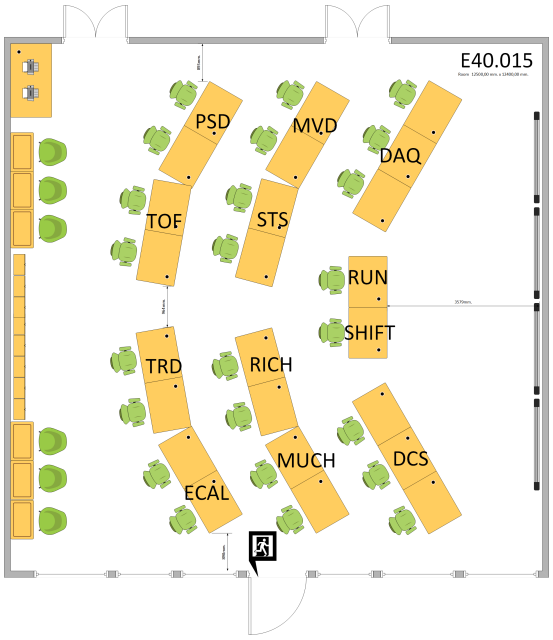

Figure 1: Control room layout: 10 subsystem with 22 seats plus run and shift leader seats. In addition six guest seats are foreseen on the left side and large monitors on the wall right.

its own workstation with up to four monitors. In particular, the four wall displays are used for global run parameters monitoring. Guest seats are prepared for laptop users.

The spaces between work places are kept at possible minimum in order to allow for emergency evacuation. Since no meeting room will be available on the premises, the ad hoc meetings during runs will be held in control room while all other meetings have to be scheduled in another location.

Computing room

The computing room (aka electronics room) is located next to the control room. The room serves as a connection node (FLES entry node) room where all glass fibers from the readout of experiment subsystems are fed into corresponding servers. Room layout shown in Fig. 2 anticipates placement of 24 server racks of standard width (80 cm) and depth (120 cm), but with integrated passive cooling doors which adds 23 cm to overall depth. The overall height of 47 HU can be used to hold up to 9 servers (4 HU each). This allows for installation of more than 200 servers, or accordingly, to optimize the number of servers and incoming fibers per rack unit.

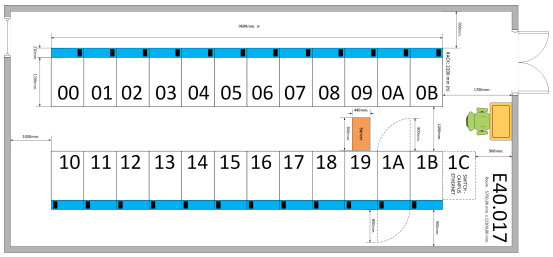

Figure 2: Computing room layout; shown are two rows of racks and other auxiliaries.

Similar to the cooling concept implemented in Green Cube, for the air circulation we relay on fans integrated in servers. The air is replenished from central corridor and exhausted towards the walls of the room. Effectively is the room kept at constant (low) room temperature. This concept also allows that cooling is engaged per single rack consequently enabling for an on-demand installation.

An additional rack (labeled 1C in Fig. 2) will be placed by Campus IT with Campus Network switch. All network connections on level E40 are patched there.

Due to the envisaged noise generated by servers, the wall between control and computing room will be additionally sound proofed.

* m.kis@gsi.de

Data Acquisition and Online Systems

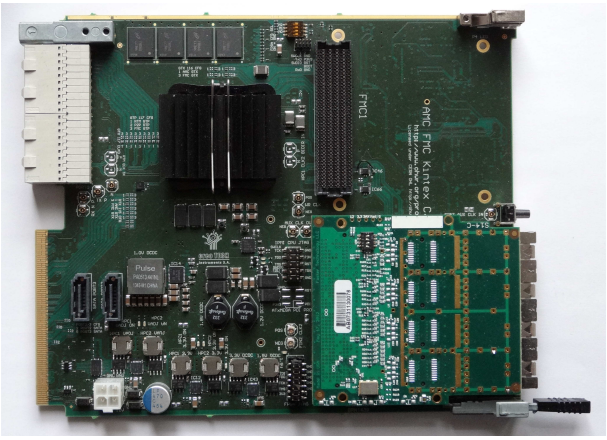

Towards Timing and Fast Control (TFC)

V. Sidorenko, S. Bähr, and J. Becker
Karlsruhe Institute of Technology, Karlsruhe, Germany

The Timing Synchroniser (TS) was previously introduced as a provisional solution for use in beam tests [1]. Eventually, it has to be replaced by the more advanced Timing and Fast Control system (TFC), which is currently under development at KIT, Karlsruhe. The TFC system is meant to provide highly accurate timestamp and clock synchronisation for all CRI boards, as well as low-latency packet delivery functionality. Those features help increase tolerance of the experimental data to event bursts and system overflows of other nature by reacting to such special cases in a timely manner with low-latency throttling decisions.

The initial concept of TFC architecture was proposed by Lukas Meder and its synchronisation principle was heavily inspired by the White Rabbit project developed at CERN [2]. Namely, it uses a PTP-like negotiation algorithm for timestamp synchronisation and the Digital Dual-Mixer Time Difference technique for accurate phase shift measurement [3]. It also reuses the soft-PLL approach to local clock phase alignment.

In the implementation that is currently under development, TFC is a tree network of FPGA boards interconnected with so-called TFC Links. Each link connects two network nodes over optical fibre and (re-)synchronises the downstream node with the upstream one using a PTP-like negotiation-based procedure.

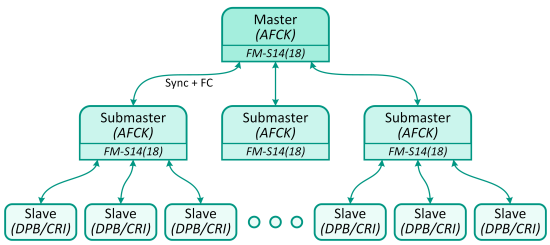

Figure 1: TFC system topology.

The TFC network architecture comprises a Master node, a multi-layered network of Submaster nodes and Slaves that are represented by data processing boards (Fig. 1). Master node defines the global time reference and the system-wide master clock that is propagated through the network to Slave devices. Besides, Master role implies fast control decision making. Submaster units act in the network as switches, having various number of connections and taking care of transporting fast control messages from Slaves to the Master and back. Slave nodes, in turn, issue fast control requests for the decision-making logic hosted in the Master node and process responses. It is also worth noting that, in its current implementation, each node in the TFC network is configured and controlled individually from a PC over IPbus [4].

AFCK boards are used as a hardware platform for the TFC network, except for the Slave units, which will eventually be integrated into the CRI firmware as a subsystem-independent interfacing IP-core - TFC Core. When integrated into online data processing firmware, TFC Core provides subsystem-specific logic with a synchronous global timestamp together with a clock signal aligned with the master clock. In terms of required hardware, the Slave-side interfacing core itself relies mainly on a local programmable clock generator, which defines synchronisation precision, a stable system clock source, Gigabit transceiver interface and IPbus connectivity infrastructure.

Development of the system is currently focused on TFC nodes themselves and the interfacing module as well as on preparing reliable clock and timestamp synchronisation procedures. Small-scale tests are carried out on the setup at KIT that consists of two AFCK boards connected with an optical cable. Such a minimal platform is perfectly sufficient for evaluation of individual nodes and communication protocols, whereas for larger-scale tests a μTCA-based system at GSI is available.

References

[1] L. D. Meder, D. Emschermann, J. Frühauf, W. F. J. Müller and J. Becker, "A Timing Synchronizer System for Beam Test Setups Requiring Galvanic Isolation," in IEEE Transactions on Nuclear Science, vol. 64, no. 7, pp. 1975-1982, July 2017.

[2] P. Moreira, J. Serrano, T. Wlostowski, P. Loschmidt and G. Gaderer, "White rabbit: Sub-nanosecond timing distribution over ethernet," 2009 International Symposium on Precision Clock Synchronization for Measurement, Control and Communication, Brescia, 2009, pp. 1-5.

[3] P. Moreira, P. Alvarez, J. Serrano, I. Darwezeh and T. Wlostowski, "Digital dual mixer time difference for sub-nanosecond time synchronization in Ethernet," 2010 IEEE International Frequency Control Symposium, Newport Beach, CA, 2010, pp. 449-453.

[4] Larrea, Carlos Ghabrous, K. Harder, Dave M. Newbold, D. P. C. Sankey, Anto Rose, Alessandro Thea and Thomas L. Williams. "IPbus: a flexible Ethernet-based control system for xTCA hardware." (2015).

Throttling strategies and optimization for the CBM DAQ chain

X. Gao[1,3], *D. Emschermann*[1], *J. Lehnert*[1], *and W. F.J. Müller*[1,2]
[1]GSI, Darmstadt, Germany; [2]FAIR, Darmstadt, Germany; [3]SIOM, Shanghai, China

Throttling model and strategies

In a free-streaming DAQ system of CBM, data will be randomly lost when the available bandwidth is saturated on individual data links, yielding fragmentary data which can't be reconstructed anymore. This can be avoided by adding a throttling mechanism, which ensures that the complete information of a subset of interaction is transported rather than fragmentary information for all interactions.

A throttling system for CBM is designed and modeled. In [1], a SystemVerilog based data flow model of the critical parts of the DAQ system is created, mainly the buffering and aggregation in the front-end ASICs and the processing of throttling information in the subsequent FPGA layer. With a very simplified data source model, the throttling model is verified with the essential performance indicators like controlled and un-controlled data loss.

Based on the available functionality of the detector front-end electronics, two strategies called "Stop" and "Clear" are developed and compared. In the "Stop" strategy acceptance of new hits is stopped system-wide when a critical fraction of buffers have filled up and data links are about to saturate and resumed when the buffers have emptied. In the "Clear" strategy, the buffers are simply cleared system-wide upon a similar buffer condition.

A preliminary research has proven that the probability of complete or almost complete events can be significantly improved through the throttling mechanism. Different strategies are compared in various experimental conditions and the throttling algorithms and parameters are optimized.

Preliminary simulation

In the hit generator of the throttling model, one event is one collision. In order to keep the initial simulation simple, the event size is random with a uniform distribution. For each event, hits have a uniform distribution on all detector channels. The hit rate R_{hit} equals the event rate multiplied by event size. For a more intuitive understanding of throttling results, the normalized hit rate R_{hit_N} is defined as the ratio of hit rate to readout bandwidth. The model implements 32 ASICs. The total simulated time is 10 ms, covering order of hundreds of throttling cycles. In the data flow model, the maximum number of 5 readout elinks/ASIC are active [2], resulting in 50 MHits/ASIC/s as bandwidth limit.

Throttling parameters are the channel thresholds for alerts per ASIC and the fraction of ASICs reporting alerts. In a first phase, the alert threshold is 1/3 out of 128 almost full channels. Throttling is triggered when half of the ASICs report busy alerts. A "good" event which can be restored in the physics analysis is defined as an event where at least 95% of hits are saved at the end of the acquisition. The absolute number of good events in the same simulation time is considered as the criterion of the comparison of different strategies and without throttling. The comparison covers a range of the R_{hit_N} which extends from a small fraction of the readout bandwidth up to twice the bandwidth limit.

Assuming a stable beam intensity, the event rate is only subject to Poissonian fluctuations. As shown in Figure 1, green lines represents "all events". The "all events" are the event counts of the hit generators. Without throttling, the good events go quickly down to 0 when exceeding the bandwidth limitation. Using throttling, the number of good events improves significantly. When the hit rate exceeds the bandwidth limit, a large fraction of the available bandwidth is still used for almost complete, good events. With "Clear" strategy, the good events stay on a plateau. However, with "Stop" strategy the good events have a slightly decreasing slope.

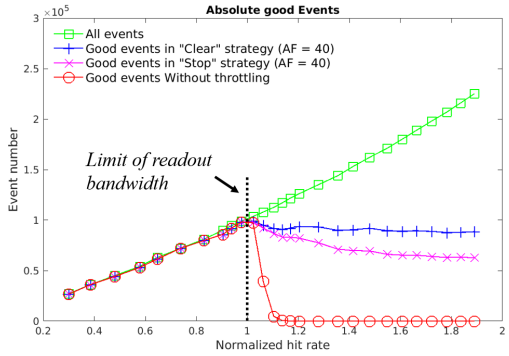

Figure 1: Simulation with stable beam intensity

Figure 2a is the realistic beam intensity structure measured at the SIS 18 accelerator in a beam time in March 2019 [3]. The measurement time resolution is 20 μs. In the simulation, the event rate is varied and scaled proportionally to the measured beam intensity, and obeys a Poisson process within each 20 μs time slot. Similar improvement of data quality with throttling can be observed in Figure 2b. Without throttling, the high intensity fluctuations lead to event losses already at rates below the bandwidth limit. The throttling significantly improves the number of good events

over all hit rates, and provides some advantage already at rates below the bandwidth limit. When the hit rate exceeds the bandwidth, the good events exhibit a plateau with both strategies. However, the good events with “Clear” strategy are a little more than “Stop” strategy.

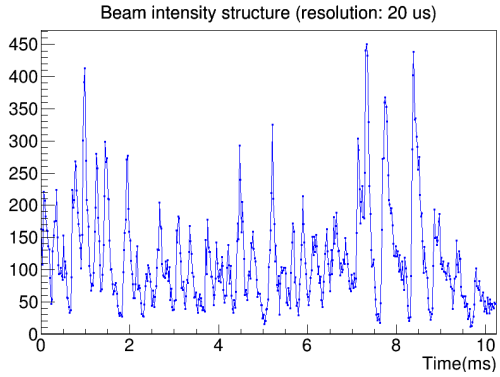

(a) Beam structure

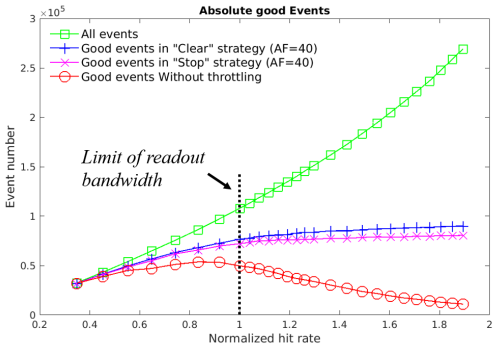

(b) Simulation comparison

Figure 2: Simulation with realistic beam intensity fluctuation

Optimization

According to our investigation, the “Stop” strategy is more sensitive to the throttling threshold than the “Clear” strategy. The “Stop” strategy reaches its best performance at a threshold of 8 almost full FIFOs per ASIC. Our model is based on the STS-XYTER ASIC. In the current version, after reset channel FIFOs, the ASIC is waiting for a command to release the FIFO reset. To reduce the latency of the throttling decision, the reset should be released automatically instead of manually. Because at least 2 downlink frames are required to release the reset by firmware, and the duration of a single downlink frame is 375ns, this modification can save 750ns. After the investigation of the alert parameters and automatic FIFO reset release in the STS-XYTER ASIC, the optimized performances of the two strategies are compared with the preliminary simulation in Figure 3. In both beam structures, the advantage of the optimization is more obvious with higher beam intensity. The tests indicate that the “Clear” strategy gives better overall performance and more robust system behaviour.

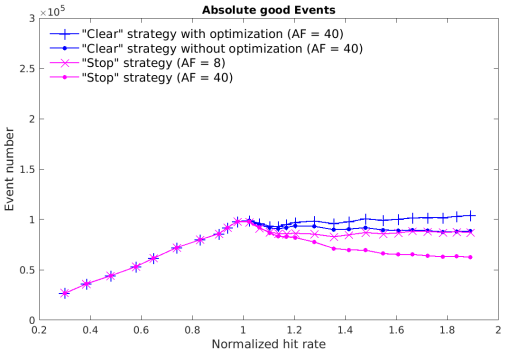

(a) Stable beam

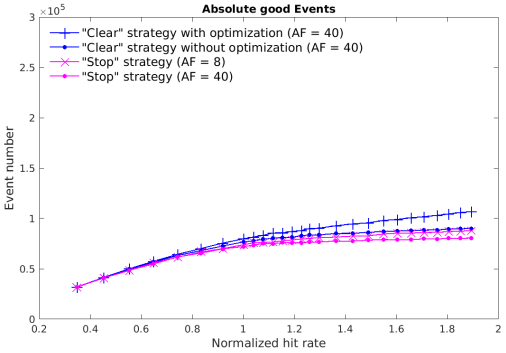

(b) Realistic beam intensity fluctuation

Figure 3: Simulation with optimized parameters

References

[1] X. Gao, D. Emschermann, J. Lehnert and W. F.J. Müller for the CBM collaboration, ”The throttling study for the CBM DAQ chain”, CBM Progress Report 2018, doi:10.15120/GSI-2019-01018

[2] K. Kasinski, R. Szczygiel and W. Zabolotny, ”Back-end and interface implementation of the STS-XYTER2 prototype ASIC for the CBM experiment”, doi: 10.1088/1748-0221/11/11/C11018

[3] A. Rost, J. Adamczewski-Musch, T. Galatyuk, S. Linev, J. Pietraszko, M. Sapinski, M. Traxler, Performance of the CVD Diamond Based Beam Quality Monitoring System in the HADES Experiment at GSI*, in: Pro- ceedings, 10th International Particle Accelerator Conference (IPAC2019): Melbourne, Australia, May 19-24, 2019, 2019, p. WEPGW019

Read-Out Chain Development for the mRICH and RICH Detectors

T. Geßler, A. Weber, E. Ovcharenko, and C. Höhne
II. Physikalisches Institut, Justus-Liebig-Universität Gießen, Gießen, Germany

The mRICH Read-Out System in mCBM

The mCBM campaigns in 2019 provided the first opportunity for a comprehensive test of the mRICH read-out system developed in 2018: the RICH DPB firmware, the TRB hub with integrated CTS, the Optolink firmware for trigger transmission to the mCBM cave, and the unpacker module for CbmRoot. For details about these developments, see the previous year's report.

Due to limited hardware availability, we could not include the full mRICH setup. The system used in December contained 44 of the 72 DiRICHs, corresponding to an active detector region to about 60 %. This region was positioned so as to achieve the greatest possible overlap of the mRICH and mTOF acceptance regions.

We confirmed the functionality of the mRICH read-out chain during common runs with the other mCBM subdetectors. The trigger mechanism, detector read-out, and data acquisition all worked reliably. It became clear that the hub's Gigabit Ethernet output link would constitute a bottleneck at high rates. This potential problem will be avoided with the change to the CRI (see below). In addition, the recorded data showed that the implemented cable-delay compensation mechanism for the trigger signals did not work as intended. The resulting systematic timestamp error can, however, be corrected during analysis.

We analyzed the data from the common runs and were able to reconstruct Cherenkov rings and find correlations with other subdetectors. For details, see the chapter on "mRICH Status and First Data Analysis" in this report.

Migration Towards CRI-Based Read-Out

In the course of the migration to the *Common Read-Out Interface* (CRI), a new generation of FPGA boards will replace the currently used DPBs and FLIBs. The most likely candidate is the FLX-712 platform developed at BNL for the ATLAS experiment. It is equipped with four transmitter MiniPODs and four receiver MiniPODs, allowing for a total of 48 duplex optical-fiber links.

The currently used RICH read-out architecture, based on DPBs, will require heavy modifications for the transition to the CRI. Two aspects of the mRICH read-out system, in particular, will need to be overhauled:

First, the TRB3sc hub board (currently interfacing the DPB with the combiner boards on the RICH front-end) will be removed. Instead, the optical interfaces of the combiner boards, running the TrbNet protocol at 2 Gbps, will be connected directly to the FLX-712. A single FLX-712 can cover up to 47 combiner boards, corresponding to 282 of the about 1 200 MAPMTs planned for the CBM RICH.

Figure 1: CRI setup in Gießen: Optical patch panel with 48 duplex LC connectors and FLES Input Node server.

Second, the currently used synchronization mechanism, based on the transmission of asynchronous "microslice triggers", will be retired. These triggers had to be generated by the DPB as the last component of the read-out chain that was synchronized to the mCBM timing system. This responsibility will be shifted to the combiner boards.

In order to kick-start CRI development for the RICH, we purchased an FLX-712 board along with a FLES server that hosts the board in one of its PCI Express slots. In addition, we ordered optical-fiber hardware for a custom patch panel that fans out the MTP-12 connections from the FLX-712 MiniPODs to individual duplex LC connectors. Figure 1 shows the CRI setup in our electronics lab.

We started the development of the "RICH-CRI" firmware for the FLX-712 and were able to port two platform-specific components from the previous TRB hub firmware, running on a Lattice ECP3 FPGA, to the Xilinx Kintex UltraScale FPGA on the FLX-712: The Ethernet media interface and the serial TrbNet interface. This allowed us to perform first tests of the direct connection between the CRI board and a combiner board without an intermediate hub.

The next goal is the synchronization of the combiner FPGA with the clock and absolute time information from the CRI using two mechanisms: clock recovery from the TrbNet link and TrbNet *Deterministic Latency Messages* (DLM). When this is possible, each front-end module can be considered free-running, recording data independently of an external trigger.

Firmware development for CBM DAQ *

W. Zabolotny[†1], *A. Byszuk*[1], *M. Guminski*[1], *G. Kasprowicz*[1], *M. Kruszewski*[1], *K. Pozniak*[1], *and R. Romaniuk*[1]

[1]Warsaw University of Technology, Institute of Electronic Systems, Warszawa, Poland

Continuation of work on GBTxEMU

The work on the GBTx emulator (GBTxEMU) started in 2018 [1] was continued in 2019. The hardware platform was still the TE0-712 module. However, the new GBTEMU-1 motherboard delivered at GSI became available. It provides the hardware jitter cleaner based on Si5344 chip and free-running boot clock generator needed for reliable initialization of the system. It also provides RJ45 and SFP+ connectors for control and data transmission. That allows the elimination of additional external Ethernet PHY connected via the RMII interface.

That enabled preparing and testing the final version of the GBTxEMU firmware. Its block diagram is shown in Fig. 1.

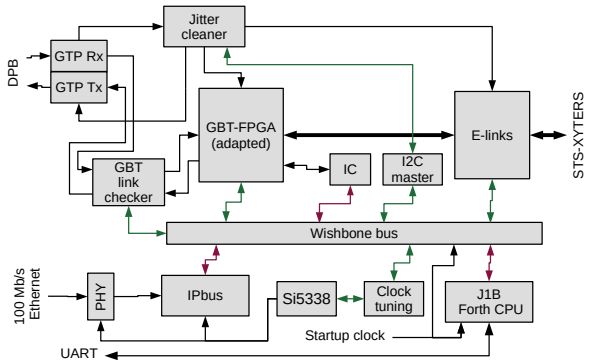

Figure 1: Block diagram of the GBTxEMU firmware for the new GBTEMU-1 motherboard.

The internal control structure of the GBTxEMU was implemented basing on the hierarchical Wishbone (WB) bus, with address management and local WB interfaces generated by the `addr_gen_wb` (AGWB) environment [2,3], subjected to significant improvements comparing to the version available in 2018. The central WB bus runs with 25 MHz clock produced from the free-running boot clock. That clock also drives the J1B Forth CPU, which initializes the whole system.

The initialized GTP receiver delivers the reference clock, that after jitter-cleaning is used to generate the E-Links base clock (160 MHz), the GBT-FPGA frame clock (40 MHz) and GBT transmit frame clock (120 MHz).

After the system is initialized, it may be controlled either via Ethernet by a 100 Mb/s version of IPbus or via the GBT link by the IC-controller. (However, J1B is still able to access the bus.) The original IC controller developed at CERN was modified to enable control of a bus with a wider address space required by GBTxEMU.

The clock-domain-crossing blocks, automatically generated by AGWB, are introduced into the hierarchical WB bus, enabling communication with blocks operating at different clock frequencies.

The E-Links blocks implemented in the GBTxEMU are capable of operating with the E-Link clock frequency 40 MHz (with 40 Mbps downlink, 80 Mbps uplink, and up to 56 E-Links) or 80 MHz (with 80 Mbps downlink, 160 Mbps uplink, and up to 28 E-Links). The E-Link blocks also offer limited control of the clock phase (with 78.125 ps resolution), and of input data sampling delay (up to 2.496 ns with 78 ps resolution, and with selectable clock edge).

The GBTxEMU is also equipped with the link checker block, which, together with a similar block in the DPB enables assessment of the GBT link quality.

Development of the DPB firmware

The DPB firmware has been extended with new diagnostic functions. The temperature of the SFP+ transceivers may be read via the I2C interface. In the configuration with GBTxEMU, the GBT link quality may be measured using the dedicated link checker block.

Support for the new version of the readout ASIC has been added. The SMX2.1 requires that the write operation must be repeated as the whole transaction consisting of "write address" and "write data" commands. The "paired commands" feature was added to the STS command transmitter to satisfy that demand.

Support for various E-Links clock frequencies (160 MHz for CROB operation, 40 MHz or 80 MHz for GBTxEMU operation) required significant modification of the DPB firmware. To avoid duplicate effort, this task was combined with the refactoring of the DPB firmware, aimed at future porting to the CRI platform.

The internal IPbus bus with mostly manually assigned addresses has been replaced with the hierarchical AGWB-generated structure with automatically assigned addresses. That approach significantly simplifies parametrization or future modifications of the blocks and registers structure.

The DPB part of the IC controller required an adaptation to support communication with the IC in the GBTxEMU

* Work partially supported by GSI, and partially by statutory funds of Institute of Electronic Systems

† wzab@ise.pw.edu.pl

due to a wider address bus.

In the previous DPB firmware, the initialization was performed by a simple state machine, controlled by a manually generated binary code. To increase flexibility and to simplify maintenance, the J1B Forth CPU has been used to initialize the AFCK board for DPB operation. That step required the implementation of the initialization routines in Forth language. An additional advantage of that modification is the possibility to read the status of the board via the UART interface (e.g., available in certain JTAG programmers) and to debug the board interactively.

Improvement of the AGWB system

To improve support for complex WB-based systems, the AGWB environment has been enhanced with the following features:

- automated support for multimaster busses,
- possibility to define limited-width register,
- possibility to define initial values of control registers (including bit-fields),
- handling hierarchical XML descriptions of the system,
- handling Python-like expressions in the definitions of values in XML files,
- automated building of documentation in the HTML format.

Modification of the build system

The build system has been ported to use the open source FuseSoc tool [4]. Its main advantages are support for many EDA (Electronic Design Automation) tools used in practice and ease of describing relationships between design units. Due to the change in the build system, the following tasks have been completed:

1. Adding .core files used by FuseSoc to the GBTxEMU project.
2. Adding .core files DPB project.
3. Adding .core files to the General Cores library.
4. Enabling the connection of an open source address generator AGWB, developed for the future implementation of the CRI platform, to the FuseSoc as a generator.

In order to facilitate the process of functional verification and regression testing, the fsva [5] program has been implemented. It enables automatic run of test targets defined in .core files. The tool also allows for seamless integration with the most known frameworks for testing code written in VHDL, i.e., UVVM [6] and OSVVM [7]. Both FuseSoc and fsva are now used in the CI/CD process on the CBM GitLab server.

Modification of software

The Python scripts used to control the DPB have been modified for operation with the new AGWB-based structure of blocks and map of addresses.

Access to the GBTxEMU registers via the IC controller was implemented using the special “raw Python” mode, which creates Python classes directly reflecting the structure of registers together with the access functions.

Compatibility between the CROB-based and GBTxEMU-based access to the FEBs has been implemented via an additional “emu” parameter in the constructor of the CROB-handling object.

Results of tests

The essential functionalities of the GBTxEMU have been confirmed in tests: stability of the GBT link, correct operation of the jitter-cleaner, correct communication with the SMX chips in connected FEBs including the link synchronization and data transmission.

The E-Link clock frequency in the DPB firmware is configurable before the compilation. Correct operation of the firmware working at 160 MHz (using CROB), at 80 MHz (using GBTxEMU), and at 40 MHz (using GBTxEMU) has also been confirmed in tests.

References

[1] W. Zabołotny, A. Byszuk and others, “Preparation of the GBTX emulator”, CBM Progress Report 2018, 2019, GSI, ISBN 978-3-9815227-6-1, ss. 141 - 141

[2] W. Zabołotny, M. Gumiński, M. Kruszewski,“Automatic management of local bus address space in complex FPGA-implemented hierarchical systems”,Proceedings of SPIE 11176 (2019), 1117642, DOI: 10.1117/12.2536259

[3] W. Zabołotny, M. Gumiński, M. Kruszewski,“Addr_gen_wb (AGWB) - register access for hierarchical Wishbone connected systems”,https://github.com/wzab/addr_gen_wb

[4] O. Kindgren,“FuseSoC”,https://github.com/olofk/fusesoc

[5] M. Kruszewski,“Fsva - FuseSoc Verification Automation”,https://github.com/m-kru/fsva

[6] “UVVM (Universal VHDL Verification Methodology)”,https://github.com/UVVM/UVVM

[7] “Open Source VHDL Verification Methodology (OSVVM) Repository”, https://github.com/OSVVM/OSVVM

mFLES Node and InfiniBand HDR Upgrade*

D. Hutter[1], *J. de Cuveland*[1], *and V. Lindenstruth*[1]
[1]FIAS Frankfurt Institute for Advanced Studies, Goethe-Universität Frankfurt am Main, Germany

Figure 1: Part of the mFLES cluster installed in the GreenCube data center. Visible are the two new compute nodes on top and one FLES entry node.

The mFLES cluster serves as a test and development cluster for the CBM FLES, as well as the central readout component of the mCBM experiment. It was used in all mCBM beamtimes to collect and record the detector data. In advance of the mCBM 2019/2020 data taking campaign and to provide extended test and development capabilities for CBM, the mFLES cluster was upgraded in 2019 with new nodes and a fast state-of-the-art InfiniBand HDR network.

The node upgrade includes a new head node for infrastructure services like user management and shared filesystems, as well as two new compute nodes. All nodes provide the newest generation Intel Xeon Skylake CPUs with up to 72 threads in the head node, 192 GB of RAM, and NVMe storage. The up to 64 threads of the compute nodes together with two AVX-512 FMA units per core allow the development and test of highly parallelized code. If required, compute nodes can be additionally equipped with up to four GPUs for GPGPU computing.

In conjunction with the nodes, parts of the InfiniBand network were upgraded to the latest HDR generation. A 40-port HDR switch forms the central part of the new network. The new nodes are equipped with ConnectX-6 HDR HCAs. A single HDR link provides a bandwidth of 200 GBit/s, which drastically exceeds the bandwidth of PCIe gen 3 x16 connections. Due to the lack of PCIe gen 4 support on x86 CPUs at the time of installation, a dual socket HCA is used. Figure 2 shows a picture of the HCA mother and daughter card installed in a PCIe riser of one of the compute nodes. The HCA uses two PCIe gen 3 x16

* Work supported by BMBF and HIC for FAIR

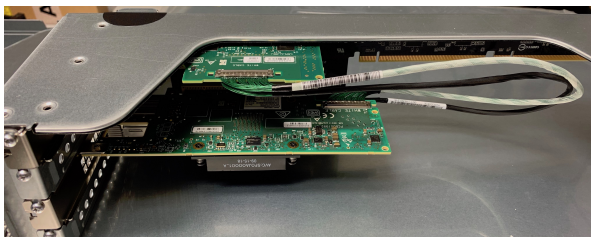

Figure 2: Dual socket ConnectX-6 HDR HCA installed in a PCIe riser of a compute node.

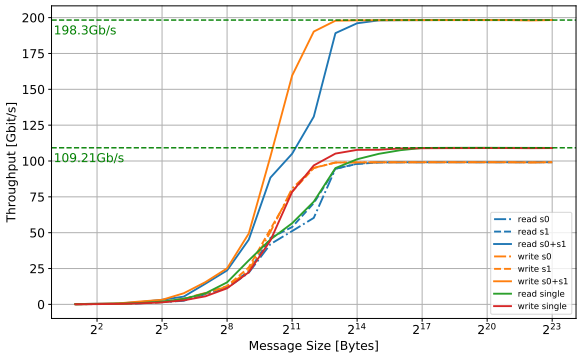

Figure 3: InfiniBand RDMA throughput for a single and two simultaneous streams versus message size.

slots simultaneously and presents itself to the host and operating system as two PCIe devices. However, both devices share the same InfiniBand link.

To verify the InfiniBand performance and assess the characteristics of the dual socket HCA architecture, a set of RDMA read and write benchmarks was performed. Figure 3 shows the archivable throughput versus the message size for four different measurement sets. The read/write single lines show the throughput for a single stream, transmitted via only one of the PCIe devices on both ends. As expected, the throughput is limited by the PCIe interface and saturates at approximately 109 Gbit/s. For the other measurements, two data streams (one per PCIe device) are transmitted simultaneously. To reduce onset effects if the streams are not perfectly synchronized, the measurement interval for each point is 240 s. The solid lines show the accumulated throughput of both streams. For RDMA read as well as write a maximum throughput of 198.3 GBit/s is archived, which is more than 99% of the advertised bandwidth. The dashed lines show the throughput of the individual streams. It is clearly visible that the HCA provides nearly perfect fairness between the two devices.

Computing

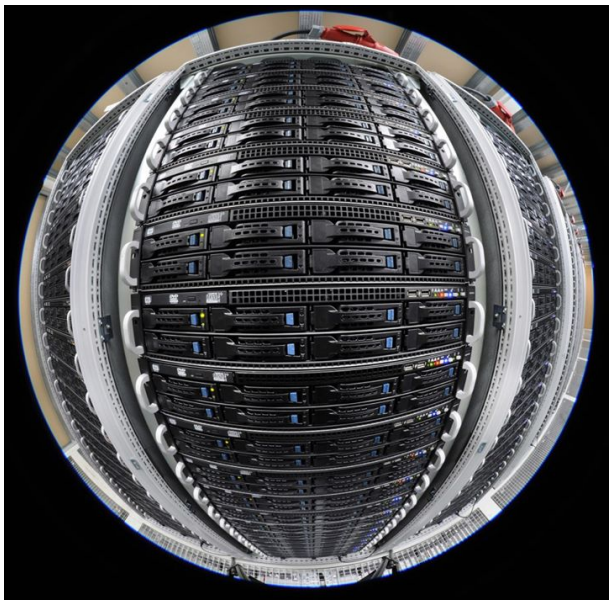

Computing - Summary

J. de Cuveland[1], *V. Friese*[2], *P.-A. Loizeau*[2], *and F. Uhlig*[2]
[1]FIAS, Goethe-Universität Frankfurt, Germany; [2]GSI, Darmstadt, Germany

The CBM computing and software efforts in 2019 were to a great extent focused to the operation of the mCBM test experiment as first opportunity to run and read out a setup with combined detector systems in a free-streaming way as intended for the full CBM experiment. The mCBM experiment enabled us thus to apply and test software that was up to now developed on the base of and benchmarked with simulated data only.

Experiment and Detector Controls

The control and configuration software developed so far allowed to run mCBM but also revealed the need to develop an integrated and scalable system for the operation of full CBM, unifying and integrating the various detector as well as DAQ controls. A first prototype for such an Experiment Control System (ECS) was developed as a baseline for this task.

Online Data Management

For the time-slice building software (flesnet), the global system architecture and the data model are designed, and a full demonstrator chain was established. The network performance was optimised to handle data rates above 1 TB/s. The software was successfully tested in various in-beam tests of CBM detector sub-systems and also with the mCBM setup. It can thus be regarded as the de-facto DAQ standard for CBM. The Infiniband HDR technology was tested, and the software was shown to saturate the hardware limits. Improvements are ongoing to enhance the monitoring capabilities and to improve automation.

Data Processing Framework

The data processing framework is still in the stage of transition from the serial, task-based CbmRoot to a parallel, message-based MQ system. A proof-of-principle for the latter was demonstrated and applied online for mCBM, however, up to now only for a portion of the data stream used for online monitoring. In the context of making our software fit for real-time data inspection, a big effort was invested into stripping the low-level data types (digis) and their containers from overhead which was inherited from times when performance was not yet an issue. This comprised the migration to lean data classes without polymorphism and the transition from ROOT to STL containers while keeping the convenient persistency scheme and analysis facilities offered by ROOT.

Data Analysis Algorithms

Several parts of the low-level reconstruction routines (cluster and hit finding, e.g., for STS) were tested successfully with mCBM data and optimised with respect to processing speed, in order to be applicable for online data analysis. These are among the first steps to establish and test with experiment data an online processing graph allowing to inspect the full data stream in real-time. Developments on higher-level reconstruction (track and event finding) comprised the extension of the cellular-automaton scheme from the central tracking system (MVD+STS) to the downstream detectors (MUCH, TRD), as well as enabling the algorithm to operate on free-streaming instead of event-sorted data. The corresponding algorithms are still subject to development and not yet production-ready. Owing to the different features of mCBM compared to full CBM (e.g., different combinations of detectors, no magnetic field), their application to mCBM necessitates major adjustments, which are in process but not yet finished. The KF Particle package developed for fast high-level analysis of CBM data was successfully applied on STAR data and is being integrated into the STAR high-level trigger system. This strongly suggests it to be a suitable choice for CBM.

Simulation Software

Simulation of the CBM experiment is well-established and, to some extent, mature. It is, of course, subject to quasi-continuous improvements of the detector geometry models (in 2019: magnet and STS) and the response models (in 2019: TRD) adjusting the software to the progress in technical planning as well as to experiment data obtained from detector tests in the laboratory or in-beam. Central efforts were dedicated to streamlining and user-friendliness of the simulation infrastructure according to the needs of the Physics Working Groups. In 2019, this was achieved by the introduction of a new user interface for the transport simulation stage, allowing to steer the simulation by a minimum set of macro commands, where user intervention is only needed when diverging from default settings. The transition to using Geant4 as the default transport engine is in progress.

Software Development Infrastructure

The efforts on the software infrastructure side were concentrated on the upcoming transition to git as a repository system, to which behalf a process of restructuring and cleaning-up of the cbmroot codebase was started. The finalisation of this process and the migration to git is expected for spring 2020.

Optimization of performance for reconstruction in STS and MVD

A. Redelbach
FIAS Frankfurt Institute for Advanced Studies, Goethe-Universität Frankfurt am Main, Germany

In order to operate the CBM experiment at interaction rates up to 10 MHz, real-time data reduction is required. More specifically, since the free-streaming readout data are processed in software, the performance of the reconstruction algorithms is a critical issue. Focusing on the reconstruction tasks performed within single detectors, the existing reconstruction algorithms for the MVD and the STS have been identified to have potential for optimization.

Monitoring of performances and quality assurance

The monitoring of the algorithms used for reconstruction tasks has been in the focus of project [1]. Developing the class *CbmRecoQa* the relevant runtimes, memory usage as well as residuals and pulls for in-depth validation can be analysed. In order to achieve the latter, corresponding data from matching reconstructed hits to Monte Carlo truth are evaluated. The FairRoot class FairMonitor [2] provides runtimes per event or per timeslice and additional information regarding memory usage is obtained from FairSystemInfo. One option particularly useful for performance evaluations is based on fitting the runtimes as a function of the underlying data numbers. Implementing new automatic tests, validations of reconstruction tasks in the time-based setup are performed regularly and the results are uploaded to the central CBM CDash server. This allows the classification of runtime intervals and thereby assigning e. g. a warning level at the CDash server if the deviation of a runtime should be noted. Analogously, a test-based deviation of a residual distribution of reconstructed hits may be classified as an error if it lies outside of an acceptable range. It is important to note that these tests can easily be extended to also monitor and validate other tasks beyond local reconstruction.

Optimizing MVD reconstruction

In the event-based setup of CbmRoot for MVD reconstruction in release APR19 a relatively large runtime has been observed for simulated minimum bias data. Investigating the subsequent tasks of cluster finding and hit finding in MVD, an inefficient processing of small amounts of input data in the *MVD HitFinder* has been identified. The original algorithm of *MVD ClusterFinder* operates at the level of MVD pixels and defines a mapping of input digis to two-dimensional coordinates. In the processing steps, all digis in the input buffer are evaluated if they are above thresholds, neighbouring channels are searched, allowing the definition of cluster arrays and their persistent storage. After reading these cluster objects, the *MVD HitFinder* calculates the hit positions in two dimensions based on the centre-of-gravity algorithm.

As explained in [3], the optimization of the code for reconstruction in MVD comprised the following steps:

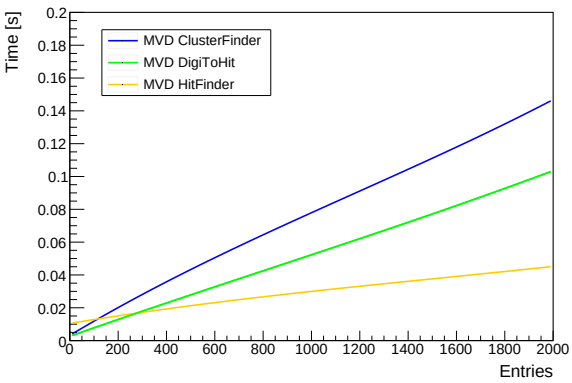

Figure 1: Runtimes for MVD reconstruction based on 1000 minimum bias events of Au-Au collisions for beam momentum of 12 AGeV at FLES node with AMD Opteron processor 6238.

- Replacing non-performant data structures by self-defined data structures being more efficient for caching
- Optimizing the algorithms by fast iterations over two-dimensional arrays of indices and also coordinates
- Combination of *MVD ClusterFinder* and *HitFinder* tasks into a single task *MvdDigiToHit* to reduce memory consumption

As a result, the mapping of input digis to two-dimensional coordinates is replaced by a 2D grid of indices and values indicating the association to a cluster, avoiding any sorting operations of the original mapping and also expensive accesses to storage. In a similar way the corresponding cluster charges are stored in a 2D grid array simplifying the direct evaluation of hit positions in both directions. Full consistency with the results for MVD clusters and hits obtained from the original MVD reconstruction tasks has been verified.

Measurements of the corresponding runtimes have been performed on FLES nodes. In summary, speedup factors

of 2.5 and 4.3 have been obtained for Au-Au events in central and minimum bias collisions, respectively, see also [3]. Using the developments of [1] for the evaluation of runtimes of different MVD reconstruction algorithms, Fig. 1 has been obtained, showing the runtimes as function of the number of entries processed, corresponding to the number of clusters for *MVD ClusterFinder* or the number of hits otherwise.

Optimizing STS reconstruction

Without a priori information of the event structure, reconstruction in the time-based mode faces more challenges in comparison to the event-based case. The algorithm used for finding clusters for free-streaming data from the STS is explained in [4]. This *STS ClusterFinder* algorithm is linear in the number of underlying measurements and should be sufficiently fast for being applied to real-time data reconstruction. However the performance of the *STS HitFinder* algorithm in release OCT19 is problematic for processing large time slices, as can be inferred from Fig. 2. This non-optimal performance could also be an issue for large time slices in the case of Mini-CBM. The optimization has been two-fold: Data-level parallelisation at the level of STS clusters and hits is conceptually straightforward since each of the about 900 modules can be processed independently. Additionally, the combination of clusters at frontside and backside is reduced to the subset of clusters only within the relevant time window. This "sliding window approach" is by default considering the time resolutions on module level, however it is possible to define alternative ranges of time intervals in the implementation. It is interesting to note that this algorithm requires time-sorted clusters and leads to an efficient reduction of combinatorics. Within the project [5] also the combination of cluster plus hit finding into the task *StsDigisToHits* has been analysed, focusing particularly on parallel processing using OpenMP. This combination into a single task has similar advantages as in the previous optimization of MVD reconstruction eliminating the need for storage of STS cluster objects as a default while still allowing their storage as an option e. g. for debugging. As a result, the runtimes needed for *StsDigisToHits* have been significantly reduced for a serial implementation of the new algorithm, see also Fig. 2. It is interesting to note that an extra speedup factor of approximately 10 has been observed for its parallel version, utilizing 16 threads. A further optimization of data structures using mainly standard C++ vector classes is foreseen. Then the compilation of the parallel OpenMP instructions is more straightforward as has been observed during tests at other linux clusters based on different versions of the gcc compiler. .

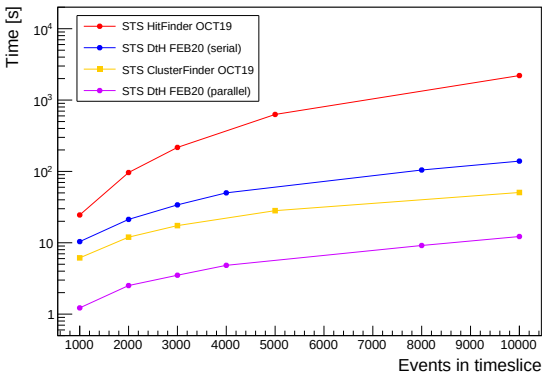

Figure 2: Runtimes for STS reconstruction for different number of min. bias events per timeslice of Au-Au collisions with beam momentum of 12 AGeV. New StsDigisToHits (DtH) task is displayed for serial and parallel execution at FLES node with Intel Xeon Gold 6130 processor.

References

[1] T. Fauerbach, Bachelor thesis 2019, Goethe-Universität Frankfurt, https://indico.gsi.de/event/8804/contributions/ 38287/attachments/27571/34450/Performance_Monitoring_der_lokalen_Rekonstruktionstasks_final.pdf

[2] R. Karabowicz, "Task monitoring tool in FairRoot", GSI Scientific Report 2015 (2016) 276

[3] K. Hunold, Bachelor thesis 2019, Goethe-Universität Frankfurt, https://indico.gsi.de/event/8804/contributions/ 38280/attachments/27576/34455/Bachelorarbeit_Kilian_Hunold.pdf

[4] V. Friese, "A cluster-finding algorithm for free-streaming data", EPJ Web Conf. 2019, 214 01008

[5] F. Boeck, Bachelor thesis 2019, Goethe-Universität Frankfurt, https://indico.gsi.de/event/8804/contributions/ 38282/attachments/27569/34448/Bachelorarbeit_Florian_Boeck_final.pdf

Handling Compute-Node Failures in FLESnet

F. Salem, F. Schintke, and A. Reinefeld
Zuse Institute Berlin

Abstract

FLESnet should tolerate failures of individual compute nodes and should continue to distribute and build timeslices without overly sacrificing the achieved aggregate throughput and latency in large scale deployments. This requires all input nodes to consistently adhere to a new schedule and distribution schema on time and might require the redistribution of not yet entirely built timeslices. We implemented such a fault-tolerance mechanism in our Data-Flow Scheduler that detects and dynamically (re-)assigns the load of failed nodes to the remaining compute nodes. We show the influence of failures on the aggregate bandwidth and latency of timeslice building on our OmniPath testbed.

Introduction

The First-Level Event Selector (FLES) compute cluster builds timeslices (TSs) for analysis using *FLESnet*[1], which was ported to Libfabric. FLESnet distinguishes 'input nodes' and 'compute nodes'. Each input node receives data from the sensor links in a single, circular memory-buffer and chops the stream into micro-timeslices (MTSs). Compute nodes collect MTS contributions from all input nodes to build complete TSs for further analysis. All input nodes distribute their MTSs timely coordinated to compute nodes in a round-robin schema to avoid congestion in endpoints and to establish parallel independent pairwise data transfers with a data flow scheduler (DFS) [1, 2, 3].

Unfortunately, one failed compute node might harm the TS building of all compute nodes. Each compute node maintains a separate memory-buffer per input node. Entries in these buffers can be freed when all contributions for a TS arrived. Missing contributions due to network delays or slow nodes lead to filling receive-buffers for other input nodes. A filled receive buffer eventually stops an input node from sending its MTSs, and consequently, its circular memory-buffer—shared for all compute nodes—starts filling as its entries cannot be freed. With a full circular buffer, sensor data is discarded, and the data distribution to other nodes would be interrupted, too.

To handle failures of compute nodes, a mechanism to detect them and then consistently change the data distribution schema of all input nodes is needed. TSs of failed compute nodes that were not yet successfully built have to be retransmitted to other compute nodes to build them. Failures of input nodes are of no concern as analyzing incomplete TSs is not planned in CBM.

[1] https://github.com/cbm-fles/flesnet

Fault Tolerance Mechanism

To tolerate failures of compute nodes, the buffer management on input-nodes has to be modified. Input-nodes use RDMA writes to transmit the MTSs to compute nodes and get an acknowledgment when its contribution is written into the memory buffer of the target compute node (we call it an *early ack*). Then the input node frees this MTS from its local memory-buffer. When a compute node fails, it probably has some partly gathered TS with contributions from several input nodes missing. Unfortunately, the contributions that already arrived might be deleted from the corresponding input nodes already due to the early ack, and these input nodes are not able to resend them to another compute node. To let input nodes keep the MTSs longer, compute nodes can send the acknowledgment later only when all contributions for a TS arrived (*late ack*). Then, input nodes can reassign the TS building to another compute node in failure cases and can resend their MTSs.

Input nodes have to detect the failure of a compute node to redistribute the MTSs among the remaining compute nodes. A compute node is considered failed when (1) the node is down, (2) the connection between an input and a compute node fails so that TSs cannot be completed, or (3) the transfer rate of a connection suddenly drops too much. To detect node failures, we implemented an eventual perfect failure detector in DFS using heartbeat messages. A compute node (DFS-CN) is considered to be failed when the input node (DFS-IN) is missing a defined number of consecutive heartbeats. DFS adapts the target heartbeat rates dynamically based on the roundtrip transmission time and observed heartbeat delays.

To react consistently to the failure of a compute node, all input nodes have to be informed. Once a DFS-IN detects or is notified about the failure of a compute node, it informs all running DFS-CNs with failure meta-data: (1) The failed node global index, (2) the last acknowledged TS (*last_ack*) from the failed node (maybe, not all input nodes received the ack message but should clean their local memory-buffer accordingly), and (3) up to which TS (*upto_ts*) DFS-IN can send contributions to other compute nodes based on the already received sensor data.

Each DFS-CN that receives a failure message from any DFS-IN informs the other DFS-INs about the failed node global index so that they stop sending contributions to that node and are triggered to send their metadata. The DFS-CN collects and aggregates the metadata of all DFS-INs, that may differ depending on their individual progress. Once the DFS-CN got the meta-data from all DFS-INs, it broad-

casts the decision of the failed node to all DFS-INs that contains the maximum *last_ack* and the minimum *upto_ts* of all DFS-INs. As all DFS-CNs get the same meta-data from all DFS-INs, they calculate the same decisions that they broadcast. DFS-INs receive the same consistent decision meta-data redundantly from any DFS-CN.

The DFS-INs adapt the MTSs distribution schema once a failure decision is received. They mark their MTSs for the failed node up to the decided *last_ack* as completed and transmit the remaining MTSs to the remaining DFS-CNs as planned previously up to the decided *upto_ts* to keep already sent data valid. DFS-INs then distribute the MTSs for the failed node, which have a lower timestamp than *upto_ts*, to other compute nodes in a round-robin manner. After that, DFS-INs continue to distribute the stream of MTSs fairly to the remaining compute nodes, excluding the failed node.

Experimental Evaluation

We tested FLESnet with Libfabric on OmniPath[2] with up to 80 nodes. Each node has 2x Intel Cascade Lake Platinum 9242 (CLX-AP) with 48 cores, 384 GB RAM, 1x Intel OmniPath host fabric adapter.

Each micro-timeslice is 1 MB, and the receive-buffer for each input node at each compute node is 1 GB. Each node embodies either an input or a compute node. The DFS divides the run time into intervals of 10,000 TSs each.

Early vs. Late Acknowledgment. Figure 1 compares the time to complete TSs between late and early ACK. The late ACK behavior synchronizes the input nodes more effectively. However, the aggregated bandwidth in the case of early ACK is about 10 % better (not shown) but this could be compensated using the speedup mechanism of DFS.

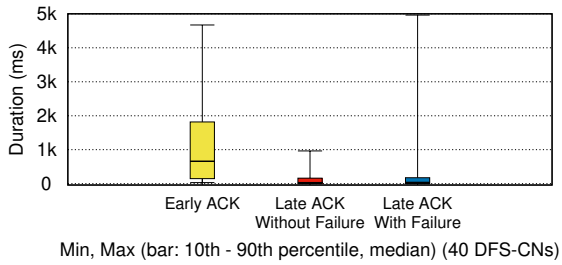

Figure 1: A comparison of the time to complete TSs from 40 DFS-INs in two different scenarios between: (1) late and early ACK, (2) with and without node failure.

Fault-Tolerance mechanism. Figure 2 compares the bandwidth statistics over time between DFS with and without a node failure. We forced the first node to die after around 350 seconds. Once the node fails and while reaching a failure agreement, the bandwidth regularly dropped until it reached zero MB/s for a second. After reaching an agreement, DFS transmits the data with higher throughput to follow the scheduler. The high variance between the 10th and the 90th percentile is either during a node failure or a DFS speedup phase. Figure 1, the lower plot, depicts the time to complete TSs. The node failure causes some TSs to complete in longer duration, which is up to 10 % of TSs.

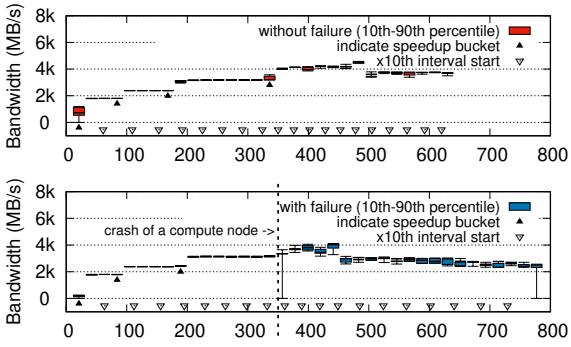

Figure 2: The bandwidth building TSs for 2k intervals (min, 10th and 90th percentile, median, and max) observed per s at 40 DFS-INs (sending to 40 DFS-CNs) bucketed per 20 s over elapsed time. Speedup intervals (25 % faster) take place when very low bandwidth variance ($< 5\,\%$) exists between all nodes.

Conclusion

We presented a mechanism to tolerate failures of compute nodes in FLESnet by delaying the acknowledgment for MTSs until completing the timeslices and reassigning the timeslice building accordingly. Thus, input nodes resend timeslices to other compute nodes in case of node failures. Nodes agree with broadcasts on node failures and the amount of MTSs to redistribute. The evaluation shows that the fault-tolerance mechanism in DFS works and that input nodes successfully adapt to fewer available compute nodes over time. The experiments also show the advantage of late acks that reduce the duration to complete timeslices at compute nodes in general.

Acknowledgments. The project was partly funded by the BMBF grants 05P15ZAFC1 and 05P19ZAFC1. We thank the HLRN for computing time on the Omnipath system.

References

[1] F. Salem, F. Schintke, T. Schütt, and A. Reinefeld, “Improving the throughput of a scalable FLESnet using the Data-Flow Scheduler”, CBM Progress Report 2018, pp. 149–150.

[2] F. Salem, T. Schütt, F. Schintke, and A. Reinefeld, “Scheduling Data Streams for Low Latency and High Throughput on a Cray XC40 Using Libfabric”, CUG Conf. Proceedings, 2019.

[3] F. Salem, F. Schintke, T. Schütt, and A. Reinefeld, “Scheduling data streams for low latency and high throughput on a Cray XC40 using Libfabric”, Concurrency and Computation Practice and Experience, pp. 1–14, 2019.

[2] https://www.hlrn.de

ANaN (ANalyse And Navigate) — a debugger for compute clusters

A. Adler and U. Kebschull
IRI, Goethe-Universität Frankfurt, Frankfurt, Germany

Not much science can be performed without the help of extensive computation and calculation, far more than can be performed by pen and paper. Therefore, any major science project uses significant computational resources, often leading up to building and maintaining its own data center. Sadly, computers need far more maintenance than pen and paper. A tool in continuous use is *monitoring*, both used to 1. *setup* the cluster (while installing and configuring the necessary software; setting up networking; ...) and 2. *operate* it (while applying security updates; patching software; ...)

Most monitoring software is developed towards the second part and is less helpful with the first part. Anecdotally, it has been found that monitoring alone lacks a certain dynamicity: Finding underlying causes of unwanted behaviours (bugs; performance issues) still requires a lot of manual work, and reconfiguring monitoring to gather precisely the necessary data is too much hassle. Even once this is done, the monitored data is not always available in an easily accessible format and needs to be imported into visualisation and analysis tools. Therefore, we report on ANaN, a debugger as an addition to monitoring.

Since the notion of a debugger as a complement to monitoring is new, a few remarks are in order to explain the relation between debugging and monitoring. Consider the case of a symbolic debugger such as the "GNU Debugger" `gdb`. Before symbolic debuggers were available (or in embedded systems or unusual architectures, where no symbolic debugger has been ported to), a pragmatic strategy asked for the placement of `printf` statements in well-chosen parts of the code. Name this strategy `printf` debugging and consider the advantages to symbolic debugging:

- It is easily available in all systems in which the program's output can be captured.
- It doesn't require any special support by hardware, software, or knowledge of the binary and linking formats applied.
- The influence on the program's runtime and resource use are predictable.

Of course, there are corresponding disadvantages:

- The program needs to be available in source form, and the complete workflow of editing, compiling, linking, deploying and restarting the program can cost a lot of time.
- Choosing the right place for the `print` statements is not trivial: Too much output is hard to sift (requiring some sort of automated evaluation), too little might easily mean that the interesting part is missing.
- Debug statements might stay in production code, later cluttering system logs.

ANaN tries to be to monitoring what symbolic debugging is to `printf` debugging while avoiding the disadvantages.

Each system under consideration (these may be virtual machines, containers or bare metal, as long as they can run POSIX processes) runs a **demon**. The demons report approximately once every second to the **debugger** — the interactive tool used by the cluster's operator. The operator can deploy one or more **sensors** to each system under consideration. The sensors are little snippets of code collecting data. Templates for sensors in common use or for site-specific sensors can be stored in a run control file.

Since much interesting information can be found in the files of the pseudo file systems `proc` and `sys` (the by far most common alternative being the device files under `/dev/` with appropriate `fcntl` or `ioctl` calls), a fitting model for sensors is the pattern scanning and processing language "AWK": A list of files is considered, split into (generalised) lines and (generalised) columns, each line is matched against a list of patterns; in case of a match, the corresponding code is executed. This highly general mode of operation enables writing most relevant sensors in a matter of a few lines, see also[1] for further details.

The debugger is operated via a command line interface, using the scripting language Lua [2] as command language. Since Lua is extensible in multiple ways, it proved easy to embed a functional language fragment in it, enabling elementary data analysis to be performed in a way similar to the UNIX pipe mechanism. All further analysis and visualisation should be relegated to specialised tools, though.

ANaN is in development, and as requirements change, new features need to be added. Currently, an installment essentially mimicking monitoring is being worked on at some part of the ALICE O^2 cluster [3]. Additionally, a synthetic benchmark with about 10000 systems under consideration is being prepared.

References

[1] A. Adler and U. Kebschull: *Debugging Computer Clusters with Techniques from Functional Programming and Text Stream Processing*. Poster, CHEP 2019, Adelaide, Australia, 2019

[2] R. Ierusalimschy: *Programming in Lua*. Lua.org 2006

[3] Ananya *et al.*, J. Phys. Conf. Ser. 513 (2014) 012037

Physics Performance

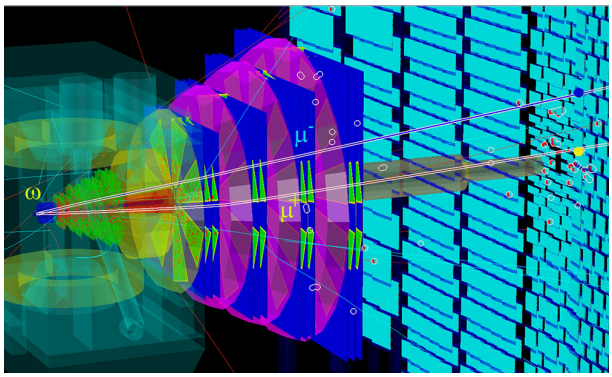

Di-electron reconstruction in Ag+Ag collisions at 4.5 AGeV beam energy in simulations for the HADES and CBM experiments

M. Becker[1], *G. Pitsch*[1], *S. Lebedev*[1], *and C. Höhne*[1,2]
[1]Justus-Liebig-Universität, Giessen, Germany; [2]GSI, Darmstadt, Germany

Detailed feasibility studies of di-electron reconstruction for the CBM detector setup have been shown in the previous progress report [1]. We performed new investigations of di-electron reconstruction for the HADES detector for the same collision system [2]. Since the HADES detector is designed for small beam energies of a few GeV at SIS18, the 4.5 AGeV of SIS100 is a rather large energy. However it might be a good compromise between HADES and CBM capabilities for a common collision system and was thus studied for HADES as well.

The standard setup for the HADES detector of its 2017 proposal is used and differs to the CBM setup. HADES, known for its high acceptance in polar angle $\theta \geq 18°$ and $\theta \leq 85°$ is using a target, segmented in 15 foils of 42 μm each [4]. The event generator UrQMD was used for both simulations with embedded signal di-electrons from PLUTO. The di-electrons from ω, ϕ and in-medium ρ and the ω-Dalitz decay have been studied. The in-medium ρ di-electrons contribution was taken from the HADES measurement of Ag+Ag collisions 1.65 AGeV and scaled by the factor 3.25 to the number of π^0 per event. Thus the same input as for CBM was used [2,3].

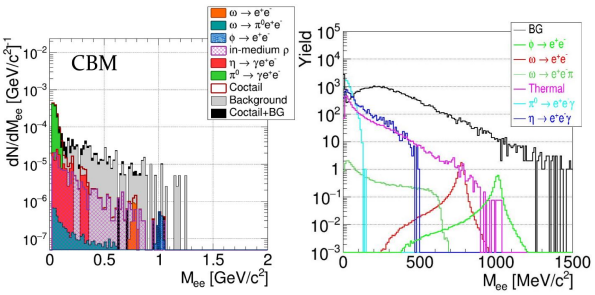

Figure 1: Di-electron invariant mass spectra after all cuts. Left: $10{\cdot}10^6$ minimum bias events reconstructed in CBM without p_t cut. Righ: $8{\cdot}10^6$ events of 40% centrality reconstructed by HADES.

The invariant mass spectra are shown in Fig. 1 for both HADES and CBM. The extracted ratios of signal to background are presented in Fig. 2. In both experiments the signal to background ratio ranges from 10^{-1} to 10^{-2} in the region 150-1000 MeV/c^2. The reconstruction efficiency as a function of p_t-y is shown in Fig. 3 (midrapidity is at 1.13).

The integrated reconstruction efficiency of the ω-meson without p_t cut in CBM is 1.7%, while for HADES it reaches 12.9%. This difference is explained by the fact that HADES covers the midrapidity region, while the CBM acceptance is in the very forward region. Both experiments

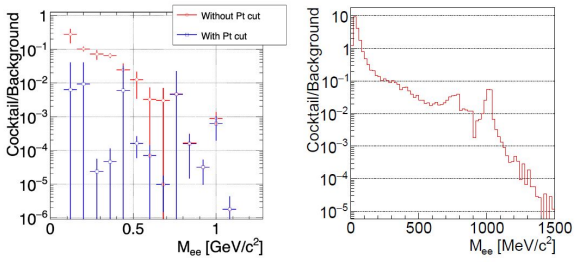

Figure 2: Signal to background ratios, left CBM, right from HADES.

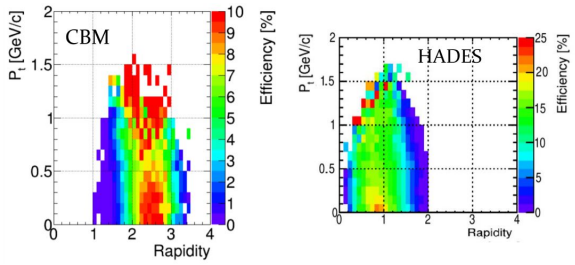

Figure 3: P_t-y coverage of calculated efficiencies for the ω-meson. For HADES we see efficiencies up to 20% at midrapidity (y_{CM}= 1.13) while CBM has a higher efficiency in forward rapidity.

together cover large areas of the phase space with a small overlap for $1.5 < y < 2$. Over all its a great benefit to have HADES as experiment complementary to CBM for confirmation of the results.

References

[1] G.Pitsch, S.Lebedev, C. Höhne, "Feasibility studies of di-electron reconstruction in Au+Au collisions at 8 AGeV beam energy and Ag+Ag collisions at 4.5 AGeV beam energy", CBM Progress Report, p. 171, 2018.

[2] M. Becker, "Di-Elektronen Simulationen in Ag+Ag Kollisionen bei 4.5 AGeV Strahlenergie mit dem HADES Detektor am SIS100 und HADES RICH Untergrundanalyse in Ag+Ag Kollisionen bei 1.58 AGeV Strahlenergie am SIS18", Masterthesis, Universität Giessen September 2019.

[3] G.Pitsch, "Machbarkeitsstudien der Di-Elektronen-Spektroskopie in Ag+Ag Kollisionen mit 4.5 AGeV Strahlenergie mit dem CBM Detektor", Masterthesis, Universität Giessen September 2018.

[4] https://hades-wiki.gsi.de/foswiki/bin/view/RICH/TargetArea

Systematic study of multi-strange hyperon reconstruction efficiency

I. Vassiliev[1] *and the CBM Collaboration*
[1]GSI, Darmstadt

Enhanced production of multi-strange hyperons and antihyperon is considered a key observable of the transition from hadron matter to a deconfined and chirally restored phase. The CBM experiment will measure such rare diagnostic probes including $\bar{\Lambda}, \Xi^-, \bar{\Xi}^+, \Omega^-$ and $\bar{\Omega}^+$ multi-differentially with unprecedented precision and statistics. In order to measure yields, dN/dy, dN/dp_t and dN/dm_t, raw data should be efficiency corrected. One of the main factor of the correction procedure systematic uncertanties is hyperon reconstruction efficiency obtained with Monte-Carlo (MC) simulation. Systematic study of the multi-differential efficiencies obtained with two different models, UrQMD [1] and PHSD [2], is presented.

The SIS-100 electron/hadron setup for the CBM detector was used for high statistics MC simulation. Multi-strange hyperons will be identified in CBM by their decay into charged hadrons, which are detected in the Micro Vertex detector (MVD), Silicon Tracking System (STS) and in the Time-of-Flight detector (TOF). Four layers of the Transition radiation detector (TRD) are used by the global tracking to propagate tracks found in STS to TOF. In addition energy deposition dE/dx measured by the TRD detector will be used to identify fragments like ^{3}He and ^{4}He.

A set of $5 \cdot 10^6$ central Au+Au UrQMD and PHSD events at 10 AGeV have been simulated with the GEANT 3 transport engine. The STS hits were produced assuming 100 kHz interaction rate with 10^4 ns length of the time-slice. Event-by-event mode was used. The KF Particle Finder package [3] was used in order to reconstruct multi-strange hyperons. High statistics allows to calculate even rare probes like $\Omega^{\pm}$ and $\Xi^{\pm}$ reconstruction efficiency directly, avoiding signal embedding into model events. It allows to investigate systematic behavior of different physics observables, e.g. direct and elliptic flow, excitation function and antihyperon-to-hyperon ratios.

The Ξ^- reconstruction efficiencies as a function of p_t are shown in Fig. 1. The average Ξ^- reconstruction efficiency obtained with UrQMD model is about 13%, while with PHSD model is about 11%. The main reasons for this 2% difference are different p_t distributios provided by the two models (average p_t value for the UrQMD model is about 0.67 GeV/c, for the PHSD model is about 0.57 GeV/c), different average track multiplicity per central collisions (343.3 for the UrQMD and 349.4 for the PHSD) and different Ξ^- average multiplicity per event (1.9 and 8.3 correspodingly).

The behaviour of Ξ^- reconstruction efficiencies is very similar in the two models - smooth increase from 0 to 0.8 GeV/c and nearly plateau from 0.8 till 2.4 GeV/c. The Ξ^- reconstruction efficiencies versus rapidity is shown in

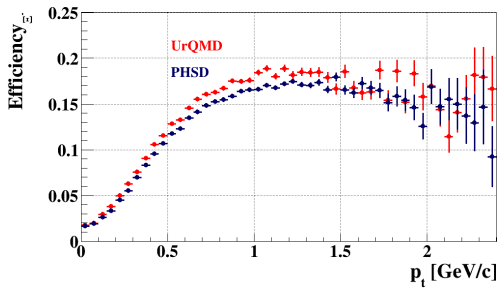

Figure 1: Ξ^- reconstruction efficiency as a function of p_t in central Au+Au collisions at 10 AGeV, calculated with UrQMD and PHSD.

Fig. 2. The main difference between the models is observed in the 1.3 - 2.5 rapidity window. The average rapidity value in the lab frame is 1.56 where the maximum difference is about 3%.

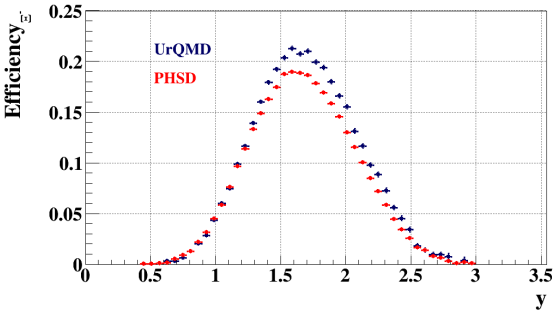

Figure 2: Ξ^- reconstruction efficiency as a function of rapidity in central Au+Au collisions at 10 AGeV, calculated with UrQMD and PHSD.

References

[1] S.A. Bass et al. *Microscopic Models for Ultrarelativistic Heavy Ion Collisions* , Prog. Part. Nucl. Phys. 41 (1998) p. 225-370

[2] W. Cassing and E.L. Bratkovskaya *Parton transport and hadronisation from the dynamical quasiparticle point of view* Phys. Rev. C78 (2008) 034919, arXiv:0808.0022 [hep-ph]

[3] I. Kisel, I. Kulakov and M. Zyzak, *Standalone First Level Event Selection Package for the CBM Experiment*, IEEE Transactions on Nuclear Science, vol. 60, No. 5, October 2013, p. 3703.

Multi-strange hyperon reconstruction with the CBM light setup

I. Vassiliev[1], *I. Kisel*[1,2,3], *and the CBM Collaboration*
[1]GSI, Darmstadt; [2]FIAS, Frankfurt am Main; [3]Goethe-Universität, Frankfurt am Main

The main goal of the CBM experiment at FAIR is to study the behavior of nuclear matter at very high baryonic density. This includes the exploration of the high density equation of state, search for the transition to a deconfined and chirally restored phase, critical endpoint. The promising diagnostic probes for this new states are the enhanced production of multi-strange (anti-)particles. The CBM detector is designed to measure such rare diagnostic probes multi-differentially with unprecedented precision and statistics. The CBM detector will provide a unique opportunity to measure yields, direct and elliptic flow, excitation functions of multi-strange hyperons at different energies and sizes of the colliding nuclei.

The start (light) version of the CBM detector may contain Magnet, beam pipe and few subdetectors: Silicon Tracking System (STS) and the Time-of-Flight detector (TOF). This setup allows to measure strange and multi-strange hyperons and some Hyper nuclei like ${}^{3}_{\Lambda}$H and ${}^{4}_{\Lambda}$H. They will be identified by their decay into charged hadrons, which are detected in the STS, and the global tracking which propagate tracks found in STS to the TOF. In addition energy deposition dE/dx measured by the STS detector will be used to identify fragments like ^{3}He and ^{4}He.

To study the performance of multi-strange hyperon reconstruction with the CBM experiment, a set of $5\cdot 10^6$ central Au+Au UrQMD events at 12 AGeV for the CBM light setup have been simulated with the GEANT 3 transport engine. The STS hits were produced assuming 100 kHz interaction rate with 10^4 ns length of the time-slice. Event-by-event mode was used.

The KF Particle Finder package [1] was used in order to reconstruct multi-strange hyperons. Currently its reconstruction scheme contains about 200 decays including $K^0_s \rightarrow \pi^+\pi^-$, $\Lambda \rightarrow p\pi^-$, $\bar{\Lambda} \rightarrow \bar{p}\pi^+$, $\Xi^- \rightarrow \pi^-\Lambda$, $\bar{\Xi}^+ \rightarrow \pi^+\bar{\Lambda}$, $\Omega^- \rightarrow K^-\Lambda$ and $\Omega^+ \rightarrow K^+\bar{\Lambda}$. The corresponding invariant mass spectra are shown in Fig. 1. All signals are clearly visible with high signal to background ratio.

Double-differential p_t versus rapidity efficiency distribution, integrated efficiency as a function of p_t and rapidity are shown in Fig. 2 for the reconstructed (filled red histogram at the lower right plot) Ξ^-s. These functions will be used for the comparison of theoretical models with measured data. The average Ξ^- reconstruction efficiency is about 10.2%, an invariant mass resolution of 2.2 MeV/c^2 with signal to background ratio of about 5.2 is obtained. The Ω^- reconstruction efficiency results to about 6.3% for central UrQMD events. An excellent signal to background ratio of about 30 is observed. The reconstructed mass value 1.672 ± 0.003 GeV/c^2 is in a good agreement with the PDG's data. An invariant mass resolution of 2.3 MeV/c^2 is obtained.

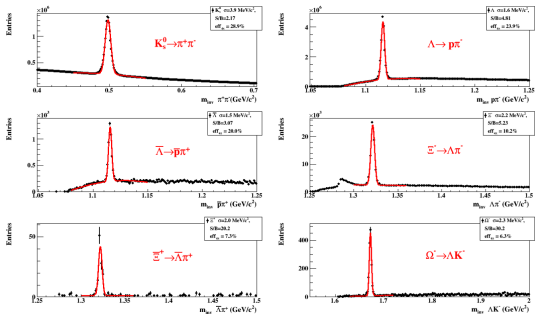

Figure 1: Reconstructed invariant mass distribution of K^0_s, Λ, $\bar{\Lambda}$, Ξ^-, $\bar{\Xi}^+$ and Ω^- in central Au+Au collisions at 12 AGeV, the red line indicates the signal plus background fit by a polynomial plus Gaussian functions.

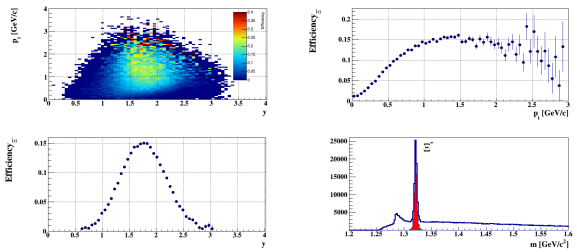

Figure 2: 2D Ξ^- reconstruction efficiency as a function of p_t and rapidity (upper left), integrated Ξ^- reconstruction efficiency as a function of p_t (upper right) and rapidity (lower left). Selected Ξ^- invariant mass signal and total mass plots (lower right).

High statistics allows to calculate even rare probes like $\Omega^{\pm}$ reconstruction efficiency directly, avoiding signal embedding into model events. It allows to investigate systematic behavior of different physics observables, e.g. direct and elliptic flow, excitation function and antihyperon-to-hyperon ratios.

References

[1] I. Kisel, I. Kulakov and M. Zyzak, *Standalone First Level Event Selection Package for the CBM Experiment*, IEEE Transactions on Nuclear Science, vol. 60, No. 5, October 2013, p. 3703.

Hadron measurements with muon setup

A. Senger[1] *and the CBM collaboration*[1]
[1]FAIR, Darmstadt, Germany

Hadron reconstruction with the STS without time-of-flight information

Short-lived hadrons can be identified without time-of-flight measurement using only information from the STS. The CBM track reconstruction software based on the Cellular Automaton algorithm [1] provides in addition to the track curvatures and momentum also secondary vertices, and, hence, the decay topology of instable particles such as hyperons. Since the Time-of-flight detector is not used in the analysis, no particle identification is provided. The Kalman Filter Particle Finder Package [2] is therefore used to reconstruct the invariant mass of the decay products, using a hypothesis on the particle identities. As examples, the reconstruction results for the decays of $K^0_S \rightarrow \pi^+\pi^-$, $\Lambda \rightarrow p\pi^-$, $\Xi \rightarrow \Lambda K^-$, and $\Omega^- \rightarrow \Lambda K^-$ are shown in figure 1, simulated for central Au+Au collisions at 12A GeV/c using the UrQMD event generator. K^0_S mesons are reconstructed from 2 tracks of opposite charged particles emerging from a secondary vertex, assuming that the particles are pions. The same decay topology is used to reconstruct Λ hyperons, assuming that the positive particle is a proton. Once a Λ is identified, which is not created in the primary vertex of the collision, the algorithm looks for another decay product, which is assumed to be either a pion or a kaon. In the first case, Ξ^- hyperons are reconstructed, in the second case Ω^- hyperons. In both cases the multi-strange hyperons are tracked back to the primary vertex.

As illustrated in figure 1, Λ and Ξ^- hyperons can be nicely identified by using information from STS only. The reconstruction of Ω^- hyperons suffers from the large background of pions, which have been considered as kaons. Also the invariant mass spectrum of the K^0_S meson has a rather high background resulting in a signal-to-background (S/B) ratio of about 1. The reason for this relatively low S/B ratio is, that due to its short decay length of $c\tau$ = 2.67 cm the K^0_S meson decays right after the target in front of the first STS station, and its reconstruction suffers from a large background of primary pions. Although the decay length of the Ξ hyperon ($c\tau$ = 4.91 cm) is shorter than the one of the Λ ($c\tau$ = 7.89 cm), the background in the Ξ spectrum is lower (S/B = 4.6) than for the Λ hyperon (S/B = 3.4). The reason is that the Ξ hyperon is reconstructed from three decay particles, which constrains the decay topology better than a two- particle decay. The S/B ratios for both the Λ and Ξ^- hyperon are sufficient to extract momentum and angular distributions for further analysis. The total reconstruction efficiency is 22% for K^0_S, 23% for Λ, 9% for Ξ^-, and 12% for Ω^- hyperons.

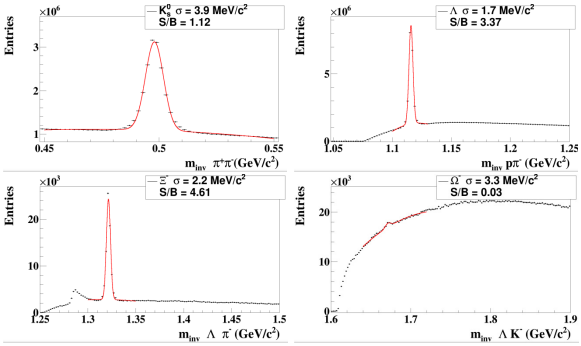

Figure 1: Invariant mass spectra of K^0_S (upper left panel, ϵ = 22%), Λ (upper right, ϵ = 23%), Ξ^- (lower left, ϵ = 9%), Ω^- hyperons (lower right, ϵ = 9%) reconstructed using information from STS only for central Au+Au events at 12A GeV/c.

In addition to hyperons, also hyper-nuclei like ${}^3_\Lambda$H$\rightarrow{}^3$He+π^- or ${}^4_\Lambda$He$\rightarrow{}^3$He+p+π^- can be reconstructed using the STS only. In this case, the dE/dx information from the STS is used to separate single charged from double charged particles. The simulated performance of the STS concerning particle identification via dE/dx is illustrated in figure 2 for two cases. Figure 2 depicts the energy loss in a 300 μm thick silicon sensor as function of momentum for particles identified by MC information (left panel), and without particle identification (right panel). In both cases only positive particles are considered, assuming q=1. The red line in the right panel of figure 2 is used to separate particles with charge 1 (dE/dx values below the line) from particles with charge 2 and more (dE/dx values above the line).

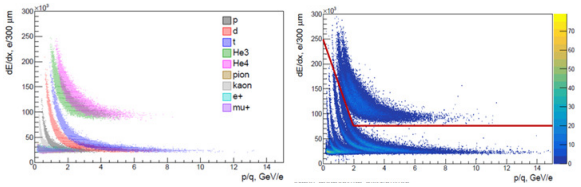

Figure 2: Calculated energy loss dE/dx in 300 μm silicon as function of particle momentum for single and double positively charged particles assuming q = 1. Left panel: with particle identification from MC. Right panel: without particle identification.

Taking into account the dE/dx information from figure 2

(right panel), the invariant mass spectra for the hypernuclei ${}^{3}_{\Lambda}$H and ${}^{4}_{\Lambda}$He have been analysed in simulations of central Au+Au collisions at 12A GeV/c. In such reactions, ${}^{3}_{\Lambda}$H and ${}^{4}_{\Lambda}$He can be reconstructed with signal-to-noise ratios of about 2 and 3.4, and with efficiencies of ϵ = 9.5% and ϵ = 5.7%, respectively, as shown in figure 3.

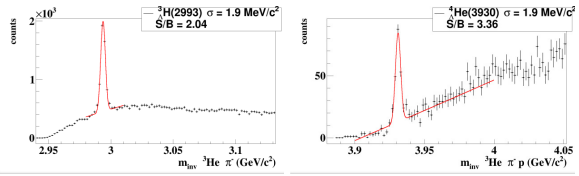

Figure 3: Invariant mass spectra of ^{3}Hπ^- (left panel) and ^{3}Hπ^-p (right panel), reconstructed in STS using dE/dx information with an efficiency of ϵ = 9.5% and ϵ = 5.7%, respectively, in central Au+Au collisions at 12A GeV/c. The hyper-nuclei ${}^{3}_{\Lambda}$H (left) and ${}^{4}_{\Lambda}$He can be clearly identified with signal-to-background ratios of S/B = 2.04 and S/B = 3.36, respectively.

Hadron identification by TOF behind MUCH

In the following, we discuss the performance for hadron identification using the CBM setup with 4 hadron absorbers together with the TRD and the TOF detectors as shown in figure 4. The hadrons are identified by cuts in the plane of mass squared versus particle momentum, as illustrated figure 5.

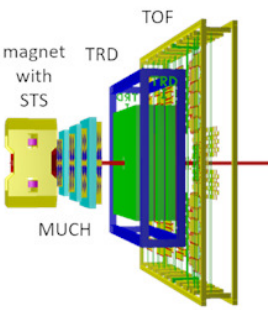

Figure 4: The CBM setup used for the simultaneous measurements of muons and hadrons consists of the STS, 4 hadron absorber layers + 4 tracking stations, the TRD and the TOF detector.

The simulation of hadron identifcation behind the MUCH is performed for central Au+Au collisions at 12A GeV/c. The left panel of figure 6 depicts the probability for particles to pass the hadron absorbers, and to produce Monte Carlo points in the TRD and in the TOF detector, as function of their momentum. In this case, only particles are taken into account, which have produced at least 4 Monte Carlo points in the STS, and, hence, can be reconstructed. The kaon yield is reduced by about a factor of hundred

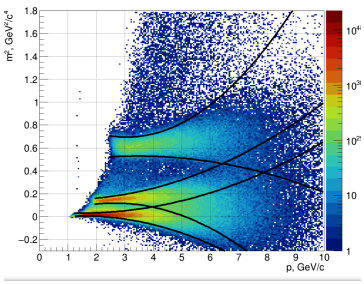

Figure 5: Mass squared as a function of momentum for particles passing through muon system. Black lines - 2σ cut for particle identification.

(black dots). Most of the kaons produced at FAIR energies are K+ mesons, which have a small inelastic hadronic cross section, and, therefore, are less suppressed than pions (red dots). On the other hand, the pion yield is 5 to 10 times higher than the kaon yield, depending on the beam energy. Protons are suppressed by a factor of about 1000. The right panel of figure 6 depicts the identification efficiency for the hadrons shown in the left panel, using the TOF information as function of momentum. Pions with momenta above 2 GeV/C can be identified with an efficiency between 80 and 90%. Similar efficiencies are reached for kaons with momenta above 3 GeV/c. The proton reconstruction efficiency is about 80% for momenta above 3 GeV/c.

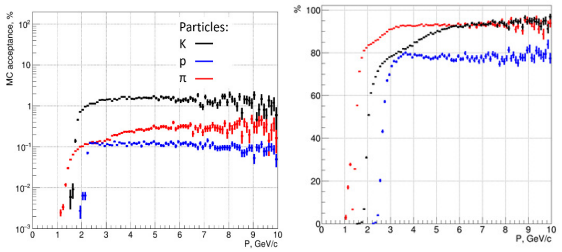

Figure 6: Left panel: Acceptance of the TOF detector for hadrons traversing the absorbers of the muon detection system as function of the hadron momentum. Right panel: Reconstruction efficiency for hadrons using TOF information in the muon setup (same color code as in the left panel). The simulation was performed for central Au+Au collisions at 12A GeV/c.

The acceptance of the TOF wall for hadrons in the plane transverse momentum versus rapidity during the muon measurements is plotted in figure 7 for kaons (left panel), protons (center pamel), and pions (right panel). The simulations were performed for central Au+Au collisions at 12A GeV/c, midrapidity is at y = 1.58. The results demonstrate, that the hadron absorbers cut out low transvere momenta around midrapidity and below, but also show, that the remaining range of rapidities is still sufficient to perform reference measurements of hadrons in parallel to the

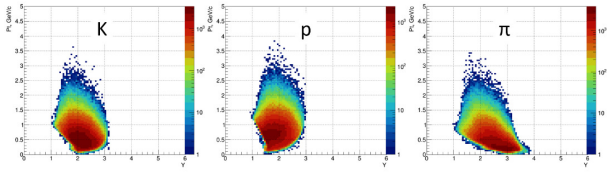

Figure 7: Acceptance for kaons (left), protons (center) and pions (right) detected in the TOF wall behind the muon system as function of rapidity simulated for Au+Au 12A GeV/c. Midrapidity is at y = 1.58.

muon experiments [3].

References

[1] S. Gorbunov and I. Kisel, IEEE Nuclear Science Symposium, Dresden 2008, http://www.gsi.de/documents/DOC-2008-Oct-94-1.pdf

[2] I. Kisel, I. Kulakov and M. Zyzak, IEEE Transactions on Nuclear Science vol. 60, No.5 (2013) 3703

[3] A. Senger for the CBM Collaboration, accepted for publication in Int. Jour. Mod. Phys. E

Efficiency correction procedure for muon-pairs from ω meson decays

A. Senger[1] *and the CBM collaboration*[1]
[1]FAIR, Darmstadt, Germany

This report presents an efficiency correction procedure for muon-pairs from ω meson decays, reconstructed with the muon system (MUCH) consisting of four hadron absorbers and four tracking stations: the first two stations consist of GEM detectors, the 3rd and 4th station are built from RPC detectors [1]. The muon track candidates are selected from tracks which are reconstructed in STS, MUCH, TRD and TOF using track quality cuts, and 2σ cut in the plane of mass squared versus momentum for particle identification. The $p_T(y)$ distribution of all muon pair candidates for central UrQMD [2] Au+Au events (background) + PLUTO [3] generated ω mesons at 8A GeV/c beam momentum is shown in the left panel of figure 1.

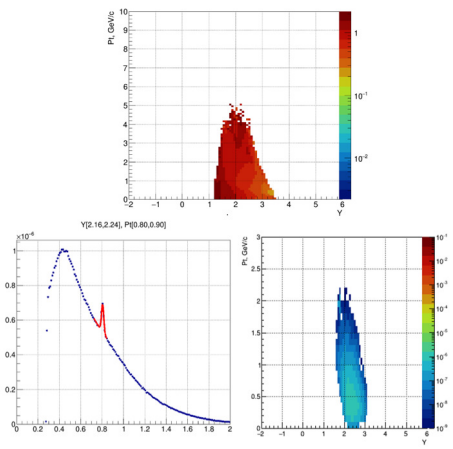

Figure 1: Top picture: The rapidity - transverse momentum ($p_T(y)$) distribution for all muon pair candidates. Left bottom picture: invariant mass distribution for particular bin of the $p_T(y)$ distribution (see plot title), fitted with the sum of a Gauss function and an exponential function (red line). Right bottom picture: $p_T(y)$ distribution of reconstructed ω mesons, after subtraction of the background.

The ω meson reconstruction proceeds as follows: for each bin in the $p_T(y)$ distribution of all muon pair candidates (top figure 1), the invariant mass distribution is calculated and shown in the bottom left panel of figure 1. Then, the mass spectrum is fitted with a sum of a gauss function for the signal, and an exponential function for the background. After subtracting the background, the signal muon pairs are plotted the bottom right panel of figure 1, representing the $p_T(y)$ distribution for reconstructed ω mesons.

The steps towards the ω efficiency correction are illustrated in figure 2 as different distributions in the $p_T(y)$ plane. The top left panel depicts the 4π distribution of ω mesons as generated by the PLUTO code. The ω mesons accepted by the setup, i.e. by STS, MUCH, TRD and TOF, are shown in the top right panel. The bottom left of figure 2 depicts the reconstructed ω mesons as shown in the bottom right panel of figure 1. The $p_T(y)$ distribution to be used for the efficiency correction ("efficiency map") is derived by calculating the ratio of the reconstructed to the accepted $p_T(y)$ distributions for ω mesons, as depicted in the second right panel of figure 2. The efficiency corrected ω meson distribution is shown in the right most panel of figure 2.

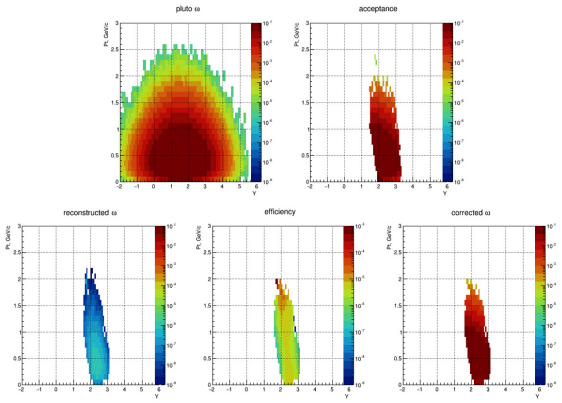

Figure 2: $p_T(y)$ distributions for ω mesons. Top row: left picture - 4π distribution as generated by the PLUTO code; right picture - accepted ω mesons. Bottom row: left picture - reconstructed ω mesons; middle picture - efficiency map; right picture - efficiency corrected ω mesons.

As the next step, a procedure for acceptance correction will be developed.

References

[1] CBM Progress Report 2018, page 67, S. Chakraborty et al.

[2] S.A. Bass et al., Prog.Part.Nucl.Phys. 41 (1998) 255

[3] I. Fröhlich et al., PoS ACAT (2007) 076, arXiv:0708.2382 [nucl-ex]

Reconstruction of ω mesons at SIS100 with realistic MuCh set up

O. Singh[1], S.Chatterjee[2], P. P. Bhaduri[3], S. Chattopadhyay[3], A. Senger[4], and T. Galatyuk[4]

[1]Aligarh Muslim University, Aligarh, India; [2]Department of Physics, Bose Institute, Kolkata, India; [3]Variable Energy Cyclotron Centre, Kolkata, India; [4]GSI, Dharmstadt, Germany

The mission of the Compressed Baryonic Matter (CBM) experiment at the future accelerator Facility for Antiproton and Ion Research(FAIR) [1] in Darmstadt Germany, is to study the QCD phase diagram in the region of high net baryon densities. In the first phase of FAIR, the SIS-100 accelerator ring, which is presently under construction, will provide accelerated beams up to an energy of 30 GeV for protons, $12A$ GeV for heavy ions (eg: Pb, Au, In, ...) and $15A$ GeV fo light ions (eg: C, Ca, Ni, ...). One of the important physics observables at SIS100 is the measurement of di-muons produced in high-energy heavy-ion collisions in the beam energy range from $4A$ to $12A$ GeV. In the present article, we report our latest results on reconstruction of $\omega \rightarrow \mu^+\mu^-$ mesons in central Au+Au collisions at the beam energy 8A GeV. The simulations are performed with the trunk version (r15516) of CbmRoot software that includes the updated di-muon analysis package. The realistic configuration of the Muon Chamber (MuCh) detector system, optimized for the measurement of $\mu^+\mu^-$ pairs coming from the decay low mass vector mesons, is described in Ref. [2] in detail. It consists of 4 detector stations and 4 hadron absorbers. Each detector station contains a triplet of gaseous detector chambers. For the first two stations GEM like detectors are implemented to account for the large particle densities and in the next two stations RPC like detectors are implemented, where the particle rates are considerably lower due to hadron absorbers. The thickness of the successive absorbers is 60 cm, 20 cm, 20 cm, 30 cm. The first absorber is made of 30 cm low-density graphite + 30 cm concrete. The rest of the absorbers are made of iron.

In our simulations, the phase space distribution and decay of the signals ($\omega \rightarrow \mu^+\mu-$) are generated by the PLUTO [3] event generator and embedded into background events generated with UrQMD [4] event generator. The GEANT3 transport code is used to transport all these particles through the CBM set up. The MuCh geometry of tag version v_19c is used for simulation which contains two GEM and two RPC detection stations. Muon track candidates for are selected from the reconstructed global tracks, based on the following selection criteria: The track must pass through 7 STS and 11 MUCH detection layers i.e. STS and MUCH hits should be greater than 6 and 10 respectively. The track must have at least one TRD hit. To ensure the track reaches the TOF detector, the track has at least one hit on TOF. To reject the secondary tracks, the primary vertex cut, $\chi^2_{Vertex}$is chosen to be less than 3.0. The track quality cuts, χ^2_{MUCH} and χ^2_{STS} are less than 3.0 and 2.0 respectively. In addition, the background is reduced further by using the flight time from TOF detector and the momentum the track to reconstruct the mass and then applying a 2σ cut on the muon mass. No pair cuts are used in the analysis.

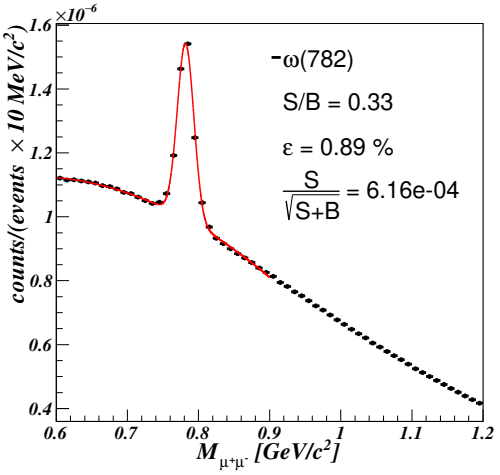

Figure 1: Reconstructed $\mu^+\mu^-$ invariant mass spectrum of ω mesons in central Au+Au collision at $8A$ GeV. The red solid line shows a fit using a Gaussian function for ω signal and a second-order polynomial function for the combinatorial background.

Fig. 1 shows the reconstructed invariant mass spectrum of ω mesons ($\omega \rightarrow \mu^+\mu^-$) after applying the selection criteria mentioned above. The method used to estimate the combinatorial background is the so-called Super Event (SE) technique. SE technique is applied to a set of UrQMD (i.e. pure background) generated tracks. In this technique, one positive track from one event satisfying all selection cuts is combined with all negative tracks from all the events. So the combinatorial background is normalized by the square of the total events whereas the signal is normalized with the total number of events.The signal is further normalized with Multiplicity $\times$ Branching ratio (di-muon channel) of ω mesons. The efficiency (ϵ_ω) and the signal-to-background ratio (S/B) are calculated within a $\pm 2\sigma$ mass range around the signal peak and found to be 0.89% and 0.33 respectively. The rapidity distribution of the input, accepted and reconstructed ω mesons with different acceptance criteria are shown in Fig. 2. The red dotted line shows the rapidity distribution of ω generated with the PLUTO generator in 4π space. As evident from Fig. 2, the peak of the rapidity distribution of the accepted and reconstructed

ω mesons is shifted towards higher value due to absorption of soft muons by the hadron absorbers.

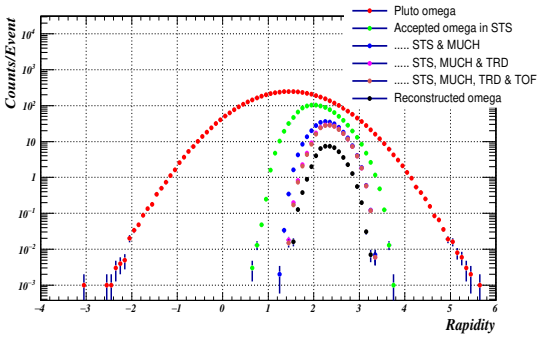

Figure 2: Rapidity distribution of the input, accepted and reconstructed ω mesons in $8A$ GeV central Au+Au collisions.

The acceptance for ω in rapidity (y) and transverse momentum (p_T) plane is shown in figure 3. The left panel is for ω generated with the PLUTO generator in 4π space. The center panel contains the decay muon pair ($\mu^+\mu^-$) of accepted ω satisfy the following cuts: STS point ($\geq$7), MUCH point ($\geq$5), TRD point ($\geq$1), and TOF point ($\geq$1). The reconstructed ω mesons which follow the selection criteria mentioned earlier are shown in the right panel of the Fig. 3.

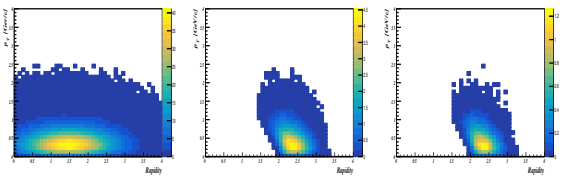

Figure 3: y-p_T distribution for ω meson decaying into two muon pairs ($\mu^+\mu^-$) in central Au+Au collision at 8A GeV. The identification of ω mesons is done by MC information. The left panel shows the 4π distribution of PLUTO generated ω whereas the middle panel is for the acceptance of ω mesons after nominal muon candidate cuts. Right panel shows the acceptance for the reconstructed ω after all selection cuts.

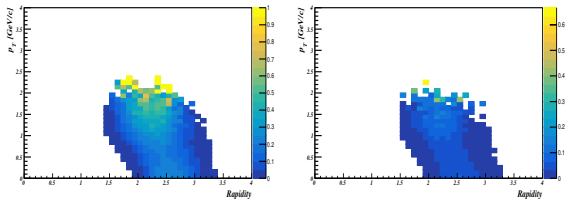

Figure 4: Left panel: Acceptance matrix of ω meson. Right panel: Efficiency matrix of ω meson

The corresponding acceptance and efficiency matrices of the ω mesons in central Au+Au collision at 8A GeV are shown in Fig. 4 Acceptance matrix is the ratio of accepted $\mu^+\mu^-$ pairs from ω mesons and PLUTO generated ω in 4π whereas efficiency matrix is defined as the ratio of reconstructed ω and PLUTO generated ω in 4π.

We have also calculated the invariant mass spectra for ω mesons in different p_T bins. Results are plotted in figure 5. The signal is fitted by Gaussian function, and the background can be well described by second-order polynomial function. The efficiency and S/B are extracted using combined fit of signal and combinatorial background are presented in table 1. From table 1, the maximum efficiency is achieved within p_T range of 0.2-0.6 GeV/c.

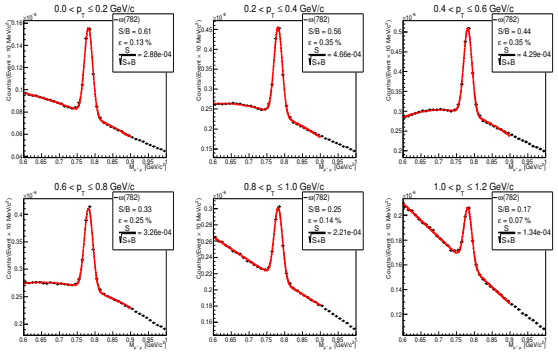

Figure 5: The invariant mass spectra for ω candidate in different p_T regions. The solid red line is a combined fit to the signal and background with a single Gaussian (signal) plus a second-order polynomial(background).

p_T **region, GeV/c**	**Efficiency** ω **,** %	**S/B**
$0.0 < p_T \leq 0.2$	0.13	0.61
$0.2 < p_T \leq 0.4$	0.35	0.56
$0.4 < p_T \leq 0.6$	0.35	0.44
$0.6 < p_T \leq 0.8$	0.25	0.33
$0.8 < p_T \leq 1.0$	0.14	0.25
$1.0 < p_T \leq 1.2$	0.07	0.17

Table 1: Reconstruction efficiency and Signal-to-background ratio for ω meson in central Au+Au collision at 8A GeV in different p_T region (inclusive Y).

References

[1] M. Durante *et. al.*, Phys. Scr. **94** (2019) 033001.

[2] Realistic Muon Chamber (MuCh) geometry simulation for the CBM experiment at FAIR; O. Singh *et al.*, CBM Progress Report 2018.

[3] I . Frohlich *et. al.*,PoS ACAT (2007) 076, arXiv:0708.2382 [nucl-ex].

[4] S.A. Bass *et al.*, Prog. Part. Nucl. Phys. **41** (1998) 255.

Reconstruction of J/ψ mesons at SIS100 energies with realistic MuCh set up

S. Chatterjee[*1], *O. Singh*[2], *A. Senger*[3], *P. P. Bhaduri*[4], *and S. Chattopadhyay*[4]

[1]Department of Physics, Bose Institute, Kolkata, India; [2]Aligarh Muslim University, Aligarh, India; [3]GSI, Darmstadt, Germany; [4]Variable Energy Cyclotron Centre, Kolkata, India

One of the major physics goals of the Muon Chamber (MuCh) detector system at CBM is the identification of J/ψ mesons via their decay into di-muons. In the present article, we report our latest results on the performance of J/ψ detection ($J/\psi \rightarrow \mu^+\mu^-$) in $10A$ GeV Au+Au and $15A$ GeV Ni+Ni collisions, based on simulation with realistic detector models optimized for SIS100 collisions.

The production of J/ψ mesons at $10A$ GeV beam energy is kinematically forbidden. However, model calculations [1] based on sub-threshold production of resonances via multiple collisions in dense baryonic medium predict non-zero J/ψ cross-sections at $10A$ GeV beam energy.

The simulations are performed with the latest CbmRoot TRUNK (Revision no. 15516). The phase-space distribution and decay of $J/\psi \rightarrow \mu^+\mu^-$ is simulated using the PLUTO event generator. The signal muon pairs are embedded into the background, generated using the UrQMD event generator. One J/ψ ($J/\psi \rightarrow \mu^+\mu^-$) from PLUTO is embedded per event into the background. All the particles are transported through the entire CBM setup using the GEANT3 transport engine. 5×10^6 events are simulated and reconstructed for both $10A$ GeV central Au+Au and $15A$ GeV central Ni+Ni collisions, using the realistic MuCh set up [2]. The foreseen muon set up for J/ψ measurements at SIS100 energies consists of 4 detector stations and 5 hadron absorbers. Each detector station is a triplet of gas detector chambers. For the first two stations GEM like detectors are implemented to account for the large particle densities and in the next two stations, RPC like detectors are implemented, where the particle rates are considerably lower due to hadron absorbers. The thickness of the successive absorbers is 60 cm, 20 cm, 20 cm, 30 cm, and 100 cm. The first absorber is made of 30 cm low-density graphite + 30 cm concrete. The rest of the absorbers are made of iron. Hits registered in the transition radiation detector (TRD) behind the 100 cm thick absorber are used to devise the di-muon trigger logic. In this study, the effect of delta electrons knocked out from the target and single-channel dead times are not taken into account.

The standard analysis procedure is followed to obtain the invariant mass spectra of the oppositely charged probable muon track candidates, coming from J/ψ decay. The muon track candidates are identified by applying a set of single track quality cuts to the reconstructed global tracks. The detail of the cuts is summarised in Table 1.

Different approaches have been employed to calculate the pair reconstruction efficiency and signal to background ratio. The first approach is based on Monte Carlo (MC) information. The signal is extracted using the *MCPDG* tag, and background is calculated using a super event (SE) technique, where one muon candidate track is combined with all the other oppositely charged muon candidate tracks to calculate the combinatorial background. The entries within the 2σ mass range of the signal, fitted with Gaussian distribution, give the signal yield and dividing that by the input yield gives the efficiency also within the same range, the background is calculated to get the S/B ratio. In the second approach, the invariant mass spectra are fitted with Gaussian (signal) + polynomial (background) and then the signal is extracted from the 2σ mass range of the fitted signal distribution by a Gaussian distribution.

System	Cut on detector hits	Cut on χ^2
Au+Au @ 10 AGeV	-	VERTEX $\chi^2 \leq 3.0$
Au+Au @ 10 AGeV	STS hits ≥ 6	STS $\chi^2 \leq 3.0$
Au+Au @ 10 AGeV	MUCH hits ≥ 11	MUCH $\chi^2 \leq 2.5$
Au+Au @ 10 AGeV	TRD hits ≥ 3	TRD $\chi^2 \leq 6.0$
Au+Au @ 10 AGeV	TOF hits ≥ 1	-
Ni+Ni @ 15 AGeV	-	VERTEX $\chi^2 \leq 2.0$
Ni+Ni @ 15 AGeV	STS hits ≥ 6	STS $\chi^2 \leq 2.5$
Ni+Ni @ 15 AGeV	MUCH hits ≥ 11	MUCH $\chi^2 \leq 2.5$
Ni+Ni @ 15 AGeV	TRD hits ≥ 3	TRD $\chi^2 \leq 4.5$
Ni+Ni @ 15 AGeV	TOF hits ≥ 1	-

Table 1: Selection cuts on the reconstructed global tracks to select muon track candidates.

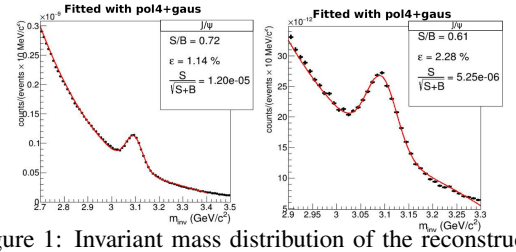

Figure 1: Invariant mass distribution of the reconstructed J/ψ mesons for 10 AGeV Au+Au (left) and 15 AGeV Ni+Ni (right) collisions fitted by 2^{nd} method.

In the third approach, in the spirit of the side band technique, the background is fitted away from the signal pole mass region separately using a polynomial function and the signal is fitted with Gaussian distribution. In all the methods, the background is normalized by the number of events squared. The signal is normalized by multiplicity$\times$branching ratio and the number of events. For 10 A GeV Au+Au collisions, J/ψ multiplicity is taken from UrQMD model prediction. For 15 GeV Ni+Ni the multiplicity is derived from the HSD predicted J/ψ multiplicity in 15 A GeV Au+Au collisions by properly normal-

* sayakchatterjee@jcbose.ac.in

izing it with the respective number of binary collisions in the two collision systems.

Method (System)	$\epsilon_{J/\psi}$(%)	S/B	Mass resolution (MeV/c)
method 1 (Au+Au)	1.39	0.44	34
method 2 (Au+Au)	1.07	0.65	33
method 3 (Au+Au)	1.37	0.52	33
method 1 (Ni+Ni)	2.97	0.42	34
method 2 (Ni+Ni)	2.28	0.61	32
method 3 (Ni+Ni)	2.97	0.47	33

Table 2: Reconstruction efficiency and S/B ratio for J/ψ mesons in central Au+Au and Ni+Ni collision at 10A GeV and 15 AGeV from different fitting methods. Metho 1, 2 & 3 are based on MC information, full fit and side band techniques respectively.

In Fig. 1, the fitted spectra using the second approach are shown and the results of the fitting are summarised in Table 2. As evident, the results from different fit procedures do not converge. This is because of the significant change in statistics above the mass of 3 GeV/c^2. Since above 3 GeV/c^2 the statistical uncertainty increases, it affects the fitting and results depend on the fitting process and its range. The laboratory rapidity (Y) and transverse momentum (p_T) distribution of the signal muon pairs, at the input level, accepted level, and reconstructed level (selected using MC information) is shown in Fig. 2. The variation of the reconstruction efficiency and S/B ratio in different p_T range is also studied over the entire rapidity range of the accepted pairs.

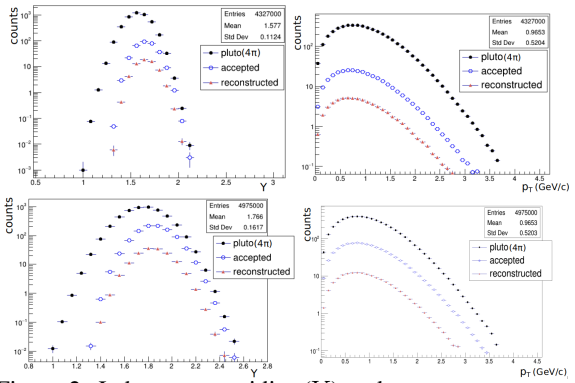

Figure 2: Laboratory rapidity (Y) and transverse momentum (p_T) distribution of input, accepted and reconstructed pairs for 10 AGeV central Au+Au (top) and 15 AGeV central Ni+Ni (bottom) collision respectively.

The entire p_T range is divied into five sub-ranges, namely $0 \leq p_T \leq 0.5$ GeV/c, $0.5 \leq p_T \leq 1.0$ GeV/c, $1.0 \leq p_T \leq 1.5$ GeV/c, $1.5 \leq p_T \leq 2.0$ GeV/c, $2.0 \leq p_T \leq 2.5$ GeV/c. The variation of efficiency and S/B ratio in different p_T bins are shown in Fig. 3. Based on the MC information, the efficiency correction is also performed for both 10 AGeV Au+Au and 15 AGeV Ni+Ni systems. The accpeted tracks are extracted, from the full phase space input signal distribution depending on the acceptance criteria of the simulated MC tracks. Among those accepted MC tracks, only a fraction is reconstructed based on the tracking algorithm and analysis criteria. The ratio of the reconstructed to the accepted tracks gives us the efficiency matrix and then the ratio of reconstructed matrix to the efficiency matrix, gives us the corrected spectra.

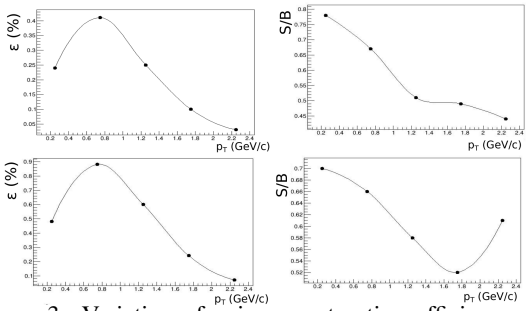

Figure 3: Variation of pair reconstruction efficiency and signal to noise ratio as function of p_T over the entire rapidity range for 10 AGeV Au+Au (top) & 15 AGeV Ni+Ni (bottom) collision. In the x-axis the mean value of the each p_T bin is ploted.

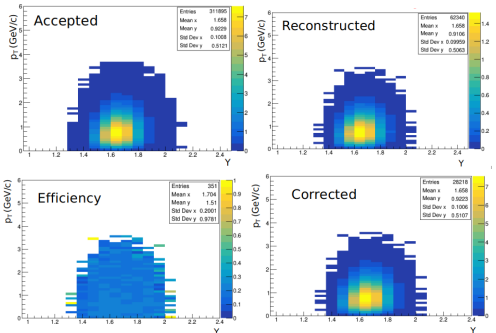

Figure 4: Accepted, reconstructed, efficiency and corrected Y-p_T matices for central 10 AGev Au+Au system.

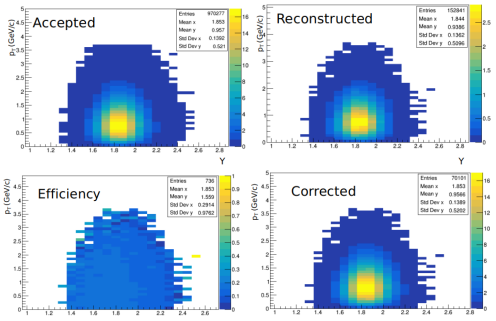

Figure 5: Accepted, reconstructed, efficiency and corrected Y-p_T matices for central 15 AGev Ni+Ni system.

In the Fig. 4 & Fig. 5, the accepted, reconstructed, efficiency and corrected matrices are shown for the central Au+Au 10 AGeV and Ni+Ni 15 AGeV respectively. The corrections on the reconstructed pairs are based on monte carlo information. Efficiency correction without MC information is also under investigation.

Acknowledgements

Authors would like to thank Michael Deveaux and Alberica Toia for useful comments during this study.

References

[1] J. Steinheimer *et al.*, Phys.Rev.C 95 (2017) , 014911

[2] O. Singh *et al.*, CBM Progress Report 2018.

Fluctuation of elliptic flow parameter at an expected FAIR energy

Soumya Sarkar[1,2] *and Amitabha Mukhopadhyay*[1]

[1]Department of Physics, University of North Bengal, Siliguri-734013, West Bengal, India; [2]Department of Physics, Siliguri College, Siliguri-734001, West Bengal, India

Elliptic flow is believed to provide information related to the transport properties and the equation of state of the matter created in high-energy heavy-ion collisions. Recent results from RHIC [1] and LHC [2] experiments show that flow-fluctuation and fluctuation in the initial spatial eccentricity are closely correlated. In this report we have tried to explore similar issues by employing A Multi Phase Transport (AMPT) model in its string melting configuration [3]. A sample of 10 million Au+Au events at $E_{\rm lab} = 30A$ GeV is used. We calculate the elliptic flow co-efficient (v_2) from two and four-particle cumulants using the Q-cumulant method [4]. The azimuthal correlation is expressed in terms of the Q vector as,

$$Q_n = \sum_{j=1}^{M} e^{in\phi_j} \tag{1}$$

where M is the multiplicity of the selected particles in an event and ϕ_j denotes their azimuthal angles. The average two-particle azimuthal correlation over all particles in the event is then calculated from

$$\langle 2\rangle = \frac{|Q_n|^2 - M}{M(M-1)} \tag{2}$$

The two-particle cumulant $c_n\{2\}$ and the anisotropic flow-parameter $v_n\{2\}$ can be obtained after averaging over all particles in all events as,

$$c_n\{2\} = \langle\langle 2\rangle\rangle,\ v_n\{2\} = \sqrt{c_n\{2\}} \tag{3}$$

However, $v_n\{2\}$ obtained in this way is susceptible to non-flow effects like resonance decays, jet fragmentations, Bose-Einstein correlations, which contribute to additional correlation not related to the reaction plane. These non-flow effects, in general short ranged in nature, can be suppressed by introducing a pseudorapidity gap between the particles used to construct the Q-cumulant [5]. An event is divided into two sub-events, say A and B, separated by a gap say $\Delta\eta$ (In our study $\Delta\eta = 1.0$). Two-particle correlation is modified to

$$\langle 2\rangle_{\Delta\eta} = \frac{Q_n^A Q_n^{B*}}{M_A M_B} \tag{4}$$

where Q_n^A and Q_n^B are the flow vectors of the sub-events A and B respectively, M_A and M_B being the corresponding multiplicities. Finally we get $c_n\{2\}$ and $v_n\{2\}$ as,

$$c_n\{2\}_{\Delta\eta} = \langle\langle 2\rangle\rangle_{\Delta\eta},\ v_n\{2,\Delta\eta\} = \sqrt{c_n\{2\}_{\Delta\eta}} \tag{5}$$

Non-flow effects can also be suppressed by exploiting the multiparticle cumulants, which in the 4^{th} order can be expressed as

$$\langle 4\rangle = \big[|Q_n|^4 + |Q_{2n}|^2 - 2.Re(Q_{2n}Q_n^*Q_n^*) - 2[2(M-2).|Q_n|^2 - M(M-3)]\big]/[M(M-1)(M-2)(M-3)\big]$$
$$c_n\{4\} = \langle\langle 4\rangle\rangle - 2\langle\langle 2\rangle\rangle^2,\ v_n\{4\} = \sqrt[4]{-c_n\{4\}}. \tag{6}$$

The flow fluctuation in terms of the cumulants are given by [6]

$$v_n\{2\} \approx \langle v_n\rangle^2 + \sigma^2_{v_n}(\text{Neglecting nonflow}),$$
$$v_n\{4\} \approx \langle v_n\rangle^2 - \sigma^2_{v_n}(\text{Assuming } \sigma_{\rm v_n} << \langle {\rm v_n}\rangle) \tag{7}$$

In Fig. 1 we plot v_2 against the number of participating nucleons $N_{\rm part}$, a measure of collision centrality. $v_2\{2\}$ and $v_2\{2, |\Delta\eta| > 1\}$ are almost always accordant to each other, which signifies that non-flow effects are small in the AMPT simulation at FAIR conditions. The marginal difference between $v_2\{2\}$ and $v_2\{4\}$ may be attributed to flow fluctuation, quantified as

$$\sigma_{v_2} = \sqrt{\frac{v_2\{2,|\Delta\eta|>1\}^2 - v_2\{4\}^2}{2}} \tag{8}$$

We also estimate $\langle v_2\rangle$ in Eq. 7 by using

$$\langle v_2\rangle\{\text{est}\} = \sqrt{\frac{{\rm v_2}\{2,|\Delta\eta|>1\}^2 + {\rm v_2}\{4\}^2}{2}} \tag{9}$$

Our simulation results underestimate the $v_2\{2\}$ values obtained from the STAR measurements at $\sqrt{s} = 7.7$ GeV [7]. The difference, nominal in central but significant in peripheral collisions, may be adjusted by using a higher partonic cross-section viz. $\mu = 10$ mb, instead of $\mu = 3$ mb as used in the present analysis. Eccentricity (ε_2) of the overlapping region of the colliding nuclei is obtained from the initial spatial distribution of the participating nucleons. Due to the fluctuating number and position of the participating nucleons ε_2 may fluctuate on an event-by-event basis even within the same cenrality class. So cumulants of ε_2 are defined in a manner similar to that of v_2 [8]. In Fig. 2 we plot ε_2 as a function of $N_{\rm part}$. Excepting the most peripheral region the average trend of the centrality dependence of ε_2 is compatible to that of v_2. We now examine the effect of ε_2 fluctuation on flow fluctuation. The eccentricity fluctuation is defined as

$$\sigma_{\varepsilon_2} = \sqrt{\frac{\varepsilon_2\{2\}^2 - \varepsilon_2\{4\}^2}{2}} \tag{10}$$

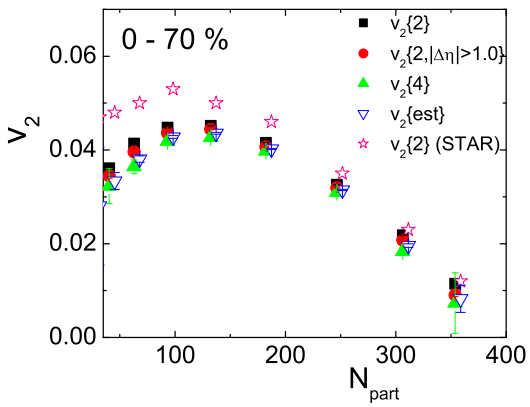

Figure 1: (Color online) v_2 as a function of $N_{\rm part}$ in Au+Au collision at $E_{\rm lab} = 30A$ GeV.

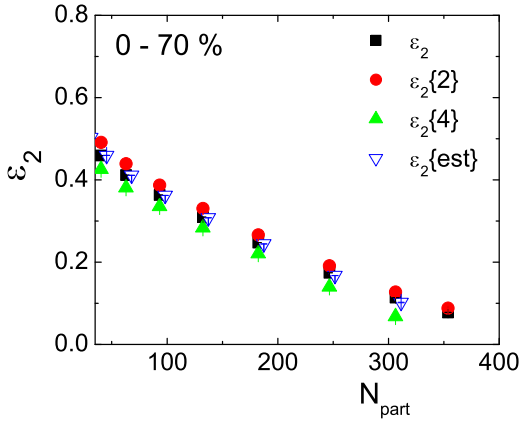

Figure 2: (Color online) (ε_2) as a function of $N_{\rm part}$ in Au+Au collisions at $E_{\rm lab} = 30A$ GeV.

Fig. 3 shows the correlation between σ_{ε_2} and σ_{v_2}. We note that within $5 - 60\%$ centrality class the centality dependence of σ_{ε_2} significantly captures the trend of σ_{v_2}. Most central and peripheral events are kept out of the purview of our analysis. This should be understood as a linear mapping of the nature like $\sigma_{v_2} \propto \sigma_{\varepsilon_2}$, which manifests that the initial eccentricity fluctuation predominantly contibutes to the elliptic flow fluctuation. The relative fluctuations in flow and eccentricity are estimated as,

$$R_{v_{2,4}} = \frac{\sigma_{v_2}}{\langle v_2 \rangle \{\rm est\}}, \quad R_{\varepsilon_{2,4}} = \frac{\sigma_{\varepsilon_2}}{\langle \varepsilon_2 \rangle \{\rm est\}} \qquad (11)$$

Their values are plotted in Fig. 4 against $N_{\rm part}$. It is observed that the nature of relative fluctuation in v_2 is not consistent with that of ε_2, which contradicts the observation of PHOBOS [1]. The magnitude of relative flow fluctuation is less than that of eccentricity, which suggests that the initial state fluctuations are not perfectly transported to the final state. However, the appropriate reason(s) for such an unusual behaviour at FAIR energy needs further investigation.

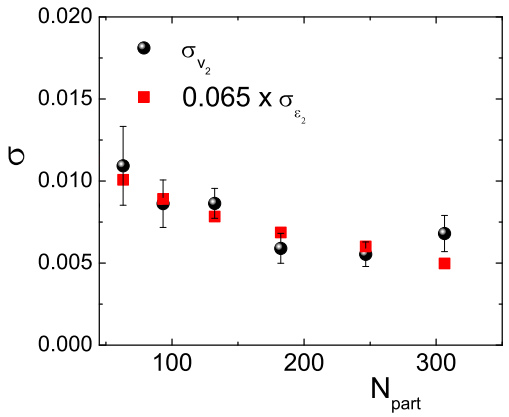

Figure 3: (Color online) Centrality dependence of elliptic flow fluctuation and eccentricity fluctuation in Au+Au collisionsat $E_{\rm lab} = 30A$ GeV.

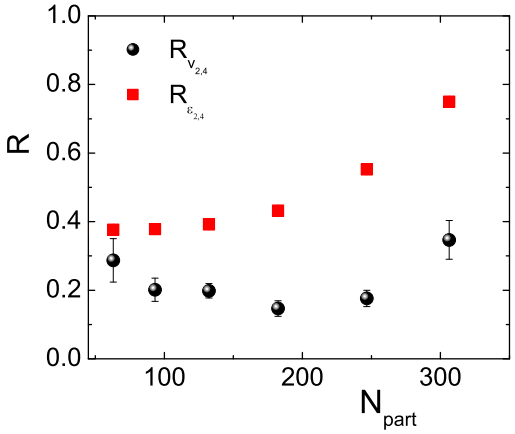

Figure 4: (Color online) Centrality dependence of relative elliptic flow fluctuation and eccentricity fluctuation in Au+Au collisions at $E_{\rm lab} = 30A$ GeV.

References

[1] B. Alver *et al.* [PHOBOS Collaboration], Phys. Rev. C **81**, 034915 (2010).

[2] M. Aaboud *et al.* [ATLAS Collaboration], J. High Energy Phys. **2020**, 51 (2020)

[3] B. Zhang, C. M. Ko, B.-A. Li, and Z.-W. Lin, Phys. Rev. C **61**, 067901 (2000).

[4] A. Bilandzic, R. Snellings, and S. Voloshin, Phys. Rev. C **83**, 064904 (2011).

[5] Y. Zhou *et al.* (ALICE Collaboration.), Nucl. Phys A **931**, 949 (2014).

[6] S. Voloshin, A. Poskanzer, A. Tang, and G. Wang, Phys. Lett. B **659**, 537 (2008).

[7] L. Adamczyk *et al.* [STAR Collaboration], Phys. Rev. C **86**, 054908 (2012).

[8] L. Ma, G. L. Ma, and Y. G. Ma, Phys. Rev. C **94**, 044915 (2016).

Event-by-event fluctuations of K/π and p/π in Au+Au collisions at 30A GeV

*P. Mali and A. Mukhopadhyay**

Department of Physics, North Bengal University, Siliguri 734013, West Bengal, India

Search for structures in the QCD phase diagram, like the first order phase transition line from hadronic to partonic degrees of freedom, and/or the location of the critical end point is one of the major objectives of the FAIR-CBM experiment. Lattice QCD calculations suggest that near the critical end point, enhanced fluctuations in the final state observabeles are expected [1]. When examined on an event-by-event (e-by-e) basis, such fluctuations may provide a connection between globally conserved charge(s) and approximately conserved quantities like the entropy. The NA49 experiment showed that the fluctuations in the ratio of inclusive yields of K^+ and π^+ in central Pb+Pb collisions exhibit a change in sign around $E_{\rm Lab} = 30A$ GeV [2], a phenomenon not very well understood. While the experimental energy dependence of p/π^+ ratio could be satisfactorily reproduced by the UrQMD model [3], the same was unsuccessful in the K^+/π^+ case. The dynamical fluctuation can be measured by [4]

$$\sigma_{dyn} = sign(\sigma^2_{data} - \sigma^2_{mix})\sqrt{|\sigma^2_{data} - \sigma^2_{mix}|},$$

where $\sigma_{data} = \sqrt{Var(A/B)}/\langle A/B\rangle$ for the experiment or for the simulated events, σ_{mix} is the same for a mixed event sample, and $\langle A/B\rangle$ and $Var(A/B)$ are respectively the mean and the variance of event-wise particle yield ratios (A/B). In experiments σ_{dyn} however, depends on detector efficiency. Recently a more robust variable (ν_{dyn}), independent of the detector acceptance and effeciency, is introduced to measure the dynamical net-charge fluctuations [5]. For a pair of particles, say of type A and type B, the dynamical fluctuation ν_{dyn} is defined as

$$\nu_{AB,dyn} = \frac{\langle N_A(N_A-1)\rangle}{\langle N_A\rangle^2} + \frac{\langle N_B(N_B-1)\rangle}{\langle N_B\rangle^2} - \frac{2\langle N_A N_B\rangle}{\langle N_A\rangle\langle N_B\rangle}$$

By definition $\nu_{dyn} = 0$ for a Poisson type single particle distribution. The same variable can also be used to measure the e-by-e fluctuations in the particle yield ratios like K/π, p/π, etc. [6]. In this report some preleminary results on dynamical fluctuations on e-by-e K/π and p/π ratios in Au+Au collisions at $E_{Lab} = 30$A GeV are presented. The event samples, one milion minimum-bias Au+Au events for each, are generated by using the UrQMD model, and a multi-phase transport (AMPT) model both in its default and in the string melting configuration [7]. Our analysis is confined to the central rapidity region $|y - y_0| < 1.0$. The protons and anti-protons are further subjected to a transverse momentum cut like $p_t > 0.4$ GeV/c.

* amphys@nbu.ac.in

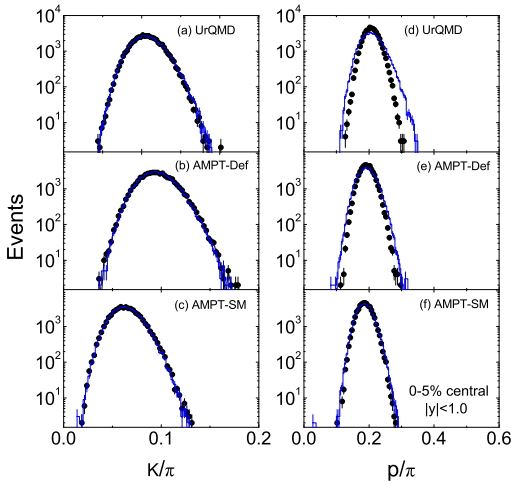

Figure 1: Distributions of e-by-e K/π (left panel) and p/π (right panel) ratios for the $0-5\%$ most central Au+Au collisions at $30A$ GeV.

Table 1: The values of σ_{dyn} (in %) for the $0-5\%$ most central Au+Au interactions at $30A$ GeV.

Ratio	URQMD	AMPT-Def	AMPT-SM
K/π	-4.00±0.353	3.924±0.374	4.022±0.580
p/π	-10.52±0.087	-7.545±0.093	-4.222±0.515

In Fig. 1 we present the distributions of event-wise K/π and p/π ratios for the $0-5\%$ most central interactions. Each simulated distribution is accompanied by the corresponding mixed event prediction. By using the first and second moments of these distributions we calculate σ_{dyn}, whose values are listed in Table 1. From the definitions, a positive (negative) value of σ_{dyn} or ν_{dyn} is an indication of the dominance of correlation between particles belonging to same (different) species. Accordingly, the URQMD predicts that the $K\pi$ $(p\pi)$ correlations are stronger than the combined strength of KK and $\pi\pi$ (pp and $\pi\pi$) correlations. In both versions of AMPT we see that correlations between same species of particles dominate in the $K\pi$ case, while that between different species of particles is stronger in the $p\pi$ case. Fig. 2 shows the centrality dependence of the fluctuation measures (a) $\nu_{K\pi,dyn}$ and (b) $\nu_{p\pi,dyn}$. For all three simulated data samples and at all centralities we get positive values of ν_{dyn} in the K/π case, whereas ν_{dyn} is always negative in the p/π case. As expected, with increasing N_{part} or equivalently with increas-

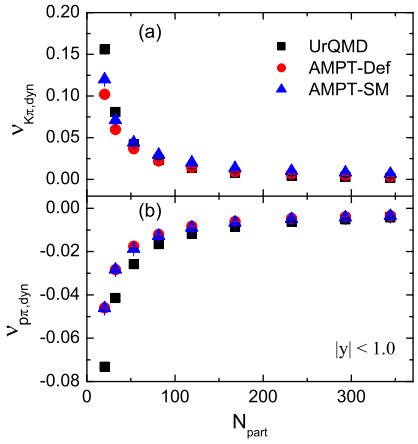

Figure 2: Dynamical fluctuations (a) $\nu_{K\pi,dyn}$ and (b) $\nu_{p\pi,dyn}$ plotted with N_{part}.

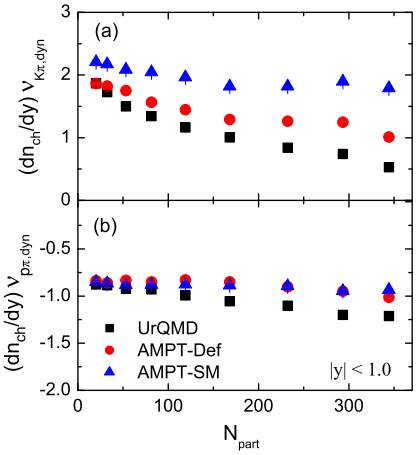

Figure 3: dn_{ch}/dy scaled dynamical fluctuations $\nu_{K\pi,dyn}$ and $\nu_{p\pi,dyn}$ plotted with N_{part}.

ing number of particle producing sources, the magnitude of dynamical fluctuation decreases. In central and mid-central collisions all three models yield almost identical values of ν_{dyn}. We scale ν_{dyn} by the charged particle rapidity density (dn_{ch}/dy) at $y = y_0$, and plot the values against N_{part} in Fig. 3. For an independent particle emission we expect that ν_{dyn} should scale inversely with the number of particle producing sources. If on an average same number of particles are produced by each source, the scaling by dn_{ch}/dy is therefore, expected to remove the centrality dependence of ν_{dyn}. We find that the N_{part} dependence of $(dn_{ch}/dy)\times\nu_{p\pi,dyn}$, though not quite zero, is indeed much weaker than that of ν_{dyn}. For all models the product in the $K\pi$ case slowly decreases in magnitude, while for the $p\pi$ case it increases in magnitude with increasing centrality. Both in the $K\pi$ and $p\pi$ cases, the centrality dependence of the URQMD simulated values are more rapid than that of AMPT. Correlations steaming out of the decays of baryonic

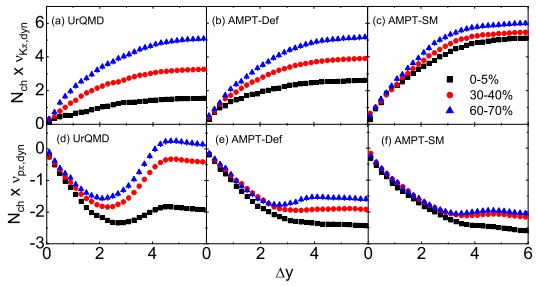

Figure 4: Rapidity window (Δy) dependence of $N_{ch} \times \nu_{K\pi,dyn}$ and $N_{ch} \times \nu_{p\pi,dyn}$ for three centrality bins.

(Δ) and mesonic (K_1 and K^*) resonances, and fluctuations in the number of same and/or opposite sign particle species might be useful to interpret the results. A more detailed study involving different charge species of particles is required for this purpose. Dependence of $N_{ch} \times \nu_{K\pi,dyn}$ and $N_{ch} \times \nu_{p\pi,dyn}$ on the rapidity window size (Δy) are shown in Fig. 4 for three different centrality bins. Here N_{ch} is the average charge multiplicity in Δy. In the upper panels the $K\pi$ results for all three models show that with increasing Δy the dynamical fluctuation monotonically increases to saturate beyond $\Delta y = 4.0$. In the lower panels of Fig. 4 we see that the behavior of the $N_{ch} \times \nu_{p\pi,dyn}(\Delta y)$ plots is quite different than that observed for the $K\pi$ case. Irrespective of the model used and the centrality class, with increasing Δy the $|N_{ch} \times \nu_{p\pi,dyn}|$ values rapidly increase at the begining. In the UrQMD model however, magnitude of the product start decreasing beyond $\Delta y = 2.0$ and ultimately saturates near $\Delta y = 4.0$. On the other hand the AMPT values show an initial rapid increase followed by some kind of saturation starting near $\Delta y = 4.0$. While the initial trend of these plots can be interpreted in terms of the diffusion of produced hadrons in rapidity space, their difference in their behavior in UrQMD and AMPT beyond $\Delta y = 2.0$ must have something to with long range correlation, which once again needs a more detailed investigation.

References

[1] Z. Fodor and S. D. Katz, JHEP 04, 050 (2004).

[2] C. Alt *et al.* (NA49 Collaboration), Phys. Rev. C 77, 024903 (2008).

[3] S. A. Bass *et al.*, Prog. Part. Nucl. Phys. 41, 255 (1998); M. Bleicher *et al.*, J. Phys. G 25, 1859 (1999).

[4] S. V. Afanasiev *et al.* (NA49 Collaboration), Phys. Rev. Lett. 86, 1965 (2001).

[5] C. Pruneau, S. Gavin, and S. Voloshin, Phys. Rev. C 66, 044904 (2002).

[6] B. Abelev, *et al.* (STAR Collaboration), Phys. Rev. Lett. 103, 092301 (2009).

[7] Z. W. Lin *et al.*, Phys. Rev. C 72, 064901 (2005).

FAIR Phase-0 Activities

Commissioning of mCBM@SIS18

C. Sturm[1], *N. Herrmann*[2] *for the CBM Collaboration*
[1]GSI, Darmstadt, Germany; [2]Ruprecht-Karls-Universität Heidelberg, Germany

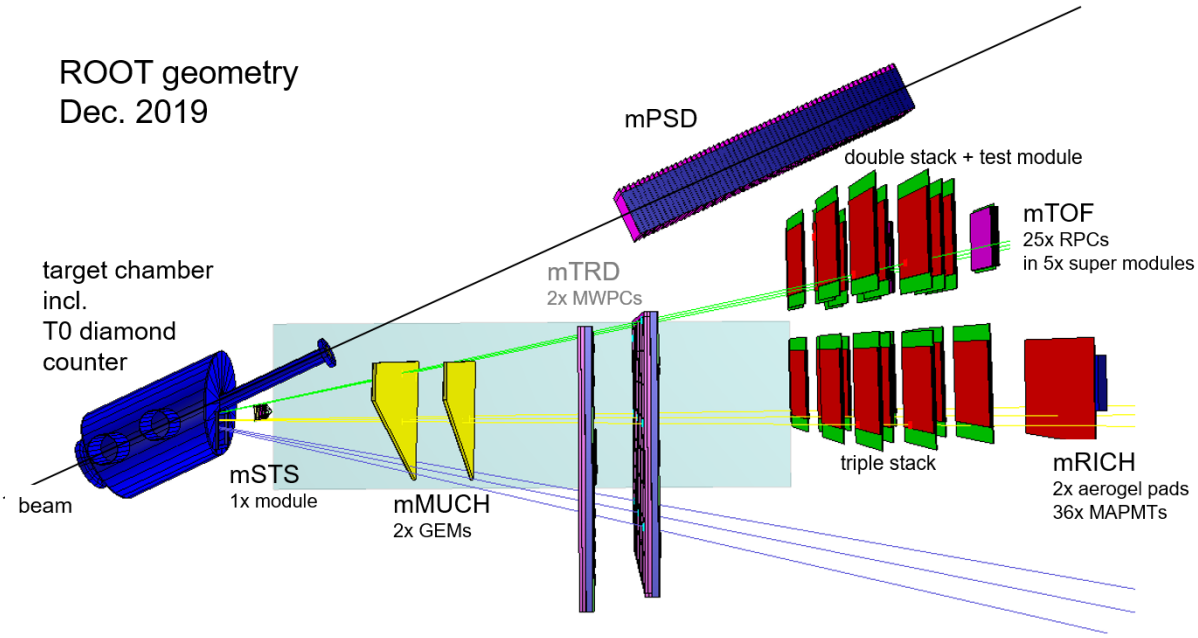

Figure 1: ROOT geometry of the mCBM setup as of December 2019, beam enters to the left.

To study extremely rare probes in nucleus-nucleus collisions with high precision, the Compressed Baryonic Matter experiment (CBM) at FAIR is designed to measure at unprecedented interaction rates up to 10 MHz. Hence, CBM will be equipped with fast and radiation hard detector systems, readout by a free-streaming data acquisition system, transporting data with up to 1 TB/s to a large scale computer farm hosted in the Green IT Cube which will provide first level event reconstruction and selection. To commission and optimize all components and their complex interplay including firmware and software under realistic conditions the CBM full-system test-setup mCBM@SIS18 ("mini-CBM" or short mCBM) has been constructed in 2017 and 2018 at the present SIS18 facility of GSI/FAIR. The installation site of mCBM is the detector test area named cave-D (HTD) situated at the beam entrance of the experimental area cave-C (HTC) hosting the nuclear structure experiment R^3B. mCBM comprises pre-series components and final prototypes of all CBM detector subsystems and their read-out chains. Details on the design of the CBM detector subsystems are given in the corresponding Technical Design Reports [1] - [6].

As depicted in Figure 1, the mCBM test-setup is positioned downstream a solid target under a polar angle of about 25° with respect to the primary beam.

While the completion of mCBM is ongoing, the setup included end of 2019 (see Figure 1):

- the time-zero (T0) diamond counter, consisting of 8x vertical strips 2mm width each, mounted inside the target chamber, 20cm upstream the target,
- the first station (station-0) of the mSTS subsystem equipped with 1x STS module [7],
- the mMUCH consisting of two GEM counters, (almost) fully readout [8],
- the mTRD containing two TRD MWPCs (the MWPCs were fully operational while the GBTx data transport failed) [9],
- the mTOF, fully equipped with five super-modules containing 5x RPC counters each, configured to a triple and double stack, enabling internal tracklet search as well as detailed efficiency studies [10],
- the mRICH, fully equipped with two aerogel radiators and 36x MAPMTs readout by 72x DiRICH modules [11],
- the mPSD with one PSD module readout by a PANDA ADC board [12].

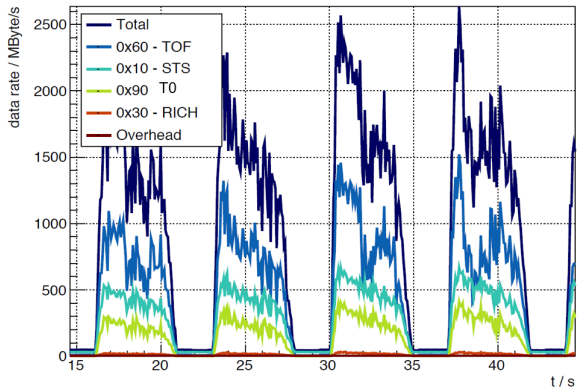

Figure 2: Data rates observed by the FLES processing nodes inside the Green IT Cube during high-rate tests, March 30, 2019.

As a part of the FAIR Phase-0 program, the commissioning of mCBM with beam has started during the machine engineering runs in December 2018, followed by the main commissioning beam time in March 2019, and during the machine engineering runs in November / December 2019. First high-rate tests could be performed during the March 2019 run, using Ag(45+) beam with an incident kinetic energy of 1.58 GeV per nucleon. Running with beam intensities up to 10^8 Ag ions per second, resulting to a top collision rate of 10 MHz, data rates up to 2.5 GB per second have been observed by the processing nodes of the first-level-event-selector (FLES) [13] inside the Green IT Cube during data taking, see Figure 2.

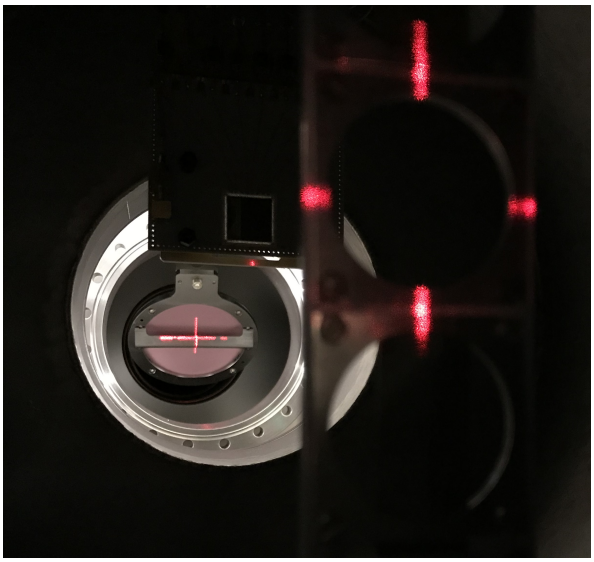

Figure 3: Upgrade of the beam diagnostics in the mCBM beam line – the photograph shows the moved-in, new scintillation screen (lower left), about 50 cm upstream the mCBM target. Along the beam (back to front), the laser alignment of the scintillation screen, and the 5-fold target ladder (empty position) in respect to the optical beam axis is visible. In-between both, the moved-out T0 diamond counter is shown.

To ensure a proper beam alignment which is essential at high beam intensities the beam diagnostics of the mCBM beam line has been upgraded by the beam diagnostic team of GSI in the second half of 2019. During the machine engineering runs in November and December 2019 the two new scintillation screens, located in front of the focusing units and inside the mCBM cave (see Figure 3), both imaged by digital CCDs, have been successfully commissioned. Hence, beam alignment and focusing could be significantly improved.

First, preliminary results obtained during data taking in December 2019 are depicted in Figure 4. The upper panels show spatial correlations between the mTOF and mMUCH subsystem (x left, y right), the lower figures between the mTOF and mRICH. Data on Ar + Au collisions at 1.7 AGeV were taken with a common, synchronized data transport of all subsystems. Individual time-offsets of the subsystems have been corrected during unpacking, fine-calibration procedures have not been applied. After cluster and hit finding, a simplified event building and event selection has been performed by cluster-finding within a fixed time window and a minimal requirement on the T0 and mTOF multiplicity.

The observed time and spatial correlations between detector subsystems demonstrate a first conceptual verification of the free-streaming DAQ system of CBM. A detailed analysis is ongoing and further tests on the synchronization stability e.g. in dependence of the collision rate and data load need to be performed during the upcoming commis-

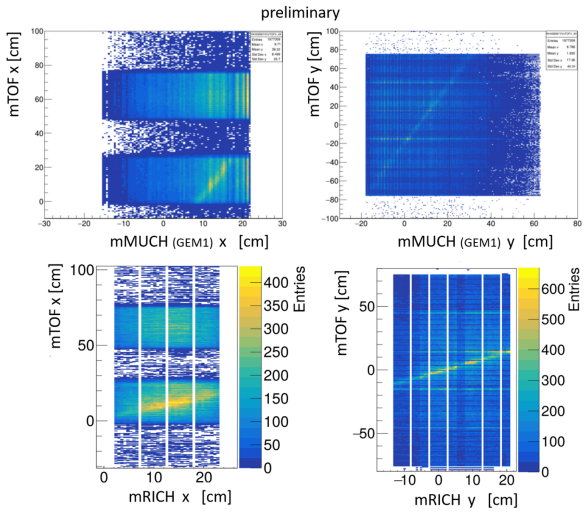

Figure 4: First preliminary results obtained during the December 2019 run – the upper pictures show correlations between spatial coordinates of the mTOF vs. the mMUCH subsystem (x left, y right), the lower figures between mTOF vs. mRICH.

sioning beam campaign in 2020. As the next steps, completion of the detector subsystems as well as major DAQ upgrades towards the final CBM configuration are foreseen.

References

[1] J. Heuser, W. F.J. Müller, V. Pugatch, P. Senger, C. J. Schmidt, C. Sturm and U. Frankenfeld, Technical Design Report for the CBM Silicon Tracking System (STS), GSI-2013-05499, http://repository.gsi.de/record/54798

[2] S. Chattopadhyay, Y. P. Viyogi, P. Senger, W. F.J. Müller and C. J. Schmidt, Technical Design Report for the CBM : Muon Chambers (MuCh), GSI-2015-02580, https://repository.gsi.de/record/161297

[3] C. Höhne et al., Technical Design Report for the CBM Ring Imaging Cherenkov Detector (RICH), GSI-2014-00528, http://repository.gsi.de/record/65526

[4] C. Blume, C. Bergmann, D. Emschermann, Technical Design Report for the CBM Transition Radiation Detector (TRD), GSI-2018-01091, http://repository.gsi.de/record/217478

[5] N. Herrmann et al., Technical Design Report for the CBM Time-of-Flight System (TOF), GSI-2015-01999, https://repository.gsi.de/record/109024

[6] F. Guber and I. Selyuzhenkov, Technical Design Report for the CBM Projectile Spectator Detector (PSD), GSI-2015-02020, https://repository.gsi.de/record/109059

[7] H.R. Schmidt, J.M. Heuser and the CBM STS working group, Silicon Tracking System – Summary,
J. Heuser et al., Test of a fully integrated STS detector module in proton beam at COSY,
(this) CBM Progress Report 2019

[8] S. Chattopadhyay, Muon Chambers (MuCh) for the Compressed Baryonic Matter (CBM) experiment at FAIR,
A. Kumar et al., Response of mMUCH modules in the mCBM campaign 2019,
A. Agarwal et al., A Study of mMuCh Response at low and high intensity Pb+Au collisions at mCBM 2020,
A. Sen and V. Singhal, Implementation of Electronic FEB Id and channel Id for MUCH,
S. Roy and V. Singhal, Automatized noise separation technique for mMUCH data,
V. Negi, J. Saini, and S. Chattopadhyay, mCBM slow control system for mMUCH Detector,
(this) CBM Progress Report 2019

[9] C. Blume and the CBM-TRD working group, Summary on the TRD project,
P. Raisig, F. Roether, P. Kähler, D. Spicker, and D. Schmidt, Preparation of the SPADIC 2.2 based readout of the TRD for the mCBM 2020 beamtime,
(this) CBM Progress Report 2019

[10] I. Deppner , N. Herrmann , and the CBM TOF working group, TOF - Summary,
Q. Zhang, I. Deppner, and N. Herrmann, mTOF performance during beam tests in 2019,
(this) CBM Progress Report 2019

[11] C. Höhne, K.-H. Kampert, C. Pauly, and the CBM RICH working group, RICH summary,
A. Weber, T. Geßler , S. Lebedev, E. Ovcharenko, and C. Höhne, mRICH status and first data analysis,
T. Geßler, A. Weber, E. Ovcharenko, and C. Höhne, Read-Out Chain Development for the mRICH and RICH Detectors,
(this) CBM Progress Report 2019

[12] F. Guber, Progress in Projectile Spectator Detector project,
(this) CBM Progress Report 2019

[13] D. Hutter , J. de Cuveland , and V. Lindenstruth, mFLES Node and InfiniBand HDR Upgrade,
(this) CBM Progress Report 2019

[14] W.M. Zabołotny and G. Kasprowicz, "Data processing boards design for CBM experiment", Proc. SPIE 9290 (2014) 929023, doi:10.1117/12.2073377

Status of eTOF at STAR*

I. Deppner[1], *D. Emschermann*[3], *J. Frühauf*[3], *T. Galatyuk*[2], *N. Herrmann*[1], *P.-A. Loizeau*[3], *F. Seck*[2], *Y. Söhngen*[1], *Y. Sun*[4], *I. Vassiliev*[3], *Y. Wang*[5], *Ph. Weidenkaff*[1], *and STAR eTOF group*

[1]Ruprecht-Karls-Universität Heidelberg, Germany; [2]Technische Universität Darmstadt, Germany; [3]Gesellschaft für Schwerionenforschung (GSI), Darmstadt, Germany; [4]USTC, Hefei, China; [5]Tsinghua University, Beijing, China

The eTOF project is part of CBM's FAIR Phase 0 program. It comprises the installation, commissioning and operation of CBM TOF modules positioned at the east pole tip of the STAR apparatus (see Fig. 1) during the Beam Energy Scan II (BESII) campaign and the participation in the data analysis obtained in runs with eTOF. The full hardware installation was completed in Nov. 2018. After a commissioning phase of about 10 weeks the first data taking started in Feb. 2019 by recording about 580 M Au+Au events at $\sqrt{s_{NN}} = 11.5\,GeV$ with an eTOF efficiency of 85%. However, due to several beam loss events causing instantaneous high currents on the readout strips all eTOF preamplifier boards got damaged and no further useful operation was possible during this campaign. After a careful analysis of the damage it was decided to replace all PADI boards with an improved version using ESD protections diodes on the input. This was a major intervention since the preamplifier boards sit inside the gas box and therefore all modules had to be dismantled. Nevertheless the total repair action including recommissioning could be finished within 2.5 weeks.

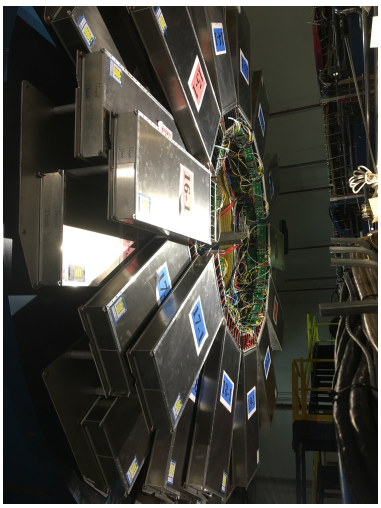

Figure 1: Photogaph of the eTOF wheel mounted on the east side magnet pole tip

Table1 summarizes the data set taken during the STAR Beam Energy Scan II campaign running from December 2019 to March 2020. The 9.2 GeV collider run could not be finished due to the Corona shut down. All fix target runs were successfully completed and about 100 M eTOF events were collected each.

The readout system for eTOF is using CBM's free-streaming architecture and CBM's hard- and software components. It comprises 216 PADI and 216 GET4 boards (108 counters) distributed over 36 modules which are grouped in 12 sectors. From each module 2×20 m long duplex fibers transport the data which were accumulated by 2 GBTx

Mode	$\sqrt{s_{NN}}$ [GeV]	E_{beam} [GeV]	# events with eTOF	Status
Col.	11.5	5.75	127 M	finished
Col.	9.2	4.6	30 M	not finished
FXT	7.7	31.2	100 M	finished
FXT	6.2	19.5	80 M	finished
FXT	5.2	13.5	89 M	finished
FXT	4.5	9.8	106 M	finished
FXT	3.9	7.3	106 M	finished
FXT	3.5	5.75	100 M	finished

Table 1: Data set taken during the STAR Beam Energy Scan II campaign running from December 2019 to March 2020

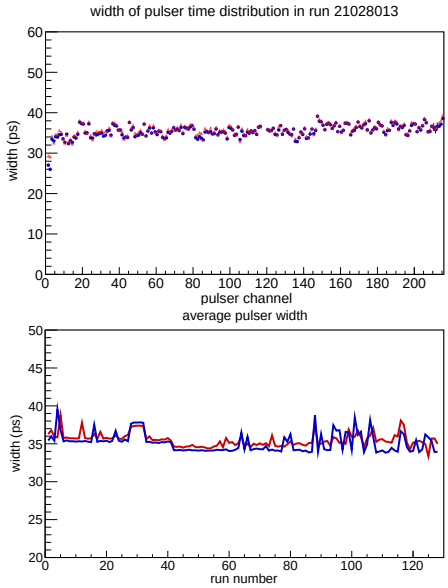

Figure 2: Upper plot: width of the time distribution obtained by measuring the arrival time of injected pulser signals on every GET4 board. Lower plot: mean of the time distribution width vs. the run number.

*This project was partially funded by BMBF 05P15VHFC1

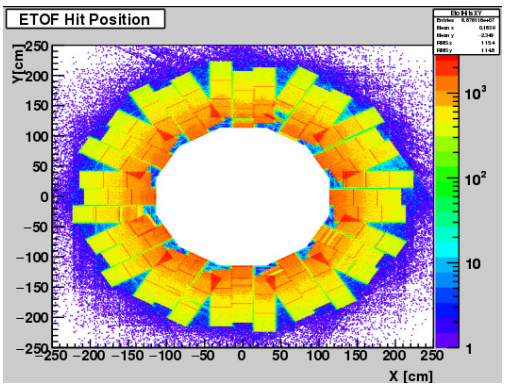

Figure 3: eTOF hit distribution monitored by the online QA plot obtained for one $\sqrt{s_{NN}} = 7.7\,GeV$ fix target run.

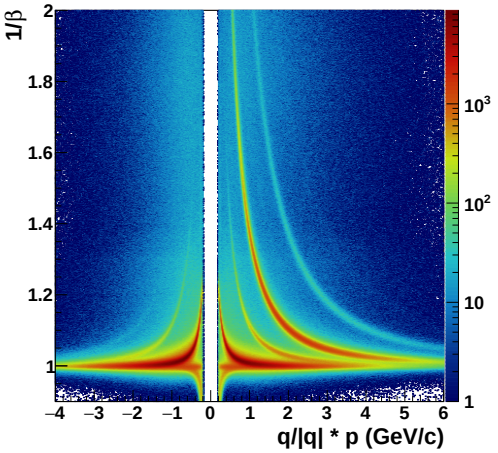

Figure 4: PID plot obtained after detector calibration for $\sqrt{s_{NN}} = 7.7\,GeV$ fix target data.

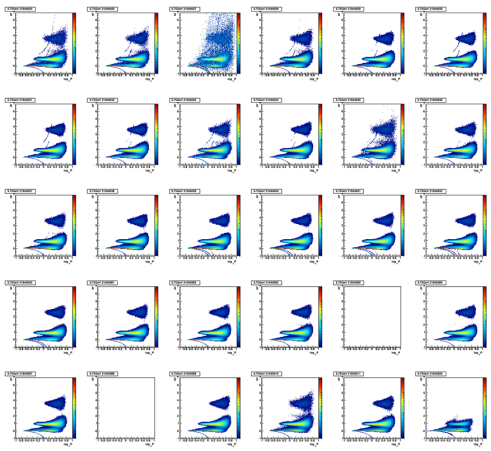

Figure 5: PID QA plots obtained with KF particle finder package for several consecutive runs for $\sqrt{s_{NN}} = 3.5\,GeV$ fix target data.

chips to a μTCA crate housing 12 AFCKs (one for each sector). From here the data are sent via 12×100 m long duplex fibers to the FLes Interface Board (FLIB) located in the DAQ room of STAR. In comparison to 2019 an improved clock distribution method was installed offering a system synchronization in the order of 35 ps over the full wheel (see upper plot in Fig. 2). This plot shows the width of the time distribution (red corresponds to the Gaussian sigma and blue to the RMS) obtained by measuring the arrival time of injected pulser signals on every GET4 board. The stability of the system is demonstrated on the lower plot of Fig. 2. Here the mean of time distribution width from all pulser channels is plotted vs. the run number. The range of 130 runs reflects a time period of several days. The online event building is performed with ZMQ in parallel on 12 CPUs and is based on the trigger token information (received from STAR) injected in the data stream at the AFCK level. A time window of 3 μs around the trigger time stamp is selected and sent to the STAR event builder where the data are monitored and stored for offline analysis.

Fig. 3 shows an online QA plot of the eTOF hit distribution in the global xy-plane obtained from one run (30 min) of $\sqrt{s_{NN}} = 7.7\,GeV$ fix target data. Even with a preliminary calibration the MRPC hits show a uniform distribution with a rate gradient towards the center and only a tiny fraction is reconstructed outside the active area. However, this plot also illustrates some observed features. The blue spot at 1'o clock position visualizes an inactive region on the RPC surface caused presumably by a beam loss event. This counter shows an increased HV current and could be replaced on the next shutdown (fall this year). Remarkable in Fig. 3 are several bands (always 4 strips together) with a lower hit density which arise from synchronization instabilities of specific FEE ASICs. Similar effects were observed in the mTOF readout and are currently under investigation.

Beside minor issues described above eTOF showed an excellence performance during RUN20. A reliable start-up procedure and control interface was implemented that allows the full system to be controlled via only 2 commands issued by the shift crew. During the last two month almost no intervention from experts was required. Currently the offline data calibration is ongoing and preliminary performance results in terms of matching efficiency with the TPC and time resolution are shown in [1] (this PR). Fig. 4 obtained with $\sqrt{s_{NN}} = 7.7\,GeV$ fix target data demonstrates the PID capability of eTOF. Kaon to pion separation is enabled up to a momentum of 2.5 GeV/c. PID quality plots can also be obtained run by run with the KF particle finder package as presented in Fig. 5 for $\sqrt{s_{NN}} = 3.5\,GeV$ fix target data. The two empty histogram denote the non-presence of eTOF within this runs. The start of the physics analysis including eTOF data will follow soon.

References

[1] Ph. Weidenkaff, "Status of eTOF performance analysis in the STAR RUN20",, CBM Progress Report 2019, (this report)

Status of the eTOF at STAR program after the 2019-2020 beam campaign*

Ph. Weidenkaff[1], *I. Deppner*[1], *N. Herrmann*[1], *F. Seck*[2], *J. Frühauf*[3], *and P. A. Loizeau*[3]

[1]Ruprecht-Karls-Universität Heidelberg, Germany; [2]Technische Universität Darmstadt, Germany; [3]Gesellschaft für Schwerionenforschung (GSI), Darmstadt, Germany

During the STAR Beam Energy Scan II campaign from December 2019 to March 2020, data from Au+Au collisions have been taken at center of mass energies of $11.5\,GeV$ and $9.2\,GeV$ in collider mode as well as at $7.7\,GeV$, $6.2\,GeV$, $5.2\,GeV$, $4.5\,GeV$, $3.9\,GeV$ and $3.5\,GeV$ in fixed target mode. A performance analysis of eTOF is shown at the example of the $7.7\,GeV$ fixed target data. We take mainly a look at matching efficiency and time resolution.

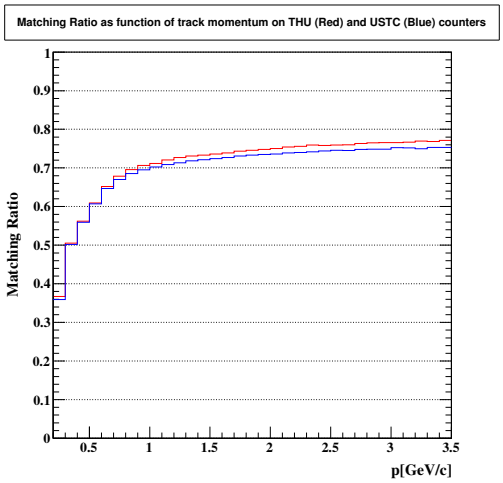

Figure 1: Matching Ratio for THU (red) and USTC (blue) counters in $7.7\,GeV$ fixed target data as function of the track momentum.

Matching efficiency is defined as the ratio of TPC tracks which intersect with eTOF and have an eTOF hit within matching distance over the total number of TPC tracks whose extrapolation intersects with eTOF. This ratio depends systematically on the intrinsic efficiency of the detector as well as helix extrapolation of the track from the TPC to eTOF. The later depends again on the number of tracking points in the TPC, the momentum resolution of the track and multiple scattering along the trajectory. The resulting matching efficiencies as function of the momentum can be seen in fig. 1. As the RPCs detector efficiency has no intrinsic momentum dependence, the drop towards lower momentum is due to multiple scattering. From around $0.8\,GeV/c$ to $3.5\,GeV/c$, the region where eTOF is most important for PiD, we see a plateau with only a weak momentum dependency. The mean efficiency of in the plateau is 73.3% and 72.41% for USTC and THU counters respectively.

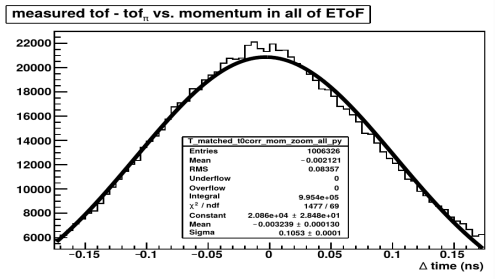

Figure 2: Time-of-flight - expected time of flight for pions for all of eTOF in $7.7\,GeV$ fixed target data.

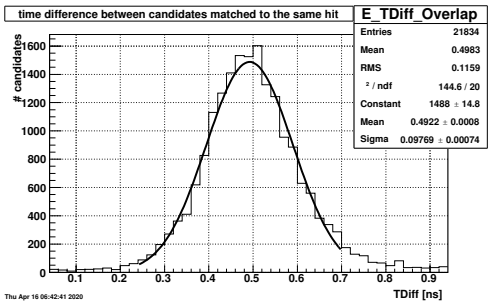

Figure 3: Time difference of hits in the overlap between Sector 17 and 18 that are matched to the same track.

The time resolution of the system is determined by comparing the measured time of flight to an expectation . This expectation is derived from the measured momentum and pathlength from the TPC and pion assumption. This system resolution (see fig. 2) contains the time resolution of the RPC as well as the resolution of the start time and the uncertainty of the momentum measurement. The start time is determined from the fastest pions in each event measured by the barrel-ToF system with resolution of $\sim 35\,ps$. Another systematic effect is the syncronisation between eTOF and STAR which is achieve by a pulser with $\sim 35\,ps$ jitter. Finally, the spectrum is also contaminated by a background of non-pions. To exclude these systematic influences, the time resolution between two RPCs is checked from the overlap of 2 sectors (see fig. 3). From this, an RPC resolution better than $70\,ps$ can be deduced.

Physics analysis of these data is the focus of future work.

*This project was partially funded by BMBF 05P15VHFC1

The KF Particle Finder approach for the online reconstruction of multi-strange hyperons and their life time determination in STAR*

I. Vassiliev[1], *Y. Fisyak*[2], *H. Ke*[2], *I. Kisel*[1,3,4,5], *and A. Tang*[2]

[1]GSI, Darmstadt, Germany; [2]Brookhaven National Laboratory, Upton, USA; [3]Goethe-Universitaet Frankfurt, Frankfurt am Main, Germany; [4]Frankfurt Institute for Advanced Studies, Frankfurt am Main, Germany; [5]Helmholtz Research Academy Hesse for FAIR, Frankfurt am Main, Germany

The exploration of the QCD phase diagram is the main goal of the CBM experiment and the prime motivation of the RHIC beam energy scan program. Strange and multistarange hyperons are sensitive probes to identify the phase boundary or the onset of deconfinement. One of the predicted signatures of the phase transition from nuclear matter to a deconfined phase is the enhanced production of multi-strange particles. Additionally the yield of particles carrying strange (anti)-quarks is expected to be sensitive to the fireball evolution and formation of the Quark Gluon Plasma (QGP).

The KF Particle Finder package [1], initially developed as a reconstruction tool for the CBM experiment, was intensively tested by the CBM collaboration during the last decade on the simulated data. The application of the KF Particle Finder package on real STAR data started a few years ago, and now is continuosly used by STAR as one of the main tools for the data analysis. The use of the CBM KF Particle Finder package for the fast analysis of real data is also an important goal of the FAIR phase 0 program.

The STAR experiment has taken data in Au+Au collisions at $\sqrt{s_{NN}}$ = 11.5 GeV in the year 2020. The detailed description of the experimental setup and the sub-detectors for tracking, particle identification, etc., can be found in [2]. The reconstructed STAR Time Projection Chamber (TPC) tracks were used as an input for the KF Particle package together with the reconstructed primary vertex. The location of the primary vertex of an event was selected within a radius r less than 2 cm, and the z-direction was in the range [-70,70] cm. The accepted amount of minimum bias events was about $216 \cdot 10^6$. The dE/dx was used for the identification of the charged daughter particles $\pi^{\pm}$, $K^{\pm}$ and $p, \bar{p}$.

Multi-strange hyperons were successfully identified online by their decay into charged hadrons, using the KF Particle Finder selection technique developed for CBM. Standard CBM-like cuts on a track χ^2_{prim}, reconstructed particle vertex cut, L/dL cut and topology constrained cut χ^2_{topo}, etc are used. In Fig. 1 the reconstructed invariant mass spectra of Λ, $\bar{\Lambda}$, Ξ^-, $\bar{\Xi}^+$, Ω^-, $\bar{\Omega}^+$ particles are shown. All signals are clearly visible with excellent signal to background ratio well above 30 even for the most challenging Ω hyperons. The position and width of the peaks are in a good agreement with the PDG data. In the collider mode, the efficiencies for the reconstruction of strange and multi-strange hyperons are well controlled and were used

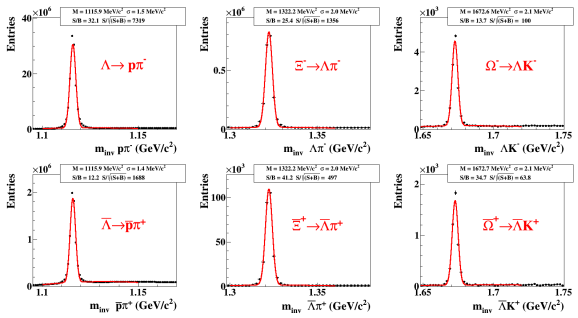

Figure 1: The reconstructed invariant-mass distribution of Λ, $\bar{\Lambda}$, Ξ^-, $\bar{\Xi}^+$, Ω^-, $\bar{\Omega}^+$ particles in Au+Au minbias collisions at $\sqrt{s_{NN}}$ = 11.5 GeV, the red line indicates the signal plus background fit by a polynomial plus Gaussian function.

for the tests of life time express analysis for Λ, Ξ^-, $\bar{\Lambda}$ and $\bar{\Xi}^+$. In Fig. 2 the reconstructed life time $c\tau$ distributions

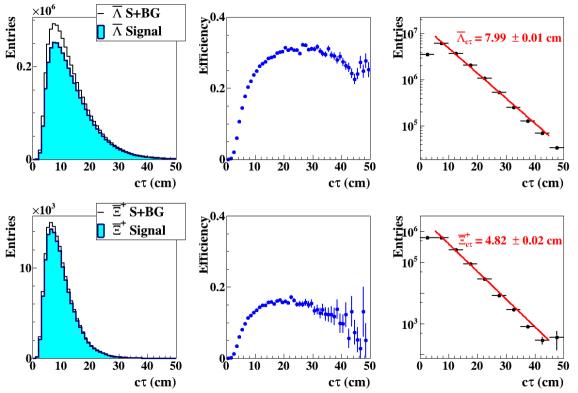

Figure 2: Reconstructed life time distributions (left) of the $\bar{\Lambda}$ and $\bar{\Xi}^+$ candidates where light blue filled histogam is the extracted signal. The black line represents the signal plus side band background. $\bar{\Lambda}$ and $\bar{\Xi}^+$ reconstruction efficiencies as function of $c\tau$ are shown in the center. Life times for $\bar{\Lambda}$ and $\bar{\Xi}^+$ obtained with exponential fit in the range 5-45 cm (right) are extracted with high presision. Systematic errors are about 1 mm.

of the $\bar{\Lambda}$ and $\bar{\Xi}^+$ candidates are shown where the light blue filled histogam is the extracted signal and the black line represents the signal plus side band background. For the efficiency calculation we use the ROOT VMC approach,

* Work supported by HICforFAIR, FIAS and BMBF.

which provides tools to account for the STAR detector misalignment from simulations. The misalignment parameters are taken from the database and are applied to the geometry used for the VMC simulation. Currently, a simplified approach for efficiency calculation is applied: 20 signal particles are simulated per each event with primary vertex positions generated using real data distributions. A thermal spectrum is assumed. Life times for $\bar{\Lambda}$ and $\bar{\Xi}^+$ obtained with an exponential fit in the range 5-45 cm are extracted with high presision. The systematic erros are about 1 mm (2%).

In conclusion, the KF Particle Finder package for the reconstrucion of short-lived particles and their life times including strange and multi-strange hyperons was successfully tested online with the STAR BES-II data at $\sqrt{s_{NN}}$ = 11.5 GeV. The most challenging Ω^- and $\bar{\Omega}^+$ particles are reproduced with excellent signal-to-background ratio. The analysis of the high quality STAR BES-II data allows to identify and develop missing tools in the KF Particle Finder package.

References

[1] I. Kisel, I. Kulakov and M. Zyzak, *Standalone First Level Event Selection Package for the CBM Experiment*, IEEE Transactions on Nuclear Science, vol. 60, No. 5, October 2013, p. 3703.

[2] K.H. Ackermann et al., Nucl. Instrum. Meth. A 499, 624 (2003).

Data quality monitoring based on the KF Particle Finder in STAR*

I. Vassiliev[1], *Y. Fisyak*[2], *H. Ke*[2], *I. Kisel*[1,3,4,5], *and A. Tang*[2]

[1]GSI, Darmstadt, Germany; [2]Brookhaven National Laboratory, Upton, USA; [3]Goethe-Universitaet Frankfurt, Frankfurt am Main, Germany; [4]Frankfurt Institute for Advanced Studies, Frankfurt am Main, Germany; [5]Helmholtz Research Academy Hesse for FAIR, Frankfurt am Main, Germany

The KF Particle Finder package [1], developed by the CBM collaboration, was used on real STAR data as a monitoring tools for data quality runs controll in the frame of the FAIR phase 0 program. A fast way from data acquisition to physics, including calibration, processing and physics analysis of the data has been developed and successfully tested in Au+Au collisions at $\sqrt{s_{NN}}$ = 3.0 GeV (Fixed target mode) in the year 2018 and was continuously developed further. The detailed description of the experimental setup and the sub-detectors for tracking, particle identification, etc., can be found in [2]. The reconstructed STAR Time Projection Chamber (TPC) tracks were used as an input for the KF Particle package together with the reconstructed primary vertex. The typical distributions of the primary vertex for fixed target runs are shown in Fig. 1. The gold target edge located at y = -2 cm is clearly seen in the XY 2D distribution, the projection on Y and X axis are shown in top right and down left correspondigly. The z-coordinate of the primary vertex is shown down right. The z-vertex resolution is about 1.2 mm and the center is located at -200.6 cm. The location of the primary vertex of an event

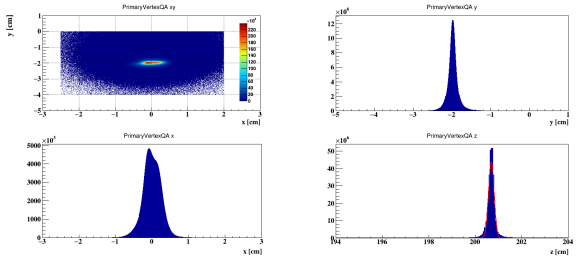

Figure 1: 2D XY primary vertex distribution (top left) for the fixed target 3.85 GeV Au+Au collisions with clearly seen gold target edge located at y = -2 cm. The projection on Y and X axis are shown in top right and down left correspondigly. Primary vertex z-coordinate distribution is shown down right. The z-vertex resolution is about 1.2 mm.

was checked by the selected within a XY-box [-3 cm, 2 cm x -4 cm, 0 cm] and the z-coordinate of the vertex was in the range [196 cm, 204 cm] run by run.

The dE/dx provides by the TPC run by run was used for the identification of the charged particles $\pi^{\pm}$, K$^{\pm}$, $p, \bar{p}$, $d^{\pm}$ and $t^{\pm}$ and heavy fragments like ^{3}He and ^{4}He shown in Fig. 2 (up). In the fixed target runs (year 2020) the eTOF detector developed for the CBM experiment was used at STAR as a part of the FAIR Phase 0 program. The eTOF is covers the rapidity range from -1.1 to -1.6. Combined with the newly installed iTPC, the eTOF provides particle identification capability in forward direction at STAR which is crucial to the Fixed Target program at BES-II. The identification capability of charged hadrons is greatly extended compared with that achieved by TPC and eTOF separately. In Fig. 2 (down) the m^2 of the $\pi^{\pm}$, K$^{\pm}$, $p, \bar{p}$, $d^{\pm}$ and ^{4}He selected by eTOF run by run are shown. This DQ plots available online and shows excellent work of the TPC and eTOF detectors achieved in year 2020.

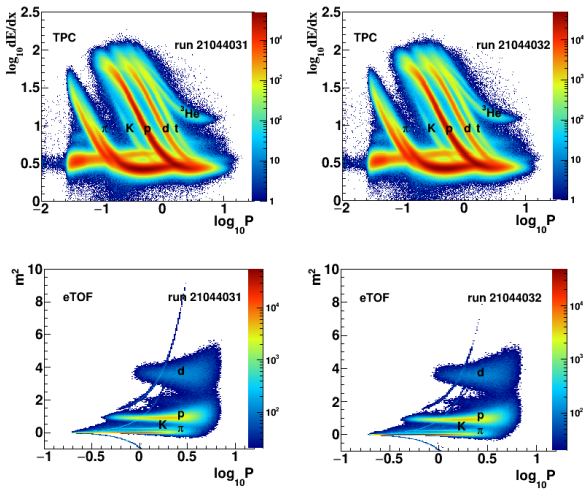

Figure 2: Run by run distribution of $log_{10}(dE/dx)$ as a function of log_{10}(p) for electrons, $\pi^{\pm}$, K$^{\pm}$, $p, \bar{p}$, $d^{\pm}$ and $t^{\pm}$ and heavy fragments like ^{3}He and ^{4}He (up). The units of dE/dx and momentum (p) are keV/cm and GeV/c, respectively. The particle locuses are follow correspondent Bichsel's prediction. The m^2 of the $\pi^{\pm}$, K$^{\pm}$, $p, \bar{p}$, $d^{\pm}$ and ^{4}He selected by eTOF (down).

The robust CA tracking in combination with excellent particle identification provied by TPC, bTOF and eTOF allows to reconstruct the complicated decay topology for multi-strange hyperons online using the KF Particle Finder package and the CBM developed selection technique. Standard CBM-like cuts on a track χ^2_{prim}, reconstructed particle vertex cut, L/dL cut and topology constrained cut χ^2_{topo}, etc are used. In Fig. 3 the reconstructed invariant mass spectra of Λ cadidates are shown. All signals are

* Work supported by HICforFAIR, FIAS and BMBF.

clearly visible with excellent signal to background ratio. The position and width of the peaks are in a good agreement with the PDG data. In Fig. 3 the online reconstructed

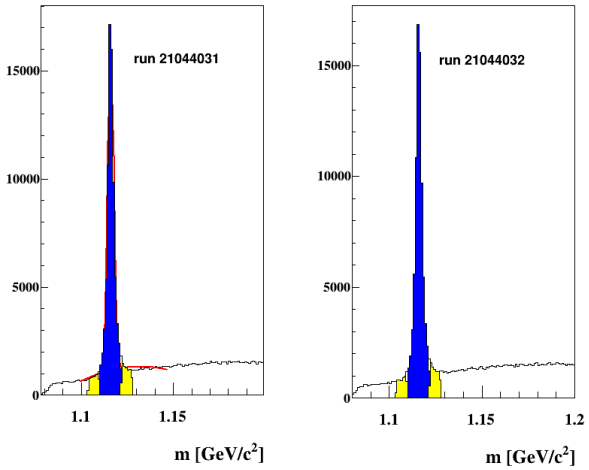

Figure 3: Run by run reconstructed invariant mass of $p\pi^-$ pairs (black). The peaks of Λ and combinatorial background under $\pm 3\sigma$ region are shown as blue histograms. The combinatorial background for the side bands analysis are shown as yellow histograms.

invariant mass of $p\pi^-$ pairs are shown as black histograms. The typical mass resolution is about 1.7 MeV/c^2.

In conclusion, the express production provides a high quality dE/dx measurement for particles up to heavy fragments and together with eTOF and bTOF measurements allows to obtain clean spectra with high significance. The method is implemented right on the HLT farm and allows to perform the physics analysis of the data during the process of data taking. The express chain provides an access to the processed data with a delay of only about one day, which is necessary for the production and copying of picoDST files from HLT to RCF, and allows to do the physics analysis of the experimental data in the regular environment. We have already processed all the currently collected energies of BES-II, which allows to study a wide range of physics including hyperons and hypernuclei in one go using the KF Particle Finder package.

References

[1] I. Kisel, I. Kulakov and M. Zyzak, *Standalone First Level Event Selection Package for the CBM Experiment*, IEEE Transactions on Nuclear Science, vol. 60, No. 5, October 2013, p. 3703.

[2] K.H. Ackermann et al., Nucl. Instrum. Meth. A 499, 624 (2003).

CBM Publications 2019

- J. Adamczeswki-Musch *et al.*
Event reconstruction of free-streaming data for the RICH detector in the CBM experiment
EPJ Web Conf. 214 (2019) 01043

- K. Agarwal *et al.*
Progress towards the development of cooling demonstrator for the STS detector of the CBM experiment at FAIR
Nucl. Instrum. Methods A 936 (2019) 691

- E. Akishina *et al.*
Experience of the Development of the Geometry Database for the CBM Experiment
EPJ Web Conf. 214 (2019) 02030

- S. Chakraborty *et al.*
A new type of RPC with very low resistive material
Nucl. Instrum. Methods A 936 (2019) 424

- S. Chatterjee *et al.*
Study of uniformity of characteristics over the surface for triple GEM detector
Nucl. Instrum. Methods A 936 (2019) 491

- I. Deppner and N. Herrmann
The CBM Time-of-Flight system
JINST 14 (2019) C09020

- M. Deveaux
Progress on the radiation tolerance of CMOS Monolithic Active Pixel Sensors
JINST 14 (2019) R11001

- V. Friese
A cluster-finding algorithm for free-streaming data
EPJ Web Conf. 214 (2019) 01008

- M. Guminski, W. Zabolotny, A. Byszuk and P. Kosniak
Sorting of STS-XYTER2 data for microslice building for CBM experiment
PoS(TWEPP2018)143 (2019)

- D. Hu *et al.*
MRPC3b mass production for CBM-TOF and eTOF at STAR
JINST 14 (2019) C06013

- N. Karpushkin *et al.* (CBM Collaboration)
The Projectile Spectator Detector for measuring the geometry of heavy ion collisions at the CBM experiment on FAIR
Nucl. Instrum. Methods A 936 (2019) 156

- N. Karpushkin, F. Guber and A. Ivashkin
Application of the Prony least squares method for fitting signal waveforms measured by sampling ADC
AIP Conf. Proc. 2163 (2019) 030006

- P. Lyu *et al.*
Study on cosmic test and QC method of high-rate MRPC for CBM-TOF
JINST 14 (2019) C09032

- V. Mikhaylov *et al.* (CBM Collaboration)
The very forward hadron calorimeter PSD for the future CBM@FAIR experiment
EPJ Web Conf. 204 (2019) 11004

- M. Petris *et al.*
Performance of a two-dimensional position sensitive MRPC prototype with adjustable transmission line impedance
Nucl. Instrum. Methods A 920 (2019) 100

- S. Roy *et al.*
Study of performances of a straw tube detector with high rate
Nucl. Instrum. Methods A 936 (2019) 488

- S. Roy *et al.*
Stability study of gain and energy resolution for GEM detector
Nucl. Instrum. Methods A 936 (2019) 485

- P. Senger *et al.* (CBM Collaboration)
Exploring Cosmic Matter in the Laboratory - The Compressed Baryonic Matter Experiment at FAIR
Particles 2 (2019) 499

- W. Zabolotny *et al.*
GBT oriented firmware for Data Processing Boards for CBM
PoS(TWEPP2018)067 (2019)

Doctoral, diploma, master and bachelor theses 2019

http://cbm-wiki.gsi.de/cgi-bin/view/Public/Thesis2019

CBM presentations 2019

http://cbm-wiki.gsi.de/cgi-bin/view/Public/PublicPresentations2019

CBM PhD Award 2018 / 2019

The CBM PhD Award decorates the best doctoral work related to the CBM experiment. With this award, the CBM collaboration especially wants to honour the contributions of students to the CBM project. The award was granted for the first time at the CBM Collaboration Meeting in April 2016 for PhD theses defended in the year 2015. It is given annually and is endowed with a prize money of 500 Euro. The criteria for the evaluation are:

- Impact on the CBM present and future activities, taking into account active participation in CBM (40%);
- Added scientific value in the field of the PhD thesis (30%);
- Publications in refereed journals to which the candidate had a significant contribution (30%).

The prize winner for 2018 is

Dr Hanna Malygina

from Goethe-Universität Frankfurt for her work on

Hit reconstruction for the Silicon Tracking System of the CBM experiment

The prize winner for 2019 is

Dr Ievgenii Kres

from Bergische Universität Wuppertal for his work on

Optimization of the CBM-RICH detector geometry and its use for the reconstruction of neutral mesons using conversion method

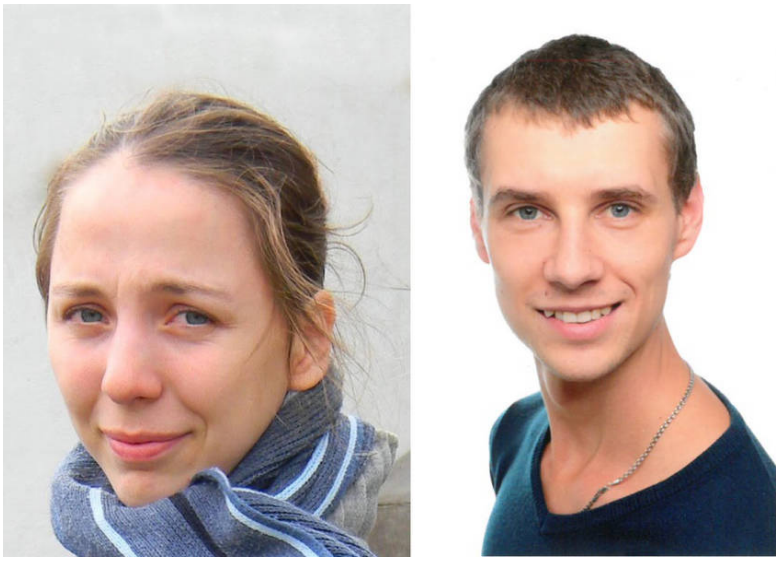

Left: Dr Hanna Malygina, winner of the CBM PhD Award 2018; right: Dr Ievgenii Kres, awardee for the year 2019

The CBM Collaboration

- **Aligarh, India, Department of Physics, Aligarh Muslim University**

  N. Ahmad, M.D. Azmi, M. Irfan, H. Jahan, M.M. Khan, O. Singh

- **Beijing, China, Department of Engineering Physics, Tsinghua University**

  Zhi Deng, Dong Han, Xinjie Huang, Yuanjing Li, Pengfei Lyu, Botan Wang, Yi Wang, Xianglei Zhu

- **Berlin, Germany, Konrad-Zuse-Zentrum für Informationstechnik Berlin (ZIB)**

  A. Reinefeld, F. Salem, F. Schintke, T. Schütt

- **Bhubaneswar, India, Institute of Physics**

  B. Mallick, P.K. Sahu, S.K. Sahu

- **Bhubaneswar, India, National Institute of Science Education and Research (NISER)**

  A. Jash, V.K.S. Kashyap, B. Mohanty, D. Roy, S. Samanta, R. Singh

- **Bucharest, Romania, Horia Hulubei National Institute of Physics and Nuclear Engineering (IFIN-HH)**

  A. Bercuci, M. Petriş, M. Petrovici, L. Radulescu, C. Schiaua

- **Bucharest, Romania, Atomic and Nuclear Physics Department, University of Bucharest**

  D. Argintaru, V. Baban, M. Călin, T. Eşanu, A. Jipa, I. Lazanu, C. Ristea, O. Ristea, N.G. Tuturas

- **Budapest, Hungary, Eötvös Loránd University (ELTE)**

  M. Csanád, A. Olar

- **Budapest, Hungary, Institute for Particle and Nuclear Physics, Wigner Research Centre for Physics, Hungarian Academy of Sciences**

  G. Balassa, T. Kiss, T. Tölyhi, D. Varga, Gy. Wolf

- **Chandigarh, India, Department of Physics, Panjab University**

  L. Kumar, N. Sharma

- **Chongqing, China, Chongqing University**

  Liang-ming Pan, Qiqi Wu, Wenxiong Zhou

- **Darmstadt, Germany, Facility for Antiproton and Ion Research in Europe GmbH (FAIR)**

  E. Clerkin, J. Eschke[1], P. Gasik[1], V. Klochkov, E. Lavrik, P.-A. Loizeau, W.F.J. Müller, A. Rost[2], A. Senger, P. Senger[3]

- **Darmstadt, Germany, GSI Helmholtzzentrum für Schwerionenforschung GmbH (GSI)**

  M. Al-Turany, M. Bajdel, D. Bertini, O. Bertini, P. Dahm, H. Deppe, A. Dubla, D. Emschermann, H. Flemming, P. Foka, U. Frankenfeld, V. Friese, J. Frühauf, Xin Gao, J. Hehner, J.M. Heuser, R. Holzmann, R. Kapell, R. Karabowicz, M. Kiš, K. Koch, P. Koczoń, D. Kresan, P. Kuhl, A. Lebedev[4], J. Lehnert, Y. Leifels, S. Löchner, O. Lubynets[3], A. Lymanets, O. Maragoto Rodriguez[3], A.M. Marin Garcia, J. Markert, D. Miskowiec, T. Morhardt, F. Nickels, W. Niebur, J. Pietraszko, C.J. Schmidt, I. Selyuzhenkov[5], M. Shiroya[3], C. Simons, C. Sturm, A. Toia[3], M. Träger, M. Traxler, F. Uhlig, I. Vassiliev, O. Vasylyev, R. Visinka, A. Wilms, P. Zumbruch, M. Zyzak

- **Darmstadt, Germany, Institut für Kernphysik, Technische Universität Darmstadt**

  T. Galatyuk[1], F. Seck

- **Dresden, Germany, Institut für Strahlenphysik, Helmholtz-Zentrum Dresden-Rossendorf (HZDR)**

  Xingming Fan[11], B. Kämpfer[11], R. Kotte, L. Naumann, D. Stach

- **Dubna, Russia, Laboratory of Information Technologies, Joint Institute for Nuclear Research (JINR-LIT)**

  T. Ablyazimov, P. Akishin, E. Alexandrov, I. Alexandrov, S. Belogurov[5], O. Derenovskaya, Victor Ivanov[5], A.V. Kryanev[5]

- **Dubna, Russia, Veksler and Baldin Laboratory of High Energy Physics, Joint Institute for Nuclear Research (JINR-VBLHEP)**

  A. Bychkov, D. Dementiev, V.V. Elsha, O. Fateev, Yu. Gusakov, G. Kekelidze, A. Kolozhvari, P. Kurilkin, S. Kuznetsov, V. Ladygin, A. Malakhov, Yu. Murin, S. Parzhitskiy, A. Shabunov, A.D. Sheremetiev, M. Shitenkow, N. Sukhov, N.I. Zamiatin, A. Zinchenko

- **Frankfurt, Germany, Frankfurt Institute for Advanced Studies, Goethe-Universität Frankfurt (FIAS)**

  A. Belousov, J. de Cuveland, S. Gorbunov, H. Hartmann, D. Hutter, I. Kisel, P. Kisel[1,4], G. Kozlov[4], V. Lindenstruth[1], A. Redelbach

- **Frankfurt, Germany, Institut für Kernphysik, Goethe-Universität Frankfurt**

  H. Appelshäuser, B. Arnoldi-Meadows, E. Bechtel, C. Blume[1], T. Bus, H. Cherif[1], M. Deveaux, M. Esen, I. Fröhlich, D. Giang, S. Gläßel, P. Klaus, M. Koziel, J. Michel, C. Müntz, M. Petri, P. Raisig, A. Rodriguez Rodriguez[1], F. Roether, D. Spicker, J. Stroth[1]

- **Frankfurt, Germany, Institute for Computer Science, Goethe-Universität Frankfurt**

  A. Adler, H. Engel, T. Janson, U. Kebschull, C. Lara, J.A. Lucio Martínez, D. Schmidt, C. Stüllein

- **Gatchina, Russia, Petersburg Nuclear Physics Institute named by B.P.Konstantinov of National Research Centre "Kurchatov Institute" (PNPI)**

  D. Ivanishchev, Vladimir Ivanov[5], A. Khanzadeev[5], L. Kochenda[5], B. Komkov, V. Kozlov, P. Kravtsov[5], E. Kryshen, L. Kudin, V. Nikulin, E. Rostchin[5], Yu. Ryabov, V. Samsonov[5,12], O. Tarassenkova, M. Zhalov

- **Gießen, Germany, Justus-Liebig-Universität Gießen**

  M. Becker, J. Bendarouach[1], M. Dürr, C. Feier-Riesen, T. Geßler, R. Haas, C. Höhne, S. Lebedev[4], E. Lebedeva, J.H. Otto, E. Ovcharenko[4], A.A. Weber, F. Zorn

- **Guwahati, India, Nuclear and Radiation Physics Research Laboratory, Department of Physics, Gauhati University**

  B. Bhattacharjee, S. Gope

- **Hefei, China, Department of Modern Physics, University of Science & Technology of China (USTC)**

  Zhiguo Ding, Dongdong Hu[6], Chao Li, Yuan Su, Yongjie Sun, Zhengyang Sun, Tianxing Wang, Xinjian Wang, Junfeng Yang, Rongxing Yang, Jianhui Yuan, Jian Zhou

- **Heidelberg, Germany, Physikalisches Institut, Universität Heidelberg**

  I. Deppner, D. Gottschalk, N. Herrmann[1], R. Kolb, E. Rubio, C. Simon, P. Weidenkaff, Qiunan Zhang[7]

- **Heidelberg, Germany, Institut für Technische Informatik, Universität Heidelberg**

  P. Fischer

- **Indore, India, Indian Institute of Technology Indore**

  S.K. Kundu, A. Roy, R. Sahoo

- **Jammu, India, Department of Physics, University of Jammu**

  A. Bhasin, A. Gupta, S. Mahajan, S.S. Sambyal

- **Karlsruhe, Germany, Karlsruhe Institute of Technology (KIT)**

  S. Bähr, M. Balzer, J. Becker, T. Blank, M. Caselle, S.P.D. Figuli, P. Pfistner, O. Sander, V. Sidorenko, E. Trifonova, K.L. Unger, M. Weber

- **Kharagpur, India, Indian Institute of Technology Kharagpur**

  T.K. Bhattacharyya, S. Sarangi, A.K. Singh, I. Som

- **Kolkata, India, Department of Physics, Bose Institute**

  R.P. Adak, S. Biswas, S. Chatterjee, Supriya Das, S.K. Ghosh, S. Mukherjee, S.K. Prasad, S. Raha, R. Ray, S. Roy, A. Sen

- **Kolkata, India, Department of Physics and Department of Electronic Science, University of Calcutta**

  A. Bhattacharyya, A. Chakrabarti, R. Ganai, G. Gangopadhyay, S. Sau

- **Kolkata, India, Variable Energy Cyclotron Centre (VECC)**

  A. Agarwal, Z. Ahammed, P.P. Bhaduri, S. Chattopadhyay[8], A.K. Dubey, C. Ghosh, Ajit Kumar, M. Mandal, E. Nandy, J. Saini, V. Singhal

- **Kraków, Poland, AGH University of Science and Technology (AGH)**

  M. Baszczyk, P. Dorosz, K. Kasiński, R. Kłeczek, W. Kucewicz, L. Mik, P. Otfinowski, R. Szczygieł, W. Zubrzycka

- **Kraków, Poland, Marian Smoluchowski Institute of Physics, Jagiellonian University**

  J. Brzychczyk, K. Łojek, Z. Majka, R. Płaneta, P. Staszel, A. Wieloch

- **Kyiv, Ukraine, High Energy Physics Department, Kiev Institute for Nuclear Research (KINR)**

  A. Chaus, O. Kot, O. Kovalchuk, V. Kyva, V. Militsija, I. Momot[3], M. Pugach, V. Pugatch, D. Ramazanov, D. Storozhyk

- **Kyiv, Ukraine, Department of Nuclear Physics, Taras Shevchenko National University of Kyiv**

  O. Bezshyyko, L. Golinka-Bezshyyko, I. Kadenko, V. Plujko

- **Moscow, Russia, Institute for Nuclear Research (INR)**

  D. Finogeev, M. Golubeva, F. Guber, A. Ivashkin, A. Izvestnyy, N. Karpushkin, A. Kurepin, N. Kurepin, A. Maevskaya, S. Morozov, O. Petukhov, A. Reshetin, A. Shabanov, N. Topil'skaya, E. Usenko

- **Moscow, Russia, Institute for Theoretical and Experimental Physics named by A.I. Alikhanov of National Research Centre "Kurchatov Institute" (ITEP) in Moscow, Russia (ITEP)**

  A. Akindinov, I. Alekseev, E. Dorenskaya, D. Golubkov, F. Khasanov, S. Kiselev, I. Korolko, N. Lyublev, D. Malkevich, K. Mikhailov, V. Plotnikov, M. Prokudin, A. Semennikov, S. Shirinkin, R. Sultanov, D. Svirida, Yu. Zaitsev, I. Zivko

- **Moscow, Russia, National Research Nuclear University MEPhI (Moscow Engineering Physics Institute)**

  E. Atkin, A. Demanov, O. Golosov, P. Ivanov, N. Kargin, E. Kashirin, E. Malankin, O. Malyatina, D. Normanov, P. Parfenov, I. Segal, V. Shumikhin, M. Strikhanov, A. Taranenko

- **Moscow, Russia, National Research Centre "Kurchatov Institute"**

  D. Blau[5], A. Kazantsev, V. Manko, I. Sibiryak, I. Yushmanov

- **Moscow, Russia, Skobeltsyn Institute of Nuclear Phyiscs, Lomonosov Moscow State University (SINP-MSU)**

  N. Baranova, D. Karmanov, M. Korolev, I. Kudryashov, M. Merkin, A. Voronin

- **Münster, Germany, Institut für Kernphysik, Westfälische Wilhelms-Universität Münster**

  A. Andronic, J. Beckhoff, R. Berendes, F. Fidorra, N. Heine, P. Kähler, Ch. Klein-Bösing, M. Kohn, A. Meyer-Ahrens, H. Morgenweck, P. Munkes, A. Puntke, P.M. Schneider, L. Wahmes, J.P. Wessels

- **Prague, Czech Republic, Czech Technical University (CTU)**

  V. Petráček, L. Škoda

- **Protvino, Russia, Institute for High Energy Physics (IHEP)**
  S. Golovnya, S. Gorokhov, A. Kiryakov, I. Lobanov, E. Lobanova, Yu. Tsyupa, A. Vorobiev
- **Pusan, Korea, Pusan National University (PNU)**
  In-Kwon Yoo
- **Řež, Czech Republic, Nuclear Physics Institute of the Czech Academy of Sciences**
  P. Chudoba, A. Kugler, V. Mikhaylov
- **Srinagar, India, Department of Physics, University of Kashmir**
  A. Ahmad, F. Ahmad, S. Bashir, S.A. Bhat, T.A. Bhat, W.A. Bhat, M.F. Mir, W. Raja
- **Tübingen, Germany, Physikalisches Institut, Eberhard Karls Universität Tübingen**
  K. Agarwal, Susovan Das, E. Friske, S. Khan, S. Mehta, I. Panasenko[9], H.R. Schmidt[1], M. Völkl, E. Volkova
- **Varanasi, India, Department of Physics, Banaras Hindu University (BHU)**
  Ajay Kumar, S. Pandey, B.K. Singh, C.P. Singh
- **Warsaw, Poland, Faculty of Physics, Warsaw University of Technology**
  J. Pluta, D. Wielanek, H. Zbroszczyk
- **Warsaw, Poland, Institute of Electronic Systems, Warsaw University of Technology**
  M. Gumiński, G. Kasprowicz, M. Kruszewski, P. Miedzik, K. Poźniak[10], R. Romaniuk, W. Zabołotny[10]
- **Warsaw, Poland, Faculty of Physics, University of Warsaw**
  T. Matulewicz, K. Piasecki, D. Wójcik
- **Wuhan, China, College of Physical Science and Technology, Central China Normal University (CCNU)**
  Wendi Deng, Sheng Dong[6], Shu He, Guangming Huang, Feng Liu, Xiaofeng Luo, Shusu Shi, Dong Wang, Zhongbao Yin, Xiaoming Zhang, Yu Zhang, Daicui Zhou
- **Wuppertal, Germany, Fakultät für Mathematik und Naturwissenschaften, Bergische Universität Wuppertal**
  K.-H. Becker, J. Förtsch, K.-H. Kampert, I. Kres, V. Patel, C. Pauly, D. Pfeifer, S. Querchfeld, J. Rautenberg
- **Yichang, China, College of Science, China Three Gorges University (CTGU)**
  Sheng-Qin Feng, Jian-Hao Ma, Ke-Jun Wu, Yan-Qing Zhao, Sheng Zheng

Additional affiliations:
[1] GSI Helmholtzzentrum für Schwerionenforschung GmbH (GSI), Darmstadt, Germany
[2] Institut für Kernphysik, Technische Universität Darmstadt, Darmstadt, Germany
[3] Institut für Kernphysik, Goethe-Universität Frankfurt, Frankfurt, Germany
[4] Laboratory of Information Technologies, Joint Institute for Nuclear Research (JINR-LIT), Dubna, Russia
[5] National Research Nuclear University MEPhI (Moscow Engineering Physics Institute), Moscow, Russia
[6] Physikalisches Institut, Universität Heidelberg, Heidelberg, Germany
[7] Department of Engineering Physics, Tsinghua University, Beijing, China
[8] Department of Physics, Bose Institute, Kolkata, India
[9] High Energy Physics Department, Kiev Institute for Nuclear Research (KINR), Kyiv, Ukraine
[10] Faculty of Physics, University of Warsaw, Warsaw, Poland
[11] also: Technische Universität Dresden, Dresden, Germany
[12] also: St. Petersburg Polytechnic University (SPbPU), St. Petersburg, Russia

Contacts

Chairman of the Collaboration Board
Nu Xu
nxy@lbl.gov

Spokesman
Norbert Herrmann
n.herrmann@physi.uni-heidelberg.de

Deputy Spokesman
Subhasis Chattopadhyay
sub@vecc.gov.in

Deputy Spokesman
Vladimir Ladygin
vladygin@jinr.ru

Technical Coordinator
Walter Müller
w.f.j.mueller@gsi.de

Physics Coordinator
Ilya Selyuzhenkov
i.selyuzhenkov@gsi.de

Computing Coordinator
Volker Friese
v.friese@gsi.de

Resource Coordinator
Jürgen Eschke
j.eschke@gsi.de

Chairman of the Conference Board
Hans-Rudolf Schmidt
h.r.schmidt@gsi.de

Management Board
Peter Senger, Joachim Stroth, Wojciech Zabołotny

http://www.fair-center.eu/for-users/experiments/cbm.html

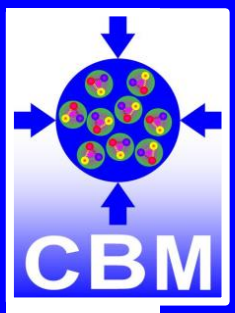
CBM


FAIR


HELMHOLTZ
GEMEINSCHAFT


GSI


Bundesministerium
für Bildung
und Forschung


HIC for FAIR
Helmholtz International Center


ESCAPE
European Science Cluster of Astronomy &
Particle physics ESFRI research infrastructures


STRONG
2020


CREMLIN PLUS
Connecting Russian and European Measures
for Large-scale Research Infrastructures